J. Hydrol. Hydromech., 67, 2019, 1, 1–3
DOI: 10.2478/johh-2018-0027

Thematic Issue on Snow Resources and Hydrological Cycle

Massimiliano Zappa[1*], Ladislav Holko[2], Martin Šanda[3], Tomáš Vitvar[3, 5], Juraj Parajka[4]

[1] Swiss Federal Research Institute WSL, Zürcherstrasse 111, 8903 Birmensdorf, Switzerland.
[2] Slovak Academy of Sciences, Institute of Hydrology, Dúbravská cesta 9, 84104 Bratislava, Slovakia.
[3] Czech Technical University in Prague, Thákurova 7, 166 29 Prague 6, Czech Republic.
[4] Institute of Hydraulic Engineering and Water Resources Management, Vienna University of Technology, Vienna, Austria.
[5] Escuela Superior Politécnica del Litoral, Guayaquil, Ecuador.
[*] Corresponding author. E-mail: massimiliano.zappa@wsl.ch

INTRODUCTION

The importance of snow in the local, regional and global cycles of freshwater is highly acknowledged (Lemke et al., 2007). In many areas of the world freshwater first accumulates in form of snow and later releases the meltwater to soils, groundwater, reservoirs and rivers.

The assessment of the impact of global warming on snow and in general on the cryosphere should be supported by high quality observations (Vaughan et al., 2013). Barnett et al. 2005 stated that the impacts of global climate change are mostly relevant for the areas where water and snow resources are closely linked, such as in the mountains of the Central and Eastern Europe (Marty et al., 2017). However, Klemeš (1990) considered mountains highly challenging in the perspective of description of hydrological processes and modelling. This is mostly linked with highly variable topography, land cover and soil properties and the complex interaction between climate and landscape elements in these environments (Gurtz et al., 1999).

Snowmelt is the key governing variable in shaping the regime of many rivers (Barnhart et al., 2016). It is predicted that the climate change will cause an increase of liquid precipitation at the cost of solid precipitation (Berghuijs et al., 2014). Therefore, sound analyses and modelling experiments are needed to understand how changing snow resources will change the way water is managed in mountain regions and in the regions where the supply of water for population, irrigation and hydro energy is linked with the seasonal dynamic of snowpack (Mankin et al., 2015; Viviroli et al., 2011). Besides the snowmelt induced floods (Vormoor et al., 2016), recent studies also highlight the role of snow cover and glaciers in soil and groundwater recharge (Jasechko et al., 2014) and hydrological drought (Fraser, 2012; Godsey et al., 2014; Jenicek et al., 2016, Van Loon et al., 2014). Field measurements of snow characteristics provide key data to calculate the amount of water stored in the snow cover, the rate of its release during the snowmelt and validation of snow models or remote sensing products. Modelling is an important tool in the research of the hydrological cycle and forecasting of the variability of its components including floods and droughts, snow and snowmelt runoff modelling (e.g. Etchevers et al., 2002; Hock, 2003; Kirnbauer et al., 1994; Martinec and Rango, 1986) benefit from the remote sensing products and it is therefore natural that hydrologists continuously try to improve model performance also by incorporating the remote sensing data (e.g. Parajka and Blöschl, 2008; Thirel et al., 2013).

This thematic issue on snow resources and hydrological cycle includes 14 authors from 14 European countries. It was designed to attract contributions on the current state of measurement and modeling of snow cover characteristics, amount and variability of water stored in snow, its release during the snowmelt and the links between the snow cover and hydrological processes. Furthermore, this collection of original articles represents a dissemination outcome of the Swiss-Czech-Georgian collaborative project focused on "Snow resources and the early prediction of hydrological drought in mountainous streams" (SREP-Drought, Zappa et al., 2015), supported by the Swiss National Science Foundation. The objective of that project was to evaluate how summer low flows and droughts are affected by winter snowpack in three mountain catchments located in the Alps (Prealps, central Switzerland, Hegg et al., 2006), in the Jizera Mountains (Kamenice, northern Czech Republic; Šanda et al., 2014), and in the Little Caucasus (Gudjaretis-Tskali, central Georgia, Melikadze et al., 2013). Some of the articles in this collection well align on the project topics and thus contribute to the know-how exchange among the European scientists. Four studies in this issue are devoted to measurements of snow characteristics in the field or their estimation from the remote sensing. Four studies are focused on sampling snow or meltwater for isotope analyses or the use of isotopic approaches in studying the hydrological cycle. Finally, three studies are devoted to snowmelt modelling and use of remote sensing data.

FIELD SNOW DATA COLLECTION

Bartík et al. (this issue) analyse the influence of the spruce forest dieback on snow characteristics (depth, density, water equivalent) in the highest part of the Carpathian Mountains (northern Slovakia). Data from five winter seasons showed that the difference in snow depth between the disturbed and living forest increased since the third winter after forest dieback. The forest dieback resulted in a significant increase (about 25%) of the water amount stored in the snow while the snowmelt characteristics (snowmelt beginning and time of snow disappearance) did not change substantially.

Komarov et al. (this issue) present data from the Khibini Mountains (northern Russia) which show that the small-scale variability of the snow characteristics can be large even in areas with uniform geomorphology and topography. In contrast with common assumptions, variability of snow density was higher than that of snow depth.

Conde et al. (this issue) introduce a new methodology of mapping snow water equivalent (SWE) at high spatial resolution (up to 20 m) from the Sentinel 1 and Synthetic Aperture Radar Interferometry. Validation of the methodology against measured SWE data from Finland provided promising results.

Parajka et al. (this issue) demonstrate the value of satellite snow data (MODIS) in the research of the links between snow

characteristics and runoff. The analysis conducted in 145 catchments located in nine European countries showed that three to six snowmelt events occurred in the majority of catchments during a year. The mean difference between the snowmelt event beginning and the peak runoff was about three days. The snow line elevation during that time rose on average by 170 m.

ISOTOPIC APPROACHES

A special focus is given to isotope measurements of precipitation and snowmelt water. Snowmelt is an important source of water recharging soils and triggering runoff generation. Stable isotopes of oxygen and hydrogen in water help to understand the movement of water in the hydrological cycle. While the sampling of rainwater and streams for stable isotopes is relatively easy, sampling of the meltwater (Penna et al., 2014) is still challenging. Vreča et al. (this issue) analyze the local-scale variability in isotopic composition of snowmelt water sampled in Slovenia by the passive capillary samplers (Penna et al., 2014). Analysis of variance and its source by ANOVA showed that due to the variability within the group of samplers (several samplers located close to each other), a large number of samplers (> 5) was needed to sample the snowmelt water.

Hürkamp et al. (this issue) present isotopic data from 18 snow profiles of two winter seasons at Mt. Zugspitze, Germany. They conclude that depth-integrated samples of entire 10 cm layers and point measurements in the same layers showed comparable isotopic compositions. Isotopic composition of the snowpack at the same sampling time in spatially distributed snow profiles was isotopically more similar than the composition observed at the same place at different times. Melting and refreezing were clearly identified as processes causing isotope fractionation in surficial, initial base or refrozen snow layers.

Rücker et al. (this issue) present a novel setup combining snowmelt lysimeters and water sampler for automatic sampling of the meltwater at daily time resolution. Simultaneous collection of rain samples provides stable isotope data to improve the identification of the contribution of snowmelt to runoff in a Swiss alpine catchment.

Šanda et al. (this issue) evaluate nine years of $\delta^{18}O$ values in precipitation, soil water and groundwater in a small Czech mountain catchment and calculate the winter/summer recharge ratios of catchment groundwater, peat organic soil water, mineral hillslope soil water and baseflow. Isotopic mass balance of individual winters showed that precipitation in warmer winters was entirely transformed into outflow until the end of the winter season, leaving no significant water storage for potential drought periods.

SNOWMELT MODELLING AND REMOTE SENSING DATA

Riboust et al (this issue) revisit a simple degree-day model for integrating the satellite data and introduce a new calibration method for the snow model that also accounts for the hysteresis-behavior (Egli and Jonas, 2009) of snow cover during the accumulation and ablation processes. Incorporation of hysteresis between the snow-covered area (SCA) and snow water equivalent improved the SCA simulation. Model parameter sets calibrated jointly against SCA and runoff observations were more robust for simulating independent periods than the parameter sets obtained from discharge calibration only.

Piazzi et al. (this issue) investigate the effectiveness of snow multivariable data assimilation in a snow modelling system designed to provide the real time applications. A series of tests in the northwestern Italian Alps revealed the limitations and constraints in implementing a multivariate Ensemble Kalman Filter scheme in the framework of snow modelling and its performance in consistently updating the snowpack state. Combined assimilation of surface temperature, snow depth and albedo observations provided the best results in snowpack modeling.

Sorman et al. (this issue) explore the feasibility of probabilistic runoff forecasts using the probabilistic snow depletion curves derived from the satellite data (MODIS) in a snow dominated basin in Turkey. Estimated runoff values indicated good consistency with the forecasts based on the derived probabilistic snow depletion curves. The proposed framework can be easily adapted to other scarce networks or ungauged snow-dominated mountain catchments to assist the decision makers responsible for the water management.

CONCLUSIONS

This thematic issue is a collection of current research efforts devoted to the role of snow in the hydrological cycle. The ten papers and the technical note present innovative methods of snow characteristics measurements, research of the relationships between snow and runoff, on the monitoring and evaluation of environmental tracers in the snow-related part of the hydrological cycle (precipitation, snowpack, soil moisture, groundwater, runoff). Modelling experiments showed how snow accumulation and melt modelling can be validated against snow and runoff observations. Data from remote sensing platforms and data assimilations procedures represent another very active field of research in contemporary snow hydrology. We thank the authors for their contributions and wish the readers of Journal of Hydrology and Hydromechanics much of new inspiration. Journal editor Dr. Lubomir Lichner is acknowledged for the very collegial and professional guidance in the process of compiling this collection of papers. We also thank all the reviewers who contributed to the improvement of the articles presented in the thematic issue. Massimiliano Zappa and Martin Šanda thank the Swiss National Science Foundation SNF (Joint Research Projects SCOPES, SREP-DROUGHT project, Grant IZ73Z0_152506) for the financial support of research activities conveyed in this thematic issue.

IN MEMORIAM

During the preparation of this special issue the editorial team learned that two scientists working on the topics presented in this compilation of articles passed away. It is therefore our wish to dedicate this issue to the memory of Associate Professor Dr. Robert Kirnbauer (Technical University of Wien, Austria) and of Dr. Stefan Pohl (University of Freiburg in Brisgau, Germany). Their work on snow processes (Pohl and Marsh, 2006) and snow modelling (Kirnbauer et al., 1994) represent a very important contribution for the understanding of snow as part of the hydrological cycle.

REFERENCES

Barnett, T.P., Adam, J.C., Lettenmaier, D.P., 2005. Potential impacts of a warming climate on water availability in snow-dominated regions. Nature, 438, 7066, 303–309.

Barnhart, T.B., Molotch, N.P., Livneh, B., Harpold, A.A., Knowles, J.F., Schneider, D., 2016. Snowmelt rate dictates streamflow. Geophys. Res. Lett., 43, 8006–8016.

Berghuijs, W.R., Woods, R.A., Hrachowitz, M., 2014. A precipita-

tion shift from snow towards rain leads to a decrease in streamflow. Nat. Clim. Change, 4, 583–586.

Egli, L., Jonas, T., 2009. Hysteretic dynamics of seasonal snow depth distribution in the Swiss Alps. Geophysical Research Letters, 36, 5 p. http://doi.org/10.1029/2008GL035545

Etchevers, P., Martin, E., Brown, R., Fierz, C., Lejeune, Y., Bazile, E., Boone, A., Dai, Y.-J., Essery, R., Fernandey, A., Gusey, Y., Jordan, R., Koren, V., Kowalczyk, E., Pyles, R.D., Schlosser, A., Shmakin, A.B., Smirnova, T.G., Strasser, U., Verseghy, D., Yamakazi, T., Yang, Z.-L., 2002. SNOWMIP, an intercomparison of snow models: comparison of simulated and observed internal state International. In: Proceedings of the International snow science workshop, Penticton, Canada, 29 Sep.–4 Oct. 2002, pp. 353–360.

Fraser, B., 2012. Melting in the Andes: Goodbye glaciers. Nature. 491, 180–182. DOI: 10.1038/491180a.

Godsey, S.E., Kirchner, J.W., Tague, C.L., 2014. Effects of changes in winter snowpacks on summer low flows: case studies in the Sierra Nevada, California, USA. Hydrol. Process., 28, 5048–5064. DOI: 10.1002/hyp.9943.

Gurtz, J., Baltensweiler, A., Lang, H., 1999. Spatially distributed hydrotope-based modelling of evapotranspiration and runoff in mountainous basins. Hydrol. Processes, 13, 2751–2768.

Hegg, C., McArdell, B.W., Badoux, A., 2006. One hundred years of mountain hydrology in Switzerland by the WSL. Hydrol. Process., 20, 371–376. DOI: 10.1002/hyp.6055.

Hock, R., 2003. Temperature index melt modelling in mountain areas. J. Hydrol., 282, 1–4, 104–115.

Jasechko, S., Birks, S.J., Gleeson, T., Wada, Y., Fawcett, P.J., Sharp, Z.D., McDonnell, J.J., Welker, J.M., 2014. The pronounced seasonality of global groundwater recharge. Water Resour. Res., 50, 8845–8867.

Jenicek, M., Seibert, J., Zappa, M., Staudinger, M., Jonas, T., 2016. Importance of maximum snow accumulation for summer low flows in humid catchments. Hydrol. Earth Syst. Sci., 20, 859–874. DOI: 10.5194/hess-20-859-2016.

Kirnbauer, R., Bloschl, G., Gutknecht, D., 1994. Entering the era of distributed snow models. Nord. Hydrol., 25, 1–24.

Klemeš, V., 1990. The modelling of mountain hydrology: the ultimate challenge. In: Molar, L. (Ed.): Hydrology of Mountainous Areas. IAHS Press, Wallingford, Vol. 190, pp. 29–43.

Lemke, P., Ren, J., Alley, R.B., Allison, I., Carrasco, J., Flato, G., Fujii, Y., Kaser, G., Mote, P., Thomas, R.H., Zhang, T., 2007. Observations: Changes in Snow, Ice and Frozen Ground. In: Solomon, S., Qin, D., Manning, M., Chen, Z., Marquis, M., Averyt, K.B., Tignor, M., Miller, H.L. (Eds.): Climate Change 2007: The Physical Science Basis. Contribution of Working Group I to the Fourth Assessment Report of the Intergovernmental Panel on Climate Change. Cambridge University Press, Cambridge, United Kingdom and New York, NY, USA.

Mankin, J.S., Viviroli, D., Singh, D., Hoekstra, A.Y., Diffenbaugh, N.S., 2015. The potential for snow to supply human water demand in the present and future. Environmental Research Letters, 10, 11, 114016. DOI: 10.1088/1748-9326/10/11/114016.

Martinec, J., Rango, A., 1986. Parameter values for snowmelt runoff modelling. J. Hydrol., 84, 197–219.

Marty, C., Schlögl, S., Bavay, M., Lehning, M., 2017. How much can we save? Impact of different emission scenarios on future snow cover in the Alps. The Cryosphere, 11, 517–529. https://doi.org/10.5194/tc-11-517-2017.

Melikadze, G., Kapanadze, N., Todadze, M., 2013.Assessment the role of snow in hydrological cycle of the Borjomula-Gudjareti-Tskali rivers basin. Journal of Georgian Geophysical Society, Phys. Solid Earth., 16a, 19–24.

Parajka, J., Blöschl, G., 2008. The value of MODIS snow cover data in validating and calibrating conceptual hydrologic models. J. Hydrol., 358, 240–258. DOI: 10.1016/j.jhydrol.2008.06.006.

Penna, D., Ahmad, M., Birks, S.J., Bouchaou, L., Brenčič, M., Butt, S., Holko, L., Jeelani, G., Martínez, D.E., Melikadze, G., Shanley, J.B., Sokratov, S.A., Stadnyk, T., Sugimoto, A., Vreča, P., 2014. A new method of snowmelt sampling for water stable isotopes. Hydrol. Process., 28, 5637–5644. DOI: 10.1002/hyp.10273.

Pohl, S., Marsh, P., 2006. Modelling the spatial–temporal variability of spring snowmelt in an arctic catchment. Hydrol. Process., 20, 1773–1792. DOI: 10.1002/hyp.5955.

Šanda, M., Vitvar, T., Kulasová, A., Jankovec, J., Císlerová, M., 2014. Runoff formation in a humid, temperate headwater catchment using a combined hydrological, hydrochemical and isotopic approach (Jizera Mountains, Czech Republic). Hydrol. Process., 28, 3217–3229. DOI: 10.1002/hyp.9847.

Thirel, G., Salamon, P., Burek, P., Kalas, M., 2013. Assimilation of MODIS snow cover area data in a distributed hydrological model using the particle filter. Remote Sens., 5, 5825–5850.

Van Loon, A.F., Ploum, S.F., Parajka, J., Fleig, A.K., Garnier, E., Laaha, G., Van Laanen, H.A.J., 2014. Hydrological drought types in cold climates: quantitative analysis of causing factors and qualitative survey of impacts. Hydrol. Earth Syst. Sci., 19, 1993–2016.

Vaughan, D.G., Comiso, J.C., Allison, I., Carrasco, J., Kaser, G., Kwok, R., Mote, P., Murray, T., Paul, F., Ren, J., Rignot, E., Solomina, O., Steffen, K., Zhang, T., 2013. Observations: Cryosphere. In: Stocker, T.F., Qin, D., Plattner, G.-K., Tignor, M., Allen, S.K., Boschung, J., Nauels, A., Xia, Y., Bex, V., Midgley, P.M. (Eds.): Climate Change 2013: The Physical Science Basis. Contribution of Working Group I to the Fifth Assessment Report of the Intergovernmental Panel on Climate Change. Cambridge University Press, Cambridge, United Kingdom and New York, NY, USA.

Viviroli, D., Archer, D.R., Buytaert, W., Fowler, H.J., Greenwood, G.B., Hamlet, A.F., Huang, Y., Koboltschnig, G., Litaor, I., López-Moreno, J.I., Lorentz, S., Schädler, B., Schreier, H., Schwaiger, K., Vuille, M., Woods, R., 2011. Climate change and mountain water resources: overview and recommendations for research, management and policy. Hydrology and Earth System Sciences, 15, 2, 471–504. DOI: 10.5194/hess-15-471-2011.

Vormoor, K., Lawrence, D., Schlichting, L., Wilson, D., Wong, W.K., 2016. Evidence for changes in the magnitude and frequency of observed rainfall vs. snowmelt driven floods in Norway. J. Hydrol., 538, 33–48. DOI:10.1016/j.jhydrol.2016.03.066.

Zappa, M., Vitvar, T., Rücker, A., Melikadze, G., Bernhard, L., David, V., Jans-Singh, M., Zhukova, N., Sanda, M., 2015. A Tri-National program for estimating the link between snow resources and hydrological droughts. Proc. IAHS, 369, 25–30, DOI: 10.5194/piahs-369-25-2015.

J. Hydrol. Hydromech., 67, 2019, 1, 4–19
DOI: 10.2478/johh-2018-0013

An EnKF-based scheme for snow multivariable data assimilation at an Alpine site

Gaia Piazzi[1*], Lorenzo Campo[1], Simone Gabellani[1], Fabio Castelli[2], Edoardo Cremonese[3], Umberto Morra di Cella[3], Hervé Stevenin[4], Sara Maria Ratto[4]

[1] CIMA Research Foundation, via Armando Magliotto, 2 - 17100 Savona, Italy.
[2] Department of Civil and Environmental Engineering, University of Florence, Via Santa Marta, 350139 Florence, Italy.
[3] Environmental Protection Agency of Aosta Valley, Loc. Grande Charrière, 44 11020 Saint-Christophe, Aosta, Italy.
[4] Regional Center of Civil Protection, Aosta Valley Region, via Promis, 2/A - 11100 Aosta, Italy.
[*] Corresponding author. Tel.: +39 019230271. Fax: +39 01923027240. E-mail: gaia.piazzi@cimafoundation.org

Abstract: The knowledge of snowpack dynamics is of critical importance to several real-time applications especially in mountain basins, such as agricultural production, water resource management, flood prevention, hydropower generation. Since simulations are affected by model biases and forcing data uncertainty, an increasing interest focuses on the assimilation of snow-related observations with the purpose of enhancing predictions on snowpack state. The study aims at investigating the effectiveness of snow multivariable data assimilation (DA) at an Alpine site. The system consists of a snow energy-balance model strengthened by a multivariable DA system. An Ensemble Kalman Filter (EnKF) scheme allows assimilating ground-based and remotely sensed snow observations in order to improve the model simulations. This research aims to investigate and discuss: (1) the limitations and constraints in implementing a multivariate EnKF scheme in the framework of snow modelling, and (2) its performance in consistently updating the snowpack state. The performance of the multivariable DA is shown for the study case of Torgnon station (Aosta Valley, Italy) in the period June 2012 – December 2013. The results of several experiments are discussed with the aim of analyzing system sensitivity to the DA frequency, the ensemble size, and the impact of assimilating different observations.

Keywords: Snow modeling; Energy-balance model; Data Assimilation; Ensemble Kalman Filter.

INTRODUCTION

The seasonal presence of snow strongly impacts both the energy balance and water resource budget, not only locally, but also at larger scale. Because of its low thermal conductivity, the snowpack produces an insulating effect over the underlying soil, whose temperature variability is severely reduced towards a stable condition (Zhang, 2005). Moreover, its high albedo entails a remarkable reduction of shortwave radiation absorption, with a resulting lowering of near surface air temperature.

Snow dynamics strongly impact hydrological processes. During the winter season the presence of snow cover reduces the effective drainage. Thus, in case of possible rainfall events the watershed time of concentration turns out to be lower than in snowless condition. Moreover, the release of the significant water volume stored in winter period considerably contributes to the total discharge during the melting period (Barnett et al., 2005; Clark and Hay, 2004; Zappa et al., 2003). Melt water supplies a significant component of the annual water budget, both in terms of soil moisture and runoff, which plays a critical role in floods generation in snow-dominated basins. Therefore, when modeling hydrological processes in snow-dominated catchments the quality of predictions deeply depends on how the model succeeds in catching snow dynamics (Wood et al., 2016).

A growing effort is aimed at enhancing the physical representation of the snowpack in hydrologic models. Despite progressive improvements, several flaws endure mainly due to uncertainty in parameterizations, errors affecting both meteorological forcing data and initial conditions and approximations in boundary conditions (Liston and Sturm, 1998; Pan et al., 2003). Moreover, there are several physical factors that make an exhaustive reconstruction of snow dynamics complicated: snow intermittence in space and time, stratification and slow phenomena like metamorphism processes, uncertainty in snowfall evaluation, wind transportation (Winstral and Marks, 2014).

Many different snowpack models have been developed with highly variable degree of complexity, mainly depending on their target application, such as hydrological forecasting, avalanche prediction, climate modeling, and the availability of computational resources and data. Snow models range from the so-called force-restore systems of composite snow-soil layer(s) (Douville et al., 1995; Yang et al., 1997) and explicit snow layer(s) schemes (Slater et al., 1998; Verseghy, 1991) up to detailed internal-snow-process schemes with physical parameterizations (Anderson, 1976; Bartelt and Lehning, 2002; Brun et al., 1989; Endrizzi et al., 2014; Jordan, 1991; Lehning et al., 2002; Vionnet et al., 2012). Intermediate-complexity systems result from simplified versions of the physical parameterization schemes with a reduced snowpack layering (Boone and Etchevers, 2001; Dutra et al., 2010, 2012). One of the main issues is the trade-off between model complexity and input data requirements. Independent studies comparing snow models with different scheme complexity agreed in stating that a simplified snowpack structure can provide nearly equivalent performance as a much more complex snow-physics model (Avanzi et al., 2016; Magnusson et al., 2011, 2015). Thus, for many applications, a simpler snowpack scheme may be an optimal compromise between model performance and computational constraints.

Several intercomparison projects aimed at assessing performance of models with different levels of detail and parameterizations with the purpose of analyzing their impact on model simulations (Boone et al., 2004; Bowlinget el., 2003; Essery et al., 2009; Etchevers et al., 2003; Nijssen et al., 2003; Schlosser et al., 2000; Slater et al., 2001). These projects stated that no

overall best model could be identified and an increasing model complexity does not ensure an improvement of simulations, whose quality depends on the application, and topographic, meteorological and vegetation features of the modeling domain (Rutter et al., 2009).

Essery et al. (2013) presented a snow multi-scheme model combining a range of existing parameterizations of different complexity (from empirical to physical ones) for the representation of each dominant process occurring within the snowpack. This approach allows generating a large ensemble of simulations with different model configurations and those employing prognostic equations for snow density and albedo generally revealed the best performance.

Fortunately, in addition to model simulations, other independent snow-related data sources are available, such as ground-based measurements and remotely sensed observations (Barrett, 2003), but both are affected by several limitations. Ground-based snow measurements only provide point values, affected by an instrumental bias and subjected to distortions due to wind action, local topographic features and vegetation interactions. Remote sensing observations cover extended areas but they supply indirect measurements affected by a usually coarse spatial resolution (passive microwave sensors) and the uncertainty in retrieval algorithms.

Data Assimilation (DA) is an objective methodology to combine these different sources of information to obtain the most likely estimate of snowpack state.

Several DA techniques with different degree of complexity have been developed and are currently employed: direct insertion (Liston et al., 1999; Malik et al., 2012; Rodell and Houser, 2004), optimal interpolation scheme (Brasnett, 1999; Liston and Hiemstra, 2008), Cressman scheme (Balsamo et al., 2015; Cressman, 1959; Dee et al., 2011; Drusch et al., 2004), nudging method (Boni et al., 2010; Stauffer and Seaman, 1990).

At a higher level of complexity, Kalman filtering is a class of sequential DA techniques (Evensen, 2003) that enables to evaluate the optimal weighting between modeled and observed states knowing model and observations errors. The main feature distinguishing this approach from more static ones is the dynamic updating of the forecast error covariance during the simulation. Several techniques based on the Kalman filter have been developed.

The standard Kalman Filter (KF) (Gelb, 1974), which can be implemented only on linear dynamic system, is based on the relative contribution of the covariance matrices of the errors of both the model predictions and the observations to obtain a statistically optimal estimate for the given parameters set and assumed uncertainties. This is achieved by applying a standard error propagation theory that produces an analysis state obtained by adding a correction to the a priori state. The correction is computed as the difference between the a priori state (produced by the model) and the observation, modulated through the Kalman Gain, a matrix that resumes the information from both the covariance matrices.

The Extended Kalman Filter (EKF) (Miller et al., 1994) is a linearized statistical approach that can be applied to nonlinear dynamic systems. This technique relies on an adjoint and tangent linear model to propagate the error covariance matrix forward in time. Thus, this technique is able to provide only a near-optimal estimate due to the linear approximation of the model through a Taylor series expansion. Sun et al. (2004) developed a one-dimensional EKF scheme to assimilate synthetically generated Snow Water Equivalent (SWE) observations into a Land Surface Model (LSM). Dong et al. (2007) used the assimilation system developed by Sun et al. (2004) to assimilate SWE data derived from the Scanning Multichannel Microwave Radiometer (SMMR) observations into a LSM. The EKF-based scheme results to well succeed in updating model simulations, even though in presence of strong nonlinearities in the system, unstable results are attended (Moradkhani, 2008).

A further approach is the Ensemble Kalman Filter (EnKF), proposed by Evensen (1994, 2003). Unlike the traditional and Extended Kalman filters, this method does not need a model linearization since the error estimates are evaluated from an ensemble of model simulations using the Monte Carlo approach. Moreover, this method is able to handle any number of variables in the update scheme. Andreadis and Lettenmaier (2005) applied an EnKF scheme to assimilate the Moderate Resolution Imaging Spectroradiometer (MODIS) snow cover extent (SCE) and the Advanced Microwave Scanning Radiometer–EOS (AMSR-E) SWE products into a macroscale hydrologic model to update SWE model predictions. Clark et al. (2006) proposed an alternative framework for assimilating synthetic remotely sensed snow cover area (SCA) data to improve streamflow simulations. Slater and Clark (2006) implemented this technique to assimilate SWE observations to update the snowpack state of a conceptual model. Su et al. (2008) investigated the feasibility of assimilating through the EnKF approach the fractional snow cover (FSC) detected by MODIS for the optimal retrieval of continental-scale SWE within a highly complex LSM. More recently, Magnusson et al. (2014) analyzed the impact of an EnKF-based assimilation of both ground-based SWE observations and snowfall and snowmelt rates on distributed SWE estimates.

All the studies generally state that the EnKF is a well-performing technique enabling to consistently update model predictions. The assimilation of snow-related observations through the EnKF scheme succeeds in improving the analysis of snowpack dynamics, especially during the melting period, with a resulting enhancement of the accuracy of hydrological simulations. Nevertheless, most publications about applications of EnKF-based scheme deal with univariate assimilation, namely the assimilation of a single data type (Griessinger et al., 2016; Huang et al., 2017). Relatively few studies aimed to investigate the simultaneous assimilation of observations of multiple model state variables. Durand and Margulis (2006) assimilated synthetic passive microwave observations at the Special Sensor Microwave Imager (SSM/I) and AMSR-E frequencies and broadband albedo observations through an EnKF scheme to study the potential of remotely sensed snow observations in improving SWE simulations. Durand and Margulis (2008) assimilated synthetic SWE and snow grain size data with different spatial resolutions into a LSM using adaptive EnKF. Su et al. (2010) developed a multisensory EnKF-based DA system assimilating both Gravity Recovery and Climate Experiment (GRACE) terrestrial water storage (TWS) and MODIS FSC with respectively the EnK Smoother (Dunne and Entekhabi, 2005, 2006) and EnKF into a LSM. De Lannoy et al. (2012) studied the impact of the joint assimilation of AMSR-E SWE and MODIS FSC products on SWE simulations with a multiscale EnKF scheme. More recently, Stigter et al. (2017) proposed a well-performing EnKF-based methodology to estimate SWE and snowmelt runoff in a Himalayan catchment. They implemented an EnKF scheme to calibrate ruling parameters of a snow model by jointly assimilating both remotely sensed snow cover observations and ground-based measures of snow depth. Current research results agree on the superior impact of the multivariate assimilation on model simulations with respect to the univariate one (Charrois et al., 2016). However, even though in atmospheric sciences the multivariate

DA is well established, most publications in the framework of terrestrial systems present synthetic case studies (Montzka et al., 2012).

In light of the promising potential of multivariate DA schemes and the lack of their application using real-world data or several types of data, this paper intends to investigate the feasibility of a multivariable EnKF-based scheme for snow modeling. The main goal is the development of a operationally effective system enabling to assimilate both ground-based measurements and remotely sensed data of several snow-related variables (surface temperature, snow depth and albedo). Since multivariate DA systems are usually very CPU-intensive, the research aims to define and analyze technical solutions and approaches allowing to reduce the required computational load by still guaranteeing successful performance. To this end, several sensitivity experiments were carried out in order to better understand system robustness and reliability.

The paper is organized as follows. Firstly, the snow dynamic model and the DA algorithm are described. After presenting the ground-based and remote sensed data used in the assimilation experiments, the experimental design is explained, whose results are then shown and widely discussed.

SMASH – SNOW MULTIDATA ASSIMILATION SYSTEM FOR HYDROLOGY

This research aimed to develop a snow modeling system suited to real-time applications and able to combine model predictions, ground-based data and satellite observations.

SMASH (Snow Multidata Assimilation System for Hydrology) consists of a multi-layer snowpack dynamics model that reproduces some of the main physical processes occurring within the snowpack (accumulation, density dynamics, melting, sublimation, radiative balance, heat and mass exchanges), and a multivariable DA algorithm.

Snow hydrological model

From a hydrological point of view, the most relevant quantities to be predicted are the SWE and the snowmelt. The evolution of snow microstructure, snowpack stratification, and snow metamorphism are ruling processes for the avalanches forecasting (Bartelt and Lehning, 2002; Vionnet et al., 2012) but they are of less interest in most hydrological applications, and thus they are here neglected. Since the aim is to develop a snow model suitable to be coupled with a multivariable DA algorithm, the degree of model complexity is limited in order to facilitate the assimilation procedure while maintaining a fundamental physical consistency (Magnusson et al., 2014; Slater and Clark, 2006). This purpose leads to some model simplifications of both snowpack scheme and physics (liquid water storage and refreezing process are not included). The introduction of a finer layering scheme with respect to the simple discretization described below would add a further challenge in the assimilation of observed data through DA techniques involving state-averaging operations. The implementation of an EnKF scheme would be much more demanding since a higher number of layers (i.e. increased state size) entails larger computational requirements.

The multilayer scheme consists of a 2-layers discretization for snowpack and 2-layers for soil (Figure 1). The scheme has a seasonally variable number of layers ranging from a minimum of two, in snow free condition, up to a maximum of four layers, in presence of snow cover. This dynamic layering scheme is adopted with the aim to solve the model energy balance in both snowy and snowless conditions without having to rely on a 'model switching' algorithm. Both snow and soil upper layers are much thinner than the underlying ones so that the top layer temperature can be considered as an acceptable approximation of the skin temperature, whose measures can be more efficiently assimilated. The model is driven by meteorological data (air temperature, wind velocity, relative air humidity, precipitation and incident shortwave solar radiation) to provide a complete estimate of snowpack state in an explicit surface energy balance framework. Model state consists of snow surface temperature (T_s [°C]), snow temperature at the interface between the two snow layers (T_m [°C]), surface soil temperature (T_0 [°C]), deep soil temperature (T_d [°C]), SWE and snow density of top (W_s [mm]; ρ_s [kg/m^3]) and bottom (W_m [mm]; ρ_m [kg/m^3]) snow layers, surface albedo (α [–]).

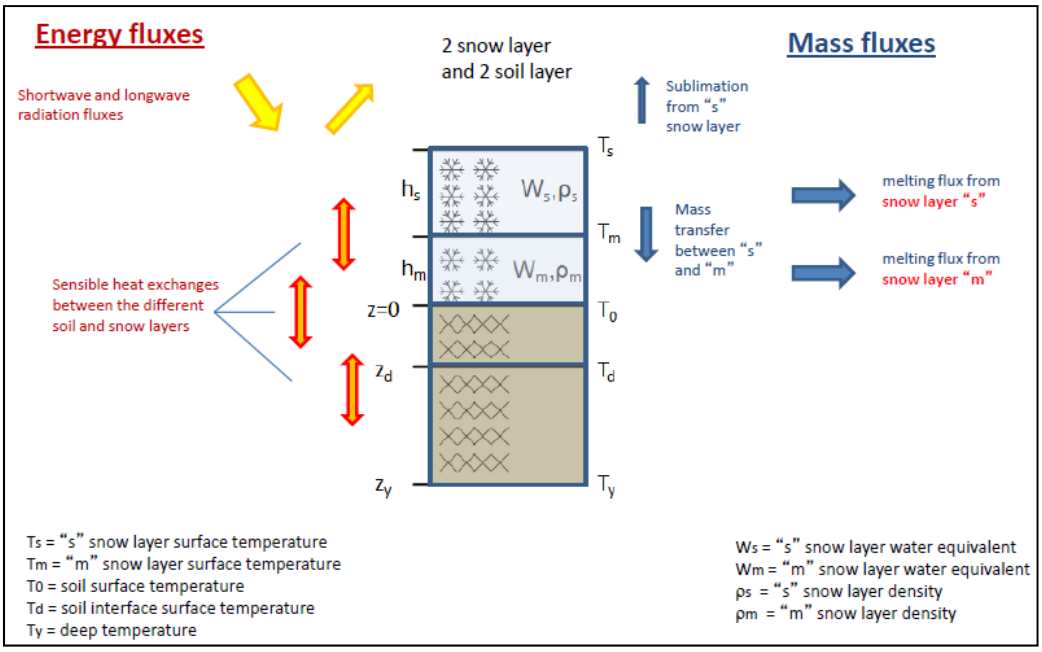

Fig. 1. SMASH scheme - Energy and mass fluxes between adjoining layers and atmosphere are shown.

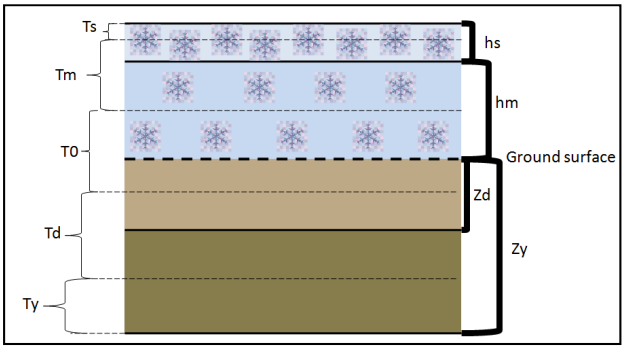

Fig. 2. SMASH scheme - Control volumes and model layers.

The thicknesses of soil layers are fixed through reference depths at 30 cm and 2 m (z_d and z_y). Snow layers vary their thickness (h_s and h_m) according to the snow dynamics (i.e. snowfalls, sublimation, density changes, and snow melting) without any constraining limit. Deep soil temperature (T_y) is the model boundary condition. Temperatures (T_s, T_m, T_0, T_d) are defined as average temperatures of the control volumes shown in Figure 2. The top and bottom boundaries of each volume are set in the middle of the thickness of the two corresponding consecutive layers.

The model solves both energy and mass balance with an integration time step of 15 minutes.

Mass balance

Snow mass balance equations evaluate SWE of each snow layer (W_s and W_m) accounting for snowfalls (Sf), sublimation process ($subl$), melting rates from both the two snow layers (M_s and M_m) and mass transfer between them (D). Since neither the liquid storage nor the refreezing process is included within the snowpack model, meltwater is assumed to be drained directly as surface runoff (no infiltration into the soil).

$$W_s(t) = W_s(t-1) + Sf - M_s - subl - D \tag{1}$$

$$W_m(t) = W_m(t-1) + D - M_m - subl \tag{2}$$

$$D = \frac{1}{X} W_s dt \tag{3}$$

The mass transfer (D) from the snow surface layer downward is empirically parameterized as a function of the SWE and a temporal scale of the process (X). This parameter was properly defined through several tests at different measurements sites in order to obtain a constant value allowing to maintain a thin snow surface layer. From a physical point of view, this parameterization can be supposed to contribute to the gravitational snowpack settling thanks to a consistent update of the snow density of both the snow layers.

Given the observed total precipitation, the snowfall rate (Sf) is evaluated as a function of air temperature (T_a) and relative humidity (U), as proposed in Froidurot et al. (2014).

Density

Snow density is updated considering both the snow compaction and the destructive thermal metamorphism according to the parameterization proposed by Anderson (1976). The snow compaction is evaluated as the ratio between the weight of the overlying snow (σ_{si}) and a viscosity coefficient (η_{si}) standing for the snow resistance to a certain pressure and evaluated as an exponential function of snow temperature and density (Kojima, 1967; Mellor, 1964). The thermal metamorphism is estimated as a function of snow temperature (T_{si}) and density (ρ_{si}). The influence of settling is higher in new snow layers (50–150 [kg/m^3]) up to a density value of 250 [kg/m^3].

$$\frac{1}{\rho_{si}} \frac{d\rho_{si}}{dt} = \frac{\sigma_{si}}{\eta_{si}(T_{si}, \rho_{si})} + \xi_i(T_{si}, \rho_{si}) \tag{4}$$

In case of snowfall, snow density of the upper layer is evaluated as a weighted average between its current value and fresh snow density. The fresh snow density is evaluated according to the air temperature (Hedstrom and Pomeroy, 1998).

Energy balance an d heat flow

The model evaluates the net heat fluxes in each layer and the conductive heat fluxes between adjoining layers according to Fourier law. The surface heat flux ($\vec{G}$) is estimated as the resulting balance among shortwave and longwave radiations $\left(\vec{R}_{Sw,net}, \vec{R}_{Lw,net}\right)$, sensible $\left(\vec{H}\right)$ and latent $\left(\overrightarrow{LS}\right)$ heat fluxes, and the advection heat flux $\left(\vec{Q}_{mix}\right)$ due to liquid precipitation:

$$\vec{G} = \vec{R}_{Sw,net} + \vec{R}_{Lw,net} + \vec{H} + \overrightarrow{LS} + \vec{Q}_{mix} \tag{5}$$

Both the incoming (positive) and outgoing (negative) longwave radiation components are estimated through the Stephan-Boltzmann law, as a function of the surface temperature (i.e. the temperature of snow/soil depending on the presence/absence of snow cover) and the air temperature, respectively. While the surface emissivities are considered as constant values, the air emissivity varies over time according to both wind speed and air temperature.

The heat flux from liquid precipitation across the snowpack surface is a function of rain emissivity (ε_p), the surface specific heat (C_s), the amount of rain (P_l) and the temperature gradient:

$$Q_{mix} = \frac{\varepsilon_p C_s P_l (T_a - T_{sup})}{dt} \tag{6}$$

The net shortwave radiation ($R_{Sw,net}$) is evaluated as a fraction of the incident solar radiation ($R_{Sw,inc}$), as a function of the surface albedo (α):

$$R_{Sw,net} = (1-\alpha) \cdot R_{Sw,inc} \tag{7}$$

In snow cover condition, the albedo is evaluated through a physical parameterization (Wiscombe and Warren, 1980):

$$\alpha = \alpha_d + 0.2(1-\alpha_d) \tag{8}$$

$$\alpha_d = (1 - 0.2 F_{AGE}) \cdot \alpha_0 \tag{9}$$

where α_d is the diffuse albedo and $\alpha_0 = 0.95$. Since snow albedo decreases with time due to the growth of snow grain size and accumulation of dirt, a reduction factor is parameterized according to the snow age (τ_{snow}):

$$F_{AGE} = \frac{\tau_{snow}}{1 - \tau_{snow}} \tag{10}$$

In case of snowfall, the snow age is reduced, hence the surface albedo.

The penetration of shortwave radiation into the snowpack is estimated after Anderson (1976). According to this formulation the solar radiation decays exponentially as a function of snow depth.

$$R_{Sw\downarrow} = R_{Sw,net} \cdot \exp(-\nu \cdot z) \quad (11)$$

where:

- $R_{Sw\downarrow}$ is the fraction of solar radiation penetrated withinthe snowpack;
- $R_{Sw,net}$ is the net shortwave radiation on the snowpack surface;
- $\nu$is the extinction coefficient [cm^{-1}];
- z is the penetration depth [cm];

Sensible and latent heat fluxes are evaluated following the bulk formulation:

$$H = c_p \rho_a C_H V (T_{sup} - T_a) \qquad \textit{Sensible heat flux} \quad (12)$$

$$LS = L_H \rho_a C_H V (q_{sup} - q_a) \qquad \textit{Latent heat flux} \quad (13)$$

Heat exchanges are proportional to the temperature (for H) and mixing ratio (for LS) gradients between the surface (T_{sup} and q_{sup}) and atmosphere (T_a and q_a). Turbulent fluxes are also function of air specific heat (c_p), latent heat (L_H) of sublimation (of vaporization when no snow cover is present), air density (ρ_a), wind velocity (V) and the turbulent transfer coefficient (C_H). The turbulent transfer coefficient C_H depends on the neutral conditions coefficient C_{HN}, evaluated as a function of the surface roughness, and the atmospheric stability (ψ_{stab}):

$$C_H = C_{HN} \psi_{stab} \quad (14)$$

The atmospheric stability is evaluated as a function of the Richardson Bulk number, which depends on potential temperatures of both air and interface surface between soil/snow and atmosphere and wind velocity, following the empirical scheme of Caparrini et al. (2004).

Temperature variation in time (ΔT_i) and snow melting rate (M_i) of each layer is evaluated as a function of the net heat flux (Q_{Ti}): at its surface, resulting from the balance of conductive fluxes among layers and the contribution of the penetration of solar radiation:

$$\Delta T_i = \frac{Q_{Ti}}{h_i \rho_i C_i} dt \qquad \text{If } T_i > T_{melt} \rightarrow M_i = \frac{Q_{Ti\_melt}}{L_m} dt \quad (15a, b)$$

where C_i is the specific heat of the layer. When the resulting temperature of the layer (T_i) exceeds the melting temperature (T_{melt} = 0°C), melting occurs in the corresponding control volume (M_i) according to the equation [15b], where L_m is the melting latent heat.

Model calibration

The snowpack model was calibrated over four winter seasons (2012/13 – 2013/14 – 2014/15 – 2015/16) through a split-sample test. A sensitivity analysis allowed to properly select the parameters exerting the most influence on model simulations. This preliminary study was manually carried out by making the parameters vary within proper ranges and analyzing the impact of their variation on the resulting model predictions. Two model parameters were selected: snow roughness and snow viscosity. Parameters ranges were estimated in order to both avoid model numerical instabilities and to comply with possible physical constraints (see Table 1). Random combinations of parameters were tested by analyzing the resulting Kling-Gupta efficiency (KGE) indices (Gupta et al., 2009) considering the observations of surface temperature, snow depth, and albedo supplied by the Torgnon station and the monthly manual measures of snow density. Starting from the best parameters combinations, local KGE optima were found over the calibration period (winter seasons 2012/13–2013/14) through a constrained nonlinear optimization algorithm (Interior-point Algorithm) (Wächter and Biegler, 2006) in order to define the best parameters set. Finally, the calibrated parameters were tested throughout the validation period (snow seasons 2014/15 – 2015/16). Table 2 shows the resulting KGE values over both calibration and validation periods.

Table 1. Parameters calibration.

	Parameter		Range	Calibrated value
1.	Snow roughness	[mm]	[0.001–0.05]	0.0226
2.	Snow viscosity	[kg/ms]	[10^6–10^8]	10^8

Table 2. Kling-Gupta efficiency coefficients over both calibration and validation periods.

	Kling-Gupta efficiency	
	Calibration period	Validation period
Snow depth [m]	0.74	0.69
Snow temperature [°C]	0.58	0.54
SWE [mm]	0.12	0.51

Data assimilation algorithm: constrained Ensemble Kalman filter

An Ensemble Kalman Filter scheme is implemented to assimilate observations of surface temperature, snow depth, and albedo. This technique requires the definition of an ensemble of model states, which are all simultaneously integrated forward in time independently of each other. Whenever an observation is available, the states of the ensemble members are updated through an optimal weighting between simulated and observed values. The weights are defined by the Kalman Gain (K), based on the covariance errors matrices of both model and observations. Model error covariances are dynamically updated at every assimilation time step (Evensen, 1994, 2003). The model state correction formula, i.e. the state analysis, is defined as:

$$x_{analysis} = x_{background} + K \cdot (obs - H \cdot x_{background}) \quad (16)$$

where $x_{analysis}$ is the updated model state, $x_{background}$ is the prior one, i.e. the model predictions, and obs are the observations. The Kalman Gain is a linear combination of the covariance errors matrices of both model (C_{mod}) and observations (C_{obs}) and a measurement operator (H), which enables the transition from the model space to the observations one (Evensen, 1994).

$$K = C_{mod} H^T \left(H C_{mod} H^T + C_{obs} \right)^{-1} \quad (17)$$

According to the main assumptions of the EnKF formulation (Evensen, 1994), model errors covariance matrix (C_{mod}) is the covariance matrix of the differences between each ensemble state (Ens_i) and the resulting average ensemble state (Ens_{mean}):

$$C_{mod} = Cov\left(Ens_i - Ens_{mean}\right) \quad (18)$$

The correlations among state variables of a highly non-linear model may be difficult to assess through simple ensemble statistics, with possible miscorrection of the model background errors, especially for those state variables which are not directly observed. In order to overcome some of these limitations and obtain an overall consistent update of the snowpack state, the model error covariance matrix is reduced to a two-blocks structure. The two blocks handle the covariances among energy- and mass-related variables independently. The implementation of this solution allows updating both energy and mass balances by limiting physically incoherent corrections. Furthermore, with the aim of avoiding possible model instabilities, any inconsistent value generated through the ensemble updating is removed by limiting each state variable into proper variables physical ranges. According to this approach, any outlier value is set equal to upper or lower limit value of the corresponding physical range of the state variable.

Ensemble Gaussian perturbations

Because this study mainly focuses on assessing the performance of a multivariable DA scheme, perturbations are restricted to the ensemble of model states. Indeed, observations are here assumed to be significantly more reliable than model predictions. The observations error covariance matrix is estimated according to the instruments uncertainties (Table 3). Since the measurements of each observed variable are here considered independent of each other, the resulting error covariance matrix is diagonal. Of course, point measurements have high uncertainties due to their limited representativeness of the spatialized snow processes (e.g. wind-driven snow redistribution) (Stigter et al., 2017). However, since this is a point application of the DA scheme, the observational error covariance matrix is supposed to be satisfactorily representative even though any other source of uncertainty is included. The uncertainty of forcing meteorological data is not taken into account.

Table 3. Uncertainties of the assimilated measures.

Observed variable	Measures uncertainty
Surface temperature [°C]	±0.5
Snow depth [cm]	±1
Albedo [%]	5

State variables are perturbed at each model time step through an additive Gaussian noise. The perturbations are generated by performing, for each state variable, a Gaussian sampling from a normal multivariate distribution with an assigned covariance matrix (De Lannoy et al., 2012). This latter prevents the introduction of possible inconsistencies among the variables of each model state due to its perturbation. The covariance matrix is evaluated as the error covariance matrix between simulated and observed time series of the state variables, when available. The sampling is carried out by choosing equidistant cumulated probability values, in order to guarantee null mean-valued perturbations and the Gaussianity even if sample size is limited. As well as the model ensemble update, also its perturbation can cause physically inconsistent values.

In this occurrence the aforementioned approach is not relevant, since the truncation of the perturbed ensemble would compromise the null mean-valued perturbations. In order to avoid the insertion of possible distortions, the model physical consistency is guaranteed by rescaling the perturbed ensemble.

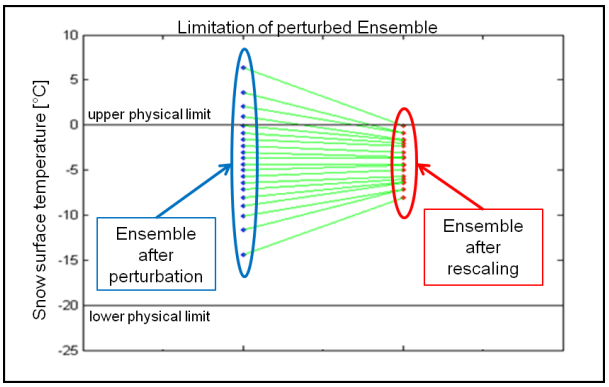

Fig. 3. Ensemble limitation after the perturbation.

This contraction allows maintaining the ensemble average and perturbations Gaussianity even after the ensemble limitation (Figure 3). These two approaches to limiting the perturbed ensemble within physical ranges are compared in the following.

In spite of the perturbation of the model states, the constraints necessarily decrease the variance of ensemble state variables, whose reduction can lead to weight more the model and weakly assimilate the observations. Thus, at each assimilation time step the model error variances are rescaled proportionally to the variance reduction with respect to the empirical variance of each state variable:

$$Cov_{mod} = Corr_{mod} \cdot \left(\sigma_{rescaled} \mathrm{x}\ \sigma_{rescaled}\right) \quad (19)$$

where:

- $Corr_{mod}$ is the model error correlation matrix;
- $\sigma_{rescaled}$ is the vector of the rescaled standard deviations of state variables.

Model physical consistency: modulating function

The model was designed to simulate the energy balance in both snowy and snowless conditions. Thus, in order to guarantee the model consistency both in case of presence and absence of snowpack, two different sets of physical limits are required to constrain each state variable into proper seasonal ranges. These ranges are statistically defined through the analysis of observed time series of the state variables (see Table 4). Moreover, the lower and upper physical limits have to be time variant, in order to well characterize the transition periods (early winter, melting season).

Table 4. Physical ranges to limit the state variables after their perturbation.

Variable		Lower limit		Upper limit	
		Snowy	Snowless	Snowy	Snowless
T_s	[°C]	–30	–	0	–
T_m	[°C]	–30	–	0	–
T_0	[°C]	–10	0	0	40
T_d	[°C]	–2	0	5	20
W_s	[mm]	0	–	–	–
W_m	[mm]	0	–	–	–
ρ_s	[kg/m^3]	80	–	550	–
ρ_m	[kg/m^3]	80	–	550	–
α	[–]	0.2		1	

Since the intermittent presence of snow cover also entails a seasonal variability of state variables correlations, also the error

covariance matrix employed to generate perturbations must be time variant. Indeed, in case of bare soil, snow-related variables are not included in the model state, and some variables are weakly correlated (e.g. deep soil temperature and albedo). In order to generate proper perturbations in snow and no-snow conditions, two different error covariance matrixes are used.

With the purpose of preventing model instabilities a modulation was introduced in order to relax the switch from snow cover to bare soil conditions, by properly setting upper and lower physical limits of the state variables and the error covariance matrix for the generation of ensemble perturbations.

The modulating function (β) allows discriminating the presence or absence of snow according to both air temperature (observed) and snow mass (modeled). This approach enables to manage the transition periods: snow cover and high air temperature (melting process) and bare soil and low air temperature (early winter). The β-function is defined according to the following formulas:

$$\beta_{Ta} = \left(\gamma - \frac{\operatorname{atan}(T_a)}{\pi} \right) \tag{20}$$

$$\beta = \beta_{Ta} + (1 - \beta_{Ta}) \cdot e^{-\left(1+\left(\frac{(W_S + W_m) - \mu}{\sigma}\right)\xi\right)^{-1/\xi}} \tag{21}$$

The functional form and the parameters were chosen to center the function on an air temperature value that could discriminate snow and no-snow conditions, assumed equal to 0°C, and asymptotically reach the desired limit values (1 for winter and 0 for summer).

Figure 4 shows the modulating function, which assumes values near to 0 when air temperature is high and there is no snow cover (mainly during summer season), and near to 1 in case of snow cover and cold temperatures (winter period). In these two limit cases, respectively summer and winter, physical ranges are assumed for all the state variables. The function assumes value near to 1 also when no snowpack is present but temperatures are very low (autumn, early winter). During transition periods β-function allows defining intermediate model run settings according to the combination of snow and air temperature information.

$$Lim_{i,SUP} = \left(Lim_{i,SUP_{snowless}} \cdot (1 - \beta) \right) + \left(Lim_{i,SUP_{snowy}} \cdot \beta \right) \tag{22}$$

$$Lim_{i,INF} = \left(Lim_{i,INF_{snowless}} \cdot (1 - \beta) \right) + \left(Lim_{i,INF_{snowy}} \cdot \beta \right) \tag{23}$$

$$COV_{pert} = \left(COV_{pert,snowless} \cdot (1 - \beta) \right) + \left(COV_{pert,snowy} \cdot \beta \right) \tag{24}$$

where $Lim_{i,SUP}$ and $Lim_{i,INF}$ are the modulated upper and lower physical limits of each state variable and COV_{pert} is the modulated error covariance matrix used to generate the ensemble perturbations.

CASE STUDY

Validation site and ground-based measurements

SMASH 1D-version was tested throughout the period June 2012–December 2013 at the Torgnon measurement site (Tellinod, Aosta Valley, 45.84°N, 7.58°E). The site is a subalpine grassland located in northwestern Italian Alps, at an elevation of 2160 m a.s.l. The area is characterized by a typical subalpine climate, with an average annual temperature of around 3°C and an average annual precipitation of 880 mm. Further details on the study site can be found in Galvagno et al. (2013) and Filippa et al. (2015).

Since 2008, an automatic weather station provides 30-min averaged records of different meteorological parameters, including air and surface temperatures (HMP45, Vaisala, SI-111 and therm107, Campbell Scientific), short- and longwave radiations and surface albedo (CNR4, Kipp & Zonen), precipitation (OTT Pluvio2, Weighing Rain Gauge), soil water content (CS-616, Campbell Scientific), snow depth (SR50A-L, Campbell Scientific) and wind speed (WINDSONIC1-L, Campbell Scientific). Monthly manual measures of snow density (snow pits) are available during the winter season.

Remotely sensed observations

With the aim of evaluating the impact of the assimilation of remote sensed observations, the assimilation of Land Surface Temperature (LST) supplied by the Meteosat Second Generation (MSG) mission was introduced instead of the surface temperature locally measured by ground-based sensor. LST is the radiative skin temperature over land, whose retrieval is based on clear-sky measurements from the Spinning Enhanced Visible and InfraRed Imager (SEVIRI) aboard the geostationary MSG satellite (Jimenez-Munoz and Sobrino, 2008). Since this is a multi-spectral sensor, imaging across the visible and near-IR,

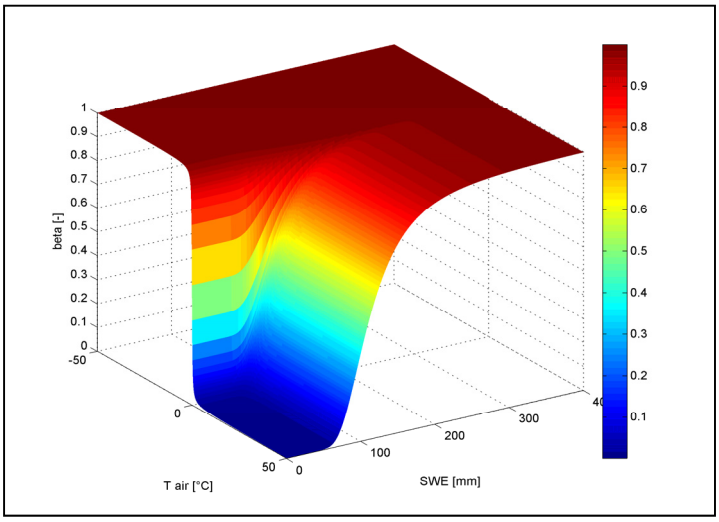

Fig. 4. Beta modulating function.

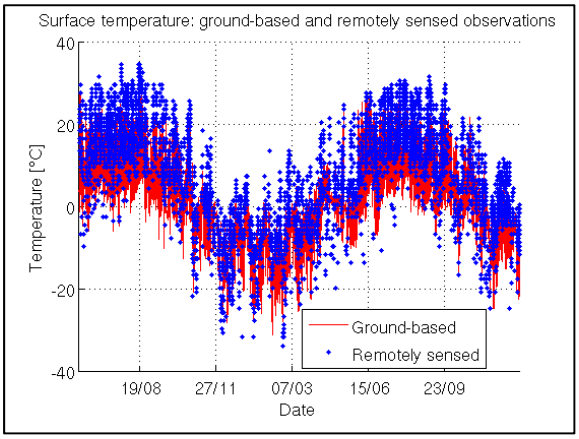

Fig. 5. Time series of ground-based and remotely sensed observations of surface temperature.

LST data are not available in cloudy condition. Despite the coarse spatial resolution of 5–6 km at the latitude of the study area, the temporal resolution of 15 minutes guaranteed by SEVIRI sensor can allow a significant reduction of the cloud cover affecting the remote sensed observations. Moreover the 15 minutes sampling makes this satellite product well suited to being employed in the DA procedure. Compared to the ground-based measurements of surface temperature at the Torgnon site, remote sensed LST is affected by a bias of about +5°C (see Figure 5), even though the two time series are well correlated (correlation coefficient equal to 0.85). A large fraction of the difference between the MSG LST and the ground-based one may be due to the kilometer-size footprint of the satellite product on a steep region where the spatial gradient of LST is of the order of degrees per kilometer.

EXPERIMENTS

Control experiments

DA impact on the accuracy of model simulations was evaluated by using an ensemble of 20 model states. Every 3 hours the in-situ data of the following variables were assimilated: surface temperature, snow depth and albedo. In the first control experiment the assimilated surface temperature observations were provided by the ground station (Exp_c1), while in the second one were supplied by MSG satellite (Exp_c2). With the aim of assessing the relative performance of DA, an open-loop simulation (no DA) is considered as control run.

Sensitivity experiments

With the purpose of analyzing SMASH performance and its sensitivity to different data assimilation settings, several experiments were carried out. Sensitivity to DA frequency was tested by assimilating the available observations every 3, 6, 12, 24 hours (Exp_s1). Sensitivity to ensemble size was evaluated by varying the number of ensemble members from 6 to 100 (Exp_s2). Moreover, the impact of the assimilation of different observed variables was investigated by assimilating different combinations of them (Exp_s3):

a. Only surface temperature (T_{sur});
b. Only snow depth (H_s);
c. Only albedo (Alb);
d. Surface temperature and snow depth (T_{sur} + H_s);
e. Surface temperature and albedo (T_{sur} + Alb);
f. Snow depth and albedo (H_s+Alb).

Since the aim is to assess the performance of the snow-related multivariable DA scheme, the experiments results are shown in terms of snowpack surface temperature, snow depth and SWE during the winter season to evaluate its efficiency in jointly updating several observed variables. Results are restricted to the winter period since in snowless conditions the DA scheme is limited to assimilation of only surface temperature.

Each experiment was quantitatively analyzed through the following statistical metrics, by considering the total amount of measurements, available every 30 minutes. Indirect SWE observations were retrieved from the monthly measures of snow density and the corresponding snow depth ones.

$$R = \frac{cov(Obs, Exp)}{\sigma_{obs} \cdot \sigma_{exp}} \qquad \text{Correlation coefficient (R)} \qquad (25)$$

$$RMSE = \sqrt{\frac{1}{N}\sum_{k=1}^{N}(Obs_k - Exp_k)^2}$$

Root Mean Square Error (RMSE) (26)

$$NER = \left(1 - \frac{RMSE_{Exp}}{RMSE_{OL}}\right) \cdot 100$$

Normalized Error Reduction (NER, Chen et al., 2011) (27)

$$Eff = \left(1 - \frac{\sum_{k=1}^{N}(Exp_k - Obs_k)^2}{\sum_{k=1}^{N}(OL_k - Obs_k)^2}\right) \cdot 100$$

Assimilation efficiency (Eff, Brocca et al., 2012) (28)

RESULTS

Control experiments

Exp_c1

Figure 6, Figure 7 and Figure 8 show the results of the Exp_c1. The open loop simulation (model run without assimilation) generally reveals an underestimation of the diurnal surface temperature peaks and a significant overestimation of the nocturnal ones. Indeed, even though the simulation gets the daily thermal cycle, it fails in reproducing the size of the temperature range. The model well represents the seasonal snowpack dynamics also in the open loop simulation, which results to be not affected by any significant bias. An overestimated snow compaction results in a underestimation trend during the accumulation period. Even though only a few SWE observations are available (monthly indirect measures), the model reveals a general underestimation of the snow mass. The multivariable DA scheme succeeds in forcing the average of the model states ensemble towards the observed values both in terms of surface temperature and snow depth. When considering the DA impact on SWE simulation, it is important to consider that no direct measurement of this variable is assimilated. However, through the multivariable DA the filter well succeeds in consistently updating the prediction of SWE dynamics with a resulting reduction of the underestimation during the accumulation period and a faster snow melting. Table 5 shows the improvement of snow depth simulations with a RMSE decrease of about 8 cm and an approximately unit correlation. Surface temperature is enhanced with a RMSE reduction of around 1°C and a resulting higher positive correlation. Despite of a poor sample, the statistical indices show that the assimilation of snow data allows a drop of the SWE RMSE of about 10 mm with a slight worsening of the correlation, which still maintains a high positive value.

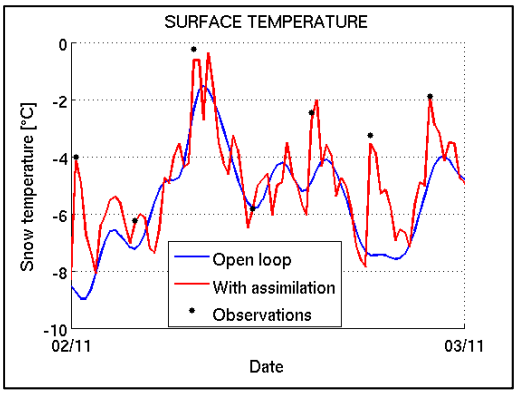

Fig. 6. Exp_c1 - Snow temperature time series 02nd - 03rd November 2012.

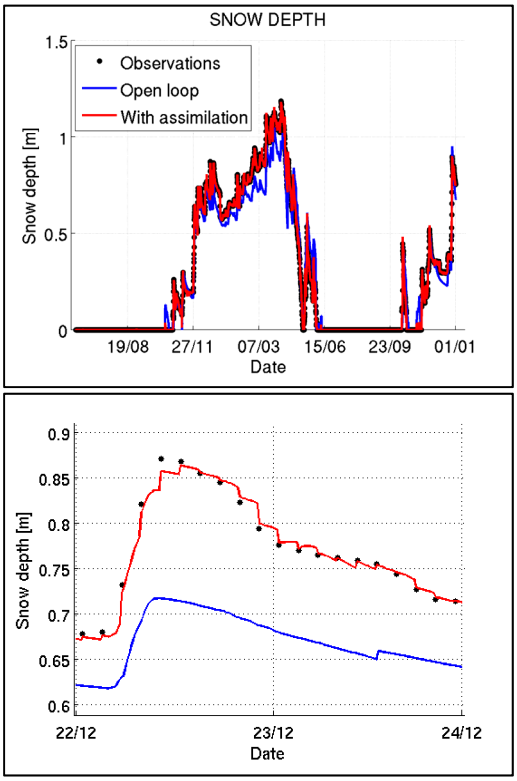

Fig. 7. Exp_c1 - Snow depth time series throughout the analysis period (top panel); Zoom from 22nd- 24th December 2012 (bottom panel).

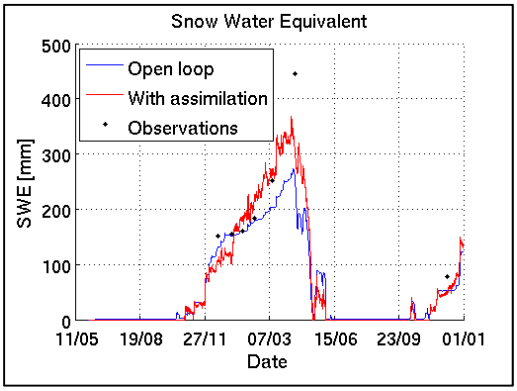

Fig. 8. Exp_c1 – SWE time series throughout the analysis period.

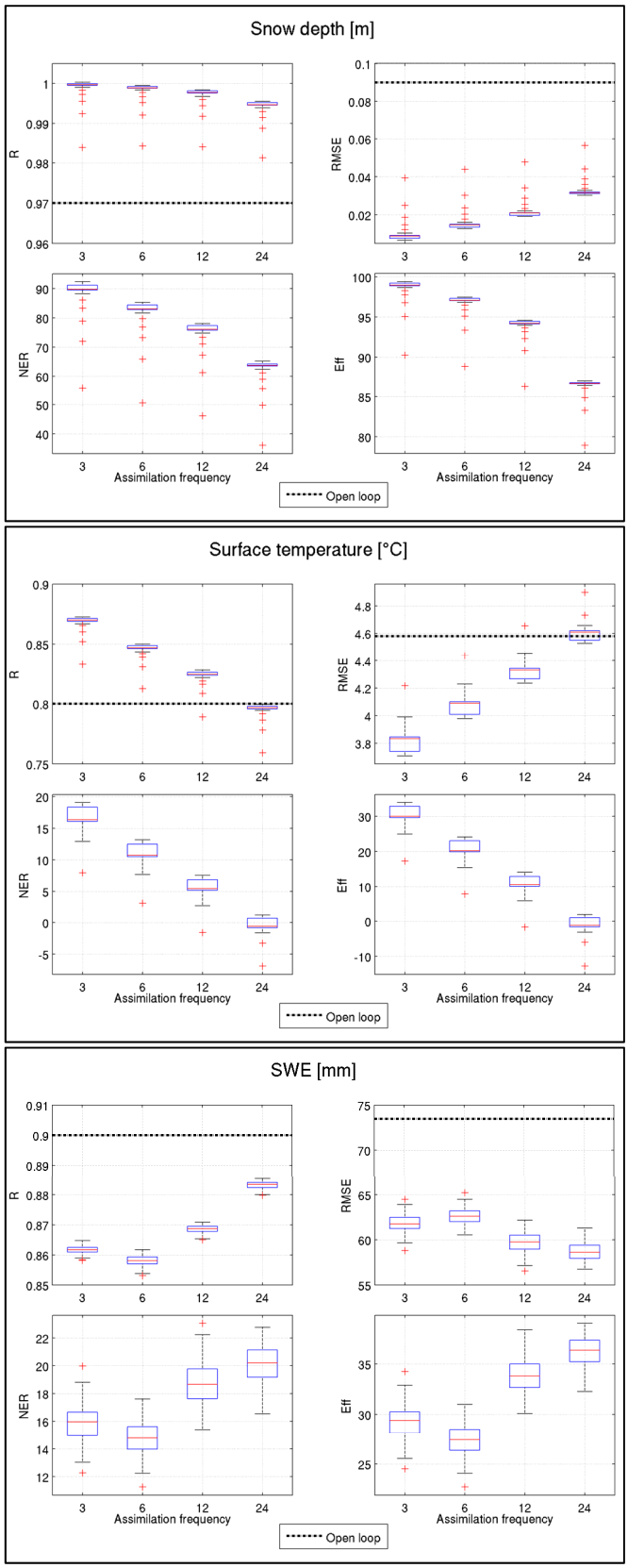

Fig. 9. Exp_s1 – Variable assimilation frequency for: a) snow depth, b) snow temperature, c) SWE.

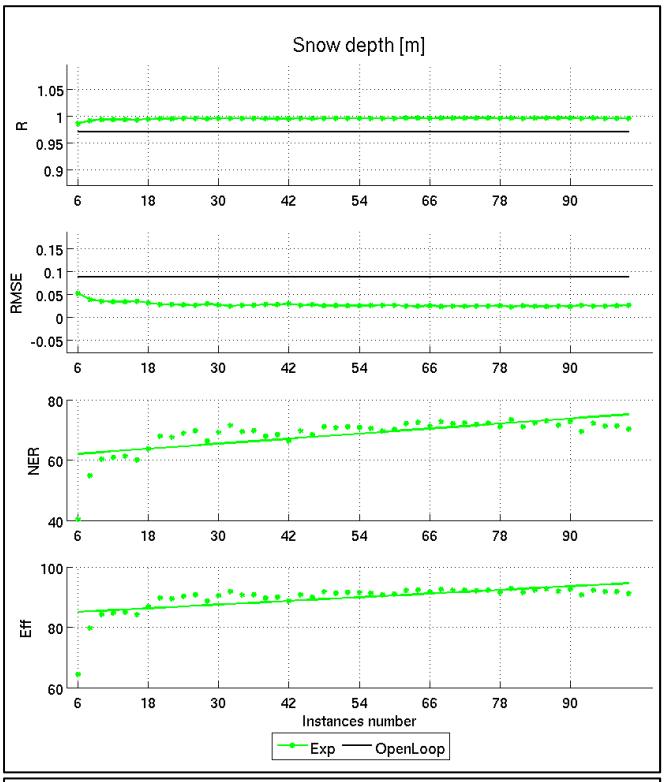

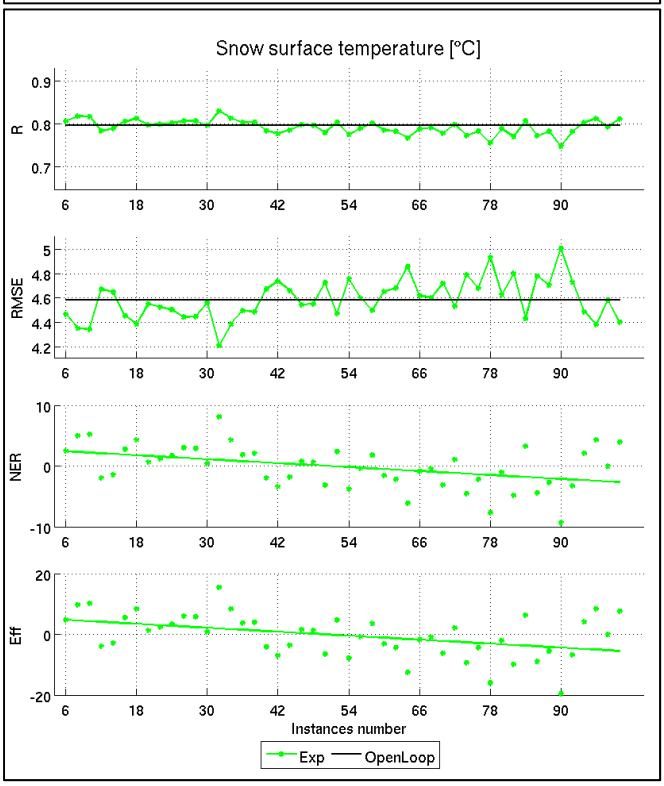

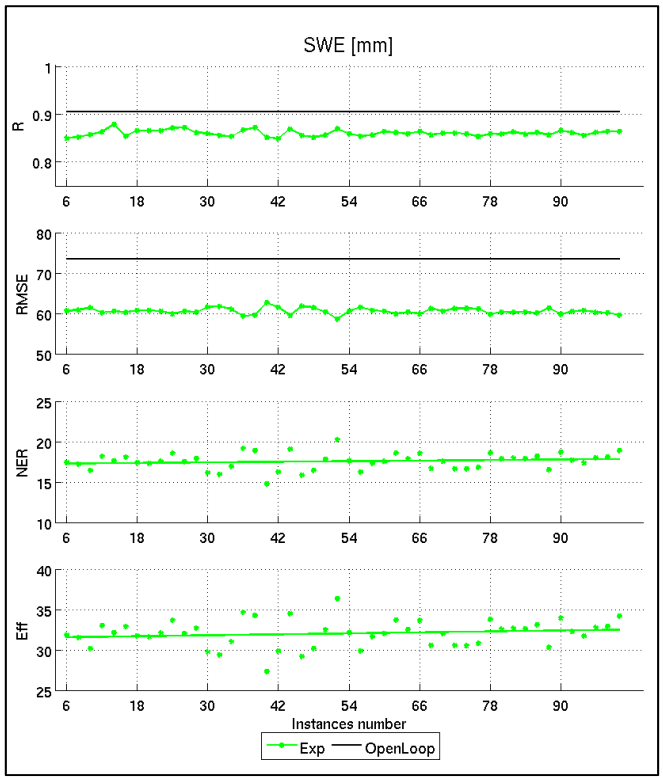

Fig. 10. Exp_s2 – Variable ensemble size for: a) snow depth, b) snow temperature, c) SWE.

Exp_c2

Table 5 shows the results of the joint assimilation of ground and satellite-based observations (Exp_c2). Since the remote sensed LST revealed an important bias, it is assimilated with a properly higher uncertainty with respect to the ground-based measurements. As expected, the overestimation affecting the satellite observations weakens the temperature simulation with a RMSE increase of about 0.5°C and poorer correlation with respect the open loop one. Nevertheless, the model performances are improved in terms of snow depth, whose RMSE decreases to less than 1 cm with an approximately unit correlation. Likewise, the multivariable DA well succeeds in improving the SWE simulations despite of the larger bias affecting the temperature observations.

Sensitivity experiments

Exp_s1

The system sensitivity to the assimilation frequency is shown in Figure 9. Statistical metrics reveal a foreseen worsening of filter performance in updating the directly assimilated variables (surface temperature and snow depth) as the assimilation frequency decreases. For these variables the 3-hours assimilation generally guarantees the best improvement. As expected, snow depth simulation (Figure 9a) is less sensitive to the assimilation time step than the temperature one (Figure 9b), mainly

Table 5. Exp_c1 and Exp_c2 – Statistical indices.

			Control experiments							
	Open loop		Exp_c1				Exp_c2			
Scores	Corr	RMSE	Corr	RMSE	NER	Eff	Corr	RMSE	NER	Eff
Snow depth [m]	0.97	0.09	0.99	0.01	88.52	98.68	0.99	0.01	89.23	98.84
Snow temperature [°C]	0.80	4.58	0.87	3.85	16.07	29.56	0.75	5.01	–9.33	–19.54
SWE [mm]	0.90	73.46	0.86	62.46	14.98	27.71	0.86	60.27	17.97	32.71

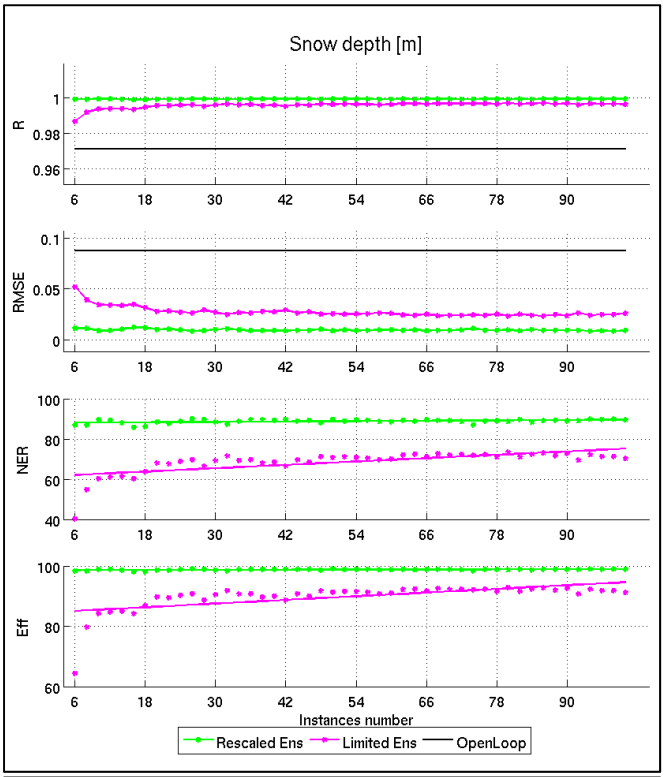

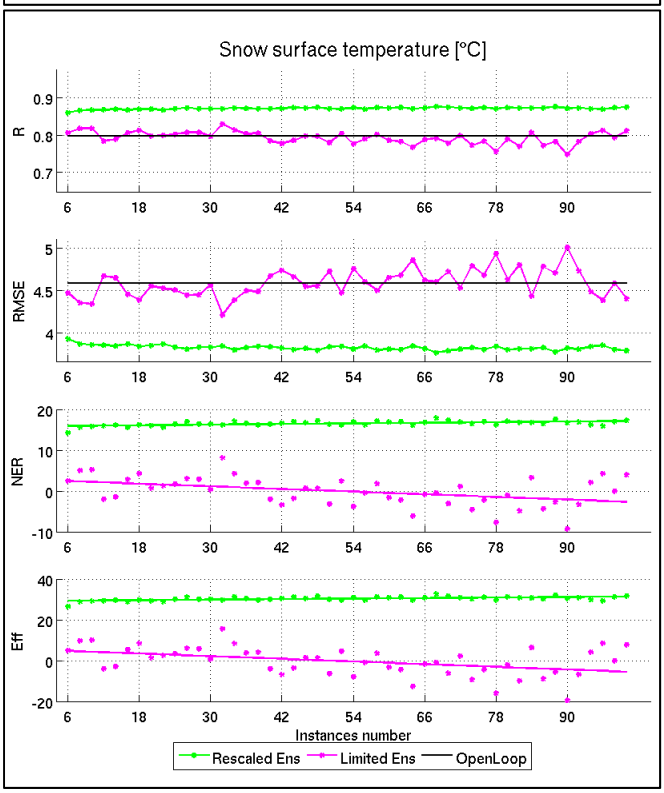

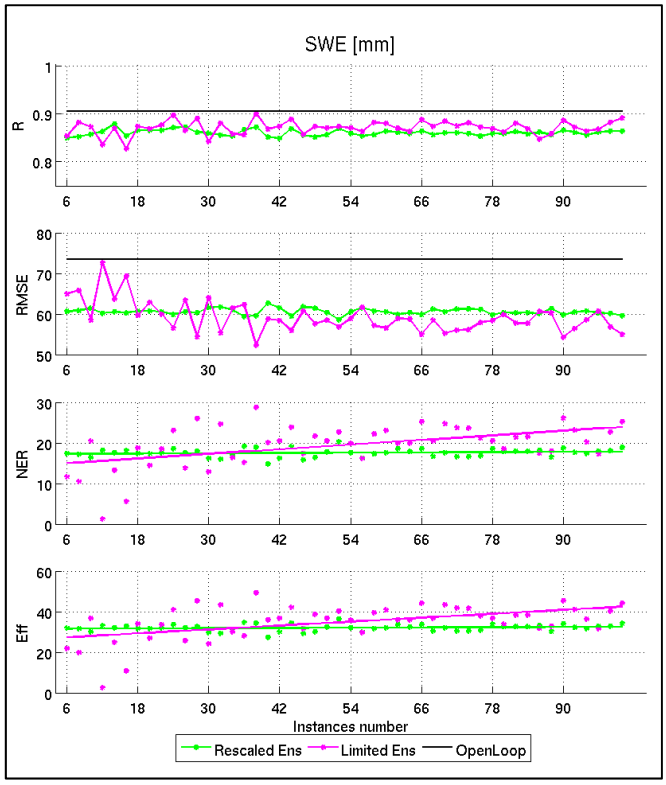

Fig. 11. Comparison between rescaling and truncation of the perturbed ensemble. Variable ensemble size for: a) snow depth, b) snow temperature, c) SWE.

thanks to the slower dynamics of snow depth changes with respect to the thermal ones. Temperature simulation considerably worsens due to the reduction of assimilation frequency, with statistical indices almost equivalent to the open loop ones with a 24-hours assimilation. Conversely, a reduction of the assimilation frequency results in a slight increasing improvement of SWE simulations (Figure 9c). The resulting scores suggest that the useful assimilation frequency for this system lies between 3 and 12 hours.

Exp_s2

The ensemble size is a critical parameter. Indeed, if the amount of model states is too limited, the evaluation of the model error covariance matrix could be not properly accurate. The uncertainty of this estimation decreases in a rate proportional to $1/\sqrt{N}$ with N model states (Evensen, 1994). On the other hand, if the ensemble is oversized, an excessive computational load could be required.

SMASH is not markedly sensitive to the ensemble size, especially in terms of correlation and RMSE. The increasing ensemble size allows an improvement of the assimilation efficiency and NER, whose upward trends are asymptotically tending to an upper limit of model performance (Figure 10).

Figure 11 shows the comparison between two different approaches of limiting the perturbed ensemble in order to guarantee the physical consistency of the system. The green time series refer to the employed method, which consists in rescaling the perturbed ensemble within proper physical limits; magenta ones represent the truncation of the inconsistent values. With respect to the open loop simulations, this latter approach allows an improvement of the snow depth modeling (Figure 11a), but the recurring discarding of inconsistent values does not allow significantly enhancing the surface temperature simulations (Figure 11b). Filter updating of SWE simulation is less sensitive to the implemented approach, with resulting almost equivalent performance (Figure 11c).

Exp_s3

This experiment aims at assessing the efficiency of the multivariable DA scheme depending on the assimilated variables.

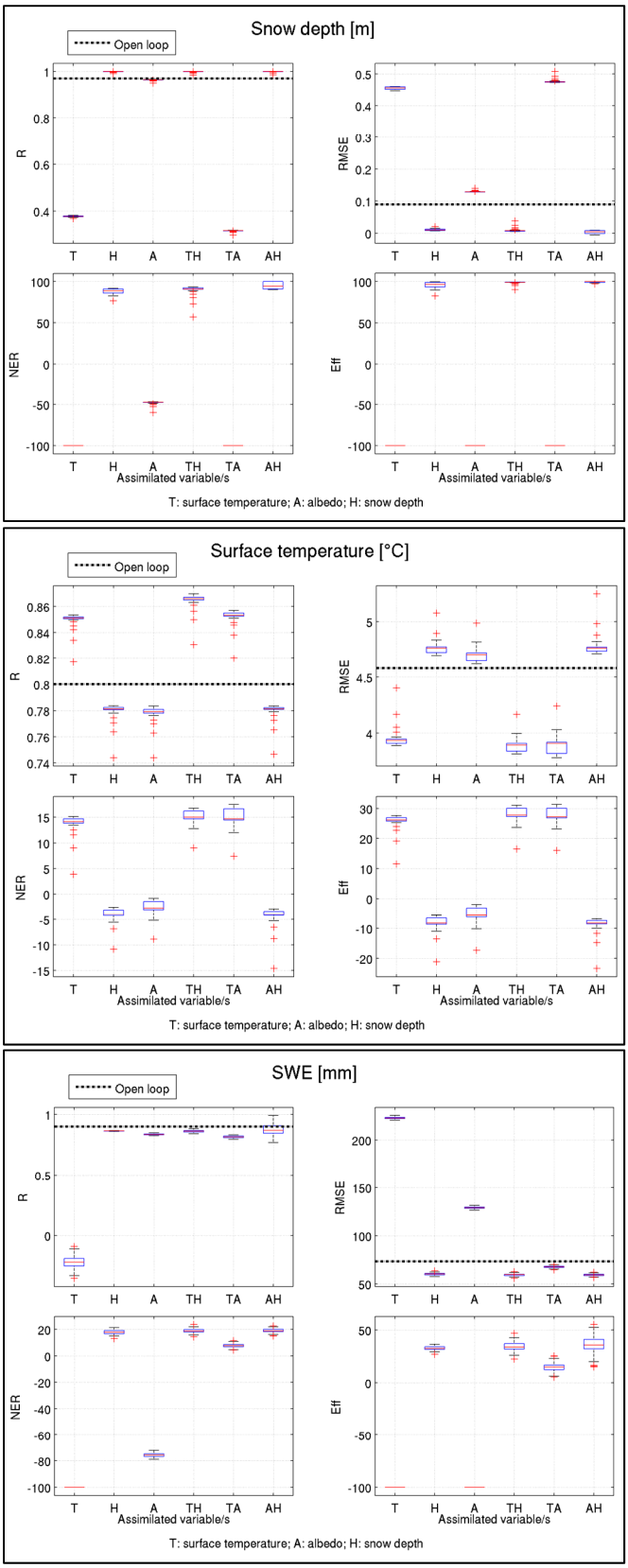

Fig. 12. Exp_s3 – Impact on model performance of the assimilation of different combinations of observed variables for a) snow depth, b) snow temperature, c) SWE.

Figure 12 shows the impact of the assimilation of different combinations of observations. The assimilation of only snow depth observations has a strong impact on snow depth and SWE also when they are assimilated in combination with other observed variables. However, the assimilation of snow depths does not succeed in improving snowpack temperature, even when assimilated together with the surface albedo. The assimilation of only surface temperature measurements has a negative effect on snowpack mass but it guarantees an expected improvement of the modeled temperature, which is even larger through its combined assimilation with snow depth or albedo measurements. The assimilation of only albedo observations has a lower impact on model performance with respect to the control run.

DISCUSSION

The combined assimilation of several ground-based observations allows improving model performance. The multivariable DA has a strong impact on snow depth simulations, both during the accumulation and the melting period. The assimilation of snow depth measurements enables to limit snowpack lowering due to the overestimation of snow compaction during the accumulation season. Moreover, snow melt events during winter and the snowmelt timing are better modeled with respect to the open loop predictions. The filter well succeeds in consistently updating the SWE through a proper handling of model nonlinearities. Indeed, even though no direct measurement of SWE is assimilated, the multivariable EnKF-based DA scheme allows improving SWE model predictions. The assimilation of surface temperature measurements ensures to catch the diurnal and nocturnal peaks, whose values are respectively under- and overestimated by the snow model. Nevertheless, the update of surface temperature introduces a saw tooth pattern in correspondence of the measures assimilation, mainly due to a low model thermal inertia driving the modeled series quickly tend towards the open loop values after the assimilation. Furthermore, it is important to consider that a sharp correction of the surface temperature is likely to generate a thermal condition remarkably different from the current one simulated by the model, which tends to restore its energy balance. The combined assimilation of ground-based measurements and the remote sensed LST entails a worsening of temperature simulations due to the overestimation bias affecting the satellite data. A weaker correction of the surface temperature entails a strengthening in both snow depth and SWE updating. Indeed, the assimilation of snow depth observations is even more effective since snowpack state is less affected by the combined temperature update, which can lead to a resulting thermal condition sensibly different from the modeled one. An expected worsening of the system performance is observed as the assimilation frequency decreases, except for SWE simulation benefiting from a less frequent updating of the energy balance affecting the snow mass. Nevertheless, the multivariable assimilation still allows a significant improvement of model simulations up to every 12 hours. SMASH reveals a low sensitivity to the ensemble size, mainly in terms of RMSE and correlation coefficient. It is important to consider that the larger is the ensemble, the more precise is the evaluation of model error covariance matrix. Anyway, consistently with the results of Durand and Margulis (2006), a sizeable increase of the ensemble (up to 100 model states) does not allow any remarkable improvement. Thus, we can assume that a limited ensemble is likely to provide a reliable assessment. Indeed, the need to enhance the quality of model error has to be balanced by considering the required computational cost.

The rescaling method adopted to constrain the ensemble after its correction and perturbation allows not compromising Gaussian distributions and it results in better performance than the truncation of inconsistent values (Su et al. 2010). Indeed,

the truncation of inconsistent values revealed poorer performance, since it does not preserve the ensemble mean and compromises the perturbations Gaussianity with a resulting bias due to the not null mean-valued perturbations.

The sensitivity analysis of the system to the assimilation of different observed variables allows highlighting the potentials of the multivariable DA scheme. The update of only the energy balance can generate a thermal condition sensibly different from the current one with a resulting worsening of the modeled snow mass. Since the simulated surface temperature is markedly biased, especially at diurnal and nocturnal peaks, its sharp update is likely to strongly impact on the snow depth. For instance, the correction of diurnal temperature peaks can cause snow melting events. On the other hand, the update of only the mass balance has no remarkable impact on the thermal state of the system. Clearly, the reduction of the model error covariance matrix to the energy- and mass-related minors does not guarantee the update of the overall system when individually assimilating energy- or mass-related variables. Nevertheless, the update of any observed variable strongly impacts on the snowpack state. In agreement with Durand and Margulis (2006) demonstrating the benefit of jointly assimilating energy- and mass-related observations, the resulting largest overall enhancement of model state is guaranteed by the combined assimilation of surface temperature, snow depth measurements and albedo.

CONCLUSION AND FUTURE DEVELOPMENTS

This research aims at investigating the feasibility of assimilating several ground-based snow observations for real-time applications by implementing new approaches allowing to better handle several limiting issues (e.g. model nonlinearities; computational demand). The main focus of the study is the assessment of the impact of different settings of the DA system on the performance of the multivariable EnKF. SMASH consists in a multi-layer model able to reproduce some of the main physical processes affecting snowpack dynamics by solving both energy and mass balances. An EnKF scheme is used to jointly assimilate observations of several variables of interest. Several constraints are introduced to maintain the model physical coherence. The model error covariance matrix is reduced to energy- and mass-related minors in order to prevent the introduction of any spurious correction of indirect state variables resulting from the nonlinear correlations among them. Moreover, any inconsistent value of the state variables resulting from the analysis procedure and/or the perturbation of the ensemble states is removed by limiting each variable into a proper physical range. Since the system is supposed to solve the energy balance both in snowy and snowless conditions, time variant physical ranges are modulated according to both air temperature and snow mass in order to properly handling transition periods (early winter and melting season) without causing model instability. SMASH 1D-version was tested at Torgnon site throughout the period June 2012 – December 2013. Several ground-based measurements were assimilated every 3 hours: surface temperature, snow depth and albedo. Data assimilation succeeds in enhancing model performance by reducing snow model biases in terms of surface temperature, SWE and snow depth. As well, the joint assimilation of ground-based measurements (snow depth and albedo) and remote sensed LST from MSG allowed improving model predictions, even though the large overestimation bias of the satellite observations compromises temperature simulations. Several sensitivity experiments were performed to assess SMASH sensitivity to different assimilation settings. With the decreasing of the assimilation frequency from 3 to 24 hours, the system revealed an expected worsening of modeling performance, except for SWE simulations. A 12-hours DA still guarantees significant improvements of model simulations. The lack of remarkable improvements with an increasing amount of model states reveals that SMASH is not markedly sensitive to the ensemble size. From a computational point of view, it is a considerable benefit since it enables to achieve well-performing results even employing a limited ensemble. The evaluation of the system sensitivity to the assimilation of different combinations of observed variables gives evidence of the potentialities of the multivariable DA. Indeed, the combined assimilation of surface temperature, snow depth and albedo observations reveals the best results in snowpack modeling. In light of the promising performance of the multivariable EnKF achieved in this point application, the development of the distributed version of the system is planned. The spatialized DA scheme is intended to enable a multisensory assimilation of several satellite products (e.g. MODIS SCA and snow albedo; Meteosat surface temperature; LiDAR measurements of snow depth; SWE from passive microwave sensors) for hydrological applications.

REFERENCES

Anderson, E.A, 1976. A point of energy and mass balance model of snow cover. NOAA Tech. Rep. NWS, 19, 150 p.

Andreadis, K.M., Lettenmaier, D.P., 2005. Assimilating remotely sensed snow observations into a macroscale hydrology model. Advances in Water Resources, 29.6, 872–886.

Avanzi, F., De Michele, C., Morin, S., Carmagnola, C.M., Ghezzi, A., Lejeune, Y., 2016. Model complexity and data requirements in snow hydrology: seeking a balance in practical applications. Hydrol. Process., 30, 2106–2118.

Balsamo, G., Albergel, C., Beljaars, A., Boussetta, S., Brun, E., Cloke, H., Dee, D., Dutra, E., Muñoz-Sabater, J., Pappenberger, F., de Rosnay, P., Stockdale, T., Vitart, F., 2015. ERA-Interim/Land: a global land surface reanalysis data set. Hydrology and Earth System Sciences, 19, 1, 389–407.

Barnett, T.P., Adam, J.C., Lettenmaier, D.P., 2005. Potential impacts of a warming climate on water availability in snow-dominated regions. Nature, 438, 7066, 303–309.

Bartelt, P., Lehning, M., 2002. A physical SNOWPACK model for the Swiss avalanche warning: Part I: numerical model. Cold Regions Science and Technology, 35, 3, 123–145.

Boni, G., Castelli, F., Gabellani, S., Machiavello, G., Rudari, R., 2010. Assimilation of MODIS snow cover and real time snow depth point data in a snow dynamic model. In: Proc. Geoscience and Remote Sensing Symposium (IGARSS). IEEE International, pp. 1788–1791.

Boone, A., Etchevers, P., 2001. An intercomparison of three snow schemes of varying complexity coupled to the same land surface model: Local-scale evaluation at an Alpine site. Journal of Hydrometeorology, 2, 4, 374–394.

Boone, A., Habets, F., Noilhan, J., Clark, D., Dirmeyer, P., Fox, S., Gusev, Y., Haddeland, I., Koster, R., Lohmann, D., Mahanama, S., Mitchell, K., Nasonova, O., Niu, G.-Y., Pitman, A., Polcher,J., Shmakin, A. B., Tanaka, K., van den Hurk, B., Vérant, S., Verseghy, D., Viterbo, P., Yang, Z.-L., 2004. The Rhone-aggregation land surface scheme intercomparison project: An overview. Journal of Climate, 17, 1, 187–208.

Bowling, L.C., Lettenmaier, D.P., Nijssen, B., Graham, L.P., Clark, D.B., El Maayar, M., Essery, R., Goers, S., Gusev, Y.M., Habets, F., van den Hurk, B., Jin, J., Kahan, D., Lohmann, D., Ma, X., Mahanama, S., Mocko, D., Nasonova,

O., Niu, G., Samuelsson, P., Shmakin, A.B., Takata, K., Verseghy, D., Viterbo, P., Xia, Y., Xue, Y., Tang, Z., 2003. Simulation of high-latitude hydrological processes in the Torne–Kalix basin: PILPS Phase 2 (e): 1: Experiment description and summary intercomparisons. Global and Planetary Change, 38, 1, 1–30.

Brasnett, B., 1999. A global analysis of snow depth for numerical weather prediction. Journal of Applied Meteorology, 38, 6, 726–740.

Brocca, L., Moramarco, T., Melone, F., Wagner, W., Hasenauer, S., Hahn, S., 2012. Assimilation of surface-and root-zone ASCAT soil moisture products into rainfall–runoff modeling. IEEE Transactions on Geoscience and Remote Sensing, 50, 7, 2542–2555.

Brun, E., Martin, E., Simon, V., Gendre, C., Coleou, C., 1989. An energy and mass model of snow cover suitable for operational avalanche forecasting. Journal of Glaciology, 35, 121, 333–342.

Caparrini, F., Castelli, F., Entekhabi, D., 2004. Estimation of surface turbulent fluxes through assimilation of radiometric surface temperature sequences. Journal of Hydrometeorology, 5, 1, 145–159.

Charrois, L., Cosme, E., Dumont, M., Lafaysse, M., Morin, S., Libois, Q., Picard, G., 2016. On the assimilation of optical reflectances and snow depth observations into a detailed snowpack model. The Cryosphere, 10, 1021–1038. http://doi.org/10.5194/tc-10-1021-2016.

Chen, F., Crow, W.T., Starks, P.J., Moriasi, D.N., 2011. Improving hydrologic predictions of a catchment model via assimilation of surface soil moisture. Advances in Water Resources, 34, 4, 526–536.

Clark, M.P., Hay, L.E., 2004. Use of medium-range numerical weather prediction model output to produce forecasts of stream-flow. J. Hydrometeorol., 5, 15–32.

Clark, M.P., Slater, A.G., Barrett, A.P., Hay, L.E., McCabe, G.J., Rajagopalan, B., Leavesley, G.H., 2006. Assimilation of snow covered area information into hydrologic and land-surface models. Advances in Water Resources, 29, 8, 1209–1221.

Cressman, G.P., 1959. An operational objective analysis system. Mon. Wea. Rev., 87, 10, 367–374.

Dee, D.P., Uppala, S.M., Simmons, A.J., Berrisford, P., Poli, P., Kobayashi, S., Andrae, U., Balmaseda, M.A., Balsamo, G., Bauer, P., Bechtold, P., Beljaars, A.C.M., van de Berg, L. Bidlot, J., Bormann, N., Delsol, C., Dragani, R., Fuentes, M., Geer, A.J., Haimberger, L., Healy, S.B., Hersbach, H., Hòlm, E.V., Isaksen, L., Kållberg, P., Köhler, M., Matricardi, M., McNally, A.P., Monge-Sanz, B.M., Morcrette, J.-J. , Park, B.-K., Peubey, C., deRosnay, P., Tavolato, C., Thépaut, J.-N., Vitart, F., 2011. The ERA-Interim reanalysis: Configuration and performance of the data assimilation system. Quarterly Journal of the Royal Meteorological Society, 137, 656, 553–597.

De Lannoy, G.J.M., Reichle, R.H., Arsenault, K.R., Houser, P.R., Kumar, S., Verhoest, N.E.C., Pauwels, V.R.N., 2012. Multiscale assimilation of advanced microwave scanning radiometer-EOS snow water equivalent and moderate resolution imaging spectroradiometer snow cover fraction observations in northern Colorado. Water Resour. Res., 48, W01522. DOI: 10.1029/2011WR010588.

Dong, J., Walker, J.P., Houser, P.R., Sun, C., 2007. Scanning multichannel microwave radiometer snow water equivalent assimilation. Journal of Geophysical Research: Atmospheres, 112, D7.

Douville, H., Royer, J.-F., Mahfouf, J.-F., 1995. A new snow parameterization for the Meteo-France climate model Part I: validation in stand-alone experiments. Climate Dynamics, 12, 1, 21–35.

Drusch, M., Vasiljevic, D., Viterbo, P., 2004. ECMWF's global snow analysis: assessment and revision based on satellite observations. J. Appl. Meteorol., 43, 1282–1294.

Dunne, S., Entekhabi, D., 2005. An ensemble-based reanalysis approach to land data assimilation. Water Resour. Res., 41, 2.

Dunne, S., Entekhabi, D., 2006. Land surface state and flux estimation using the ensemble Kalman smoother during the Southern Great Plains 1997 field experiment. Water Resour. Res., 42, 1.

Durand, M., Margulis, S.A., 2006. Feasibility test of multifrequency radiometric data assimilation to estimate snow water equivalent. Journal of Hydrometeorology, 7, 3, 443–457.

Durand, M., Margulis, S.A., 2008. Effects of uncertainty magnitude and accuracy on assimilation of multiscale measurements for snowpack characterization. J. Geophys. Res. Atmos., 113, D02105.

Dutra, E., Balsamo, G., Viterbo, P., Miranda, P.M., Beljaars, A., Schär, C., Elder, K., 2010. An improved snow scheme for the ECMWF land surface model: description and offline validation. Journal of Hydrometeorology, 11, 4, 899–916.

Dutra, E., Viterbo, P., Miranda, P.M., Balsamo, G., 2012. Complexity of snow schemes in a climate model and its impact on surface energy and hydrology. Journal of Hydrometeorology, 13, 2, 521–538.

Endrizzi, S., Gruber, S., Dall'Amico, M., Rigon, R., 2014. GEOtop 2.0: simulating the combined energy and water balance at and below the land surface accounting for soil freezing, snow cover and terrain effects. Geoscientific Model Development, 7, 2831–2857.

Essery, R., Rutter, N., Pomeroy, J., Baxter, R., Stahli, M., Gustafsson, D., Barr, A., Bartlett, P., Elder, K., 2009. SNPWMIP2: An evaluation of forest snow process simulations. Bull. Amer. Met. Soc., 90, 1120–1135.

Essery, R., Morin, S., Lejeune, Y., Ménard, C.B., 2013. A comparison of 1701 snow models using observations from an Alpine site. Advances in Water Resources, 55, 131–148.

Etchevers, P., Martin, E., Brown, R., Fierz, C., Lejeune, Y., Bazile, E., Boone, A., Dai, Y.J., Essery, R., Fernandez, A., Gusev, Y., Jordan, R., Koren, V., Kowalczyk, E., Nasonova, N.O., Pyles, R.D., Schlosser, A., Shmakin, A.B., Smirnova, T.G., Strasser, U., Verseghy, D., Yamazaki, T., Yang, Z.L., 2003. Validation of the energy budget of an alpine snowpack simulated by several snow models (SnowMIP project). Annals of Glaciology, 38, 1, 150–158.

Evensen, G., 1994. Sequential data assimilation with a nonlinear quasi-geostrophic model using Monte Carlo methods to forecast error statistics. Journal of Geophysical Research: Oceans, 99, C5, 10143–10162.

Evensen, G., 2003. The ensemble Kalman filter: Theoretical formulation and practical implementation. Ocean Dynamics, 53, 4, 343–367.

Filippa, G., Cremonese, E., Galvagno, M., Migliavacca, M., Di Cella, U.M., Petey, M., Siniscalco, C., 2015. Five years of phenological monitoring in a mountain grassland: inter-annual patterns and evaluation of the sampling protocol. International journal of biometeorology, 59, 12, 1927–1937.

Froidurot, S., Zin, I., Hingray, B., Gautheron, A., 2014. Sensitivity of precipitation phase over the Swiss Alps to different meteorological variables. Journal of Hydrometeorology, 15, 2, 685–696.

Galvagno, M., Wohlfahrt, G., Cremonese, E., Rossini, M., Colombo, R., Filippa, G., Julitta, T., Manca, G., Siniscalco, C., Migliavacca, M., Morra di Cella, U., 2013. Phenology and carbon dioxide source/sink strength of a subalpine grassland in response to an exceptionally short snow season. Environmental Research Letters, 8, 2, 025008.

Gelb, A., 1974. Optimal linear filtering, in Applied Optimal Estimation, edited by A. Gelb, pp. 102–155, MIT Press, Cambridge, Mass.

Griessinger, N., Seibert, J., Magnusson, J., Jonas, T., 2016. Assessing the benefit of snow data assimilation for runoff modeling in Alpine catchments. Hydrology and Earth System Sciences, 20, 9, 3895–3905.

Gupta, H.V., Kling, H., Yilmaz, K.K., Martinez, G.F., 2009. Decomposition of the mean squared error and NSE performance criteria: Implications for improving hydrological modelling. Journal of Hydrology, 377, 1, 80–91.

Hedstrom, N.R., Pomeroy, J.W., 1998. Accumulation of intercepted snow in the boreal forest: measurements and modelling. Hydrological Processes, 12, 1611–1625.

Huang, C., Newman, A.J., Clark, M.P., Wood, A.W., Zheng, X., 2017. Evaluation of snow data assimilation using the ensemble Kalman filter for seasonal streamflow prediction in the western United States. Hydrology and Earth System Sciences, 21 1, 635–650.

Jordan, R., 1991. A one-dimensional temperature model for a snow cover: Technical documentation for SNTHERM. 89 (No. CRREL-SR-91-16). Cold Regions Research and Engineering Lab Hanover, NH.

Jimenez-Munoz, J.C., Sobrino, J.A., 2008. Split-window coefficients for land surface temperature retrieval from low-resolution thermal infrared sensors. IEEE geoscience and remote sensing letters, 5, 4, 806–809.

Kojima, K., 1967. Densification of a seasonal snow cover, in Physics of Snow and Ice, Proc. Int. Conf. Low Temp. Sci., vol. I, part 2, S.929-S.952.

Lehning M., Bartelt, P.B., Brown, R.L., Fierz, C., Satyawali, P., 2002. A physical SNOWPACK model for the Swiss Avalanche Warning Services. Part II: Snow Microstructure. Cold regions science and technology, 35, 3, 147–167.

Liston, G.E., Sturm, M., 1998. A snow-transport model for complex terrain. Journal of Glaciology, 44, 148, 498–516.

Liston, G.E., Pielke, R.A., Greene, E.M., 1999. Improving first-order snow-related deficiencies in a regional climate model. Journal of Geophysical Research: Atmospheres, 104(D16), 19559–19567.

Liston, G.E., Hiemstra, C.A., 2008. A simple data assimilation system for complex snow distributions (SnowAssim). Journal of Hydrometeorology, 9, 5, 989–1004.

Magnusson, J., Farinotti, D., Jonas, T., and Bavay, M., 2011. Quantitative evaluation of different hydrological modelling approaches in a partly glacierized Swiss watershed. Hydrol. Process., 25, 2071–2084.

Magnusson, J., Gustafsson, D., Hüsler, F., Jonas, T., 2014. Assimilation of point SWE data into a distributed snow cover model comparing two contrasting methods. Water Resources Research, 50, 10, 7816–7835.

Magnusson, J., Wever, N., Essery, R., Helbig, N., Winstral, A., Jonas, T., 2015. Evaluating snow models with varying process representations for hydrological applications: Snow model evaluation. Water Resour. Res., 51, 2707–2723.

Malik, M.J., van der Velde, R., Vekerdy, Z., Su, Z., 2012. Assimilation of satellite-observed snow albedo in a land surface model. Journal of hydrometeorology, 13, 3, 1119–1130.

Mellor, M., 1964. Properties of snow, Cold Reg. Sci. Eng. Monogr., III-A1.

Miller, R.N., Ghil, M., Gauthiez, F., 1994. Advanced data assimilation in strongly nonlinear dynamical systems. Journal of the atmospheric sciences, 51, 8, 1037–1056.

Montzka, C., Pauwels, V., Franssen, H.J.H., Han, X., Vereecken, H., 2012. Multivariate and multiscale data assimilation in terrestrial systems: A review. Sensors, 12, 12, 16291–16333.

Moradkhani, H., 2008. Hydrologic remote sensing and land surface data assimilation. Sensors, 8, 5, 2986–3004.

Nijssen, B., Bowling, L.C., Lettenmaier, D.P., Clark, D.B., El Maayar, M., Essery, R.,Goers, S., Gusev, Y.M., Habets, F., van den Hurk, B., Jin, J., Kahan, D., Lohmann, D., Ma, X., Mahanama, S., Mocko, D., Nasonova, O., Niu, G., Samuelsson, P., Shmakin, A.B., Takata, K., Verseghy, D., Viterbo, P., Xia, Y., Xue, Y., Yang, Z., 2003. Simulation of high latitude hydrological processes in the Torne–Kalix basin: PILPS Phase 2 (e): 2: Comparison of model results with observations. Global and Planetary Change, 38, 1, 31–53.

Pan, M., Sheffield, J., Wood, E.F., Mitchell, K.E., Houser, P.R., Schaake, J.C., Robock, A., Lohmann, D., Cosgrove, B., Duan, Q., Luo, L., Higgins, R.W., Pinker, R.T., Tarpley, J.D., 2003. Snow process modeling in the North American Land Data Assimilation System (NLDAS): 2. Evaluation of model simulated snow water equivalent. Journal of Geophysical Research: Atmospheres, 108, D22.

Rodell, M., Houser, P.R., 2004. Updating a land surface model with MODIS-derived snow cover. Journal of Hydrometeorology, 5, 6, 1064–1075.

Rutter, N., Essery, R., Pomeroy, J., Altimir, N., Andreadis, K., Baker, I., Barr, A., Bartlett, P., Boone, A., Deng, H., Douville, H., Dutra, E., Elder, K., Ellis, C., Feng, X., Gelfan, A., Goodbody, A., Gusev, Y., Gustafsson, D., Hellström, R., Hirabayashi, Y., Hirota, T., Jonas, T., Koren, V., Kuragina, A., Lettenmaier, D., Li, W.-P., Luce, C., Martin, E., Nasonova, O., Pumpanen, J., Pyles, R.D., Samuelsson, P., Sandells, M., Schädler, G., Shmakin, A., Smirnova, T.G., 27, Stähli, M., Stöckli, R., Strasser, U., Su, H., Suzuki, K., Takata, K., Tanaka, K., Thompson, E., Vesala, T., Viterbo, P., Wiltshire, A., Xia, K., Xue, Y., Yamazaki, T., 2009. Evaluation of forest snow processes models (SnowMIP2). Journal of Geophysical Research: Atmospheres, 114, D6.

Schlosser, C.A., Slater, A.G., Robock, A., Pitman, A.J., Vinnikov, K.Y., Henderson-Sellers, A., Speranskaya, N.A., Mitchell, K., and the PILPS2 contributors, 2000. Simulations of a boreal grassland hydrology at Valdai, Russia: PILPS Phase 2 (d). Monthly Weather Review, 128, 2, 301–321.

Slater, A.G., Pitman, A.J., Desborough, C.E., 1998. The validation of a snow parameterization designed for use in general circulation models. International journal of climatology, 18, 6, 595–617.

Slater, A.G., Schlosser, C.A., Desborough, C.E., Pitman, A.J., Henderson-Sellers, A., Robock, A., Vinnikov, K.Y., Mitchell, K., Boone, A., Braden, H., Chen, F., Cox, P.M., de Rosnay, P., Dickinson, R.E., Dai,Y.-J., Duan ,Q., Entin, J., Etchevers, P., Gedney, N., Gusev, Y.M., Habets, F., Kim, J., Koren, V., Kowalczyk, E.A., Nasonova, O.N., Noilhan, J., Schaake, S., Shmakin, A.B., Smirnova, T.G., Verseghy, D., Wetzel, P., Xue, Y., Yang, Z.-L., Zeng, Q., 2001. The representation of snow in land surface schemes: Results from PILPS 2 (d). Journal of Hydrometeorology, 2, 1, 7–25.

Slater, A.G., Clark, M.P., 2006. Snow data assimilation via an ensemble Kalman filter. Journal of Hydrometeorology, 7, 3, 478–493.

Stauffer, D.R., Seaman, N.L., 1990. Use of four-dimensional data assimilation in a limited-area mesoscale model. Part I: Experiments with synoptic-scale data. Monthly Weather Review, 118, 6, 1250–1277.

Stigter, E.E., Wanders, N., Saloranta, T.M., Shea, J.M., Bierkens, M.F.P., Immerzeel, W.W., 2017. Assimilation of snow cover and snow depth into a snow model to estimate snow water equivalent and snowmelt runoff in a Himalayan catchment, Cryosph., 1647–1664.

Su, H., Yang, Z.L., Niu, G.Y., Dickinson, R.E., 2008. Enhancing the estimation of continental-scale snow water equivalent by assimilating MODIS snow cover with the ensemble Kalman filter. Journal of Geophysical Research: Atmospheres, 113, D8.

Su, H., Yang, Z.L., Dickinson, R.E., Wilson, C.R., Niu, G.Y., 2010. Multisensor snow data assimilation at the continental scale: The value of gravity recovery and climate experiment terrestrial water storage information. Journal of Geophysical Research: Atmospheres, 115, D10.

Sun, C., Walker, J.P., Houser, P.R., 2004. A methodology for snow data assimilation in a land surface model. Journal of Geophysical Research: Atmospheres, 109, D8.

Verseghy, D.L., 1991. CLASS–A Canadian land surface scheme for GCMs. I. Soil model. International Journal of Climatology, 11, 2, 111–133.

Vionnet, V., Brun, E., Morin, S., Boone, A., Faroux, S., Le Moigne, P., Martin, E., Willemet, J.M., 2012. The detailed snowpack scheme Crocus and its implementation in SURFEX v7. 2. Geoscientific Model Development, 5, 773–791.

Wächter, A., Biegler, L.T., 2006. On the implementation of an interior-point filter line-search algorithm for large-scale nonlinear programming. Mathematical Programming, 106, 1, 25–57.

Winstral, A., Marks, D., 2014. Long-term snow distribution observations in a mountain catchment: Assessing variability, time stability, and the representativeness of an index site. Water Resources Research, 50, 1, 293–305.

Wiscombe, W.J., Warren, S.G., 1980. A model for the spectral albedo of snow. I: Pure snow. Journal of the Atmospheric Sciences, 37, 12, 2712–2733.

Wood, A.W., Hopson, T., Newman, A., Brekke, L., Arnold, J., Clark, M., 2016. Quantifying streamflow forecast skill elasticity to initial condition and climate prediction skill. Journal of Hydrometeorology, 17, 2, 651–668.

Zappa, M., Pos, F., Strasser, U., Warmerdam, P., Gurtz, J., 2003. Seasonal water balance of an Alpine catchment as evaluated by different methods for spatially distributed snowmelt modelling. Hydrology Research, 34, 3, 179–202.

Zhang, T., 2005. Influence of the seasonal snow cover on the ground thermal regime: An overview. Reviews of Geophysics, 43, 4.

Yang, Z.L., Dickinson, R.E., Robock, A., Vinnikov, K.Y., 1997. Validation of the snow submodel of the biosphere–atmosphere transfer scheme with Russian snow cover and meteorological observational data. Journal of Climate, 10, 2, 353–373.

Received 18 May 2017
Accepted 11 December 2017

J. Hydrol. Hydromech., 67, 2019, 1, 20–31
DOI: 10.2478/johh-2018-0007

An optimized snowmelt lysimeter system for monitoring melt rates and collecting samples for stable water isotope analysis

Andrea Rücker[1, 2*], Massimiliano Zappa[1], Stefan Boss[1], Jana von Freyberg[2, 1]

[1] Swiss Federal Institute for Forest, Snow and Landscape Research (WSL), Zürcherstrasse 111, 8903 Birmensdorf, Switzerland.
[2] Department of Environmental Systems Science, ETH Zurich, Universitätsstr. 16, 8092 Zurich, Switzerland.
[*] Corresponding author. Tel.: +41 44 739 2487 or +41 44 6329 171. Fax: +41 44 7392 215. E-mail: andrea.ruecker@wsl.ch

Abstract: The contribution of snow meltwater to catchment streamflow can be quantified through hydrograph separation analyses for which stable water isotopes (^{18}O, ^{2}H) are used as environmental tracers. For this, the spatial and temporal variability of the isotopic composition of meltwater needs to be captured by the sampling method. This study compares an optimized snowmelt lysimeter system and an unheated precipitation collector with focus on their ability to capture snowmelt rates and the isotopic composition of snowmelt. The snowmelt lysimeter system consists of three individual unenclosed lysimeters at ground level with a surface of 0.14 m^2 each. The unheated precipitation collector consists of a 30 cm-long, extended funnel with its orifice at 2.3 m above ground. Daily snowmelt samples were collected with both systems during two snowfall-snowmelt periods in 2016. The snowmelt lysimeter system provided more accurate measurements of natural melt rates and allowed for capturing the small-scale variability of snowmelt process at the plot scale, such as lateral meltwater flow from the surrounding snowpack. Because of the restricted volume of the extended funnel, daily melt rates from the unheated precipitation collector were up to 43% smaller compared to the snowmelt lysimeter system. Overall, both snowmelt collection methods captured the general temporal evolution of the isotopic signature in snowmelt.

Keywords: Snowmelt lysimeter; Snowmelt collection; Snowmelt rate; Stable water isotopes.

INTRODUCTION

Snowpacks in mountainous headwater catchments comprise important freshwater resources in many regions of the world (Stewart, 2009). In Switzerland, about 42% of river discharge is fed by snow meltwater (Zappa et al., 2012), so that hydropower production strongly depends on the seasonal water storage in higher elevations (Beniston, 2003). In some mountainous snow-dominated regions, predicted effects of climate change, such as higher air temperatures and lower precipitation rates, will result in decreasing snow volumes, as well as in earlier and shortened snowmelt (Barnett et al., 2005; Beniston, 2003; Berghuijs et al., 2014). Hereby, the mid and lower altitudes will be affected the most by changes in water storage (Barnett et al., 2005), because the snowline rises about 150 m in elevation with every of 1°C increase in air temperature (Beniston, 2003). By the end of the 21st century, mountainous catchments in Switzerland are expected to receive up to 50% less snow at 2000 m a.s.l. and up to 90% less snow at about 1000 m a.s.l. (Beniston, 2003). As a consequence, the risk for summer low flows in downstream valleys is likely to increase (Stewart, 2009).

In order to adapt water management strategies to future changes in the hydrological cycle, the physical mechanisms that control streamflow generation from snowmelt, have to be understood (Bierkens and van Beek, 2009; Šanda et al., 2010; Singla et al., 2012; Staudinger and Seibert, 2014).

Environmental tracers, such as stable water isotopes (^{18}O, ^{2}H), can be used to identify water sources that contribute to river streamflow (Klaus and McDonnell, 2013). In the last decades, stable water isotopes have been applied in hydrograph separation analyses to quantify the contribution of snowmelt to catchment outflow (Ala-aho et al., 2017; Dinçer et al., 1970; Hooper and Shoemaker, 1986; Huth et al., 2004; Laudon, 2004; Penna et al., 2014b; Rodhe, 1998; Šanda et al., 2014; Taylor et al., 2002b). Hereby, the isotope signal of snowmelt can be highly variable in time during individual melt periods similar to the short-term isotopic evolution of liquid precipitation (Munksgaard et al., 2012; von Freyberg et al., 2017). This isotopic variability in snowmelt is driven by mixing with incoming precipitation (rain or snow), snow redistribution by wind, and isotopic fractionation of snowmelt during (re-)freezing and condensation in the snowpack (Ala-aho et al., 2017; Cooper, 1998; Lyon et al., 2010; Rodhe, 1998; Taylor, 2001; Unnikrishna et al., 2002).

During rain-on-snow events, rainwater can mix with the snow and thus significantly change the isotopic composition of melt from the snowpack (Juras et al., 2016; Penna et al., 2014a; Unnikrishna et al., 2002). In addition, the snowpack becomes progressively isotopically enriched during the melt-out, which is directly linked to the rate of snowmelt (Ala-aho et al., 2017; Hooper and Shoemaker, 1986; Laudon, 2004; Lee et al., 2010; Taylor et al., 2001; Unnikrishna et al., 2002).

In order to use stable water isotopes of snowmelt for hydrograph separation analyses, the spatial and temporal variability of the isotopic composition of meltwater needs to be captured by the sampling method (Earman et al., 2006; Laudon et al., 2002; Schmieder et al., 2016; Taylor et al., 2002b). In addition, snowmelt rates have to be recorded to volume-weight the isotope values of composite samples.

Different methods exist to measure the snowmelt rates and to collect samples for isotope analysis. Snowmelt can be collected, for instance, from the base of a snow pit (Taylor et al., 2002b) or from soil cores (Frisbee et al., 2010). In remote and mountainous terrain, these manual methods are often the only possibility to obtain snowmelt samples, however, sample collection in such catchments is laborious, can be dangerous and may be prone to sampling errors. An alternative method for direct meltwater collection is a passive capillary sampler to capture an integrated meltwater sample throughout the melt season (Frisbee et al., 2010; Penna et al., 2014a). For more

frequent sampling, a melt pan can be installed beneath a snowpack from which meltwater drains through a pipe into a sample collector (Bales et al., 1993; Taylor et al., 2001). Alternatively, an unheated precipitation collector can be deployed to sample snowmelt (Earman et al., 2006; Gröning et al., 2012). Two different types of unheated precipitation collectors were evaluated by Earman et al. (2006) by collecting six-month bulk snowmelt for subsequent isotope analysis. The unheated precipitation collectors were designed to capture the snowmelt composition at 1 m above ground by using extension tubes on top of the 10 cm-diameter funnels. The extension tubes of the two systems were 7.5 cm (regular funnel) and 15 cm long (extended funnel) respectively. Earman et al. (2006) found that the samples from the collector with the extended funnel were "[…] more representative of infiltration water isotope composition than a fresh snow sample because the snow in the extended collector is subject to many of the snow metamorphism effects that impact snow on the ground.". To test whether accelerated melt caused isotope effects in the snowmelt sample, two of the extended funnel precipitation collectors were painted in either black or white colour (Earman et al., 2006). However, the colouring of the funnel was not found to significantly affect the isotopic composition of the bulk melt sample (Earman et al., 2006). Hence, the extended funnel collector might be a suitable method for collecting a sample that is representative for the isotopic composition of the snowpack. Rates of snowmelt are, however, likely to remain highly uncertain due to under-catch and wind drift (Rasmussen et al., 2012).

Snowmelt lysimeters provide another approach to combine the measurements of snowmelt rates and the collection of snowmelt samples. Snowmelt lysimeters were primarily developed to measure only snowpack outflow for the evaluation of snowmelt process representations in snowmelt modelling studies (Haupt, 1969; Kattelmann, 2000; Martinec, 1987; Obled and Rosse, 1977; Würzer et al., 2017). The first systems were developed at the Central Sierra Snow Laboratory in the 1950s and were commonly applied since the late 1970s (e.g., Helvey and Fowler, 1980; Kattelmann, 2000; Martinec, 1987; Shanley et al., 1995; Tekeli et al., 2005). Further technical improvements of snowmelt lysimeter systems enabled the collection of meltwater samples for subsequent isotope analysis (Herrmann, 1978; Laudon, 2004; Unnikrishna et al., 2002).

Originally, a snowmelt lysimeter consists of a collector that traps meltwater flowing out of the snowpack. The collector is connected by a tube or conduit to a flow-recording device (Kattelmann, 2000; Tekeli et al., 2005). There exist two types of snowmelt lysimeters that are (i) enclosed with high barriers (extending the maximum snow depth to create an isolated snow column that only drains into the melt outlet), or (ii) unenclosed with a short rim above the base (usually 10–50 cm). In natural systems, however, the enclosed system is difficult to build and to operate and therefore, unenclosed snowmelt lysimeters are commonly deployed (Kattelmann, 2000). A major disadvantage of unenclosed lysimeters is the spatial variability of melt rates due to lateral inflow of meltwater from the surrounding snowpack (Kattelmann, 2000; Unnikrishna et al., 2002). For this reason, a set of at least three individual unenclosed snowmelt lysimeters is recommended to capture the spatio-temporal variability of melt processes at a sampling location (Kattelmann, 2000). In the past, melt rates were recorded quasi-continuously with tipping buckets (e.g., Bales et al., 1993; Juras et al., 2016; Taylor et al., 2001) or continuously with water level recorders (e.g., Haupt, 1969; Hermann, 1978). Most studies integrated melt rate measurements from several locations, while samples for isotope analysis were generally obtained from only one meltwater collection system (Lee et al., 2010; Taylor et al., 2001; Unnikrishna et al., 2002). Occasionally, melt water sampling for subsequent isotope analysis was adjusted to capture individual melt events at a high temporal resolution, however, regular meltwater sampling over the entire period with snow cover was rarely done (Hooper and Shoemaker, 1986; Schmieder et al., 2016; Taylor et al., 2001).

Based on snowmelt lysimeter measurements, a recent study successfully simulated the spatiotemporal variability of the isotopic composition of snowmelt at the catchment scale by considering fractionation processes in the snowpack and different landscape characteristics (Ala-aho et al., 2017). The isotope signature of the meltwater leaving the snowpack during rain-on-snow events could, however, not be represented adequately because the model assumes complete mixing in the snowpack (Ala-aho et al., 2017). In addition, the transferability of the model to catchments with different landscape characteristics (i.e., elevation, slope, vegetation) is limited, because only a few snowmelt collection systems exist worldwide that sample snowmelt at high temporal resolution and at different locations during the entire snow cover period.

So far, snowmelt lysimeters are among the most sophisticated meltwater collection systems, although their application is often technically complicated and cost-intensive. Thus, we designed a fully automated snowmelt lysimeter system (for snowmelt sampling and melt rate monitoring) based on standard technical components, which can potentially be rebuild at other sites with moderate effort and costs.

Alternative low-cost methods, such as unheated extended funnel collectors may also be suitable to capture melt rates and meltwater isotopic composition, especially in remote areas. To the best of our knowledge, a detailed comparison of the two sampling methods has not yet been carried out. Therefore, the objective of the present study was to present a detailed evaluation of the optimized snowmelt lysimeter systems with regard to the measured snowmelt rates and the isotopic composition of snowmelt. In addition, the functionality of the unheated precipitation collector with extended funnel as a low-cost alternative to a lysimeter system was tested. Both snowmelt collection systems were installed at a grassland site in a pre-alpine catchment in central Switzerland. The comparison was carried out based on measurements during two individual snowfall-snowmelt periods in April and November 2016.

METHODOLOGY

Field site

The snowmelt lysimeter system and the unheated precipitation collector with extended funnel were installed at the field site Erlenhöhe (1216 m a.s.l.), which is located in the central Swiss pre-Alps in the hydrological research catchment Erlenbach (Burch et al., 1996; Hegg et al., 2006). The catchment vegetation is dominated by forests (53%), while 22% of the area is partly-forested and 25% is covered with grassland (Fischer et al., 2015). The bedrock is composed of Flysch, a calciferous tertiary sediment with limited permeability (Burch et al., 1996).

A meteorological station at the field site Erlenhöhe provides measurements of climatological parameters, such as air temperature and snow depth at 10-minute temporal resolution (Stähli and Gustafsson, 2006). Incoming precipitation is measured with a heated rain gauge at 1.50 m above ground. This rain gauge did not allow for sample collection, and thus in this study it was used only to provide reference measurements for incoming precipitation. Average annual precipitation at the site is

2300 mm/y (Feyen et al., 1999) from which around one-third falls as snow (Stähli and Gustafsson, 2006). Average air temperature is 6°C with its minimum in February (–2°C) and its maximum in August (17°C) (Feyen et al., 1999).

Snowmelt collection

Snowmelt lysimeter system

An unenclosed snowmelt lysimeter system was developed to measure melt rates at 1-minute temporal resolution and to sample meltwater at daily temporal resolution over an area of approximately 3x4 m (Figure 1). The snowmelt lysimeter system consists of three PE-HD funnels (each 0.14 m^2 in diameter) with rims of 5.9 cm, that were each located above a tipping bucket (ECRN-100 High-Resolution Rain Gauge, Decagon Devices Inc., Pullman (WA), USA). The tipping bucket recorded melt rates at 5 ml volume increments (i.e., 0.04 mm m^{-2}) with a measurement uncertainty of 10%. To avoid freezing in the mechanism of the tipping bucket, a 12 W heating patch (110 mm x 77 mm) was attached to the inside wall of the rain gauge funnel. The meltwater drains from each funnel by gravity through a silicon tube (ca. 3–4° gradient, diameter 10x14 mm) to its respective PE-HD 10 l vessel. The vessels were situated in a watertight metal container embedded in the ground downhill of the lysimeter funnels.

Once a day at 05:40, the snowmelt samples were pumped individually from each vessel by an automatic water sampler equipped with 24 bottles (April 2016 period: 6712-Fullsize Portable Sampler, Teledyne Isco, Lincoln (NE), USA, November 2016 period: Maxx P6L – Vacuum System, Maxx GmbH, Rangendingen, Germany). Because only one automatic water sampler was used during each period, the connection between the vessels and the pumping tube of the automatic water sampler was controlled through pinch solenoid valves (ASCO Numatics Sirai Srl, Bussero, Italy), operated by a Datalogger (CR-1000, Campbell Scientific, Loughborough, Great Britain). Up to 300 ml was pumped from each collection vessel into one separate dry 1 l bottle in the automatic water sampler.

After each pump cycle, remaining water in the suction tube was blown back into the sampled vessel to reduce carry-over effects. After all three vessels were samples (ca. 20 min), pinch solenoid valves situated at the outlets of the vessels were opened simultaneously to release the remnant water through an outlet pipe. The 6 m long outlet pipe ran downhill of the lysimeter system which allowed for free drainage of the vessels without tailback. At 06:00, the valves at the outlets of the vessels were closed again and meltwater collection started for the next 1-day sampling period. Once a week, the filled sample bottles of the automatic water sampler were replaced with empty bottles. The filled sample bottles were sealed with lids to avoid leakage during the transport to the laboratory.

A webcam (Webcam ROLINE RBOF4-1 Bullet IP 4MP, Secomp, Bassersdorf, Switzerland) took hourly pictures of the snowmelt lysimeter system, which allowed for documenting the timing of snowfall and melt. The snowmelt lysimeter system and the webcam were connected to the local power grid. This set-up of the snowmelt lysimeter system cost around 4000 US$ (excluding the webcam and the automatic water sampler).

Unheated precipitation collector with extended funnel

For the unheated precipitation collector, we used the basic parts of the "Palmex" collector (Palmex d.o.o., Zagreb, Croatia), such as the plastic funnel (13.5 cm in diameter) and the extended aluminium funnel (15 cm diameter, 30 cm long), which was installed on top of the plastic funnel (Figure 2) (Gröning et al., 2012). The extended funnel was modified by painting it with black colour to accelerate the snowmelt of the accumulated snow and thus prevent evaporative fractionation effects of the meltwater sample in the funnel (Earman et al., 2006). This set-up of the unheated precipitation collector cost around 200 US$.

The unheated precipitation collector was installed at the field site at Erlenhöhe so that the orifice of the extended funnel was at a height of 2.3 m above ground. With this set-up, the unheated precipitation collector sampled a mixture of liquid precipitation,

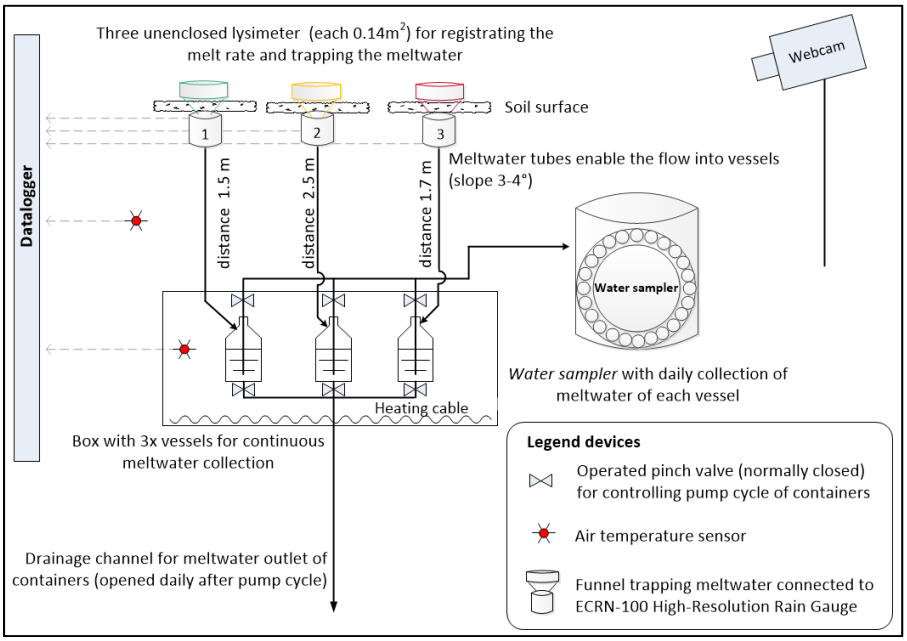

Fig. 1. Set-up of the snowmelt lysimeter system at the field site Erlenhöhe on a 3 m x 4 m area. Three funnels (1, 2 and 3) collect snowmelt which is draining through silicon tubes to the three collection vessels. The data logger controls three pinch valves to pump the meltwater into sample bottles of an automatic water sampler. Remnant meltwater in the vessels is released simultaneously to the drainage pipe after each pump cycle by opening the three valves at the outlets of the collection vessels (see also Figure A1 and Figure A2).

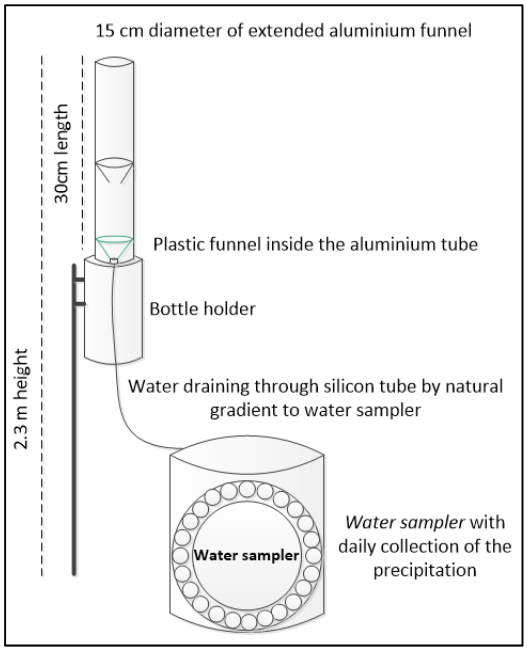

Fig. 2. Set-up of the unheated precipitation collector with extended funnel connected to an automatic water sampler installed at Erlenhöhe. The meltwater drains by gravity to the automatic water sampler (see also Figure A3).

snow and snowmelt. Despite the black-coloured funnel, fractionation of the snow sample in the funnel of the unheated precipitation collector might still occur when meltwater refreezes, depending on ambient air temperature and incoming solar radiation.

The meltwater samples from the unheated precipitation collector drained by gravity into a dry HDPE sample bottle in an automatic water sampler (6712-Fullsize Portable Sampler, Teledyne Isco, Lincoln (NE), USA), that was connected to the local power grid. Every day at 05:40, the automatic water sampler rotated the injection arm to a new sample bottle. Since these sample bottles were replaced in a 3-weeks cycle, the bottles were modified to reduce evaporation and isotopic fractionation. This was done by plugging a 100 ml syringe housing (i.e., without piston) into the opening of the sample bottle in order to avoid evaporation and isotopic fractionation. For the collection and transport of the samples, the 1 l sample bottles were sealed with a lid to avoid leakage. In the laboratory, the meltwater sample volumes were determined by weighting the filled sample bottles and subtracting the known weights of the empty sample bottles.

Isotope analysis

Until sample preparation for isotope analysis, the samples from both collection systems remained sealed and refrigerated at 4°C. Prior to analysis, all water samples were melted at room temperature, if necessary, filtrated through 0.45-µm Teflon filters (DigiFilter micron Teflon) and filled into 2-ml glass vials. The water samples were analysed for the stable water isotopes (^{18}O, ^{2}H) by laser spectroscopy (Los Gatos Research, Isotopic Water Analyzer LGR IWA-45-EP; ABB Los Gatos Research, San Jose, California, USA.) at the laboratory of the Swiss Federal Institute for Forest, Snow and Landscape Research (WSL). The measurement precision of the analyser was 0.5‰ for $\delta^{18}O$ and 1.0‰ for $\delta^{2}H$. Isotopic abundances are reported through the δ notation relative to the IAEA-VSMOW-II standards.

Comparison analysis

Two snowfall periods with subsequent snowmelt were monitored between 24 April and 2 May 2016 (referred to as April period), as well as between 6 and 22 November 2016 (referred to as November period). Because the duration and depth of snow cover were different for these two periods, they provided ideal data sets to compare the snowmelt lysimeter system and the unheated precipitation collector with regard to melt rates (daily temporal resolution), timing of melt and the isotopic composition of the daily meltwater samples. In addition, total volumes of incoming precipitation (rain and snowmelt) captured by both collection systems during the April and November periods were compared with the measurements (rain and snow) of the heated rain gauge.

The three individual lysimeters of the snowmelt lysimeter system allowed for analysing the spatial variations in snowmelt and its isotopic composition at the plot scale. For this, the 1-minute melt rate recordings of the tipping buckets underneath each individual lysimeter were aggregated to 10-minute sums for easier comparison. Additionally, the peak times during six melt events during the April period (SM-April-a-b-c) and the November period (SM-Nov-a-b-c) were calculated. Peak times were defined as the time of the highest 10-minute melt rate during a melt event.

RESULTS

For both snowfall periods in April and November 2016, the initial snowpacks were established during high-intensity rainfall event that became snowfall when air temperature decreased (Figure 3a, Figure 4a). During the April period, the snowpack started to build up on 23 April 21:00 and was completely melted on 30 April 13:00, i.e. the snow cover lasted for about seven days. During that period, individual snowfall events occurred that started on 24 April 20:00 and on 26 April 22:00, respectively, resulting in maximum snow depths of around 30 cm. On 1 May 00:30, a small snow pack (5 cm) was built up again that lasted until 2 May 01:30. Because this event occurred after the continuous snowpack was completely melted, the cumulative sum of total melt during the April period was calculated from 23 April 21:00 to 30 April 13:00.

The snowpack during the November period lasted from 6 November 08:20 to 22 November 09:30, and thus seven days longer than that of the April period (Figure 4a). The maximum snow depth of 44 cm was reached on 12 November 03:00, after air temperature decreased during a heavy precipitation event that started on 11 November 02:10. During the melt-out, the snowpack increased again by 3 cm on 19 November because of another precipitation event with a mixture of rain and snow (19 mm).

Comparison of the two snowmelt collection systems with regard to total precipitation and snowmelt volumes

The cumulative sums of meltwater collected with the heated rain gauge, the unheated precipitation collector, the three individual snowmelt lysimeters, as well as the snowmelt lysimeter system (i.e., the average of the three individual lysimeters) during the April and November periods are presented in Table 1, as well as in Figure 3b.

For the April period, the heated rain gauge recorded 61.1 mm incoming precipitation (rain and snow). The individual snowmelt lysimeters recorded slightly larger volumes of snowmelt and rain that were between 62.3 and 73.4 mm. The average value for the entire snowmelt lysimeter system was

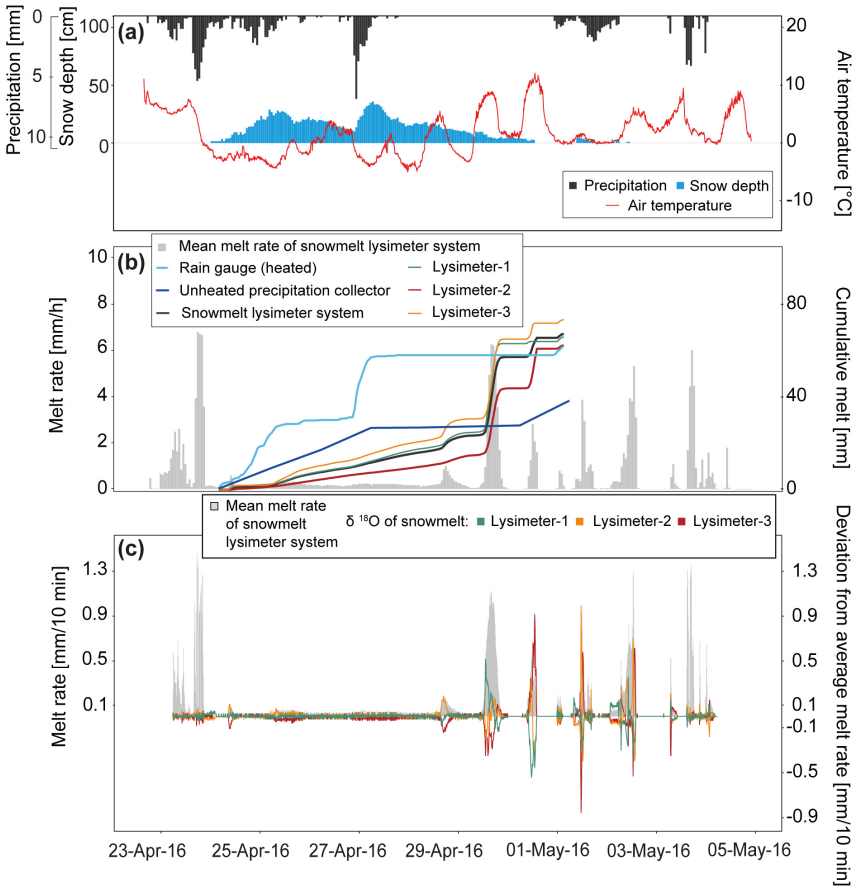

Fig. 3. The snowfall-snowmelt period in April 2016. (a) Precipitation and snow depth (left axis) and air temperature (right axis) at the field site Erlenhöhe. (b) Melt rates measured with the snowmelt lysimeter system (left axis), their cumulative sum (calculated from the mean of the three individual lysimeters), as well as the cumulative sum of the three individual lysimeters, the unheated precipitation collector and the heated rain gauge (right axis). (c) 10-minute aggregated melt rates of the snowmelt lysimeter system (left axis) and the absolute difference from the mean for each individual lysimeter (right axis).

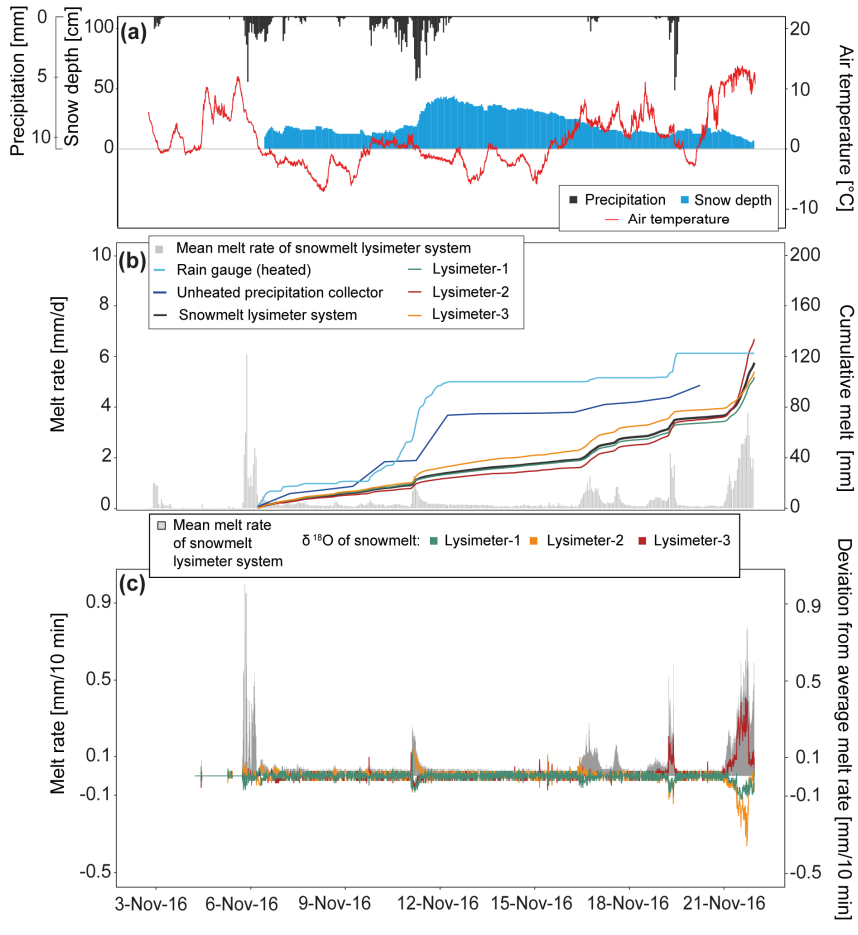

Fig. 4. The snowfall-snowmelt period in November 2016. (a) Precipitation and snow depth (left axis) and air temperature (right axis) at the field site Erlenhöhe. (b) Melt rates measured with the snowmelt lysimeter system (left axis), their cumulative sum (calculated from the mean of the three individual lysimeters), as well as the cumulative sum of the three individual lysimeters, the unheated precipitation collector and the heated rain gauge (right axis). (c) 10-minute aggregated melt rates of the snowmelt lysimeter system (left axis) and the absolute difference from the mean for each individual lysimeter (right axis).

Table 1. Cumulative snowmelt during the April and November period in 2016 recorded with the three individual snowmelt lysimeters, the snowmelt lysimeter system (mean of the three individual snowmelt lysimeters; incl. standard error) and the unheated precipitation collector. The total amount of precipitation measured with a heated rain gauge is included for comparison.

	Total snowmelt and precipitation [mm]	
	24–30 April	6–22 November
Lysimeter-1	65.8	110.1
Lysimeter-2	62.3	151.4
Lysimeter-3	73.4	120.6
Snowmelt lysimeter system (mean ± std. error)	67.2 ± 3.3	127.4 ± 12.4
Unheated precipitation collector	38.4	97.2
Heated rain gauge (rain and snow)	61.1	121.2

67.2 ± 3.3 mm (mean ± standard error), and thus 9% larger than the measurement of the heated rain gauge. The total amount of meltwater and rain registered by the unheated precipitation collector was 38.4 mm, which was much lower (37%) than that of the measurement of the heated rain gauge.

For the November period, total incoming precipitation (rain and snow) measured with the heated rain gauge was 121.2 mm. In comparison, the three individual lysimeters recorded values between 110.0 mm and 151.4 mm, with the average value of 127.4 ± 12.4 mm, i.e. 5% more than what was recorded by the heated rain gauge. The unheated precipitation collector (97.2 mm) underestimated total precipitation (rain and melt) by 20% relative to the heated rain gauge.

Figures 6a,c and Figures 7a,c show the daily melt rates measured with the snowmelt lysimeter system and the unheated precipitation collector. No comparison was made to the heated rain gauge because it did not measure melt from a snowpack. Overall, the melt rates recorded with the unheated precipitation collector were smaller than those of the snowmelt lysimeter system, except for the times when the initial snowpack was built up (24–27 April and 6–7 November, 10 and 12 November). For instance, on 10 and 12 November, the unheated precipitation collector recorded 19 mm and 36 mm of snowmelt, while only 6 mm and 3 mm of snowmelt was registered by the snowmelt lysimeter system, respectively. During the melt-out of the snowpack, the snowmelt lysimeter system recorded substantially more snowmelt than the unheated precipitation collector, such as on 29 April (34 mm and 0 mm, respectively) and 21 November (50 mm and 0 mm, respectively).

Stable water isotopes in precipitation and snowmelt

The $\delta^{18}O$ and $\delta^{2}H$ values of the snowmelt samples collected with both the snowmelt lysimeter system and the unheated precipitation collector were highly correlated with each other (R^2 better than 0.98), and therefore the following analysis is based on the $\delta^{18}O$ values only. The respective figures showing the $\delta^{2}H$ values are presented in the supplementary material (Figure A4, Figure A5). During the April period, the $\delta^{18}O$ values of the samples from the unheated precipitation collector ranged from –14.5‰ to –6.9‰, while the $\delta^{18}O$ values of the snowmelt lysimeter-based samples were between –16.5‰ and –11.5‰ (Figures 6b,c). During the November period, the meltwater samples were isotopically lighter than during the April period, with $\delta^{18}O$ values ranging between –22.6‰ and –9.9‰ for the unheated precipitation collector, and between –23.5‰ and –13.8‰ for the snowmelt lysimeter system (Figures 7b,c). On average, the meltwater samples from the unheated precipitation collector were isotopically heavier than those from the snowmelt lysimeter system (i.e. average difference of by 3.2‰ and 2.5‰ for the April and November periods, respectively). For both snowmelt collection systems, the temporal variability of $\delta^{18}O$ between the daily meltwater samples shows a distinct decrease in $\delta^{18}O$ at the beginning of the snowfall (i.e. for the lysimeter system: until 25 April by –4.3‰, 2 May by –2.9‰ and 7 November by –5.6‰, Figures 6b,c and Figures 7b,c). This decrease in $\delta^{18}O$ is followed by a slower increase until the complete melt-out of the snowpack. This general temporal pattern of stable isotopes in snowmelt was captured by both sampling systems, the unheated precipitation collector and the snowmelt lysimeter system. In addition, the three individual snowmelt lysimeters captured a very similar isotopic signature of the snowmelt over time (Figure 6c and Figure 7c). The meltwater $\delta^{18}O$ values from the unheated precipitation collector showed a larger short-term variability (e.g., 28 April, 10 and 17 November), as well as a one-day time shift relative to the snowmelt lysimeter system.

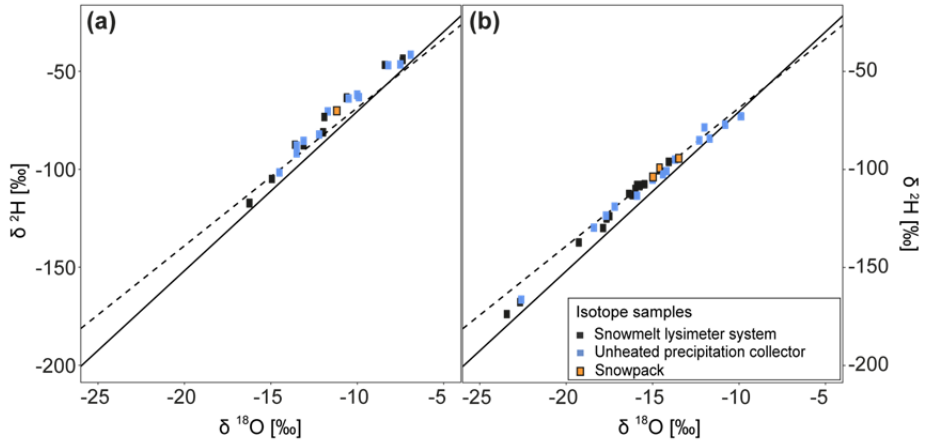

Fig. 5. Dual isotope plots for the April and November period showing the isotopic composition of the samples collected with the snowmelt lysimeter system (black) (i.e., average of the three individual lysimeters) and the unheated precipitation collector (blue). Bulk snow samples that were collected manually at weekly intervals at the field site are shown for comparison (orange). The global meteoric water line after Clark and Fritz (1997) is: $\delta^{2}H = 8.13*\delta^{18}O - 10.8$ (solid black line). The linear regression line is $\delta^{2}H = 7.04*\delta^{18}O - 1.75$ (dashed black line) and was obtained from rainwater samples collected at the field site in Erlenhöhe during the snow-free seasons (May till October) in 2016 and 2017.

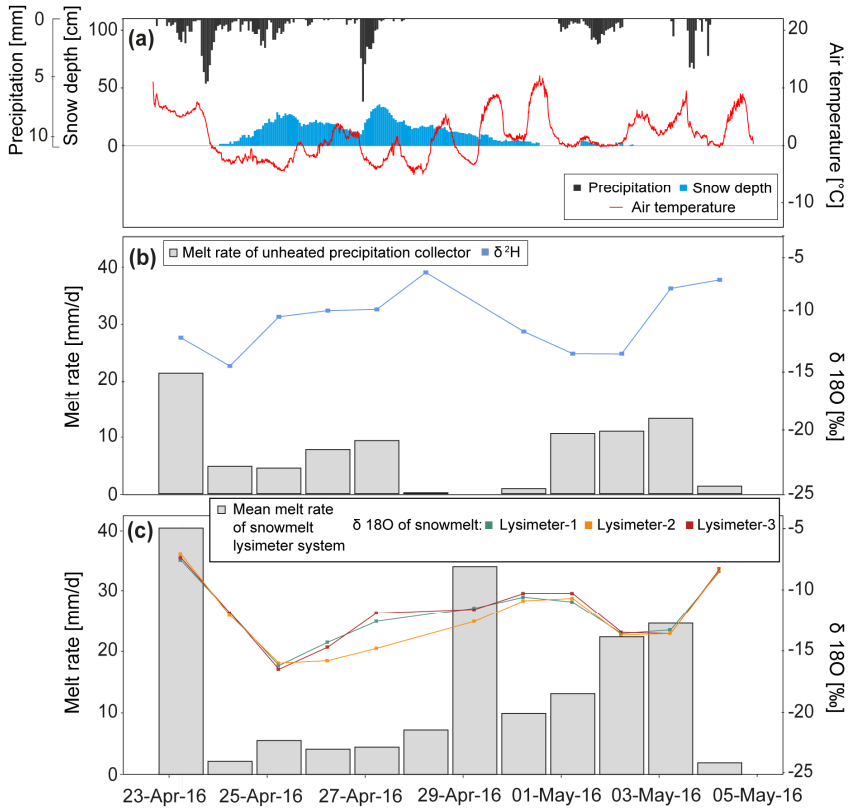

Fig. 6. The snowfall-snowmelt period in April 2016. (a) Precipitation and snow depth (left axis) as well as air temperature (right axis) at the field site Erlenhöhe. (b) Daily meltwater sample volume (left axis) and their $\delta^{18}O$ (right axis) from the unheated precipitation collector with extended funnel values. (c) Daily meltwater sample volume (left axis) and $\delta^{18}O$ values (right axis) from the snowmelt lysimeter system.

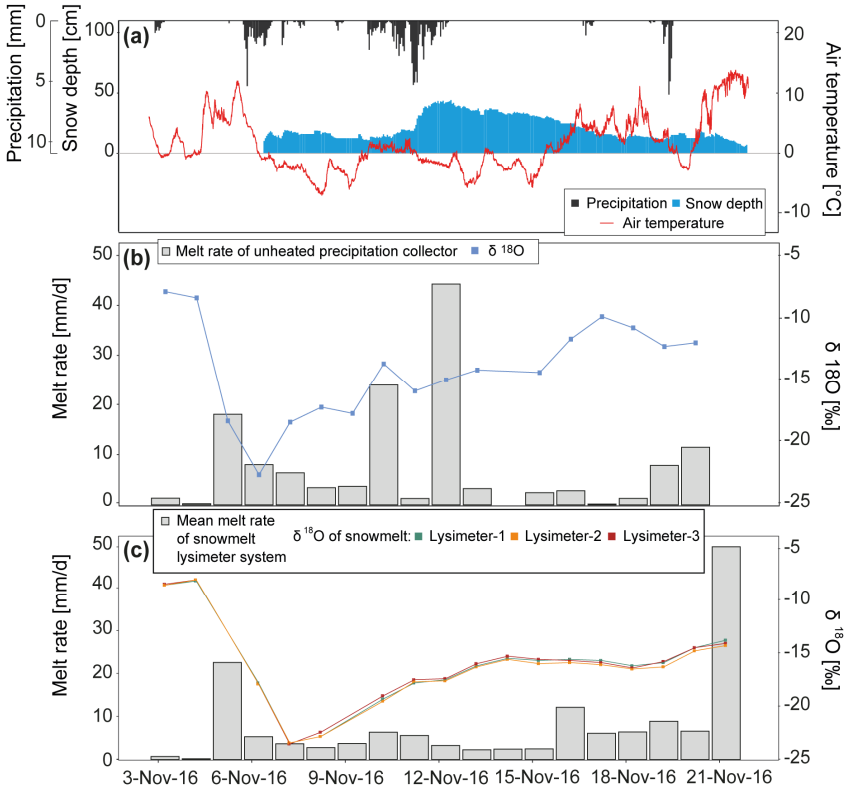

Fig. 7. The snowfall-snowmelt period in November 2016. (a) Precipitation and snow depth (left axis) as well as air temperature (right axis) at the field site Erlenhöhe. (b) Daily meltwater sample volume (left axis) and their $\delta^{18}O$ (right axis) from the unheated precipitation collector with extended funnel values. (c) Daily meltwater sample volume (left axis) and $\delta^{18}O$ values (right axis) from the snowmelt lysimeter system.

In the dual isotope space, most of the meltwater samples from both sampling systems plot on the linear regression line (Figure 5). This linear regression line, which was obtained from rainwater samples collected at the same field site during the snow-free seasons (May till October) in 2016 and 2017, is used here as first approximation of the local meteoric water line. Except for the three most negative meltwater samples of the November period (Figure 5b), none of the meltwater samples plot substantially below the linear regression line.

Table 2. Temporal variation of melt rates and melt volumes measured with the three individual lysimeters during six melt events in April (SM-April-a-b-c) and November (SM-Nov-a-b-c) in 2016. Peak times are defined as the time of the highest 10-minute melt rate during a melt event. Deviations were calculated with regard to the average of all three individual lysimeters (i.e. of the snowmelt lysimeter system).

	Snowmelt lysimeter system		Lysimeter-1		Lysimeter-2		Lysimeter-3	
Melt event	Melt rate (mm 10 min^{-1})	Peak time (mm/dd/yy hh:mm)	Deviation from avg. melt rate (mm 10 min^{-1})	Deviation from avg. peak time (min)	Deviation from avg. melt rate (mm 10 min^{-1})	Deviation from avg. peak time (min)	Deviation from avg. melt rate (mm 10 min^{-1})	Deviation from avg. peak time (min)
SM-April-a 28.04. 14:30–21:40	0.20	28.04. 16:50	–0.02	33	–0.13	–37	0.16	3
SM-April-b 29.04. 10:50–20:40	1.22	29.04. 15:40	0.08	3	–0.02	–37	–0.06	33
SM-April-c 01.05. 07:50–14:20	1.32	01.05. 11:50	–0.50	–17	–0.20	33	0.70	–16
SM-Nov-a 11.11. 01:30–09:50	0.31	11.11. 04:10	0.05	–20	–0.06	0	0.01	20
SM-Nov-b 16.11. 09:10–17.11. 02:10	0.28	16.11. 18:20	–0.02	–7	0.01	3	0.01	3
SM-Nov-c 21.11. 00:10–22.11. 05:10	0.88	21.11. 20:30	–0.16	–133	0.28	–133	–0.12	266

Spatial and temporal variability of snowmelt during individual melt events measured with the snowmelt lysimeter system

The snowmelt lysimeter system with its three individual lysimeters potentially allows for monitoring the heterogeneous melt-out of the snowpack at the plot scale. To test this, melt rates and peak times of the individual snowmelt lysimeters were compared among each other for six melt events that occurred during the April and November periods. In addition, the individual melt rate measurements were compared against the average melt rates of the entire snowmelt lysimeter system.

Three melt events occurred in April due to rising air temperatures (28 April 14:30–21:40 SM-April-a, 29 April 10:50–20:40 SM-April-b and 1 May 07:50–14:20 SM-April-c). In November, three major snowmelt events were recorded on 11 November from 01:30 to 09:50 (SM-Nov-a), between 16 November 09:10 and 17 November 02:10 (SM-Nov-b) and between 21 November 01:10 and 22 November 05:10 (SM-Nov-c).

Figure 3c and Figure 4c show that for the six snowmelt events, the 10-minute average melt rates were within the range of 0.2 mm (28 April) and 1.32 mm (1 May). The data shown in Table 2 indicate that the deviations from the 10-minute average melt rates can be large, especially during the major melt events. The largest deviations from the 10-minute average melt rates occurred on 1 May (SM-April-c), which were around 0.66 mm for Lysimeter-3 and around –0.45 mm for Lysimeter-1, indicating a high temporal variability of the melt-out from the snowpack. Overall, the three individual lysimeters showed no consistent bias of melt rate measurements. Similar to the melt rates, there was no consistent bias of the peak times of the three individual lysimeters (Table 2). From the six snowmelt events, the 21 November event resulted in the longest offsets of peak times relative to the average (i.e., –133 min for Lysimeters-1 and 2 and 266 min for Lysimeter-3). For the other five events, the temporal offsets were generally much shorter and ranged between –37 min and 33 min.

DISCUSSION: PERFORMANCE OF THE SNOWMELT LYSIMETER SYSTEM

Capturing snowmelt rates

The comparison of the total precipitation and melt rates during the April and November periods showed a good agreement between the snowmelt lysimeter system and the heated rain gauge (Table 1). This suggests that the snowmelt lysimeter system provides a representative estimate of incoming precipitation and naturally occurring snowmelt volume at the plot scale.

The deviations between the 10-minute melt rates from the three individual lysimeters and their average melt rate (i.e. the snowmelt lysimeter system) suggests large spatial and temporal variability of the snowmelt process at the plot scale (Table 2). Additionally, differences in peak times occurred during small- but also high-intensity melt rates. As reported by Kattelmann (2000), unenclosed lysimeters might facilitate lateral flow of meltwater from the surrounding snowpack into the funnel of the individual snowmelt lysimeters. After the snow depth decreases to the ridge of the funnel, however, the unenclosed lysimeter becomes an enclosed lysimeter, which restricts meltwater contribution from the surrounding snowpack (Kattelmann, 2000). Further, snow distribution by wind may affect the amount of snow accumulated on the lysimeter funnel and thus, the snowmelt volume registered by the individual lysimeters.

The unheated precipitation collector significantly underestimated the total precipitation and melt volumes compared to the snowmelt lysimeter system and the heated rain gauge by up to 43% (Table 1). Daily melt rates measured with the unheated precipitation collector were often lower than the respective values from the snowmelt lysimeter system (Figure 6, Figure 7). One of the main reasons for the underestimation of snowmelt with the unheated precipitation collector was the extended funnel that only allowed a restricted snow volume to accumulate. This snow volume was likely to be much smaller than the accumulated snowpack on the ground and thus, the snowmelt from the snow volume in the unheated precipitation collector might not be representative for the snowmelt occurring naturally from the snowpack on the ground. As a result, the smaller amount of snow volume in the extended funnel of the unheated precipitation collector generated outflow more rapidly when air temperature increased. In addition, during high intensity snowfall events, the extended funnel was likely to be filled up completely with snow so that remaining snowfall could not be captured by the unheated precipitation collector. Also, if the air temperature and/or incoming solar radiation were low during snowfall events, the black colour of the extended funnel was not sufficient to accelerate the melt process, and thus the extended funnel might have filled up with snow completely.

Further, wind can cause significant errors of solid precipitation records due to under-catch by around 20%–50% (Rasmussen et al., 2012). In addition, if the extended funnel of the unheated precipitation collector was completely filled with snow, wind was likely to blow off additional incoming snow. Another potential reason for the under-catch of snowmelt in the unheated precipitation collector is evaporation from the snow accumulated in the extended funnel. Long storage times and/or wind gusts reaching into the extended funnel may have en-

hanced evaporation (Nespor and Sevruk, 1999; Earman et al., 2006). Overall, the comparison analysis suggests that the unheated precipitation collector with extended funnel is not applicable for melt rate monitoring at daily temporal resolution.

Capturing the isotopic signature of snowmelt

Figure 6 and Figure 7 show distinct decreases in the meltwater $\delta^{18}O$ values during the initial snowmelt events on the 1st and 2nd day of the April and November periods. After that, the meltwater $\delta^{18}O$ values increased continuously over several days until the snowpack was completely melted. Both collection systems captured this general pattern in the isotope values. Figure 5 shows that most snowmelt samples of both collection systems plotted on the approximated local meteoric water line. The three most negative meltwater samples of the November period plotted below the linear regression line, suggesting that isotopic fractionation occurred within the snowpack. Such isotopic fractionation processes may be driven by vapour condensation and (re-)freezing of liquid water resulting in a depletion of the meltwater leaving the snowpack (Ala-aho et al., 2017; Cooper, 1998; Lyon et al., 2010; Rodhe, 1998; Taylor et al., 2001; Unnikrishna et al., 2002). Both sampling systems captured this isotopic response of the early melt period. Since there were no other snowmelt samples that plotted substantially off the linear regression line, we conclude that other kinetic fractionation effects within the two sampling systems (e.g., due to evaporation or sublimation) might be insignificant.

Overall, the isotopic signature of the samples from the unheated precipitation collector was more variable in time during both snowmelt periods compared to the isotopic signature of the samples from the individual snowmelt lysimeters. This can partly be explained with the design of the unheated precipitation collector. The funnel limited the volume of snow to be collected, which resulted in a substantial under-catch compared to the snowmelt lysimeter system and the heated rain gauge (Chapter "Capturing snowmelt rates"). Since the unheated precipitation collector sampled only distinct volume increments of precipitation events, the isotopic variability between the collected samples can potentially be large. In addition, the isotopic composition of incoming precipitation can be highly variable during individual events, (Dansgaard, 1964; McDonnell, 1990; Munksgaard et al., 2012; von Freyberg et al., 2017), which might further intensify this incremental sampling effect of the unheated precipitation collector. The more damped isotopic signature of the lysimeter snowmelt samples can be explained by vertical and lateral mixing of meltwater percolating through the isotopically variable layers of the snowpack. Such mixing processes have been found to depend on the ambient conditions such as incoming solar energy input, temperature of the air and of the ground and layering of the snowpack, as well as on the amount and intensity of incoming precipitation (Lee et al., 2010; Penna et al., 2017; Unnikrishna et al., 2002). Because the snowmelt lysimeter system collected samples from the snowpack that naturally formed on the ground, it integrated the isotopic signature of all snowfall events compared to the unheated precipitation collector with its constrained funnel volume.

During both observation periods, the samples from the unheated precipitation collector were marginally but consistently heavier in $\delta^{18}O$ compared to the samples from the snowmelt lysimeter system (Figures 6b,c and Figures 7b,c). However, the isotope signal of the meltwater samples from the unheated precipitation collector did not suggest a strong kinetic fractionation effect (i.e., evaporation) in the dual isotope plots as most of the snowmelt samples plot on the linear regression line (Figure 5). As a consequence, this behaviour can mainly be explained by the incremental sampling effect (more heavy snow was sampled compared to the snowmelt lysimeters system) and simple mixing. Other factors, such as fractionation during phase transitions (sublimation/condensation/evaporation, freeze/melt) are less obvious from our data set (Earman et al., 2006; Kendall and Caldwell, 1998; Taylor et al., 2001).

Our results showed that the isotope signature of the snowmelt samples from the snowmelt lysimeter system was delayed compared to the samples from the unheated precipitation collector. This can be explained by the generally larger snow volume captured by the snowmelt lysimeter system compared to the extended funnel of the unheated precipitation collector. Consequently, under similar ambient conditions, the snowpack on top of the snowmelt lysimeter system requires more time to melt. In addition, the black-coloured extended funnel of the unheated precipitation collector was specifically designed to accelerate the melt process to reduce the exposure time of the meltwater in the funnel. Thus, in order to capture the isotopic signature of natural meltwater from a snowpack on the ground, the snowmelt lysimeter system may provide more representative samples at daily resolution. The unheated precipitation collector, on the other hand, often fails to capture this signature because of accelerated melt and incremental sampling effect. This collection system may, however, still provide a reasonable estimate of the relative day-to-day variability of snowmelt, depending on the purpose of the study.

Both collection systems captured an initial decrease of $\delta^{18}O$ in meltwater, which was followed by a systematic increase of $\delta^{18}O$ until the entire snowpack was melted (Figures 6b,c and Figures 7b,c). A possible explanation may be fractionation during re-freezing of the initial meltwater that percolated from the snow surface through the snowpack. As a consequence, the snowpack becomes isotopically heavier, and so does the meltwater draining from this snowpack with progressive melting (Herrmann, 1978; Stichler et al., 1981; Taylor et al., 2001; Unnikrishna et al., 2002). Alternatively, the isotopic signature of the meltwater samples may simply reflect the melt-out of the individual layers of the snowpack that build up during the individual precipitation events. However, we did not measure the isotopic signature of incoming precipitation at the field site, and thus, cannot draw any conclusions about the sources or processes causing the isotope pattern in the daily snowmelt samples.

CONCLUSION

This study compared two snowmelt collection systems with focus on their ability to properly capture snowmelt rates and the isotopic composition of meltwater. A low-cost, unheated precipitation collector (ca. 200 US$, excluding automatic water sampler) was evaluated against a newly developed snowmelt lysimeter system (ca. 4000 US$, excluding automatic water sampler) consisting of three individual unenclosed lysimeters. The comparison analysis was carried out for samples from two snowfall-snowmelt periods in April and November 2016.

Although the unheated precipitation collector sampled much less snow than the snowmelt lysimeter system (under-catch of up to 43%), both systems were able to capture very similar isotope patterns during both periods. Thus, despite the substantial under-catch, the low-cost unheated precipitation collector seems sufficient to capture the general isotope signal of snowmelt over the course of a snowfall and snowmelt period. Since the unheated precipitation collector requires only low maintenance and because its automatic water sampler can potentially

be run on battery power, possible areas of applications are at remote locations or at sites where many locations have to be sampled. In order to adequately capture the rates of incoming precipitation (and melt) at a site, an additional heated rain gauge and a temperature logger would have to be installed. The strength of the snowmelt lysimeter system is its ability to capture both the variability in melt rates, as well as the isotopic composition of snowmelt at daily resolution and thus, to provide valuable information about the snowmelt processes at the plot scale. The system is based on standard technical components, and thus can potentially be rebuilt at other sites with moderate effort and costs. Compared to the unheated precipitation collector, the lysimeter system is more cost-intensive and requires more extensive maintenance. In addition, its complex set-up and the high power requirements prohibit an installation of the system at remote locations.

For catchment scale studies that aim at quantifying the fraction of snowmelt in streamflow based on hydrograph separation, other important factors such as topography, vegetation cover and soil depth control the melt process (Schmieder et al., 2016; Unnikrishna et al., 2002). Ongoing research in the Erlenbach and neighbouring catchments focuses on the effects of elevation and vegetation cover on the isotopic evolution of snowmelt. For this, two additional snowmelt lysimeters were installed at a forested site (1185 m a.s.l.) and at another grassland site (1405 m a.s.l.) in December 2016. This extended sampling network of snowmelt lysimeter systems will provide further insights into how landscape and climatic properties control snowmelt and its isotopic evolution.

Acknowledgements. This project is supported by the Swiss National Science Foundation SNF through the Joint Research Projects (SCOPES) Action (Grant IZ73Z0_152506). We thank the staff of the Swiss Federal Institute for Forest, Snow and Landscape Research (WSL), especially Karl Steiner for great support in the field and Alessandro Schlumpf for the sample analysis. We also thank Prof. James Kirchner, Physics of Environmental Systems (ETH), his lab facility staff, Björn Studer, Daniel Meyer for help in the laboratory. We also thank the anonymous reviewers for their valuable suggestions that have helped to improve the manuscript.

REFERENCES

Ala-aho, P., Tetzlaff, D., Mcnamara, J.P., Laudon, H., Kormos, P., Soulsby, C., 2017. Modeling the isotopic evolution of snowpack and snowmelt: Testing a spatially distributed parsimonious approach. Water Resour. Res., 2404–2418. DOI: 10.1002/2016WR019638.

Bales, R.C., Davis, R.E., Williams, M.W., 1993. Tracer release in melting snow: diurnal and seasonal patterns. Hydrol. Process., 7, 389–401. DOI:10.1002/hyp.3360070405.

Barnett, T.P., Adam, J.C., Lettenmaier, D.P., 2005. Potential impacts of a warming climate on water availability in snow-dominated regions. Nature, 438, 303–309. DOI: 10.1038/nature04141.

Beniston, M., 2003. Climatic Change in Mountain Regions: A Review of Possible Impacts. 1st Ed. Climatic Change. Kluwer Academic Publishers, Dordrecht. DOI: 10.1023/A:1024458411589.

Berghuijs, W.R., Woods, R.A., Hrachowitz, M., 2014. A precipitation shift from snow towards rain leads to a decrease in streamflow. Nat. Clim. Chang., 4, 583–586. DOI: 10.1038/NCLIMATE2246.

Bierkens, M.F.P., van Beek, L.P.H., 2009. Seasonal Predictability of European Discharge: NAO and Hydrological Response Time. J. Hydrometeorol., 10, 953–968. DOI: 10.1175/2009JHM1034.1.

Burch, V.H., Forster, Felix, Schleppi, P., 1996. Zum Einfluss des Waldes auf die Hydrologie der Flysch-Einzugsgebiete des Alptals. Schweizerische Zeitschrift fur Forstwes. D, 925–938.

Clark, I.D., Fritz, P., 1997. Environmental Isotopes in Hydrogeology. CRC Press LLC, Florida, USA.

Cooper, L.W., 1998. Isotopic Fractionation in Snow Cover, Isotope Tracers in Catchment Hydrology. Elsevier B.V. DOI: 10.1016/B978-0-444-81546-0.50011-2.

Dansgaard, W., 1964. Stable isotopes in precipitation. Tellus, 16, 436–468. DOI: 10.3402/tellusa.v16i4.8993.

Dinçer, T., Payne, B.R., Florkowski, T., Martinec, J., Tongiorgi, E., 1970. Snowmelt runoff from measurements of tritium and oxygen-18. Water Resour. Res., 6, 110. DOI: 10.1029/WR006i001p00110.

Earman, S., Campbell, A.R., Phillips, F.M., Newman, B.D., 2006. Isotopic exchange between snow and atmospheric water vapor : Estimation of the snowmelt component of groundwater recharge in the southwestern United States. Journal of Geophysical Research, 111, D09302. DOI: 10.1029/2005JD006470.

Feyen, H., Wunderli, H., Wydler, H., Papritz, A., 1999. A tracer experiment to study flow paths of water in a forest soil. J. Hydrol., 225, 155–167. DOI: 10.1016/S0022-1694(99)00159-6.

Fischer, B.M.C., Rinderer, M., Schneider, P., Ewen, T., Seibert, J., 2015. Contributing sources to baseflow in pre-alpine headwaters using spatial snapshot sampling. Hydrol. Process., 29, 5321–5336. DOI: 10.1002/hyp.10529.

Frisbee, M.D., Phillips, F.M., Campbell, A.R., Hendrickx, J.M.H., 2010. Modified passive capillary samplers for collecting samples of snowmelt infiltration for stable isotope analysis in remote, seasonally inaccessible watersheds 1: laboratory evaluation. Hydrol. Process., 24, 7, 825–833.

Gröning, M., Lutz, H.O., Roller-Lutz, Z., Kralik, M., Gourcy, L., Pöltenstein, L., 2012. A simple rain collector preventing water re-evaporation dedicated for δ18O and δ2H analysis of cumulative precipitation samples. J. Hydrol., 448–449, 195–200. DOI: 10.1016/j.jhydrol.2012.04.041.

Haupt, H., 1969. A Simple Snowmelt Lysimeter. Water Resour. Res., 5, 3, 714–718.

Hegg, C., McArdell, B.W., Badoux, A., 2006. One hundred years of mountain hydrology in Switzerland by the WSL. Hydrol. Process., 20, 371–376. DOI: 10.1002/hyp.6055.

Helvey, J.D., Fowler, W.B., 1980. A new method for sampling snow melt and rainfall in forests. JAWRA Journal of the American Water Resources Association, 16, 5, 938–940.

Herrmann, A., 1978. A recording snow lysimeter. J. Glaciol., 20, 82, 209–213.

Hooper, R.P., Shoemaker, C.A., 1986. A comparison of Chemical and Isotopic Hydrograph Separation. Water Resour. Res., 22, 1444–1454. DOI: 10.1029/WR022i010p01444.

Huth, A.K., Leydecker, A., Sickman, J.O., Bales, R.C., 2004. A two-component hydrograph separation for three high-elevation catchments in the Sierra Nevada, California. Hydrol. Process., 18, 1721–1733. DOI: 10.1002/hyp.1414.

Juras, R., Pavlásek, J., Vitvar, T., Šanda, M., Holub, J., Jankovec, J., Linda, M., 2016. Isotopic tracing of the outflow during artificial rain-on-snow event. J. Hydrol., 541, 1145–1154. DOI: 10.1016/j.jhydrol.2016.08.018.

Kattelmann, R., 2000. Snowmelt lysimeters in the evaluation of snowmelt models. Ann. Glaciol., 31, 406–410. DOI: 10.3189/172756400781820048.

Kendall, C., Caldwell, E., 1998. Chapter 2: Fundamentals of Isotope Geochemistry, Isotope Tracers in Catchment Hydrology. Elsevier B.V. doi:http://dx.doi.org/10.1016/B978-0-444-81546-0.50009-4.

Klaus, J., McDonnell, J.J., 2013. Hydrograph separation using stable isotopes: Review and evaluation. J. Hydrol., 505, 47–64. DOI: 10.1016/j.jhydrol.2013.09.006.

Laudon, H., 2004. Hydrological flow paths during snowmelt: Congruence between hydrometric measurements and oxygen 18

in meltwater, soil water, and runoff. Water Resour. Res., 40, 1–9. DOI: 10.1029/2003WR002455.

Laudon, H., Hemond, H.F., Krouse, R., Bishop, K.H., 2002. Oxygen 18 fractionation during snowmelt : Implications for spring flood hydrograph separation. Water Resour. Res., 38, 11, 1–10. DOI: 10.1029/2002WR001510.

Lee, J., Feng, X., Faiia, A.M., Posmentier, E.S., Kirchner, J., Osterhuber, R., Taylor, S., 2010. Isotopic evolution of a seasonal snowcover and its melt by isotopic exchange between liquid water and ice. Chem. Geol., 270, 126–134. DOI: 10.1016/j.chemgeo.2009.11.011.

Lyon, S.W., Laudon, H., Seibert, J., Mörth, M., Tetzlaff, D., Bishop, K.H., 2010. Controls on snowmelt water mean transit times in northern boreal catchments. Hydrol. Process., 24, 1672–1684. DOI: 10.1002/hyp.7577.

Martinec, J., 1987. Meltwater percolation through an alpine snowpack. In: Proc. Avalanche Formation, Movement and Effects. (Davos Symposium, September 1986). IAHS Publ. no. 162. IAHS, Wallingford, pp. 255–264.

McDonnell, J.J., 1990. A rational for old water discharge through macroporos in a steep, humid catchment. Water Resour. Res., 26, 2821–2832. DOI: 10.1029/WR026i011p02821.

Munksgaard, N.C., Wurster, C.M., Bass, A., Bird, M.I., 2012. Extreme short-term stable isotope variability revealed by continuous rainwater analysis. Hydrol. Process., 26, 3630–3634. DOI: 10.1002/hyp.9505.

Nespor, V., Sevruk, B., 1999. Estimation of wind-induced error of rainfall gauge measurements using a numerical simulation. J. Atmosperic Ocean. Technol., 16, 450–464.

Obled, C., Rosse, B., 1977. Mathematical models of a melting snowpack at an index plot. J. Hydrol., 32, 139–163. DOI: 10.1016/0022-1694(77)90123-8.

Penna, D., Ahmad, M., Birks, S.J., Bouchaou, L., Brenčič, M., Butt, S., Holko, L., Jeelani, G., Martínez, D.E., Melikadze, G., Shanley, J.B., Sokratov, S.A., Stadnyk, T., Sugimoto, A., Vreča, P., 2014a. A new method of snowmelt sampling for water stable isotopes. Hydrol. Process., 28, 5637–5644. DOI: 10.1002/hyp.10273.

Penna, D., Engel, M., Mao, L., Dell'Agnese, A., Bertoldi, G., Comiti, F., 2014b. Tracer-based analysis of spatial and temporal variation of water sources in a glacierized catchment. Hydrol. Earth Syst. Sci. Discuss., 11, 4879–4924. DOI: 10.5194/hessd-11-4879-2014.

Penna, D., Engel, M., Bertoldi, G., Comiti, F., 2017. Towards a tracer-based conceptualization of meltwater dynamics and streamflow response in a glacierized catchment. Hydrol. Earth Syst. Sci., 21, 23–41. DOI: 10.5194/hess-2016-334.

Rasmussen, R., Baker, B., Kochendorfer, J., Meyers, T., Landolt, S., Fischer, P.A., Black, J., Thériault, J.M., Kucera, P., Gochis, D., Smith, C., Nitu, R., Hall, M., Ikeda, K., Gutmann, E., 2012. How Well Are We Measuring Snow ? Am. Meteorol. Soc., 811–829. DOI: 10.1175/BAMS-D-11-00052.1.

Rodhe, A., 1998. Chapter 12 – Snowmelt-Dominated Systems, Isotope Tracers in Catchment Hydrology. Elsevier B.V. DOI: 10.1016/B978-0-444-81546-0.50019-7.

Šanda, M., Kulasov, A., Milena, C., 2010. Runoff formation in a small catchment at hillslope and catchment scales. Hydrol. Process., 2256, 2248–2256. DOI: 10.1002/hyp.7614.

Šanda, M., Vitvar, T., Kulasová, A., Jankovec, J., Císlerová, M., 2014. Run-off formation in a humid , temperate headwater catchment using a combined hydrological , hydrochemical and isotopic approach (Jizera Mountains, Czech Republic). Hydrol. Process., 3229, 3217–3229. DOI: 10.1002/hyp.9847.

Schmieder, J., Hanzer, F., Marke, T., Garvelmann, J., Warscher, M., Kunstmann, H., Strasser, U., 2016. The importance of snowmelt spatiotemporal variability for isotope-based hydrograph separation in a high-elevation catchment. Hydrol. Earth Syst. Sci., 20, 5015–5033. DOI: 10.5194/hess-20-5015-2016.

Shanley, J.B., Sundquist, E.T., Kendall, C., 1995. Water, Energy, and Biochemical Budget Research At Sleepers River Research Watershed, Vermont. U.S. Geological Survey, Bow, New Hampshire.

Singla, S., Céron, J.P., Martin, E., Regimbeau, F., Déqué, M., Habets, F., Vidal, J.P., 2012. Predictability of soil moisture and river flows over France for the spring season. Hydrol. Earth Syst. Sci., 16, 201–216. DOI: 10.5194/hess-16-201-2012.

Stähli, M., Gustafsson, D., 2006. Long-term investigations of the snow cover in a subalpine semi-forested catchment. Hydrol. Process., 20, 411–428. DOI: 10.1002/hyp.6058.

Staudinger, M., Seibert, J., 2014. Predictability of low flow – An assessment with simulation experiments. J. Hydrol., 519, 1383–1393. DOI: 10.1016/j.jhydrol.2014.08.061.

Stewart, I.T., 2009. Changes in snowpack and snowmelt runoff for key mountain regions. Hydrol. Process., 23, 1, 78–94. DOI: 10.1002/hyp.7128.

Stichler, W., Rauert, W., Martinec, J., 1981. Environmental isotope studies of an alpine snowpack. Nord. Hydrol., 12, 297–308.

Taylor, S., Feng, X., Kirchner, J.W., Osterhuber, R., 2001. Isotopic evolution of a seasonal snowpack and its melt. Water Resour. Res., 37, 759–769.

Taylor, S., Feng, X., Renshaw, C.E., Kirchner, J.W., 2002a. Isotopic evolution of snowmelt 2. Verification and parameterization of a one-dimensional model using laboratory experiments. Water Resour. Res., 38, 10. DOI: 10.1029/2001WR000815.

Taylor, S., Feng, X., Williams, M., Mcnamara, J., 2002b. How isotopic fractionation of snowmelt affects hydrograph separation. Hydrol. Process., 3690, 3683–3690. DOI: 10.1002/hyp.1232.

Tekeli, A.E., Şorman, A.A., Şensoy, A., Şorman, A.Ü., Bonta, J., Schaefer, G., 2005. Snowmelt lysimeters for real-time snowmelt studies in Turkey. Turkish J. Eng. Environ. Sci., 29, 29–40.

Unnikrishna, P. V., McDonnell, J.J., Kendall, C., 2002. Isotope variations in a Sierra Nevada snowpack and their relation to meltwater. J. Hydrol., 260, 38–57.

von Freyberg, J., Studer, B., Kirchner, J.W., 2017. A lab in the field : high-frequency analysis of water quality and stable isotopes in stream water and precipitation. Hydrol. Earth Syst. Sci., 21, 1721–1739. DOI: 10.5194/hess-21-1721-2017.

Würzer, S., Wever, N., Juras, R., Lehning, M., Jonas, T., 2017. Modelling liquid water transport in snow under rain-on-snow conditions – considering preferential flow. Hydrol. Earth Syst. Sci., 21, 1741–1756. DOI: 10.5194/hess-21-1741-2017.

Zappa, M., Bernhard, L., Fundel, F., Jörg-Hess, S., 2012. Vorhersage und Szenarien von Schnee- und Wasserressourcen im Alpenraum. Forum für Wissen 19–27.

Received 3 July 2017
Accepted 9 December 2017

APPENDIX

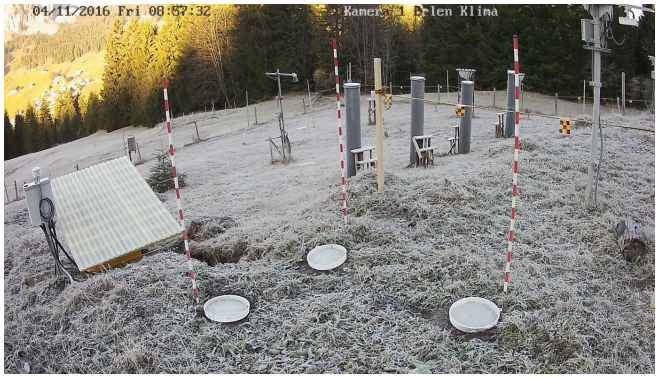

Fig. A1. Webcam picture before the snowfall event in November 2016 (04.11.2016 08:57).

Fig. A2. Webcam picture during the snowfall event in November 2016 (06.11.2016 10:57).

Fig. A3. Unheated precipitation collector with extended funnel connected to the 6712-Teledyne Isco automatic water sampler during the winter season 2015/16.

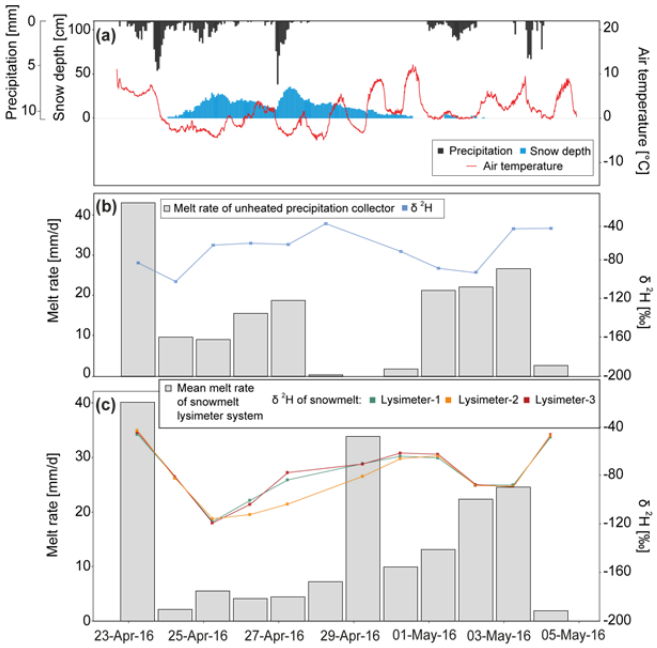

Fig. A4. The snowfall-snowmelt period in April 2016. (a) Precipitation and snow depth (left axis) as well as air temperature (right axis) at the field site Erlenhöhe. (b) Daily meltwater sample volume (left axis) and δ^2H values (right axis) from the unheated precipitation collector with extended funnel. (c) Daily meltwater sample volume (left axis) and δ^2H values (right axis) from the snowmelt lysimeter system.

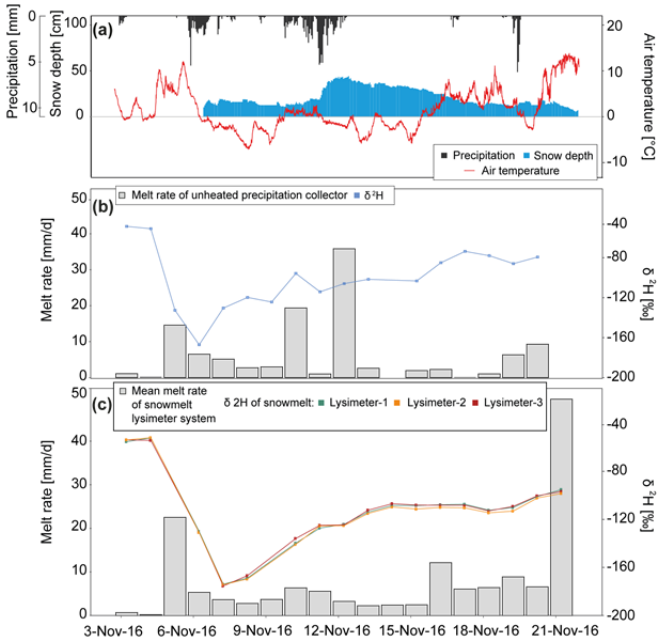

Fig. A5. The snowfall-snowmelt period in November 2016. (a) Precipitation and snow depth (left axis) as well as air temperature (right axis) at the field site Erlenhöhe. (b) Daily meltwater sample volume (left axis) and δ^2H values (right axis) from the unheated precipitation collector with extended funnel. (c) Daily meltwater sample volume (left axis) and δ^2H values (right axis) from the snowmelt lysimeter system.

J. Hydrol. Hydromech., 67, 2019, 1, 32–40
DOI: 10.2478/johh-2018-0017

Application of passive capillary samplers in water stable isotope investigations of snowmelt – A case study from Slovenia

Polona Vreča[1*], Mihael Brenčič[2, 3], Anja Torkar[2]

[1] Jožef Stefan Institute, Department of Environmental Sciences, Ljubljana, Slovenia. E-mail: polona.vreca@ijs.si
[2] Department of geology, Faculty of Natural Sciences and Engineering, University of Ljubljana, Ljubljana, Slovenia. E-mails: mihael.brencic@geo.ntf.uni-lj.si, anja.torkar@geo.ntf.uni-lj.si
[3] Geological Survey of Slovenia, Ljubljana, Slovenia.
[*] Corresponding author. Tel.: +386 15885304. Fax: +386 15885346. E-mail: polona.vreca@ijs.si

Abstract: In this paper we describe the use of modified passive capillary samplers (PCSs) to investigate the water isotope variability of snowmelt at selected sites in Slovenia during winter 2011/2012 and during winter 2012/2013. First, PCS with 3 fibreglass wicks covering approximately 1 m^2 were tested to determine sample variability. We observed high variability in the amount of snowmelt water collected by individual wick (185 to 345 g) and in the isotope composition of oxygen ($\delta^{18}O$ −10.43‰ to −9.02‰) and hydrogen ($\delta^{2}H$ −70.5‰ to −63.6‰) of the collected water. Following the initial tests, a more detailed investigation was performed in winter 2012/2013 and the variability of snowmelt on the local scale among the different levels (i.e. within group, between the close and more distant groups of wicks) was investigated by applying 30 fibreglass wicks making use of Analysis Of Variance (ANOVA) and a balanced hierarchical sampling design. The amount of snowmelt water collected by an individual wick during the whole experiment was between 116 and 1705 g, while the isotope composition varied from −16.32‰ to −12.86‰ for $\delta^{18}O$ and from −120.2‰ to −82.5‰ for $\delta^{2}H$. The main source of variance (80%) stems from the variability within the group of wicks (e.g. within group) while other sources contribute less than 20% of the variability. Amount weighted samples for the 2012–2013 season show no significant differences among groups, but significant differences for particular sampling events were observed. These investigations show that due to the variability within the group of wicks, a large number of wicks (> 5) are needed to sample snowmelt.

Keywords: Snowmelt; Passive capillary sampler; Oxygen and hydrogen isotopes; Balanced hierarchical sampling design; ANOVA; Slovenia.

INTRODUCTION

Snow and snowmelt significantly contribute to river discharge and groundwater recharge (Bavay et al., 2013; DeWalle and Rango, 2008). The role of mountains in providing the indispensable water resources for municipal and industrial water supply, irrigation, hydropower production and other environmental services is well known and unquestioned (Fayad et al., 2017; Mankin et al., 2015). In Europe in particular, the Alps, with their seemingly vast water resources, are of immeasurable importance for the economic and cultural development of not only the Alpine Arc, but also the lowlands and major urban areas far beyond (Viviroli and Weingartner, 2004; Viviroli et al., 2011). In the Alpine climate zone, the amount of water stored in the snowpack and the amount released during snowmelt varies considerably in space and time and substantially influences the water cycle and aquifers recharge during the snowmelt period (Weber et al., 2016). Therefore, an accurate snow balance study is necessary in mountain areas for determining water storage capacity and for assessing water residence times, which are crucial for protecting alpine water resources. Recent climate warming and changes in atmospheric circulation patterns have resulted in reductions in the duration of the snow cover season, the amount of water stored in the snowpack, and a trend towards an earlier melt (Hohenwallner et al., 2011). Therefore, monitoring the effects of climate change on water resources requires techniques capable of identifying and quantifying the relative contribution of snowmelt to surface water flow and groundwater recharge (Penna et al., 2014).

Isotopes of oxygen and hydrogen in water molecule proved to be useful tracers of water cycle and have played an important role in hydrology in investigating of snow and its influence on runoff (e.g. Engel et al., 2016; Friedman et al., 1991; Jeelani et al., 2017; Moser and Stichler, 1974; Sokratov and Golubev, 2009). A major challenge when using these methods is identifying the contribution of snowmelt to runoff and determining the appropriate isotope composition of the snowmelt (Lee et al., 2010; Penna et al., 2014), which is variable at the local and regional scale (DeWalle and Rango, 2008; Pomeroy and Brun, 2001). Historically, different approaches were adopted like investigating snow cores, using snowmelt lysimeters or in-situ sampling of snowmelt (Penna et al., 2014 and references therein). Recently, in the frame of the project "Use of environmental isotopes in assessing water resources in snow glacier and permafrost dominated areas under changing climatic conditions" managed by the International Atomic Energy Agency (IAEA), passive capillary samplers (PCS) based on a modified design by Frisbee at al. (2010), were placed at 11 sites in ten partner countries (Penna et al., 2014). A novel approach for obtaining snowmelt water samples for isotope analysis was presented including the strengths and weaknesses of proposed PCS method in comparison to other techniques. In each participating country, the PCSs were deployed according to its own specific research questions and requirements (Jeelani et al., 2016; Krajči et al., 2016; Massone et al., 2016; N'da et al., 2016; Penna et al., 2014, 2017).

In Slovenia, previous isotope investigations (Brenčič and Vreča, 2016; Ogrinc et al., 2008; Ortar et al., 2013; Torkar, 2016; Torkar et al., 2016; Vreča et al., 2013) revealed large

seasonal variations in the isotope composition of hydrogen and oxygen in precipitation, surface waters, groundwater and the snowpack. The influence of snowmelt, although known to be an important driver of these isotopic fluctuations, was not quantified. Information on snowmelt isotope composition is important for estimating recharge components, residence times and the recharge area. To obtain this information it is important to investigate the variability of the snowmelt in time and space.

The aim of the present paper is to present in detail the results of testing modified PCSs and the evaluation of the stable isotope composition of snowmelt based on a balanced Analysis of Variance where sources of variance at different levels (at the temporal and spatial scales) were predefined.

MATERIALS AND METHODS

Study area

PCSs were positioned on the flat plain above the resurgence area of the River Radovna. The Radovna valley is situated in north-west Slovenia in the eastern Julian Alps (Figure 1). It lies between the two high karstic plateaus of Pokljuka and Mežakla. Both plateaus together along with the eastern part of the Julian Alps represent the Radovna River watershed. The bottom of the valley is filled with fluvioglacial and alluvial sediments creating a large unconfined porous aquifer used as drinking water supply for 29,700 inhabitants. A detailed description of the River Radovna valley and of the study site can be found in Torkar et al. (2016).

The wider area of the Julian Alps is characterised by high precipitation, rapid runoff, and low evaporation (Dolinar et al., 2008; Frantar et al., 2008). Its climate is defined by long cold winters and short summers with frequent precipitation. In the upper Radovna River valley a meteorological station is located at Zgornja Radovna (ZR, Figure 1; 46°25'41.88'' N, 13°56'36.24'' E, altitude 750 m a.s.l.) where precipitation and snow depth are measured daily (Nadbath, 2012). Snow starts to accumulate in late autumn. The snow cover is regular and typically lasts for more than 100 days. In the spring/summertime, snowmelt feeds the streams (Torkar et al., 2016). In recent years, the snow cover season has become shorter and the average snow depth has reduced, which has affected the discharge regime (Dolinar et al., 2008; Frantar et al., 2008).

Our investigations were performed during winter 2011/2012 and winter 2012/2013. The maximum snow depth at station ZR was only 18 cm in winter 2011/2012 and 109 cm in winter 2012/2013. In winter 2011/2012 the first appearance of snow was in the middle October followed by two periods with snow cover, one from the middle of December (17.12.2011) to the beginning of January (10.1.2012) and one at the beginning of February (4.2.2012) where snow remained on the ground until the end of February (28.2.2012). In winter 2012/2013, the first appearance of snow was at the end of October and then again in the beginning of December (1.12.2012) lasting until the beginning of January (4.1.2013) and then again from the middle of January (14.1.2013) until the end of April 2013 (20.4.2013) (ARSO, 2017).

Sampling

Modified PCSs as described in Penna et al. (2014) were used for the first time in winter 2011/2012 in six different countries. We performed the first tests at the meteorological station ZR (Figure 1). We used one PCS constructed from a plastic box with 3 fibreglass wicks (IAEA) passing through the lid of a sample collection bottle (1L) with the fiddleheads placed directly on the ground. The whole PCS covered an area of 1 m^2 and was installed on 26 November 2011. The snowmelt samples were collected on 10 May 2012.

Based on the results from winter 2011/2012 we performed more extensive investigations in winter 2012/2013 to determine the variability of snowmelt isotope composition associated with the PCS at the local and regional scales (Penna et al., 2014). Variance component analysis based on an Analysis Of Variance (ANOVA) and a balanced hierarchical sampling design (Figure 2) was used to identify different possible sources of variability of amount of collected water and its stable isotope composition to compare: 1) wicks inside of a group (level A – defined as within group variability); 2) groups of wicks that are close to each other (level B – defined as variability between sampling clusters); 3) variability in the wider space (level C – defined as variability between sampling locations) on plain where level B samplers are separated for several hundred meters at the same altitude. The area selected for installation of the PCS was considered as homogenous with no significant differences in climate and morphology.

PCSs were prepared according to a common protocol (IAEA) including construction and installation (Penna et al, 2014). The most important part of the PCS is the wick (a fiberglass rope with a core, 10 mm, No. 167 7 995, Bergal Erfurter Flechttechnik GmbH). The PCSs for our experiment were prepared in the laboratory as follows:

1. The rope (wick) was washed with deionized water until the measured electrical conductivity reached <100 µS/cm.
2. The wick was then dried and cut into 80 cm sections.
3. Plastic tubing was cut into 60 cm sections and the wick was pulled through the plastic tubing allowing 20 cm of the wick to remain exposed. The exposed wick was then rolled and secured with plastic band.
4. The wick was then fed through lid of a sample collection 1L bottle. The final PCS consisted of a box with 5 wicks connected to bottles (Penna et al., 2014).
5. Finally, the exposed wicks were placed on the top of a plastic barrier and secured to the ground using a u-shaped pin (Penna et al., 2014).

We installed the PCSs at 2 locations in the Radovna River valley near to the precipitation station ZR (Figure 1) approximately 250 m apart at an altitude of 740 m a.s.l. The locations were as follows:

- Gogala – G (46°25'50.14'' N, 13°57'2.18'' E)
- Guhar – Gu (46°25'47.21'' N, 13°56'51.58' E)

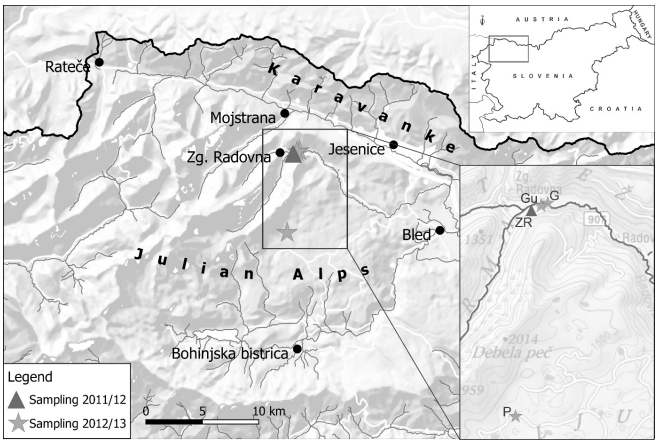

Fig. 1. Relief map showing sampling locations: ZR – Zgornja Radovna, G – Gogala, Gu – Guhar and P – Pokljuka.

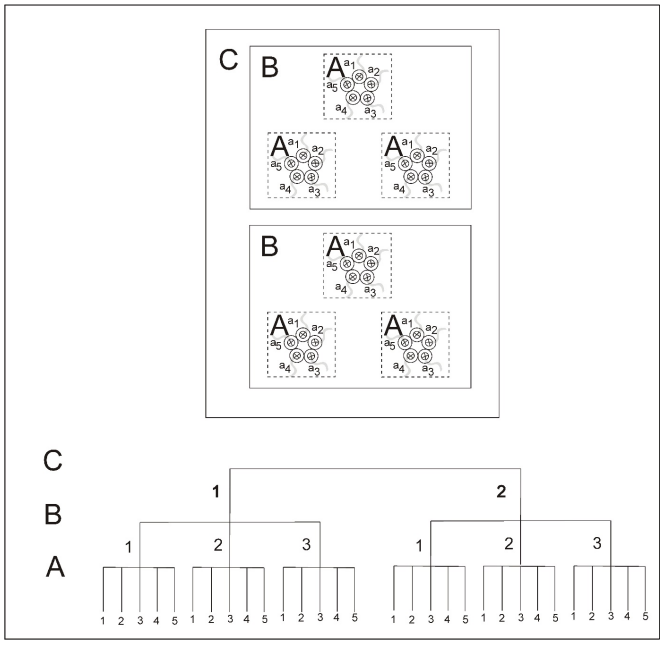

Fig. 2. Sampling design for PCS snowmelt investigations at G and Gu in winter 2012/2013.

At each location a cluster of 3 PCS boxes each with 5 wicks were installed (4 December 2012) according to sampling design shown in Figure 2. We collected the samples at G and Gu twice during winter 2012/2013, i.e. at the end of 2012 (location G) and beginning of 2013 (location (Gu) and at the end of the snow season in April 2013. The samples were transported back to the laboratory where the amount of sample (expressed in g) was recorded and stored in 30 mL high-density polyethylene (HDPE) bottles prior to isotope analysis.

To assess the variability at the different altitudes we installed a PCS with 5 wicks in the recharge area of the Radovna River on the Pokljuka plateau (location P; 46°21'54.80'' N, 13°56'15.50'' E, 1330 m a.s.l., Figure 1), south of the Radovna sampling site on the 1.12.2012. The sampler was emptied only at the end of the snow season (18 May 2013). Due to high snow cover in winter 2012/2013 not all of the snowmelt water was collected at location P (maximum 1115 g) and as a result the data were used only for a qualitative comparison and were not included in the ANOVA.

Isotope analysis

The oxygen stable isotope composition (δ^{18}O in ‰) of three samples collected in 2012 was determined using isotope ratio mass spectrometry (IRMS). For these samples we used a Iso-Prime MultiFlow-Bio module while all of the other samples were analysed using a Varian MAT 250 IRMS at the Jožef Stefan Institute (JSI) by means of water-CO_2 equilibration technique. All measurements were carried out against laboratory standards periodically calibrated against primary IAEA calibration standards to VSMOW/SLAP scale. Long-term measurement precision of control sample was better than 0.07 ‰. Hydrogen (δ^2H in ‰) was determined in the Isotope Hydrology Laboratory (IHL) at the IAEA by means of off-axis integrated cavity output laser spectroscopy (OA-ICOS, Los Gatos Research, Mountain View CA, United States of America). All measurements were carried out against laboratory standards calibrated against primary IAEA calibration standards to VSMOW/SLAP scale. The typical uncertainty reported as the long-term standard-deviation of a control sample was 0.5‰ for δ^2H.

Data evaluation

Basic descriptive statistics, i.e. weighted mean, minimum, maximum and range and the deuterium excess ($d = \delta^2\text{H} - 8\times\delta^{18}\text{O}$; Dansgaard, 1964) were calculated for each PCS. These statistics are illustrated as box-plots (i.e. min – max, first and third quartiles, median and mean). The weighted mean was calculated for data from G and Gu since the bottles were emptied twice during the winter 2012/2013 and consequently isotope composition of water for the first and second sampling period was measured separately. The mean δ^{18}O, δ^2H and d values weighted according to the amount of water were calculated based on two sampling events for the whole sampling period.

Samples were collected based on a balanced sampling design (Figure 2). Such a design enables the evaluation of the results using ANOVA - two way crossed classification interaction model with the balanced data for the random model. The first level C, defines the different sampling locations where sampling clusters were separated by more than 250 m; the second level B relates to sampling clusters at each location separated by a few meters, while the third level A is defined as within groups interaction and is observed for variability within an area of approximately 1 m^2. Variance components estimations are solved for the variance components based on a linear model. The model of variance components can be defined as: $s^2_{TOT} = s^2_A + s^2_B + s^2_{INT} + s^2_C$. Where s^2_{TOT} is the estimated total variance, s^2_{INT} is the estimated interaction variance and s^2_i is the estimated variance of each variance component A, B, C. All calculations were performed using Microsoft® Excel for Mac Version 15.123. ANOVA and variance component analysis were performed for each sampling campaign and for the whole amount of water weighted mean data set. Readers interested in theoretical details of the variance component analysis should consult Searle et al. (2006).

RESULTS AND DISCUSSION

During the first snowmelt investigations in winter 2011/2012 we collected only 3 samples (ZR1-1, ZR1-2 and ZR1-3; Table 1). The amount of the collected water varied from 185 to 345 g (mean 248 g, range 160 g) and was smaller than expected in an average winter but reasonable due to particular climatic characteristics during winter 2011/2012 when the ground was mostly uncovered by snow and the maximum snow depth at location ZR was only 18 cm. The δ^{18}O, δ^2H and d values varied between −10.43 and −9.02‰ (weighted mean −9.96‰, range 1.41‰), −70.5 and −63.6‰ (weighted mean −68.0‰, range 6.9‰), and 8.5 to 13.1‰ (weighted mean 11.7‰, range 4.6‰), respectively. The data obtained showed high variability in the amount of the collected water and its isotope composition inside of a group of wicks (1 m^2).

During winter 2012/2013 we performed sampling according to the balanced design (Figure 2). Results for all 35 wicks installed at G, Gu and P are summarized in Tables 1 to 3 while the descriptive statistics are presented in Table 4. Results for G and Gu are presented in Tables 2 and 3 while weighted means for each wick are included in Table 1. Similarly as for winter 2011/2012, we observed considerable variation in the amount of collected water and its isotope composition at all locations and also between the two sampling campaigns at G and Gu (Table 4, Figures 3–5). In addition, we observed at both locations a large variability in the amount of water collected

Table 1. Amount of collected water (Amount), isotope composition of oxygen (δ^{18}O) and hydrogen (δ^{2}H) and deuterium excess (d) for all wicks installed at ZR, G, Gu and P.

Wick label	Sampling period (from–to)		Amount [g]	δ^{18}O [‰]	δ^{2}H [‰]	d [‰]
ZR1-1	26.11.2011	10.5.2012	185	−10.17	−68.3	13.1
ZR1-2	26.11.2011	10.5.2012	345	−10.43	−70.6	13.0
ZR1-3	26.11.2011	10.5.2012	215	−9.02	−63.7	8.6
G1-1	4.12.2012	23.4.2013	1140	−14.76	−107.8	10.3
G1-2	4.12.2012	23.4.2013	463	−14.19	−97.6	16.0
G1-3	4.12.2012	23.4.2013	430	−15.56	−111.9	12.6
G1-4	4.12.2012	23.4.2013	1705	−14.84	−103.4	15.4
G1-5	4.12.2012	23.4.2013	216	−15.55	−112.7	11.8
G2-1	4.12.2012	23.4.2013	645	−13.49	−95.0	13.0
G2-2	4.12.2012	23.4.2013	727	−14.33	−100.7	14.0
G2-3	4.12.2012	23.4.2013	703	−13.71	−91.5	18.2
G2-4	4.12.2012	23.4.2013	1361	−13.66	−95.0	14.3
G2-5	4.12.2012	23.4.2013	828	−15.09	−108.7	12.1
G3-1	4.12.2012	23.4.2013	1500	−13.64	−95.3	13.8
G3-2	4.12.2012	23.4.2013	259	−14.39	−103.3	11.8
G3-3	4.12.2012	23.4.2013	1385	−14.55	−103.5	13.0
G3-4	4.12.2012	23.4.2013	1236	−14.94	−107.7	11.9
G3-5	4.12.2012	23.4.2013	291	−14.48	−106.6	9.3
Gu1-1	4.12.2012	23.4.2013	880	−14.06	−100.7	11.8
Gu1-2	4.12.2012	23.4.2013	1184	−14.18	−102.2	11.3
Gu1-3	4.12.2012	23.4.2013	1558	−14.19	−100.9	12.7
Gu1-4	4.12.2012	23.4.2013	116	−16.28	−120.3	10.0
Gu1-5	4.12.2012	23.4.2013	1351	−14.46	−106.2	9.6
Gu2-1	4.12.2012	23.4.2013	652	−14.24	−103.9	10.0
Gu2-2	4.12.2012	23.4.2013	247	−14.72	−105.3	12.5
Gu2-3	4.12.2012	23.4.2013	656	−14.34	−104.4	10.4
Gu2-4	4.12.2012	23.4.2013	847	−14.00	−103.5	8.6
Gu2-5	4.12.2012	23.4.2013	507	−12.86	−82.5	20.4
Gu3-1	4.12.2012	23.4.2013	1216	−15.14	−108.8	12.4
Gu3-2	4.12.2012	23.4.2013	985	−14.47	−104.4	11.4
Gu3-3	4.12.2012	23.4.2013	1477	−14.03	−99.5	12.7
Gu3-4	4.12.2012	23.4.2013	746	−12.94	−92.4	11.1
Gu3-5	4.12.2012	23.4.2013	1461	−13.79	−97.8	12.5
P1-1	1.12 2012	18.5.2013	1100	−14.84	−106.1	12.7
P1-2	1.12 2012	18.5.2013	465	−13.95	−96.7	14.9
P1-3	1.12 2012	18.5.2013	215	−16.32	−117.0	13.7
P1-4	1.12 2012	18.5.2013	1100	−14.51	−102.7	13.5
P1-5	1.12 2012	18.5.2013	830	−14.51	−102.0	14.2

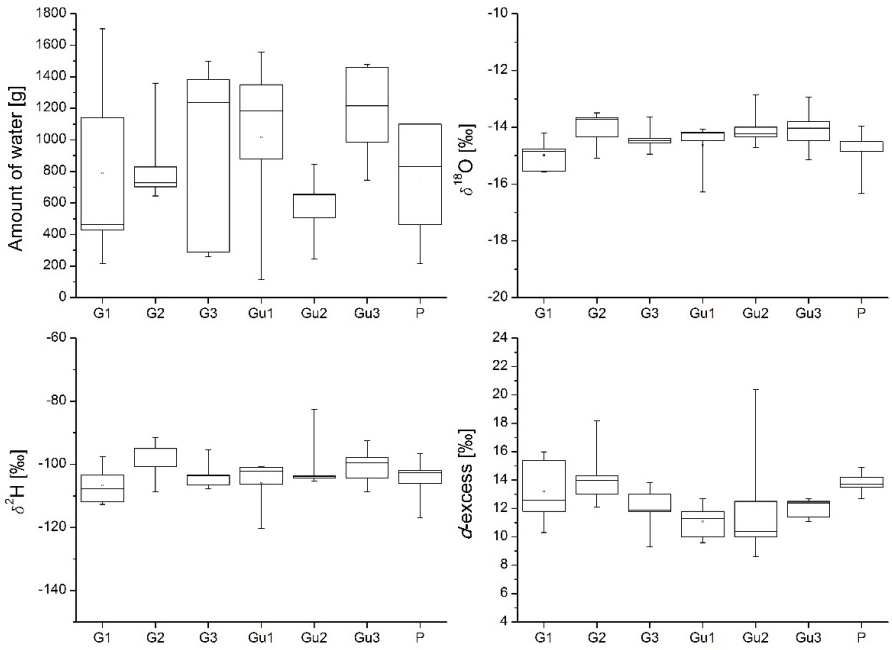

Fig. 3. Box plots of snowmelt and its isotopic composition collected using seven PCSs instaled at G, Gu and P. Sampling period at G and Gu was between 4 December 2012 and 23 April 2013, and at P between 1 December 2012 and 18 May 2013.

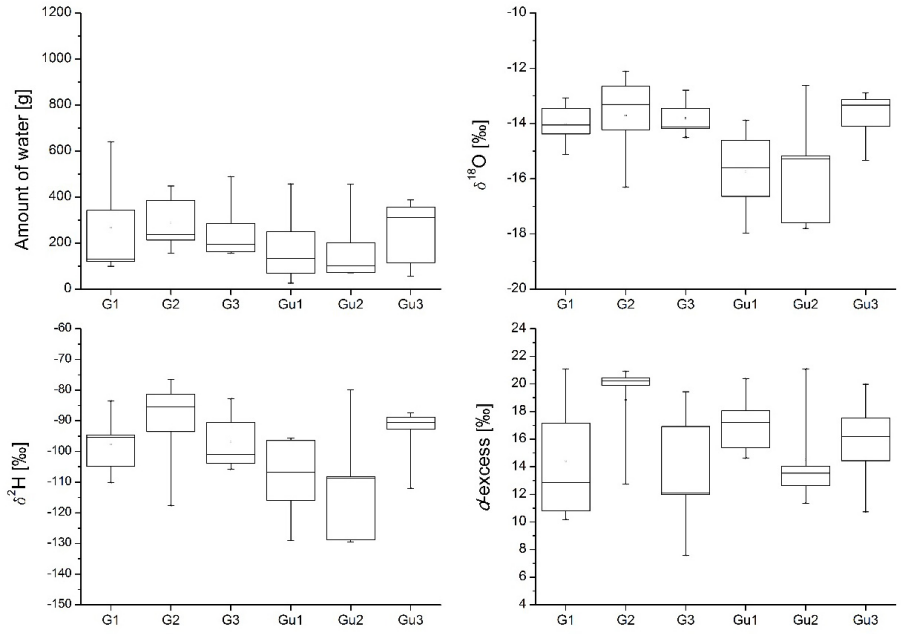

Fig. 4. Box plots of snowmelt and its isotopic composition collected during the first sampling in winter 2012/2013 using 6 PCSs instaled at G and Gu. Sampling period at G was between 4 December 2012 and 27 December 2012 and at Gu between 4 December 2012 and 12 January 2013.

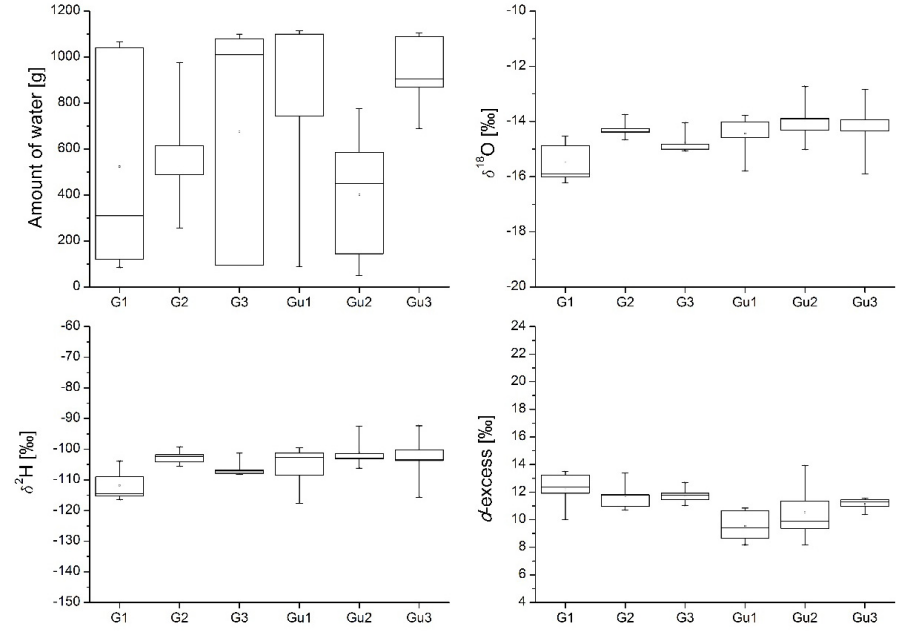

Fig. 5. Box plots of snowmelt and its isotopic composition collected during the second sampling in winter 2012/2013 using 6 PCSs instaled at G and Gu. The sampling period at G was between 27 December 2012 and 23 April 2013 and at Gu between 12 January 2013 and 23 April 2013.

and a small variability in the $\delta^{18}O$, $\delta^{2}H$ and d values (Table 4) during the second sampling period. At P, we collected on average less snowmelt water than at G and Gu (Table 4). As expected, the water was depleted in heavier isotopes (^{18}O and ^{2}H) due to the higher altitude of P.

Results of ANOVA and variance component analysis are presented in Tables 5 and 6. In all cases, the estimated interaction was not significant at the $\alpha = 0.05$ level. It also follows that the mean square for the interaction is smaller than the mean square error of the model meaning that the variance of interaction is less than zero. We interpret it as that sampling at one location does not influence the data obtained from other sampling locations. Accordingly, such variance does not exist and consequently no statistical interaction is present. This conclusion agrees with the selected design and conditions in the field. If we did observe an interaction, another, more complicated model of ANOVA with no interaction would have to be applied.

When performing ANOVA on the data from G and Gu during both sampling campaigns the situation appears more complicated. For instance, for amount of water, we observe no significant differences in the mean amount of water sampled, while for $\delta^{18}O$ the differences are significant between the dif-

ferent sampling locations. We also observe a significant difference between locations in the second sampling period for *d*-excess. For the second observation period, significant differences in averages can be observed between clusters for δ^2H.

From the variance component analysis it follows that the largest part of the variability is present at level A - *within groups*, inside of the PCS clusters (Tables 5 and 6). The variability at level A in amount of water is similar as in the case of

Table 2. Amount of collected water (Amount), isotope composition of oxygen (δ^{18}O) and hydrogen (δ^2H) and deuterium exces (*d*) for all wicks installed at G, first and second sampling campaigns.

Wick label	Sampling period (from–to)		Amount [g]	δ^{18}O [‰]	δ^2H [‰]	*d* [‰]
G1-1	4.12.2012	27.12.2012	100	−13.44	−94.7	12.9
G1-2	4.12.2012	27.12.2012	343	−14.06	−95.3	17.2
G1-3	4.12.2012	27.12.2012	120	−14.38	−104.9	10.2
G1-4	4.12.2012	27.12.2012	640	−13.08	−83.5	21.1
G1-5	4.12.2012	27.12.2012	131	−15.12	−110.2	10.8
G2-1	4.12.2012	27.12.2012	155	−12.65	−81.3	19.9
G2-2	4.12.2012	27.12.2012	237	−14.22	−93.5	20.2
G2-3	4.12.2012	27.12.2012	448	−13.31	−85.6	20.9
G2-4	4.12.2012	27.12.2012	386	−12.11	−76.4	20.4
G2-5	4.12.2012	27.12.2012	213	−16.30	−117.7	12.7
G3-1	4.12.2012	27.12.2012	490	−12.79	−82.9	19.4
G3-2	4.12.2012	27.12.2012	164	−14.13	−101.1	12.0
G3-3	4.12.2012	27.12.2012	285	−13.44	−90.6	16.9
G3-4	4.12.2012	27.12.2012	156	−14.50	−103.9	12.1
G3-5	4.12.2012	27.12.2012	196	−14.18	−105.8	7.6
G1-1	27.12.2012	23.4.2013	1040	−14.88	−109.0	10.0
G1-2	27.12.2012	23.4.2013	120	−14.53	−103.9	12.4
G1-3	27.12.2012	23.4.2013	310	−16.01	−114.6	13.5
G1-4	27.12.2012	23.4.2013	1065	−15.90	−115.3	11.9
G1-5	27.12.2012	23.4.2013	85	−16.21	−116.5	13.2
G2-1	27.12.2012	23.4.2013	490	−13.75	−99.3	10.7
G2-2	27.12.2012	23.4.2013	490	−14.38	−104.1	11.0
G2-3	27.12.2012	23.4.2013	255	−14.40	−101.8	13.4
G2-4	27.12.2012	23.4.2013	975	−14.26	−102.3	11.8
G2-5	27.12.2012	23.4.2013	615	−14.66	−105.5	11.8
G3-1	27.12.2012	23.4.2013	1010	−14.04	−101.3	11.0
G3-2	27.12.2012	23.4.2013	95	−14.82	−107.1	11.4
G3-3	27.12.2012	23.4.2013	1100	−14.83	−106.7	11.9
G3-4	27.12.2012	23.4.2013	1080	−15.00	−108.2	11.8
G3-5	27.12.2012	23.4.2013	95	−15.07	−107.9	12.7

Table 3. Amount of collected water (Amount), isotope composition of oxygen (δ^{18}O) and hydrogen (δ^2H) and deuterium exces (*d*) for all wicks installed at Gu, first and second sampling campaigns.

Wick label	Sampling period (from–to)		Mass [g]	δ^{18}O [‰]	δ^2H [‰]	*d* [‰]
Gu1-1	4.12.2012	12.1.2013	135	−15.61	−106.8	18.1
Gu1-2	4.12.2012	12.1.2013	69	−16.64	−115.9	17.2
Gu1-3	4.12.2012	12.1.2013	458	−14.61	−96.5	20.4
Gu1-4	4.12.2012	12.1.2013	26	−17.96	−129.1	14.6
Gu1-5	4.12.2012	12.1.2013	251	−13.88	−95.6	15.4
Gu2-1	4.12.2012	12.1.2013	202	−17.60	−129.4	11.4
Gu2-2	4.12.2012	12.1.2013	102	−15.28	−108.2	14.1
Gu2-3	4.12.2012	12.1.2013	71	−17.80	−128.9	13.5
Gu2-4	4.12.2012	12.1.2013	72	−15.18	−108.8	12.7
Gu2-5	4.12.2012	12.1.2013	457	−12.62	−79.9	21.1
Gu3-1	4.12.2012	12.1.2013	311	−12.90	−88.8	14.4
Gu3-2	4.12.2012	12.1.2013	115	−15.34	−112.0	10.7
Gu3-3	4.12.2012	12.1.2013	387	−13.12	−87.4	17.5
Gu3-4	4.12.2012	12.1.2013	56	−14.09	−92.7	20.0
Gu3-5	4.12.2012	12.1.2013	356	−13.33	−90.5	16.2
Gu1-1	12.1.2013	23.4.2013	745	−13.77	−99.5	10.7
Gu1-2	12.1.2013	23.4.2013	1115	−14.02	−101.3	10.8
Gu1-3	12.1.2013	23.4.2013	1100	−14.01	−102.7	9.4
Gu1-4	12.1.2013	23.4.2013	90	−15.79	−117.7	8.7
Gu1-5	12.1.2013	23.4.2013	1100	−14.59	−108.5	8.2
Gu2-1	12.1.2013	23.4.2013	450	−12.72	−92.4	9.4
Gu2-2	12.1.2013	23.4.2013	145	−14.31	−103.1	11.4
Gu2-3	12.1.2013	23.4.2013	585	−13.91	−101.4	9.9
Gu2-4	12.1.2013	23.4.2013	775	−13.89	−103.0	8.2
Gu2-5	12.1.2013	23.4.2013	50	−15.01	−106.2	13.9
Gu3-1	12.1.2013	23.4.2013	905	−15.90	−115.6	11.6
Gu3-2	12.1.2013	23.4.2013	870	−14.35	−103.4	11.4
Gu3-3	12.1.2013	23.4.2013	1090	−14.34	−103.7	11.0
Gu3-4	12.1.2013	23.4.2013	690	−12.84	−92.4	10.4
Gu3-5	12.1.2013	23.4.2013	1105	−13.93	−100.2	11.3

Table 4. Descriptive statistics for amount of collected water (Amount), isotope composition of oxygen (δ^{18}O) and hydrogen (δ^{2}H) and deuterium exces (*d*) for all wicks installed at G, Gu and P in winter 2012/2013.

Location	Sampling period (from–to)		Parameter	Min	Max	Range	Mean (weighted)
G	4.12.2012	23.4.2013	Amount [g]	100	640	540	271
			δ^{18}O [‰]	–16.30	–12.11	4.19	–13.57
			δ^{2}H [‰]	–117.7	–76.4	41.2	–91.1
			d [‰]	7.6	21.1	13.5	17.4
	27.12.2012	23.4.2013	Amount [g]	85	1100	1015	588
			δ^{18}O [‰]	–16.21	–13.75	2.46	–14.78
			δ^{2}H [‰]	–116.5	–99.3	17.2	–106.7
			d [‰]	10.0	13.5	3.5	11.5
	4.12.2012	23.4.2013	Amount [g]	216	1705	1489	859
			δ^{18}O [‰]	–15.56	–13.49	2.07	–14.40
			δ^{2}H [‰]	–112.6	–91.5	21.2	–101.8
			d [‰]	9.3	18.2	8.9	13.4
Gu	4.12.2012	12.1.2013	Amount [g]	26	458	432	205
			δ^{18}O [‰]	–17.96	–12.62	5.34	–14.19
			δ^{2}H [‰]	–129.4	–79.9	49.6	–96.6
			d [‰]	10.7	21.1	10.3	16.9
	12.1.2013	23.4.2013	Amount [g]	50	1115	1065	721
			δ^{18}O [‰]	–15.90	–12.72	3.18	–14.15
			δ^{2}H [‰]	–117.7	–92.4	25.3	–102.9
			d [‰]	8.2	13.9	5.8	10.3
	4.12.2012	23.4.2013	Amount [g]	116	1558	1442	926
			δ^{18}O [‰]	–16.28	–12.86	3.42	–14.15
			δ^{2}H [‰]	–120.2	–82.5	37.7	–101.5
			d [‰]	8.5	20.4	11.8	11.7
P	1.12.2012	18.5.2013	Amount [g]	215	1100	885	742
			δ^{18}O [‰]	–16.32	–13.95	2.37	–14.64
			δ^{2}H [‰]	–116.9	–96.7	20.2	–103.6
			d [‰]	12.6	14.9	2.3	13.6

Table 5. Results of the variance component analysis (contributions of components to the total variance are represented in shares expressed by %) for amount of collected water.

Sampling mass	Total sampling	First sampling	Second sampling
Between locations	1.4	10.6	7.3
Between clusters	8.0	0.3	9.6
Within groups	90.6	89.1	83.2

Table 6. Results of the variance component analysis (contributions of components to the total variance are represented in shares expressed by %) for δ^{18}O, δ^{2}H and *d* values.

Parameter	Level	Weighted mean – total sampling	First sampling	Second sampling
δ^{18}O	Between locations	6.2	33.4	29.8
	Between clusters	16.1	7.0	12.1
	Within groups	77.6	59.7	58.0
δ^{2}H	Between locations	0.3	24.9	18.5
	Between clusters	14.8	3.8	16.7
	Within groups	84.8	71.3	64.8
d	Between locations	16.6	0.2	49.4
	Between clusters	4.5	4.4	1.6
	Within groups	78.9	95.4	49.0

the total amount. In the case of total amount of collected water, during the first and second sampling campaigns only a small redistribution in the variability source at other two levels appears (Table 5). The variability at level A for δ^{18}O and δ^{2}H still predominates but is smaller compared to the amount of water weighted means (Table 6). In both cases, a relatively high variability component exists between locations for δ^{18}O i.e., 33.4 % and 29.8 % for each sampling campaign, respectively. A similar relation is observed for δ^{2}H where this component represents 24.9 % and 18.5 %, respectively. According to the significance of differences for δ^{18}O it means that at the level of particular sampling campaign they have to be considered. For *d* values we obtained different results (Table 6) that can be explained by distribution of *d*-excess which is statistically a derived distribution from empirical parent distributions of δ^{2}H and δ^{18}O. Because ANOVA results are not identical for δ^{2}H and δ^{18}O the *d*-excess for ANOVA is different. For the first sampling campaign nearly all variability is at the level A, but for the second sampling campaign the variation sources are nearly similar for levels A and C.

The ANOVA for weighted mean isotope composition and cumulative sampling volume shows that between all levels and groups no significant differences in averages are present. In this case variance components reveal how nearly all variability is present for the variance source *within groups* (Tables 5 and 6), meaning that a large part of the variability is present inside of the sampling cluster of the PCSs. Following the applied model some variability is also present between sampling clusters, but variability between locations is small and can be neglected. The reverse is observed for *d*-excess (Table 6); here variability is relatively large between the sampling sites but negligible between the clusters. A comparison of the results obtained for winter 2012/2013 at P with the results from G and Gu (Table 1) reveals no visual significant difference between the sites (Figure 3). The range of variability at P is very similar to other sites.

The differences between the results obtained at G and Gu for winter 2012/2013 (Figure 3) and for the two sampling campaigns (Figures 4 and 5) have important implications for interpreting the isotope composition of snowmelt when several snowmelt events are possible during winter such as in the case of Radovna. The data obtained from the first and the second sampling campaigns in winter 2012/2013 at G and Gu show differences in variability structure. When we calculate the means weighted by the amount of water, the differences between variability structures representative for particular period diminish and integrate (Tables 5 and 6). This can have important consequences when interpreting residence times in groundwater based on this data. If residence times are short

(e.g. in karstic aquifers), it is important to observe the isotope composition of each snowmelt event. Contrary, when residence times are long (e.g. in porous aquifers with relatively low permeability), integrated data for all snowmelt events are needed.

Our findings regarding variance component analysis have important implications for the future sampling strategies of snowmelt with PCSs. We have shown that most of the variability is present inside of the PCSs sampling clusters (level A, *within groups*) and that the share of other variability components is relatively small in homogeneous regions. This shows that the variability in the isotope composition of snowmelt at one location (approx. 1 m^2) is high and should be sampled using a large number of wicks (more than 5) and at the same time there is no need to sample snowmelt at other places with similar conditions. With a small number of wicks we cannot define the variability in isotope composition. As shown before, the lack of information on isotope composition variability can have important consequences in the case of other models where isotope composition of snowmelt represents input data.

We observed also a large variability in the amount of water collected inside of the PCSs clusters (at level A). This indicates that suction of water by the fiberglass rope and therefore its physical characteristics (permeability and transmissivity) affects the amount of snowmelt water collected in each sampling bottle. Suction of water through the fibreglass wicks also depends on its pre-event state. If the wick is saturated it will behave completely differently than if it is dry. The amount of water collected by the sampler can also be influenced by the fiddlehead position on the ground and how it is exposed on top of the plastic barrier. Similarly, the variance structure between the amount of snowmelt and the stable isotope composition of the snowmelt indicates that it is possible that the amount of collected snowmelt water can influence its isotope composition. Therefore, the physical characteristic of wicks and their influences on the stable isotope composition of snowmelt water must be further investigated.

There are several strengths and weaknesses in applying the PCS method and some of the questions that remain open are already discussed in detail in Penna et al. (2014). During our sampling campaigns we have recorded similar problems. The large variability in the amount of water collected shows that the maximum was somehow limited because some bottles were full or almost full (in our case 34% of bottles in the second sampling campaign) and therefore we assume that not all the melt water was collected. Similarly, as reported by Penna et al. (2014) there are indications that due to the rapid melting of the snow, not only snowmelt but also the overland flow over still frozen ground was sampled and some rain events were recorded. In addition, snow was already on the ground when we installed the PCS and the samples were not collected immediately after all the snow had melted.

CONCLUSIONS

In this paper, we present detailed results of snowmelt isotope investigations performed using modified PCS in Slovenia during two winters. The differences were expected in snowmelt isotope composition at different levels due to space and time heterogeneity characteristic for snowpack in temperate areas and related to changes in air temperature, wind, relative humidity and precipitation (snow and rain) events. Testing of the PCS was performed to determine the variability of collected snowmelt water and the stable isotope composition of the samples within a group of wicks distributed over a small area, within sampling clusters at each location separated by a few meters and between locations separated by a few 100 m but with similar conditions.

Results of applied balanced sampling design and ANOVA revealed no significant differences in the mean values between all levels and groups for amount of water weighted mean values for the entire winter. However, if snow is not permanently present on the ground through the winter and the snowmelt is sampled more often, the variability between locations becomes significant for the oxygen and hydrogen isotope composition. For all sampling events and the whole data set, nearly all of the variability is related to source of variance related to a particular group of wicks (e.g. within group variability).

Our results show that the isotope composition of snowmelt should be sampled using a relatively large number of wicks on site. In relatively homogeneous regions (e.g the same altitude, snow exposition and similar meteorological conditions) the variability among the different sampling sites is relatively small and makes only a small contribution to total variability.

Further work is needed to characterise the isotope composition of infiltrated melt water, particularly in karstic areas where snowmelt begins at different times, at different altitudes and it is often mixed with rain which blurs the snowmelt isotope signal in the runoff.

Acknowledgement. This study was financially supported by Slovenian Research Agency in the frame of basic research programmes (P1-0143, P1-0020), the EU Horizon 2020 project MASSTWIN (grant agreement No. 692241) and was part of IAEA CRP F3.20.06, the Slovenian subproject "Use of environmental isotopes in investigations of influence of snowmelt on stream runoff in the area of Julian Alps, NW Slovenia". We thank all who helped, particularly S. Žigon, J. Herič, M. Grm, J. Hictaler, R. Rudolf, for their invaluable assistance with field sampling and laboratory work. We also acknowledge fruitful discussions with IAEA CRP partners during the meetings and thank the staff of the Isotope Hydrology Section at IAEA for assistance during the project, including providing the fiberglass rope (used for PCS experiment) and for the stable hydrogen analyses. Sincere thanks to David J. Heath for linguistic corrections.

REFERENCES

ARSO, 2017. Monthly bulletin Naše okolje. Ministry of the Environment and Spatial Planning, Slovenian Environment Agency [http://www.arso.gov.si/o%20agenciji/knji%C5%BEnica/mese%C4%8Dni%20bilten/]. Accessed 11.6.2017.

Bavay, M., Grünewald, T., Lehning, M., 2013. Response of snow cover and runoff to climate change in high Alpine catchments of Eastern Switzerland. Advances in Water Resources, 55, 4–16.

Brenčič, M., Vreča, P., 2016. Hydrogeological and isotope mapping of the karstic River Savica in NW Slovenia. Environmental Earth Sciences, 75, 651.

Dansgaard, W., 1964. Stable isotopes in precipitation. Tellus, 16, 436–468.

DeWalle, D.R., Rango, A., 2008. Principles of Snow Hydrology. Cambridge University Press, Cambridge, 410 p.

Dolinar, M., Frantar, P., Kurnik, B., 2008. The characteristics of the water balance of Slovenia in the period 1971−2000. In: Proc. Mišičev vodarski dan 2008, pp. 19–25 (In Slovenian.)

Engel, M., Penna, D., Bertoldi G., Dell'Agnese, A., Soulsby, C., Comiti, F., 2016. Identifying run-off contributions during melt-induced run-off events in a glacierized alpine catchment. Hydrological Processes, 30, 343–364.

Fayad, A., Simon Gascoin, S., Faour, G., López-Moreno, J.I., Drapeau, L., Le Page, M., Escadafal, R., 2017. Snow hydrology in Mediterranean mountain regions: A review. Journal of Hydrology, 551, 374–396.

Frantar, P., Nadbath, M., Ulaga, F., 2008. Water balance impact factors. In: Water Balance of Slovenia 1971–2000. Ministrstvo za okolje in prostor, Agencija za okolje, Ljubljana, pp. 15–27.

Friedman, I., Benson, C., Gleason, J., 1991. Isotopic changes during snow metamorphism. In: Taylor, H.P., O'Neil, J.R., Kaplan, I.R. (Eds.): Stable Isotope Geochemistry. A Tribute to Samuel Epstein. Special Publication no. 3. Geochemical Society, San Antonio, TX, USA, pp. 211–221.

Frisbee, M.D., Phillips, F.M., Campbell, A.R., Hendrickx, J.M.H., 2010. Modified passive capillary samplers for collecting samples of snowmelt infiltration for stable isotope analysis in remote, seasonally inaccessible watersheds 1: Laboratory evaluation. Hydrological Processes, 24, 825–833.

Hohenwallner, D., Saulnier, G., Castaings, W., Astengo, A., Brenčič, M., Bruno, C., Carolli, M., Chenut, J., De Bona, A., Doering, M., Dutto, E., Freundl, G., Harum, T., Holzeis, F., Jamsek, A., Klemenčič-Kosi, S., Kopeinig, C., Kozel, R., Klug, H., Lascours, S., Maiolini, B., Mignone, N., Neuwirth, J., Paccard, P., Pascariello, A., Pergher, P., Poltnig, W., Pušenjak, M., Rampazzo, R., Reszler, C., Robinson, C., Rollando, A., Rosso, M., Salvaro, M., Schlamberger, J., Scussel, R., Siligardi, M., Suette, G., Valentar, V., Varolo, E., Vecellio, C., Wagner, K., Zadravec, D., Zalavari, P., Zessar, H., Zolezzi, G., Brancelj, A., Bertoncelj, I., Brun, A., Cadoux-Rivollet, M., Calvi, C., Defrancesco, C., Janetschek, H., Komma, J., Lachenal, P., Leskošek, T., Mezek, T., Mori, N., Mourembles, C., Rikanovic, R., 2011. Water Management in a Changing Environment. Strategies against Water Scarcity in the Alps. University of Savoie, Chambéry, 73 p.

Jeelani, G., Shah, R.A., Jacob, N., Deshpande, R.D., 2016. Estimation of snow and glacier melt contribution to Liddar stream in a mountainous catchment, western Himalaya: an isotopic approach. Isotopes in Environmental and Health Studies, 53, 18–35.

Jeelani, G., Shah, R.A., Deshpande, R.D., Fryar, A.E., Perrin, J., Mukherjee, A., 2017. Distinguishing and estimating recharge to karst springs in snow and glacier dominated mountainous basins of the western Himalaya, India. Journal of Hydrology, 550, 239–252.

Krajčí, P., Danko, M., Hlavčo, J., Kostka, Z., Holko, L., 2016. Experimental measurements for improved understanding and simulation of snowmelt events in the Western Tatra Mountains. Journal of Hydrology and Hydromechanics, 64, 316–328.

Lee, J., Feng, X., Faiia, A.M., Posmentier, E.S., Kirchner, J.W., Osterhuber, R., Taylor, S., 2010. Isotopic evolution of a seasonal snowcover and its melt by isotopic exchange between liquid water and ice. Chemical Geology, 270, 126–134.

Massone, H., Martinez, D., Vich, A., Londoño, M.Q., Trombotto, D., Grondona, S., 2016. Snowmelt contribution to the sustainability of the irrigated Mendoza's Oasis, Argentina: an isotope study. Environmental Earth Sciences, 75, 520.

Mankin, J.S., Viviroli, D., Singh, D., Hoekstra, A.Y., Diffenbaugh, N.S., 2015. The potential for snow to supply human water demand in the present and future. Environmental Research Letters, 10, 114016.

Moser, H., Stichler, W., 1974. Deuterium and oxygen-18 contents as an index of the properties of snow covers. International Association of Hydrological Sciences Publication, pp. 122–135.

N'da, A.B, Bouchaou, L., Reichert, B., Hanich, L., Ait Brahim, Y., Chehbouni, A., Beraaouz, E.H., Michelot, J.L., 2016. Isotopic signatures for the assessment of snow water resources in the Moroccan high Atlas mountains: contribution to surface and groundwater recharge. Environmental Earth Sciences, 75, 755.

Nadbath, M., 2012. Meteorološka postaja Zgornja Radovna. Naše okolje, Bilten Agencije RS za okolje, XIX, pp. 1–5.

Ogrinc, N., Kanduč, T., Stichler, W., Vreča, P., 2008. Spatial and seasonal variations in $\delta^{18}O$ and δD values in the river Sava in Slovenia. Journal of Hydrology, 359, 303–312.

Ortar, J., Volk Bahun, M., Pavšek, M., Sinjur, I., Vertačnik, G., Brenčič, M., Polajnar, D., Sokratov, S.A., Vreča, P., 2013. Physical and isotopic chatacteristics of snowpack in NW Slovenia. International Snow Science Workshop Grenoble – Chamonix Mont-Blanc, pp. 65–68.

Penna, D., Ahmad, M., Birks, S.J., Bouchaou, L., Brenčič, M., Butt, S., Holko, L., Jeelani, G., Martínez, D.E., Melikadze, G., Shanley, J.B., Sokratov, S.A., Stadnyk, T., Sugimoto, A., Vreča, P., 2014. A new method of snowmelt sampling for water stable isotopes. Hydrological Processes, 28, 5637–5644.

Penna, D., Zuecco, G., Crema, S., Trevisani, S., Cavalli, M., Pianezzola, L., Marchi, L., Borga, M., 2017. Response time and water origin in a steep nested catchment in the Italian Dolomites. Hydrological Processes, 31, 768–782.

Pomeroy, J.W., Brun, E., 2001. Physical properties of snow. In: Jones, H.G., Pomeroy, J.W., Walker, D.A., Hoham, R.W. (Eds.): Snow Ecology: An Interdisciplinary Examination of Snow-Covered Ecosystems. Cambridge University Press, Cambridge, UK, pp. 45–118.

Searle, S.R., Casella, G., Culloch, C.E., 2006. Variance Components. John Wiley & Sons, 501 p.

Sokratov, S.A., Golubev, V.N., 2009. Snow isotopic content change by sublimation. Journal of Glaciology, 55, 823–828.

Torkar, A., 2016. Analysis of groundwater outflow through springs in fluvioglacial intergranular aquifers. PhD Thesis. University of Ljubljana, 135 p.

Torkar, A., Brenčič, M., Vreča, P., 2016. Chemical and isotopic characteristics of groundwater-dominated Radovna River (NW Slovenia). Environmental Earth Sciences, 75, 1296.

Viviroli, D., Weingartner, R., 2004. The hydrological significance of mountains: from regional to global scale. Hydrology and Earth System Sciences, 8, 1016–1029.

Viviroli, D., Archer, D.R., Buytaert, W., Fowler, H.J., Greenwood, G.B., Hamlet, A.F., Huang, Y., Koboltschnig, G., Litaor, M.I., López-Moreno, J.I., Lorentz, S., Schädler, B., Schreier, H., Schwaiger, K., Vuille, M., Woods, R., 2011. Climate change and mountain water resources: overview and recommendations for research, management and policy. Hydrology and Earth System Sciences, 15, 471–504.

Vreča, P., Brenčič, M., Sinjur, I., Vertačnik, G., Volk, M., Ortar, J., Torkar, A., Stibilj, V., Pavšek, M., 2013. The isotopic composition of precipitation and snow in the area of the Julian Alps and the Karavanke. In: Kuhar, M. (Eds.): Proc. 18. strokovno srečanje Slovenskega združenja za geodezijo in geofiziko Raziskave s področja geodezije in geofizike 2012. Fakulteta za gradbeništvo in geodezijo, Ljubljana, pp. 17–25. (In Slovenian.)

Weber, M., Bernhardt, M., Pomeroy, J.W., Fang, X., Härer, S., Schulz, K., 2016. Description of current and future snow processes in a small basin in the Bavarian Alps. Environmental Earth Sciences, 75, 1223.

Received 7 August 2017
Accepted 5 February 2018

J. Hydrol. Hydromech., 67, 2019, 1, 41–48
DOI: 10.2478/johh-2018-0018

Seasonal subsurface water contributions to baseflow in the mountainous Uhlířská catchment (Czech Republic)

Martin Šanda*, Tomáš Vitvar, Jakub Jankovec

Department of Irrigation, Drainage and Landscape Engineering, Faculty of Civil Engineering, Czech Technical University in Prague, Thákurova 7, 166 29 Prague 6, Czech Republic.
* Corresponding author. E-mail: martin.sanda@fsv.cvut.cz

Abstract: Nine years of seasonal $\delta^{18}O$ values in precipitation, soilwater and groundwater were evaluated in the Uhlířská catchment between 2008 and 2016 and recharge winter/summer ratios were calculated using $\delta^{18}O$ values. The longterm average ^{18}O content in groundwater is lower than the mean weighted ^{18}O content in precipitation. This is explained by more than 50% of winter- and snowmelt- induced groundwater recharge that occurs in all years except of 2010 and 2013. The recharge of the peat organic soil water is balanced between summer and winter, whereas the mineral hillslope soil is dominantly recharged by summer precipitation. The 67% portion of baseflow, dominantly generated in the winter season, is composed of groundwater and peat organic soil water, according to the hydrochemical distribution of runoff components. Isotopic mass balance of individual winters shows that precipitation in warmer winters is entirely transformed into outflow until the end of the winter season, generating no significant water storage for potential drought periods.

Keywords: ^{18}O isotope; Precipitation; Soil water and groundwater; Snowmelt/recharge ratios; Winter; Summer.

INTRODUCTION

The relation between snowmelt and groundwater recharge in catchments remains poorly understood. The role of groundwater in runoff generation (Sayama et al., 2011) and baseflow (Fenicia et al., 2006) is generally recognized and assessed in terms of temporally invariable tracer-derived groundwater residence times (McDonnell et al., 2010) and their links to spatial distribution of various geological, topographical and landscape characteristics (Cody Hale and McDonnell, 2016; Dóša et al., 2011; Soulsby et al., 2010). However, little has been carried out to understand the role of snowmelt in the groundwater recharge and, conversely, in the hydrological drought. This topic has become more popular in the hydrological research over the past years, being widely recognized crucial in the context of climate-induced shifts of the hydrological cycle and groundwater recharge (Van Loon and Laaha, 2015).

Despite these efforts, the spatial and temporal variability of snowmelt-induced groundwater recharge remains poorly understood. One of the reasons is that the simultaneous monitoring of snowmelt, runoff and groundwater and its isotopic or other tracer characteristics in catchments has been rare. The vast majority of catchment studies has considered the isotopic average content in streamwater as a catchment-average value, that is nearly equal to annual isotopic average content in precipitation and presumably also to the average isotopic content in groundwater. These assumptions are, however, rarely met; instead, the isotopic variations in streamwater often indicate catchment water residence times (Hrachowitz et al., 2009; Pfister et al., 2017) biased toward the faster runoff components, poorly addressing the residence time of the groundwater components (Kirchner, 2016).

The difference between average isotopic values of precipitation, streamwaters and groundwaters is very variable in time and space. It is widely accepted that groundwater recharge in temperate regions is generally stronger towards winter and snowmelt periods. Various studies (Earman et al., 2006; Penna et al., 2014) have revealed that more than 50% of recharge is generated by snowmelt. The strong contribution of snowmelt to groundwater in cold-temperate catchments has been also highlighted in stable isotope applications over the past decades to intuitively explain groundwaters depleted in ^{18}O and ^{2}H (Maulé et al., 1994; O'Driscoll et al., 2005; Šanda et al., 2014). In turn, the isotopically depleted groundwater recharge in tropical regions is typically explained by isotopic amount effect (Demlie et al., 2007; Lapworth et al., 2013) or paleoclimatic conditions (Jasechko et al., 2015). In an arid catchment, Turner et al. (1987) observed that the average stable isotope values in groundwater match the average values in streamwater. Reddy et al. (2006) have identified various site-specific relations between average isotopic values in streamwater and groundwater that were linked to various direct interactions between streamwater and groundwater. Darling et al. (2003) identified a winter-dominant groundwater recharge in sandstones, resulting in a depleted average isotopic content on groundwater compared to streamwater. In contrast, chalk aquifers did not show any winter groundwater recharge bias, presumably due to limited percolation of winter precipitation and snowmelt-induced water to recharge.

To assess the winter-summer groundwater recharge variations, Jasechko et al. (2014) have analyzed the long-term average spatial distribution of the isotope-derived groundwater recharge rates over a large set of Canadian and some selected worldwide catchments. They have proven that the isotopic groundwater depletion in the majority of temperate-humid catchments was dominantly associated with recharge of winter precipitation. However, little understanding exists of the temporal (annual and decadal) changes in the snowmelt induced groundwater recharge. This paper therefore explains, using readily available isotopic data in precipitation and groundwater, the seasonality of groundwater recharge in the well-instrumented mountainous catchment Uhlířská, over the 9-year period 2008–2016. The study is also part of the trinational initiative aimed at the snowmelt-recharge-drought assessment (Zappa et al., 2015).

STUDY SITE

The Uhlířská catchment is located in the Jizera Mountains near the northern border of the Czech Republic. Focus in this study is given to its subcatchment at the Porsche gauge profile (Fig. 1). It is a small (1,18 km^2) forested granitic headwater catchment with average altitude 822 m a.s.l. in cold humid climate, characterized by mean annual precipitation amount of 1300mm and mean annual temperature 4.7°C (Hrnčíř et al., 2010). Mineral soil hillslopes cover approximately 90% of the catchment area and their 0.6 - 0.9 m thick soil profile consists of highly permeable Dystric Cambisols, Podzols or Cryptopodzols (Nikodem et al., 2013). Wetlands along the stream course are formed by Histosol soil types. They are up to 3 m deep, with permeability values substantially lower as compared to the soils on the hillslopes (Šanda et al., 2014). Wetlands are located on a layer of sediments deposited in the catchment valley with a various depth reaching up to 50 m proven by geoelectrical resistivity measurements along the valley bottom and in perpendicular hillslope profiling. A more detailed recent description of the Uhlířská catchment can be also found in Šanda et al. (2014), Vitvar et al. (2016), Votrubova et al. (2017) and Jankovec et al. (2017).

Studies at Uhlířská using long term stable isotopes measurements (^{18}O) along with analysis of diluted SiO_2 proved that the wetland is predominantly groundwater-supplied, as its SiO_2 concentration is close to the range of SiO_2 concentration in the perennial groundwater (Šanda et al., 2014). Water in stream is partly supplied also with the event water component (direct flow), which is quickly transferred via upslope saturated soil-weathered bedrock interface. Recent works at Uhlířská revealed that the BFLOW approach to separate runoff components delivered about 67% of baseflow (Šanda et al, 2014), which corresponds with the inverse hydrochemical modelling approach NETPATH (Vitvar et al., 2016). This approach was employed in three scenarios on the October 2015 dataset, characterizing hydrological conditions close to the average discharge of about 38 l/s at the Porsche gauge profile. Carbon, sodium and ^{18}O were selected as model constraints in the mixing of initial waters (rain, mineral soils, peat soils, and wetland groundwater) towards the streamflow. The most reliable scenario distributed the runoff contributions among the wetland groundwater (28%), peat (42%) and mineral soil (23%) water and 7% rainfall. The sum of wetland groundwater and peatwater (about 70%) can be therefore considered as baseflow amount, corresponding to the 67% obtained by the discharge data approach BFLOW (Šanda et al., 2014; Vitvar et al., 2016).

MATERIAL AND METHODS

This study used ^{18}O data measured between the hydrological years 2008 and 2016 in precipitation, hillslope pore soil water (Cambisols, Podzols and Cryptopodzols) (further denoted as mineral soil water), valley peat pore soil water (Histosols) (further denoted as peatwater), shallow groundwater and streamwater. Soil water and groundwater is manually sampled in 1–2 month interval throughout the whole year, whereas streamwater is sampled weekly manually in winter period excluding snowmelt time (November–February/March). Streamflow is sampled once a day at midnight at low flows or every 6 hours (4times a day) during high flows (summer stormflow and snowmelt period, i.e. February/March–October) by carousel samplers at the Porsche profile (Fig. 1). Downslope Histosols and upslope Cambisols/Podzols in young and mature forest are instrumented with total of4pairs of suction cups (each pair of 30 and 60 cm depth), at two sites each (Fig. 1 shows pore water and ground water in one symbol due to their vicinity). The suction cups are emptied (vacuum of 600-700 mbar is applied for 24 hours) and closed. At the sampling time, they are depressurized and accumulated water sample are collected. Four shallow boreholes (2.4-5.2 m deep) of 40-50 mm in diameter are sampled is sediments below the Histosols. Boreholes are close to each other (distance below 50 m) along the mild hillslope transect covered by Histosols. Due to their low yield, the boreholes are fully emptied by peristaltic vacuum pump (maximum of 5 minute pumping) and left for 24 hours to refill. They are finally sampled with the same vacuum pump.

Monthly liquid total precipitation samples are collected manually by means of 24 cm wide funnel directed to 50 liter container located partly in the soil subsurface. A thin film of light oil is applied to prevent evaporation of collected precipitation. Solid precipitation is sampled manually in two replicates as weekly and monthly sample in two 10 cm wide and 100 cm long cylinders raised to 3 m height above the soil surface. The monthly ^{18}O contents in precipitation and streamwater are included in the global monitoring databases of stable isotopes in precipitation GNIP (IAEA/WMO, 2017) and in rivers GNIR (IAEA, 2017). The $\delta^{18}O$ values in water samples were obtained by means of the Czech Technical University in Prague (CTU) laser water isotope analyzer.

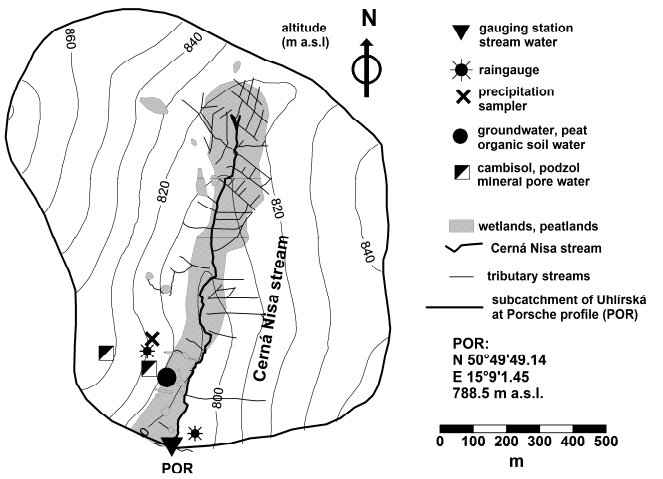

Fig. 1. The Uhlířská-Porsche catchment with location of sampling stations.

The isotope sampling in the Uhlířská catchment is supported by a wide hydrometeorological monitoring that was established in the 1980´s. The runoff gauge Porsche is gauging 2/3 of whole Uhlířská catchment (i.e. 1.18 km^2) and it is equipped with 120 degree open V-notch sensed by pressure transducer in 10 minute interval.

The $\delta^{18}O$ data interpretation was based on seasonal grouping of monthly $\delta^{18}O$ values from the principal compartments. The recharge index (after Jasechko et al., 2014) is expressed as

$$\frac{\left(R/P\right)_{winter}}{\left(R/P\right)_{summer}} = \frac{\left(\frac{\delta_{terrestrial\,(annual)} - \delta_{precip.(summer)}}{\delta_{precip.(annual)} - \delta_{precip.(summer)}}\right)}{\left(\frac{\delta_{terrestrial\,(annual)} - \delta_{precip.(winter)}}{\delta_{precip.(annual)} - \delta_{precip.(winter)}}\right)} \quad (1)$$

where P is precipitation, R is runoff, *terrestrial* is consecutively used for groundwater, mineral soil pore water or peat organic pore water, and *summer* and *winter* are average values for the months May–October and November–April, respectively. We are aware that this approach does not consider intra-seasonal isotopic differences such as isotopic content of melting snow during various phases of the snowmelt process.

The baseflow amount at the Porsche profile for the period 2008–2016 was obtained by three approaches: BFLOW tool (digital filter approach), the monthly minimum approach and the Kliner-Kněžek approach. The approach BFLOW (Arnold et al., 1995) analyses the frequency spectrum of daily hydrographs, associating long waves with baseflow and high-frequency variability with direct run-off. The Kliner-Kněžek approach (Kliner and Kněžek, 1974) applies the relationship between stream discharge and groundwater level in the nearby borehole P20 (2 m deep). The baseflow amount was computed in absolute volume values for a 6 month-period and not in percentages of daily total flow. We are aware that the seasonal stream baseflow amount is not necessarily equal to seasonal groundwater recharge amount. In this study we consider baseflow as seasonally generated mixture of subsurface water components. It should be also noted that the three selected baseflow separation methods represent different approaches (Holko and Špánková, 2014): digital filter, simple statistics and more physically-based Kliner-Kněžek method, which all deliver non identical baseflow results. The eq. 1 was therefore applied for winter/summer recharge ratios, where R is the mean baseflow value of the three baseflow separation methods, accompanied by a corresponding band width of two sigma-values of standard deviations of the three methods.

The relations between the seasonal isotopic content of various groundwater compartments were also explored by the use of summation curves (isotopic mass curves). They sum up (over the winter period) the weighted isotopic content of precipitation, streamwater and groundwater, weighted by the respective runoff amount. The summation curves of precipitation sum the monthly precipitation amounts multiplied by the respective isotopic content, the streamflow summation curves sum the hourly runoff amounts multiplied by the respective streamwater isotopic content, (where weekly, daily or 6-hourly values of isotopes are linearly interpolated for respective streamflow data) and the baseflow summation curves sum the hourly runoff amounts multiplied by the respective groundwater isotopic content as its average for a given hydrological year. The latter therefore creates a summation curve of a hypothetical runoff formed only by groundwater. This concept is widely analogous to the typology of post-winter droughts developed by Van Loon et al. (2014), in our case presented through summation curves and additional isotope mass balance.

RESULTS AND DISCUSSION

Isotopic records in precipitation and groundwater

Table 1 presents the seasonal and annual precipitation, runoff and air temperature parameters for the period 2008–2016. It shows that although the winter precipitation (577 mm in average) contributes by less than 50% to the total annual precipitation (1318 mm on average), the winter precipitation is more sustainable and contributes substantially to runoff through subsurface water components. Three winter seasons (2008, 2009 and 2012) provide more than 650 mm of precipitation and can be therefore considered wet. Winter air temperature in the catchment is typically near the freezing point, however three warm winters (2008, 2014 and 2016) showed mean winter season air temperature values around 1 centigrade.

Table 1 also shows higher runoff coefficients in winter season (0.96) than in summer season (0.58). This reveals that groundwater storage and release are dominant in the winter season (in absence of winter evapotranspiration).

Average groundwater $\delta^{18}O$ values (–10.34‰) are overall more depleted in comparison to the downhill peat water (–9.96‰), uphill mineral soil water (–9.47‰) and the weighted precipitation (–10.06‰) (Fig. 2). It is assumed that this is caused by the groundwater recharge supplied dominantly from winter precipitation and snowmelt. Isotopically depleted winter precipitation in 2010 and 2011, however, cause that the average values of peat water and groundwater in 2011 are nearly identical (see also Table 2).

Table 1. Hydrological and climatic paramaters of hydrological years 2008–2016.

hydrological year	precipitation annual (mm)	precipitation winter (mm)	precipitation summer (mm)	precipitation winter (%)	precipitation summer (%)	day of max.snow water equivalent	max.snow water equivalent (mm)	runoff annual (mm)	runoff winter (mm)	runoff summer (mm)	runoff coef. annual	runoff coef. winter	runoff coef. summer	air terperature annual	air temperature winter	air temperature summer
2008	1256	685	572	0.54	0.46	1.2.	196	917	673	244	0.73	0.98	0.43	6.52	1.75	11.29
2009	1390	658	732	0.47	0.53	27.2.	486	1090	603	487	0.78	0.92	0.66	5.15	–0.49	10.79
2010	1643	472	1171	0.29	0.71	19.3.	274	1224	459	765	0.74	0.97	0.65	4.59	–1.50	10.69
2011	1465	573	892	0.39	0.61	18.4.	169	1149	585	564	0.78	1.02	0.63	5.38	–0.78	11.55
2012	1384	777	607	0.56	0.44	29.2.	462	1025	712	314	0.74	0.92	0.52	5.52	–0.52	11.56
2013	1630	629	1001	0.39	0.61	2.4.	310	1295	570	725	0.79	0.91	0.72	4.92	–1.49	11.33
2014	996	404	592	0.41	0.59	27.3.	78	767	413	354	0.77	1.02	0.60	5.87	1.39	10.35
2015	803	439	364	0.55	0.45	15.1.	196	575	414	161	0.72	0.94	0.44	6.06	0.29	11.84
2016	1294	557	737	0.43	0.57	17.2.	127	912	518	393	0.70	0.93	0.53	6.32	0.93	11.71
average	**1318**	**577**	**741**	**0.45**	**0.55**		**255**	**995**	**550**	**445**	**0.75**	**0.96**	**0.58**	**5.59**	**–0.05**	**11.23**

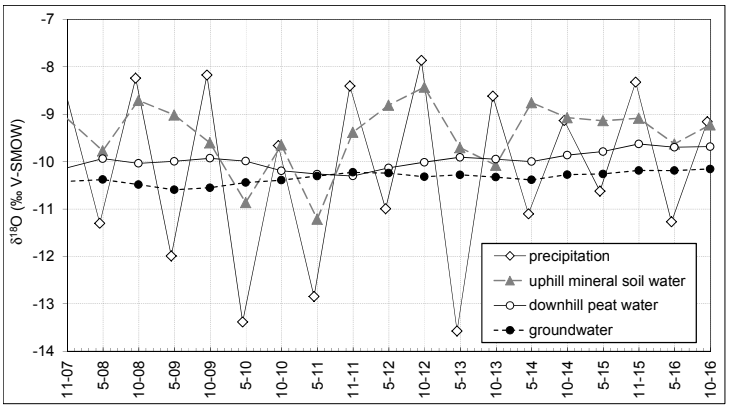

Fig. 2. Stable isotopes of oxygen in various catchment compartments (6-month averages).

Table 2. Isotope signatures of precipitation, groundwater, mineral soil pore water, organic-peat pore water, of hydrological years 2008–2016.

hydrological year	$\delta^{18}O$ precipitation annual (‰ V-SMOW)	$\delta^{18}O$ precipitation winter (‰ V-SMOW)	$\delta^{18}O$ precipitation summer (‰ V-SMOW)	$\delta^{18}O$ groundwater annual (‰ V-SMOW)	$\delta^{18}O$ groundwater winter (‰ V-SMOW)	$\delta^{18}O$ groundwater summer (‰ V-SMOW)	$\delta^{18}O$ mineral soil pore water annual (‰ V-SMOW)	$\delta^{18}O$ organic peat water annual (‰ V-SMOW)
2008	–9.91	–11.30	–8.24	–10.43	–10.38	–10.49	–9.24	–9.98
2009	–9.98	–11.99	–8.18	–10.57	–10.59	–10.55	–9.40	–9.96
2010	–10.73	–13.38	–9.66	–10.42	–10.44	–10.39	–10.31	–10.08
2011	–10.14	–12.85	–8.41	–10.26	–10.30	–10.23	–10.28	–10.28
2012	–9.62	–11.00	–7.86	–10.28	–10.24	–10.32	–8.66	–10.08
2013	–10.53	–13.57	–8.62	–10.31	–10.28	–10.33	–9.93	–9.93
2014	–9.93	–11.10	–9.14	–10.33	–10.39	–10.28	–8.86	–9.92
2015	–9.58	–10.62	–8.32	–10.22	–10.26	–10.19	–9.11	–9.71
2016	–10.07	–11.27	–9.16	–10.17	–10.19	–10.16	–9.43	–9.69
average	**–10.06**	**–11.86**	**–8.60**	**–10.34**	**–10.35**	**–10.33**	**–9.47**	**–9.96**

Fig. 3 reveals the differences in the isotopic composition of precipitation in relation to their signal in the subsurface water components. A decrease of the isotopic content of summer precipitation and an increase of the isotopic content of winter precipitation can be observed. This may cause the general isotopic enrichment of all subsurface water components over the 9-year period. The difference in the isotopic composition of summer and winter uphill soil water in the years 2010 and 2011 is caused by the abundant summer precipitation in 2010 followed by isotopically very depleted winter precipitation. These two winters were the only cases within the entire 9 year-period where uphill soil water was isotopically more depleted than groundwater (Fig. 3a). These effects led to the differences in 2010 and 2011 (Fig. 3b), whereas the overall low isotopic values in the peat water in 2011 seem to be the consequence of the mixing of these isotopically depleted waters in the deeper peat horizon (Fig. 3c). In turn, the groundwater carries also isotopic signals of longer memories, which may explain the low values in 2009 that have no obvious background in the recent-to-date precipitation values.

Seasonal and annual isotopic differences and ratios

Table 2 provides seasonal $\delta^{18}O$ values of groundwater, mineral soil water, peat water and precipitation. Based on these data, Fig. 4 exhibits the difference between summer and winter precipitation isotopic compositions from the 9 winters. The difference between summer (April to September) and winter (October to March) $\delta^{18}O$ values is between 2 and 5‰ V-SMOW from the annual mean and it is negatively correlated with the amount-weighted $\delta^{18}O$ values in precipitation (annual). Jasechko et al. (2014) found similar differences for a worldwide set of catchments, stating that the difference around 5‰ V-SMOW in between summer and winter $\delta^{18}O$ values in precipitation is typical for isotopically depleted precipitation in the extratropics, whereas the difference around 2‰ V-SMOW is typical for tropical areas. Our study shows, however, that a catchment can exhibit the full spectrum of winter-summer differences within a decade. The difference between summer (May to October) and winter (November to April) $\delta^{18}O$ is about 5‰ for the coldest years with most depleted annual precipitation, and about 2‰ V-SMOW for months with isotopically more enriched precipitation.

No correlation was found between the annual groundwater - precipitation isotopic difference and shallow groundwater (Fig. 5). This difference is typically negative, showing that for most of the time the mean isotopic content in groundwater is lower than in precipitation. This occured in seven out of nine years where the isotopic content of groundwater oscilled between –10.1‰ and –10.6‰ V-SMOW. It shows the dominance of the groundwater winter isotopic content regardless of the isotopic composition of groundwater in particular years. Similar trend can be observed in the peatwater, highlighting that the isotopic differences between peatwater and precipitation do not depend on the annual mean isotope average. In contrast, the difference mineral soil water - precipitation is related ($R^2 = 0.63$) to the annual isotopic content of the mineral soil water, revealing that the mineral soilwater can be used as proxy for the annual long-term amount-weighted isotopic composition of precipitation in the Uhlířská catchment.

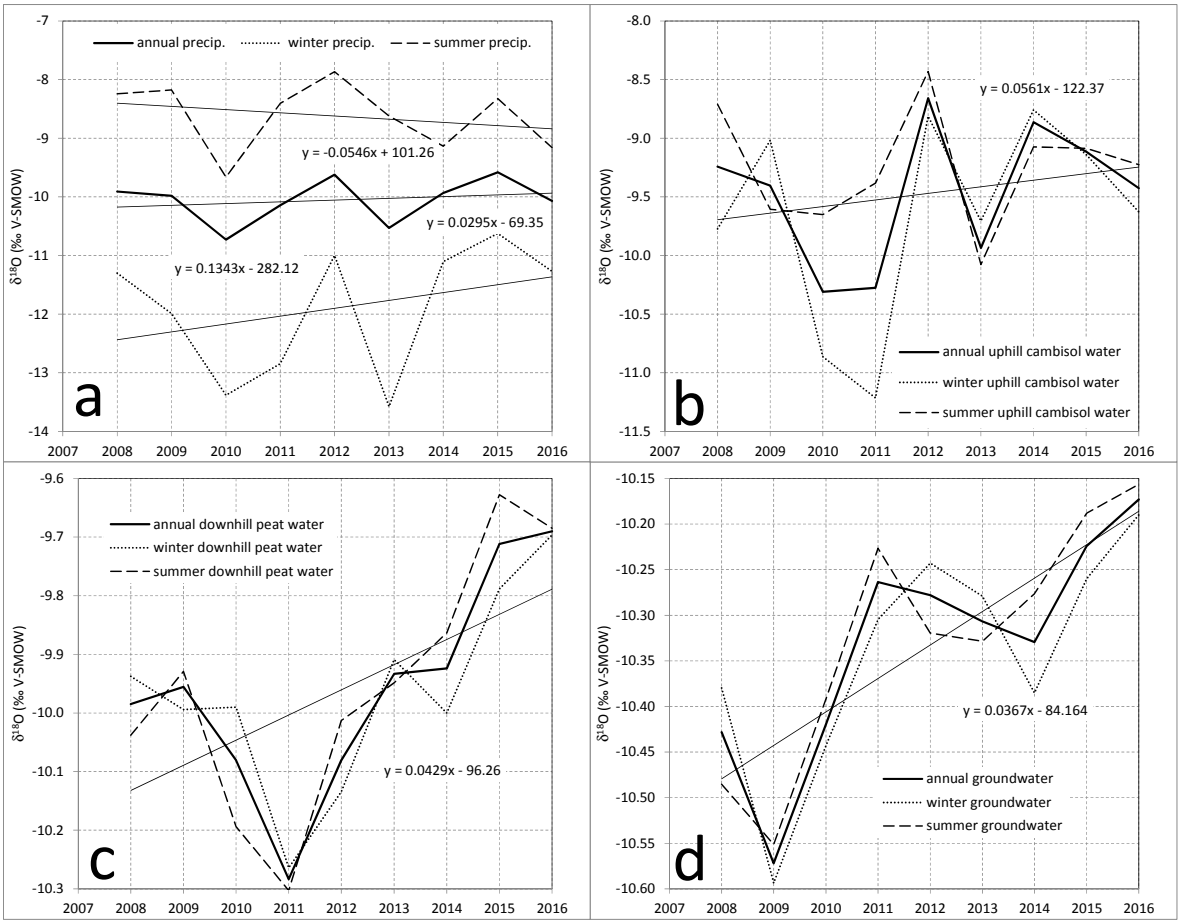

Fig. 3. abcd (from top left to bottom right) – Stable isotopes of oxygen in precipitation (a), uphill mineral soil (Cambisol or Podzol) water (b), downhill peat water (c) and shallow groundwater (d) (6-month averages: summer: May–Oct, winter: Nov–Apr and 12 months averages Nov–Oct of hydrological year). Note the different scales on the y-axes.

Table 3. Recharge ratios by isotope and hydrological hydrograph separation methods of hydrological years 2008–2016. Groundwater represents average of four shallow wells (2.7–5.2 m deep) according to fig. 1 in the valley, where groundwater discharges from the aquifer, sampled in 1-2 month intervals and averaged for 12 months (or 6 summer/6 winter months, thus average of maximum of 48 values or 24 values respectively).

hydrological year	recharge/precipitation in winter/summer ratio for groundwater by isotopes (–)	recharge/precipitation in winter/summer ratio for organic soil pore water by isotopes (–)	recharge/precipitation in winter/summer ratio for mineral soil pore water by isotopes (–)	recharge/precipitation in winter/summer ratio for baseflow by hydrograph separation: average of 3 methods (–)	recharge/precipitation in winter/summer ratio for baseflow by hydrograph separation: average of 3 methods - 1σ interval (–)	recharge/precipitation in winter/summer ratio for baseflow by hydrograph separation: average of 3 methods + 1σ interval (–)
2008	2.09	1.11	0.41	1.89	1.36	2.37
2009	1.88	0.97	0.53	1.25	0.97	1.44
2010	0.63	0.31	0.52	1.05	0.92	1.14
2011	1.12	1.14	1.13	1.28	1.07	1.42
2012	2.62	1.89	0.27	1.64	1.09	2.03
2013	0.82	0.58	0.58	0.93	0.86	0.97
2014	2.26	0.98	–0.18	1.30	1.07	1.45
2015	3.94	1.26	0.43	1.52	1.29	1.68
2016	1.22	0.19	0.19	1.28	1.01	1.44
average	**1.84**	**0.94**	**0.43**	**1.35**	**1.07**	**1.55**

Table 3 also shows the relative winter/summer recharge index calculated using Eq. (1) for the groundwater, peat water and hillslope water through the period 2008–2016. It reveals that the winter groundwater recharge was always greater than the summer recharge (index greater than 1), except for the years 2010 and 2013 with highly abundant summer precipitation (more than 1000 mm). This result (Fig. 6a) therefore underlines the overall winter dominance of isotopically depleted groundwater recharge, as reported by Jasechko et al. (2014) in non-tropical areas. Other catchment compartments show a more (hillslope mineral soil water, summer groundwater recharge bias in 8 years out of 9) or less (peat soil water, summer groundwater recharge bias in 5 years out of 9) substantial tendency to dominant summer recharge. Fig. 6a also shows the winter/summer recharge ratio in form of a winter/summer relation of baseflow volumes averaged from three approaches

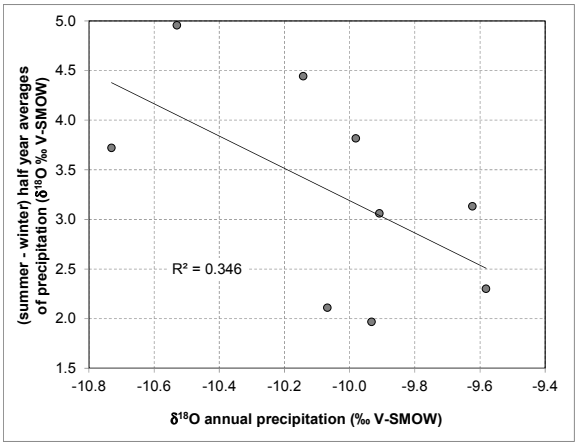

Fig. 4. Absolute value of difference in between precipitation-weighted $\delta^{18}O$ differences of summer and winter half years (May–October and November–April) for the period of 2008–2016.

(BFLOW, monthly minima and Kliner-Kněžek). This relation is almost entirely greater than 1, indicating the winter dominance of groundwater on baseflow. Fig. 6b compares the winter/summer baseflow ratio from Fig. 6a with a combined winter/summer recharge ratio, composed by a combination of three isotopic winter/summer recharge ratios calculated using Eq. (1) – wetland groundwater, peat organic soil water and mineral soil water. Best combination of these three isotopic winter/summer recharge ratios was identified, that delivered the baseflow R value in Eq. 1 as close as possible to the mean winter/summer baseflow ratios determined by the three separation methods and also to the 2σ intervals of three annual baseflow ratios obtained by the same approach. This procedure was employed each year (Table 3). It is obvious that the annual winter/summer ratios of the baseflow indicating the mean and 2σ intervals are not symmetric to the mean, because those ratios are determined independently for each year. The resulting contributions yield 29% (25%–34% as 2σ interval of three baseflow separation methods) ofthe isotopic content of groundwater, 50% of peat organic soil water (41%–63% as 2σ) and 22% (3%–33% as 2σ) of hillslope mineral soil water. As described in Vitvar et al. (2016), the NETPATH approach distributed the runoff contributions among the groundwater (28%), peat water (42%) and mineral hillslope soil with rainfall (30%) (combination of mineral soil hillslope water (23%) and rainfall (7%)) (Vitvar et al., 2016).

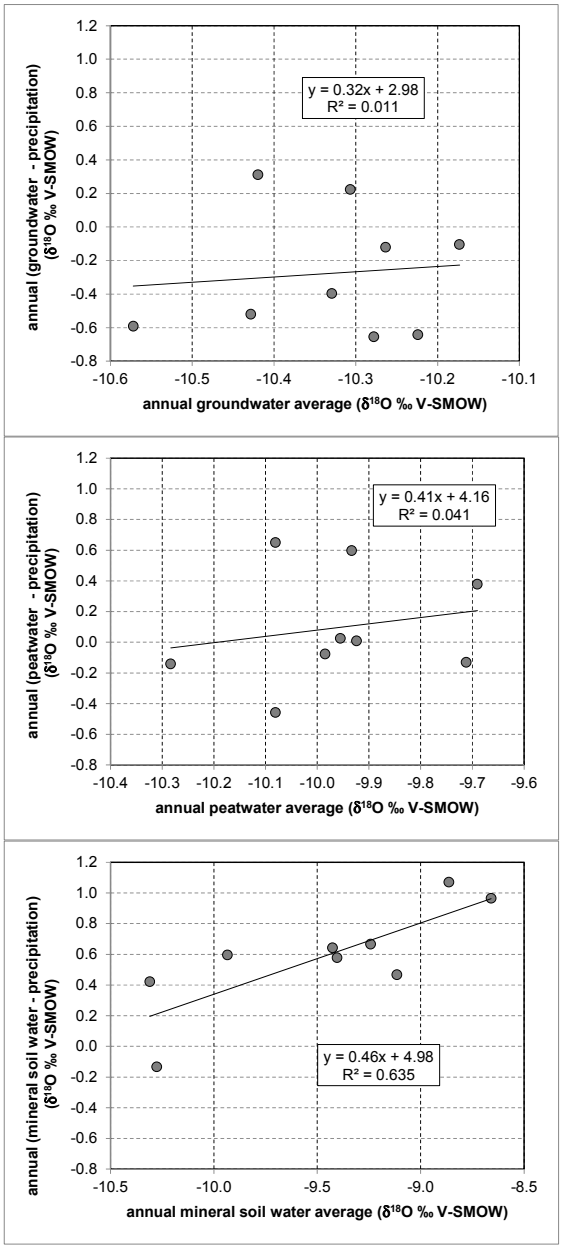

Fig. 5. Difference in the isotopic composition of groundwater, peatwater and mineral soil water and the amount-weighted precipitation for the years 2008–2016.

Isotopic summation curves

Fig. 7 depicts nine occasions of the snowmelt-runoff-recharge relationship, characterized by summation curves (isotopic mass curves) of precipitation, streamflow and baseflow. The computed summation curves show that all nine winters are grouped along the relative criteria Wetter, Drier, Colder, Warmer. Colder winters show rapid increase of the isotopic mass balance of streamflow caused by the onset of one or two distinct snowmelt periods (mid-March 2010, end of December 2012 and begin of April 2013, and end of February 2012). Milder and drier winters (for example, 2013/2014) exhibit largely parallel summation curves of precipitation and streamflow, indicating that the accumulated isotopic mass flows out in the same winter. Colder and wetter winters also show greater difference between the sum of isotopic masses in baseflow and in precipitation at the end of the winter (for example, 2011/2012), due to the accumulated isotopic mass in precipitation. The accumulated isotopic mass in precipitation is typically greater than the accumulated mass in streamwater. This shows that the winter precipitation discharged into the stream not only during, but also after snowmelt periods. The accumulation of isotopic mass in baseflow in all types of winters is sustainable and does not show any particular differences. In contrast, in a mild winter with low precipitation amounts such as 2013/2014 the isotopic mass balance at the end of the winter is closed, revealing that the winter precipitation is completely transformed into outflow during the same winter period.

CONCLUSIONS

The study has demonstrated that the nearly 10-year isotope monitoring in the Uhlířská catchment delivers significant information on how different amounts and temporal distributions of winter accumulation and release affect the subsurface water transition and storage in mineral soil, peat and ground-

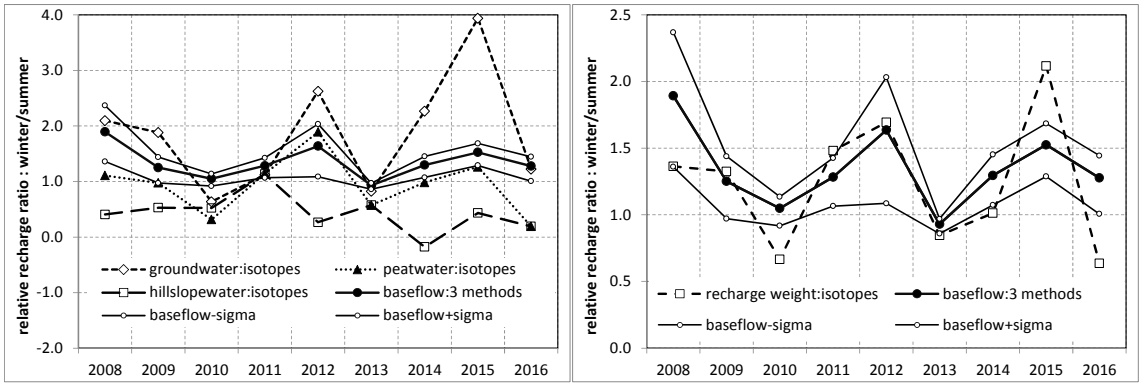

Fig. 6. a) (left) Annual relative ^{18}O- recharge ratios winter/summer in groundwater, peatwater and hillslope soilwater. Also included are the stream baseflow winter/summer ratios obtained as average of three methods: separation software BFLOW, monthly minimum approach and Kliner-Kněžek approach b) (right) Stream baseflow winter/summer ratios obtained by the three abovementioned approaches and stream baseflow winter/summer recharge ratios obtained by weighting the baseflow components (hillslope, peatwater and groundwater) by the identified in the isotopic approach. Plus a minus sigma denote the annual relative recharge ratios winter/summer standard deviations from the mean value of the three baseflow separation methods.

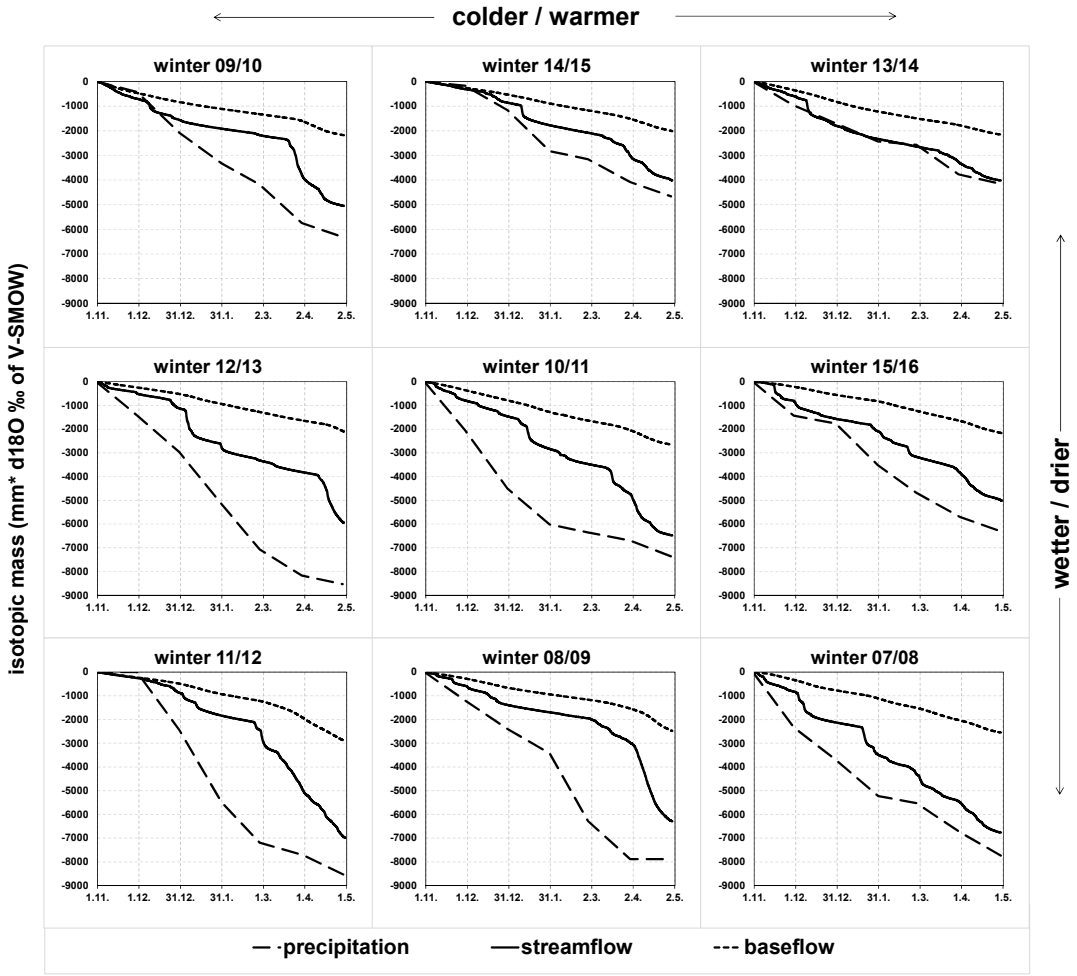

Fig. 7. Summation curves of isotopic mass across the winter season (November – April) for precipitation, streamflow and baseflow.

water. It also showed that the readily available approaches such as recharge ratios or baseflow separation can explain not only the spatial, but also the seasonal distribution of recharge patterns in a catchment. These approaches also explain why the average ^{18}O content in groundwater at Uhlířská remains below the ^{18}O content in streamwater. Although the overall isotopic composition tendency highlights the winter precipitation accumulation as the principal origin of the baseflow, a detailed examination of nine winters reveals several types of winters characterized by individual isotopic patterns and potential water storage for summer drought periods. Because the applied approaches require a monthly isotopic monitoring of various types of subsurface waters, they can be presently used only in a limited number of catchments.

Acknowledgement. This contribution is supported by Swiss National Foundation Scopes IZ73Z0_152506 and Czech Science Foundation 16-05665S.

REFERENCES

Arnold, J.G., Allen, P.M., Muttiah, R., Bernhardt, G., 1995. Automated baseflow separation and recession analysis techniques. Ground Water, 33, 1010–1018.

Cody Hale, V., McDonnell, J.J., 2016. Effect of bedrock permeability on stream base flow mean transit time scaling relations: 1. A multiscale catchment intercomparison. Water Resour. Res., 52, 1358–1374.

Darling, W.G., Bath, A.H., Talbot, J.C., 2003. The O&H stable isotopic composition of fresh waters in the British Isles. 2. Surface waters and groundwater. Hydrol. Earth Syst. Sci., 7, 2, 183–195.

Demlie, M., Wohnlich, S., Gizaw, B., Stichler, W., 2007. Groundwater recharge in the Akaki Catchment, Central Ethiopia: Evidence from Environmental Isotopes ($\delta^{18}O$, $\delta^{2}H$ and ^{3}H) and chloride mass balance. Hydrol. Proc., 21, 807–818.

Dóša, M., Holko, L., Kostka, Z., 2011. Estimation of the mean transit times using isotopes and hydrograph recessions. Die Bodenkultur, 62, 47–52.

Earman, S., Campbell, A.R., Phillips, F.M., Newman, B.D., 2006. Isotopic exchange between snow and atmospheric water vapor: Estimation of the snowmelt component of groundwater recharge in the southwestern United States. J. Geophys. Res., 111 D09302. DOI:10.1029/2005JD006470.

Fenicia, F. Savenije, H.H.G., Matgen, P., Pfister, L., 2006. Is the groundwater reservoir linear? Learning from data in hydrological modelling. Hydrol. Earth Syst. Sci., 10, 139–150.

Holko, L., Špánková, D., 2014. Základný odtok v horskom povodí Jaloveckého potoka v hydrologických rokoch 1988–2013. Acta Hydrologica Slovaca 15, 2, 229–237.

Hrachowitz, M., Soulsby, C., Tetzlaff, D., Dawson, J.J.C., Malcolm, I.A., 2009. Regionalization of transit time estimates in montane catchments by integrating landscape controls. Water Resour. Res., 45, W05421. DOI: 10.1029/2008WR007496.

Hrnčíř, M., Šanda, M., Kulasová, A., Císlerová, M., 2010. Runoff formation in a small catchment at hillslope and catchment scales. Hydrol. Proc., 24, 2246–2256.

IAEA, 2017. Global Network of Isotopes in Rivers. The GNIR Database. Accessible at: http://www.iaea.org/water

IAEA/WMO, 2017. Global Network of Isotopes in Precipitation. The GNIP Database. Accessible at: http://www.iaea.org/water

Jankovec, J., Vitvar, T., Šanda, M., Matsumoto, T., Han, L-F., 2017. Groundwater recharge and residence times evaluated by isotopes of hydrogen and oxygen, noble gases and CFCs in a mountain catchment in the Jizera Mts., northern Czech Republic. Geochem. J., 51, 5, 423–437. DOI: 10.2343/geochemj.2.0469.

Jasechko, S., Birks, S.J., Gleeson, T., Wada, Y., Fawcett, P.J., Sharp, Z.D., McDonnell, J.J., Welker. J.M., 2014. The pronounced seasonality of global groundwater recharge. Water Resour. Res., 50, 8845–8867.

Jasechko, S., Lechler, A., Pausata, F.S.R., Fawcett, P.J., Gleeson, T., Cendón, D.I., Galewsky, J., LeGrande, A.N., Risi, C., Sharp, Z.D., Welker, J.M., Werner, M., Yoshimura, K., 2015. Late-glacial to late-Holocene shifts in global precipitation $\delta^{18}O$. Clim. Past, 11, 1375–1393.

Kirchner, J., 2016. Aggregation in environmental systems – Part 2: Catchment mean transit times and young water fractions under hydrologic nonstationarity. Hydrol. Earth Syst. Sci., 20, 299–328.

Kliner, K., Kněžek, M., 1974. The underground runoff separation method making use of the observation of groundwater table. (In Czech with English abstract). J. Hydrol. Hydromech., 22, 5, 457–466.

Lapworth, D.J., Macdonald, A.M., Tijani, M.N., Araguás-Araguás, L., 2013. Residence times of shallow groundwater in West Africa: implications for hydrogeology and resilience to future changes in climate. Hydrogeol. J., 21, 673–686.

Maulé, C.P., Chanasyk, D.S., Muehlenbachs, K., 1994. Isotopic determination of snow-water contribution to soil water and groundwater. J. Hydrol., 155, 73–91.

McDonnell, J.J., McGuire, K., Aggarwal, P., Beven, K.J., Biondi, D., Destouni, G., Dunn, S., James, A., Kirchner, J., Kraft, P., Lyon, S., Maloszewski, P., Newman, B., Pfister, L., Rinaldo, A., Rodhe, A., Sayama, T., Seibert, J., Solomon, K., Soulsby, C., Stewart, M., Tetzlaff, D., Tobin, C., Troch, P., Weiler, M., Western, A., Wörman, A., Wrede, S., 2010. How old is streamwater? Open questions in catchment transit time conceptualization, modelling and analysis. Hydrol. Proc., 24, 1745–1754.

Nikodem, A., Kodešová, R., Bubeníčková, L., 2013. Simulation of the influence of rainfall redistribution in spruce and beech forest on the leaching of Al and SO_4^{2-} from forest soils. J. Hydrol. Hydromech., 61, 39–49.

O´Driscoll, M. A., DeWalle, D.R., McGuire, K.J., Gburek, W.J., 2005. Seasonal ^{18}O variations and groundwater recharge for three landscape types in central Pennsylvania, USA. J. Hydrol., 303, 108–124.

Penna, D., Engel, M., Mao, L., Dell'Agnese, A., Bertoldi, G., Comiti, F., 2014. Tracer-based analysis of spatial and temporal variations of water sources in a glacierized catchment. Hydrol. Earth Syst. Sci., 18, 5271–5288, DOI: 10.5194/hess-18-5271-2014.

Pfister, L., Martínez-Carreras, N., Hissler, C., McDonnell, J.J., 2017. Bedrock geology controls on catchment storage, mixing and release: a comparative analysis of 16 nested catchments. Hydrol. Proc., 31, 10, 1828–1845. DOI: 10.1002/hyp.11134.

Reddy, M.M., Schuster, P., Kendall, C., Reddy, M.B., 2006. Characterization of surface and ground water $\delta^{18}O$ seasonal variation and its use for estimating groundwater residence times. Hydrol. Proc., 20, 1753–1772.

Sayama, T., McDonnell, J.J., Dhakal, A., Sullivan, K., 2011. How much water can a watershed store? Hydrol. Proc., 25, 3899–3908.

Šanda, M., Vitvar, T., Kulasová, A., Jankovec, J., Císlerová, M., 2014. Run-off formation in a humid, temperate headwater catchment using a combined hydrological, hydrochemical and isotopic approach (Jizera Mountains, Czech Republic). Hydrol. Proc., 28, 3217–3229.

Soulsby, C., Tetzlaff, D., Hrachowitz, M., 2010. Spatial distribution of transit times in montane catchments: conceptualization tools for management. Hydrol.Proc., 24, 22, 3283–3288.

Turner, J.V., Macpherson, D.K, Stokes, R.A., 1987. The mechanisms of catchment flow processes using natural variations in deuterium and oxygen-18. J. Hydrol., 94, 143–162.

Van Loon, A.F., Laaha, G., 2015. Hydrological drought severity explained by climate and catchment characteristics. J. Hydrol., 526, 3–14.

Van Loon, A.F., Ploum, S.F., Parajka, J., Fleig, A.K., Garnier, E., Laaha, G., Van Laanen, H.A.J., 2014. Hydrological drought types in cold climates: quantitative analysis of causing factors and qualitative survey of impacts. Hydrol. Earth Syst. Sci., 19, 1993–2016.

Vitvar, T., Šanda, M., Marx, A., Hubert, E., Jankovec, J., Barth, J. A. 2016. Hydrochemical and isotopic tracing of runoff generation in the small mountainous catchment Uhlířská (Czech Republic), using the Netpath approach. Acta Hydrologica Slovaca, 17, 2, 190–198.

Votrubova, J., Dohnal, M., Vogel, T., Sanda, M., Tesar, M., 2017. Episodic runoff generation at Central European headwater catchments studied using water isotope concentration signals. J. Hydrol. Hydromech., 65, 2, 114–122 . DOI: 10.1515/johh-2017-0002.

Zappa, M., Vitvar, T., Ruecker, A., Melikadze, G., Bernhard, L., David, V., Jans-Singh, M., Zhukova, N., Sanda, M., 2015. A Tri-National program for estimating the link between snow resources and hydrological droughts. Proc. IAHS, 369, 25–30.

Received 4 September 2017
Accepted 16 February 2018

J. Hydrol. Hydromech., 67, 2019, 1, 49–58
DOI: 10.2478/johh-2018-0019

Spatial and temporal variability of snow isotopic composition on Mt. Zugspitze, Bavarian Alps, Germany

Kerstin Hürkamp[1*], Nadine Zentner[1, 2], Anne Reckerth[1], Stefan Weishaupt[3], Karl-Friedrich Wetzel[3], Jochen Tschiersch[1], Christine Stumpp[2, 4]

[1] Helmholtz Zentrum München, German Research Center for Environmental Health, Institute of Radiation Protection, Ingolstädter Landstraße 1, 85764 Neuherberg, Germany.
[2] Helmholtz Zentrum München, German Research Center for Environmental Health, Institute of Groundwater Ecology, Ingolstädter Landstraße 1, 85764 Neuherberg, Germany.
[3] University of Augsburg, Institute of Geography, Alter Postweg 118, 86159 Augsburg, Germany.
[4] University of Natural Resources and Life Sciences, Institute of Hydraulics and Rural Water Management, Muthgasse 18, 1190 Vienna, Austria.
[*] Corresponding author. Tel.:+49 89 3187 2582. Fax: +49 89 3187 3363. E-mail: kerstin.huerkamp@helmholtz-muenchen.de

Abstract: High amounts of precipitation are temporarily stored in high-alpine snow covers and play an important role for the hydrological balance. Stable isotopes of hydrogen (δ^2H) and oxygen (δ^{18}O) in water samples have been proven to be useful for tracing transport processes in snow and meltwater since their isotopic ratio alters due to fractionation. In 18 snow profiles of two snowfall seasons, the temporal and spatial variation of isotopic composition was analysed on Mt. Zugspitze. The δ^{18}O and δ^2H ranged between –26.7‰ to –9.3‰ and –193.4‰ to –62.5‰ in 2014/2015 and between –26.5‰ to –10.5‰ and –205.0‰ to –68.0‰ in 2015/2016, respectively. Depth-integrated samples of entire 10 cm layers and point measurements in the same layers showed comparable isotopic compositions. Isotopic composition of the snowpack at the same sampling time in spatially distributed snow profiles was isotopically more similar than that analysed at the same place at different times. Melting and refreezing were clearly identified as processes causing isotope fractionation in surficial, initial base or refrozen snow layers. For the future, a higher sampling frequency with detailed isotopic composition measurements during melt periods are recommended to improve the understanding of mass transport associated with snowmelt.

Keywords: Stable isotopes of oxygen and hydrogen in water; Snow profile; Snowmelt runoff; Isotope fractionation.

INTRODUCTION

In high alpine environments, meltwater from catchments with temporary snow cover and glaciers plays an important role for the hydrological balance and peak discharge in spring during melt periods (Holko et al., 2011). Runoff patterns are clearly influenced by the temporal storage of precipitation in the form of snow and ice (Viviroli et al., 2003, 2011). Snow has a high efficiency for washout of contaminants from the atmosphere. They can be accumulated in the snow cover and released into surface waters in relatively short time periods after snowmelt initiation in spring and affect water quality (e.g., Johannessen and Henriksen, 1978; Kępski et al., 2016). For balancing the water and contaminant budgets, knowledge of the snow processes involving accumulation, metamorphism and snowmelt is necessary. Measurements of the stable isotopes of hydrogen (δ^2H) and oxygen (δ^{18}O) in water samples (in the following referred to as "stable isotopes") have been proven to be useful for tracing flow paths and transport processes in snow since their isotopic ratio alters due to fractionation processes (e.g., Ala-aho et al., 2017; Clark and Fritz, 1997; Juras et al., 2016). In addition, variations in the stable isotope content in precipitation, which are mainly influenced by rainout processes and temperatures, are reflected in fresh snow covers (Stichler, 1987). Generally, higher summer, autumn and spring temperatures correspond to higher isotope ratios in precipitation, whereas lower winter temperatures result in lower isotope ratios. Therefore, snow and snowmelt are depleted in heavy isotopes. This can be traced in catchments for identifying the impact of glacier or snow meltwater in the hydrological cycle (Stichler and Schotterer, 2000). Furthermore, precipitation formed at higher altitudes is usually more depleted in heavy isotopes than at lower altitudes (Dansgaard, 1964). This was also observed on Mt. Zugspitze (Lauber and Goldscheider, 2014). A linear δ^{18}O decrease of –0.2 ‰/100 m was found for the Alps (Siegenthaler and Oeschger, 1980). This altitude effect is the result of the temperature effect combined with higher humidity at high altitude as low temperatures and high humidity lead to pronounced fractionation (Clark and Fritz, 1997). An altitude effect has been also observed in solid precipitation in several studies, e.g. by Moser and Stichler (1970) or Dietermann and Weiler (2013). These studies showed that the effect is less pronounced in solid than in liquid precipitation. However, an altitude effect has only been found in fresh snow and snow samples from the beginning of the snow period as the snow undergoes further fractionation processes with time. In altered snow, isotopic signatures change due to condensation, evaporation, sublimation, snow metamorphism, snowmelt processes and water vapour diffusion caused by temperature variations (e.g., Sokratov and Golubev, 2009; Unnikrishna et al., 2002; van der Wel et al., 2011). Evaporation and sublimation processes due to solar irradiance of the upper layers of the snowpack result in enrichment of the heavy isotopes in the snow (Moser and Stichler, 1974; Stichler et al., 2001). Water vapour diffusion between pore spaces and snowmelt can lead to isotopic smoothing and homogenisation (Arnason et al., 1972; Martinec et al., 1977). In melting snow the light isotopes will prevail in the initial runoff fractions (Stichler and Schotterer, 2000). With time meltwater becomes enriched in heavy isotopes as a consequence of isotopic exchange between liquid

water and ice as the meltwater percolates down in the snowpack (Taylor et al., 2001). Also external influences like wind, rain-on-snow events (Juras et al., 2016, 2017) or ground heat fluxes lead to isotope fractionation processes (Stichler, 1987; Stichler and Schotterer, 2000).

Most of the previous studies analysing isotope ratios in snow focus on the investigation of specific processes during melting (Martinec et al., 1977; Moser and Stichler, 1974; Stichler et al., 2001; Taylor et al., 2001; Unnikrishna et al., 2002) or compare the isotopic composition in the snow depth profiles with isotopes in precipitation at the end of the winter period (Arnason et al., 1972; Holko, 1995; Moser and Stichler, 1974). However, it remains to be tested whether conditions affecting the isotopic composition within the snowpack at the plot scale can be generalised to larger areas of snow accumulation in local alpine areas. Further, the temporal variation of isotopes in the snowpack during the accumulation period could give more detailed information about the potential local effects like redistribution of snow, interim snowmelt or homogenisation processes. This study aims (a) to characterise the temporal variation of stable isotopes in snow profiles at the same location, (b) to identify the spatial variability of stable isotopes in snow, and (c) to give implications that can be drawn from the isotope fractionation for mass transport processes in the snowpack. These objectives were achieved by investigating snow pits at Zugspitzplatt, Mt. Zugspitze (2962 m a.s.l.), Bavarian Alps, Germany.

MATERIAL AND METHODS

Study Site

Investigations were carried out at the so-called Zugspitzplatt, a karstic plateau of 1500–2800 m of altitude (mean 2229 m a.s.l.) composed of 600–800 m thick bedded limestones ("Wettersteinkalk", Ladin) with a slightly undulating relief. It is surrounded by several summits and inclined to the east (Fig. 1). The underlying layer consists of 300–400 m of marly claystone ("Partnach-Schichten"), which serves as an aquiclude (Miller, 1962). Zugspitzplatt shows forms of glacial erosion and accumulation from the Younger Dryas and of the Little Ice Age (1550–1850). Large areas covered by frost debris are also existent (Hüttl, 1999). Abundant soil covers do not exist. At the eastern margin of the 11.4 km² catchment, surface water infiltrating and draining through the karst aquifer discharges at a geological fault in the Partnach spring (1440 m a.s.l., Wetzel, 2004). The Partnach gauge (see Fig. 1), where discharge is continuously recorded, is situated 200 m downstream and 75 m of altitude beneath the spring. 3.5% (0.4 km²) of the catchment is permanently covered with snow and ice (Nördlicher and Südlicher Schneeferner glacier, data from 2009 (Rappl et al., 2010)). Average annual temperature on the highest summit (Mt. Zugspitze, 2962 m a.s.l.) is –4.8°C. Between 1998–2011, in the lower parts of the catchment (<1900 m), temperatures only exceeded 0°C in 54 days, in the upper parts (>2500 m) in 6 days during the snow accumulation period (Weber et al., 2016). The average annual precipitation on Mt. Zugspitze is 2071 mm (1981–2010); mainly snow at 58% of all days and 90% of the precipitation days per year (DWD, 2017). The variability of snow cover duration is between 33 and 338 days (1998–2011, Weber et al., 2016). The region is strongly wind exposed and experiences intensive solar radiation. Wind characteristics differ between Zugspitzplatt and Mt. Zugspitze summit, where fresh precipitation samples were taken. Wind velocities at the summit are approximately twice as high as at the plateau. Wind directions are limited at the plateau, because it is surrounded by wind-sheltering mountain ridges to the north, south and west.

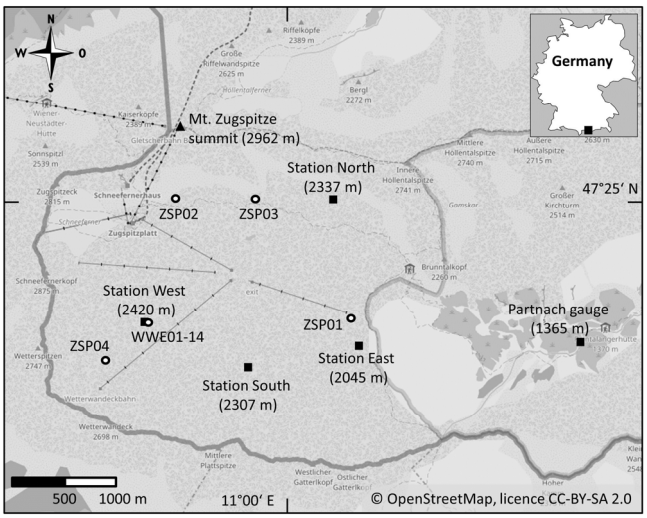

Fig. 1. Spatial distribution of snow profiles at Zugspitzplatt ("WWE" and "ZSP", bullets) as well as location of the meteorological stations (squares).

Nevertheless, small-scaled turbulences lead to different local wind fields.

Snow and fresh precipitation sampling

For the investigation of the temporal variation of stable isotope contents in the snow, snow pits were dug every two weeks (generally on the 1st and 15th day of a month between December 2014 and May 2015 and again from January to May 2016) at Station West (2420 m a.s.l.) on Zugspitzplatt (Fig. 1). An area of approximately 20 m x 20 m surrounding an installed meteorological station was fenced for it to protect the undisturbed snow cover from ski tourism. The profile excavations started in one corner at the beginning of the snow accumulation season each year and followed a grid of 5 m x 5 m to the adjacent profile each 15 days. The order of the profiles was the same in both seasons, but the day of the first sampling was different, related to a minimum snow depth of 50 cm. For the investigation of the spatial variability of isotopes in snow, four profiles (labelled with "ZSP01-04", Fig. 1) were additionally excavated on March 14th to 16th, 2016 at different remote locations on Zugspitzplatt. The choice of sites was limited to only a few areas that are not affected by extreme wind induced snow drift, steep slope gradients or ski tourism. All sampling locations are situated on solid bedrock or coarse block debris without soil cover.

The time period for the sampling of ZSP01-04 was kept short (3 days) in order to minimise strongly variable climatic influences. It enables a better comparison of all profiles related to their location rather than to external impact. The Zugspitzplatt is inclined to the east and receives sun during the mornings. The northern parts which are exposed to the south are illuminated in the afternoons. The locations in the south are most often shaded, since they are shielded by the southern mountain ridge. Wind patterns vary due to local roughness of the relief and rapidly changing wind directions of gusts. East-west directions dominate, even though the turbulence is high (Risius et al., 2015). The selected locations are representing sites with different slopes, solar and wind exposure and are expected to give a representative distribution of stable isotopes in the entire Zugspitzplatt catchment.

Eighteen snow profiles were excavated up to the depth of the solid bedrock (Table 1). Snow characteristics were described in detail according to Fierz et al. (2009). Snow layers were distin-

Table 1. Snow profile parameters and statistics of the $\delta^{18}O$ and $\delta^{2}H$ values.

profile ID	sampling date	altitude (m a.s.l.)	location coordinates latitude	location coordinates longitude	total depth[1] (cm)	sampling interval	number of samples	SWE[2] (mm)	$\delta^{18}O$ min (‰)	$\delta^{18}O$ max (‰)	$\delta^{2}H$ min (‰)	$\delta^{2}H$ max (‰)	SWE[2]-weighted mean $\delta^{18}O$ (‰)	SWE[2]-weighted mean $\delta^{2}H$ (‰)
WWE01	2014-12-15	2420	47°24'22.75"N	10°59'00.39"E	90	layer-wise	6	357.9	–21.6	–13.5	–160.1	–92.2	–16.3	–115.0
WWE02	2014-12-31	2420	47°24'22.75"N	10°59'00.39"E	196	layer-wise	10	494.0	–26.7	–13.3	–193.4	–92.5	–18.2	–129.8
WWE03	2015-02-01	2420	47°24'22.75"N	10°59'00.39"E	225	layer-wise	8	803.8	–23.5	–13.4	–175.7	–94.8	–20.4	–150.5
WWE04	2015-03-01	2420	47°24'22.75"N	10°59'00.39"E	221	layer-wise	6	797.8	–17.8	–14.2	–131.0	–102.8	–16.4	–118.9
WWE05	2015-03-29	2420	47°24'22.75"N	10°59'00.39"E	245	layer-wise	12	989.1	–21.1	–11.0	–156.6	–77.9	–16.5	–119.7
WWE06	2015-04-14	2420	47°24'22.75"N	10°59'00.39"E	319	layer-wise	10	1364.9	–16.6	–10.4	–121.1	–68.8	–14.9	–106.8
WWE07	2015-04-30	2420	47°24'22.75"N	10°59'00.39"E	276	layer-wise	12	1395.7	–18.1	–10.2	–132.9	–65.3	–16.1	–116.1
WWE08	2015-05-13	2420	47°24'22.75"N	10°59'00.39"E	223	layer-wise	23	1203.3	–20.0	–9.3	–152.3	–62.5	–15.1	–108.3
WWE09	2016-01-15	2420	47°24'22.75"N	10°59'00.39"E	198	layer-wise	12	570.1	–19.1	–13.7	–146.2	–103.6	–16.9	–124.2
WWE10	2016-02-15	2420	47°24'22.75"N	10°59'00.39"E	280	10	28	1047.9	–24.9	–12.7	–192.9	–89.7	–17.6	–127.6
WWE11	2016-03-14	2420	47°24'22.75"N	10°59'00.39"E	260[4]	10	26	1041.5	–26.5	–12.1	–205.0	–86.5	–18.3	–134.0
WWE12	2016-04-01	2420	47°24'22.75"N	10°59'00.39"E	410	30	14	1843.2[3]	–22.3	–13.6	–173.5	–101.8	–17.3	–130.7
WWE13	2016-04-16	2420	47°24'22.75"N	10°59'00.39"E	228	30	10	1073.3	–18.9	–13.5	–140.5	–93.5	–17.0	–125.3
WWE14	2016-05-03	2420	47°24'22.75"N	10°59'00.39"E	270	10	29	1223.6	–20.4	–10.5	–153.9	–68.0	–16.4	–121.3
ZSP01	2016-03-15	2053	47°24'22.05"N	11°00'22.07"E	290	20	15	1107.4[3]	–24.2	–12.8	–188.4	–94.3	SWE[2] not determined	
ZSP02	2016-03-15	2528	47°24'56.10"N	10°59'06.34"E	220	20	11	807.7[3]	–21.7	–11.9	–159.5	–89.5	SWE[2] not determined	
ZSP03	2016-03-16	2446	47°24'55.10"N	10°59'42.67"E	230	20	12	867.7[3]	–26.0	–12.5	–201.9	–93.8	SWE[2] not determined	
ZSP04	2016-03-16	2509	47°24'09.49"N	10°58'38.72"E	170	20	9	628.0[3]	–22.8	–14.0	–179.8	–106.2	SWE[2] not determined	

[1] snow and profile depth above solid bedrock (no soil cover)
[2] SWE = snow water equivalent
[3] SWE taken from a contemporaneous snow profile dug by the Bavarian Avalanche Warning Service at WWE-location
[4] depth of bedrock was not reached, total depth of profile is 395 cm

guished considering differences in snow texture, grain size, roundness, hardness and water content of the snowpack. Snow densities were determined *in situ* in 30 cm depth intervals (independent of layers) with a metal tube of known volume. A spring scale was used to measure the sample weight. Snow water equivalents (SWE) were calculated from the *in situ* snow densities for each snow layer (Table 1). SWE was used to quantify the amount of precipitation fallen between two sampling dates. It is also used for the correlation of the isotopic composition in the snow profiles compared to that of fresh precipitation, determined in samples of Mt. Zugspitze summit. Additional data useful in the interpretation of the results were provided by the snow pack analyser sensor (Sommer and Fiel, 2009) which measured the liquid water content of the snowpack 10 cm above the bedrock. Meteorological information was delivered by four additional meteorological stations (Station North, South, East, West, Fig. 1) that cover the entire Zugspitzplatt.

Bulk snow samples for the determination of stable isotopes were generally taken as depth-integrated samples over the total depth of the recorded snow layers in 2015. The thickness varied between a few millimetres for ice layers and maximum 123 cm. In 2016, the procedure was changed and uniform sampling depth intervals of 10 cm layers were applied without considering the snow layering. In the profiles of April 2016 (WWE12 and –13) snow of 30 cm layers was merged. Samples were taken by scratching the snow from the profile walls with 100 ml plastic vials, which were tightly sealed for storage. Icy layers were dissected from the surrounding snow and broken into small pieces with a knife to put them into the vials.

The isotopic composition of the snow profiles was compared to that in fresh precipitation of the same time period. The German Meteorological Service (Deutscher Wetterdienst, DWD) collected daily samples of freshly fallen precipitation from the ground at Zugspitze summit (2962 m a.s.l.) and merged them to biweekly bulk samples (Table 2). For the amounts of precipitation, SWE was continuously recorded at Station West using a snow balance (Smith et al., 2017). Even though this method is more prone to SWE losses/gains due to wind drift or intermediate snowmelt, assessing the solid precipitation amount at wind exposed sites is even more difficult and imprecise when using traditional precipitation gauges (Lundberg et al., 2016b), that are also available at Zugspitze summit and at Station West. Unless there is mass loss of snow due to meltwater runoff at the snow base, as it is proven for the study site during the winter months (see section "Snow cover and meltwater runoff development 2014–2016 at Zugspitzplatt"), it is feasible to compare SWE of precipitation and accumulated snowpack.

Sample pre-treatment and measurement of stable isotopes

Snow and ice samples were melted under closed conditions within the sampling vials before analysis. Precipitation and melted snow samples were analysed for $\delta^{18}O$ and $\delta^{2}H$ ratios using laser spectroscopy (Picarro L2120-i). A two point calibration with laboratory reference material calibrated against VSMOW-SLAP (Vienna Standard Mean Ocean Water-Standard Light Antarctic Precipitation) scale was used. Each sample was measured up to nine times. Precision of the instrument (1σ) was better than 0.15‰ and 0.6‰ for $\delta^{18}O$ and $\delta^{2}H$, respectively. Results of stable isotope compositions in precipitation and snow are presented as the ratio of isotopes (R_{sample}), given in the delta notation as δ-value (‰), which is the relative deviation of the sample from a standard ($R_{standard}$):

$$\delta(‰) = \frac{Rsample - Rstandard}{Rstandard} \cdot 1000$$

All samples were referenced to the VSMOW-SLAP scale. More details about measurement techniques and principles of isotope hydrology are given by IAEA (1983), Wassenaar et al. (2014) and Leibundgut et al. (2009).

For the comparison of the stable isotopic composition between precipitation samples taken at Zugspitze summit (2962 m a.s.l.) and snow samples of Zugspitzplatt (2420 m a.s.l.) an altitude correction factor was introduced accounting for the 542 m elevation difference. From comparison of measured stable isotopes in mainly solid precipitation sampled at the summit with samples at Hoher Peißenberg (988 m a.s.l.) between 2014–

2015 an altitude correction factor of –0.12‰/100 m for $\delta^{18}O$ and of –0.78‰/100 m for $\delta^{2}H$ was determined (not part of this study, personal communication C. Stumpp). Accordingly, corrections of +0.65 ‰ and +4.23 ‰ were applied to the measured $\delta^{18}O$ and $\delta^{2}H$ ratios for fresh precipitation at Mt. Zugspitze summit, respectively, to compare them with the isotopic composition of snow at Zugspitzplatt (Table 2).

Craig (1961) observed that the $\delta^{18}O$ and $\delta^{2}H$ values of precipitation that has not been evaporated are linearly related by $\delta^{2}H = 8\ \delta^{18}O + 10$, known as the "Global Meteoric Water Line" (GMWL). The slope and intercept of a "Local Meteoric Water Line" (LMWL), which is the line derived from precipitation collected from a single site, can be significantly different from the GMWL. In this study, LMWL were calculated from the precipitation samples applying an ordinary least squares regression according to Hughes and Crawford (2012) with the equation $\delta^{2}H = a\ \delta^{18}O - b$. With the same method also dual isotope regression lines were calculated for the snow samples using mean snow water equivalent (SWE)-weighted values of all isotope ratios. Parameters for the two lines were compared and discussed. Deuterium (d)-excess was calculated as $d = \delta^{2}H - 8\ \delta^{18}O$, and used in identification of water evaporation and comparison of isotopic composition of precipitation at Mt. Zugspitze and other German stations. Evaporated water typically plots below the meteoric water line along lines that intersect the MWL at the location of the original unevaporated composition of the water.

RESULTS

Snow cover and meltwater runoff development 2014–2016 at Zugspitzplatt

The measured snow parameters at Station West ("Wetterwandeck") since 2012 revealed that there was almost no mass loss of snow during the winter months from November to April, as shown for the winters 2014/2015 and 2015/2016 in Fig. 2. This means, the altitude and recent meteorological conditions at this site induced a continuous accumulation of snow and prevented meltwater runoff at the snow base during the winters. However, surface melting and snowpack compaction certainly occurred. Fig. 2 shows the daily means of snow height, snow water equivalent (SWE), density and liquid water content at the snow base at Station West in the snowfall seasons 2014/2015 and 2015/2016. The corresponding water discharge, recorded at the Partnach gauge (1365 m a.s.l.), initiated in late April in both years.

Table. 2. Precipitation amount and altitude-corrected isotopic composition of precipitation measured at Mt. Zugspitze summit (2962 m a.s.l.).

sampling date		amount	$\delta^{18}O_{corr.}$	$\delta^{2}H_{corr.}$	d-excess	accumulated weighted mean	
from	to	(mm)	(‰)	(‰)	(‰)	$\delta^{18}O_{corr.}$ (‰)	$\delta^{2}H_{corr.}$ (‰)
2014-10-17	2014-10-31	159.1	–11.0	–69.1	18.9	–11.0	–69.1
2014-11-01	2014-11-16	40.4	–18.0	–132.1	11.8	–12.4	–81.8
2014-11-17	2014-11-30	23.1	–14.9	–112.6	6.8	–12.7	–85.0
2014-12-01	2014-12-16	15.6	–13.4	–92.4	14.8	–12.7	–85.5
2014-12-17	2014-12-31	190.9	–22.7	–174.1	7.6	–17.2	–124.9
2015-01-01	2015-01-16	108.5	–12.0	–87.4	8.8	–16.1	–117.4
2015-01-16	2015-01-31	140.2	–19.9	–148.3	11.2	–16.9	–123.7
2015-02-01	2015-02-16	69.3	–16.0	–112.9	15.4	–16.8	–122.7
2015-02-16	2015-02-28	22.9	–19.6	–145.7	11.3	–16.9	–123.4
2015-03-01	2015-03-16	158.9	–12.3	–89.4	9.3	–16.1	–117.6
2015-03-16	2015-03-31	79.5	–12.2	–83.6	14.0	–15.8	–114.9
2015-04-01	2015-04-16	180.0	–12.5	–91.1	9.3	–15.3	–111.3
2015-04-16	2015-04-30	17.8	–13.1	–95.7	9.5	–15.3	–111.1
2015-05-01	2015-05-16	40.8	–15.9	–118.4	8.4	–15.3	–111.3
2015-11-17	2015-11-30	182.1	–20.4	–155.1	8.1	–20.4	–155.1
2015-12-01	2015-12-16	43.3	–14.2	–101.3	12.0	–19.2	–144.8
2015-12-17	2015-12-31	24.8	–12.6	–87.2	13.7	–18.5	–139.1
2016-01-01	2016-01-15	215.3	–17.7	–130.1	11.6	–18.2	–134.9
2016-01-16	2016-01-31	141.8	–17.4	–122.7	16.6	–18.0	–132.1
2016-02-01	2016-02-15	200.2	–14.3	–104.2	10.2	–17.1	–125.2
2016-02-16	2016-02-29	129.4	–19.0	–146.9	5.4	–17.3	–128.2
2016-03-01	2016-03-16	55.6	–17.0	–129.6	6.1	–17.3	–128.3
2016-03-17	2016-03-31	35.1	–12.0	–96.2	0.2	–17.1	–127.2
2016-04-01	2016-04-16	38.5	–10.2	–71.4	10.3	–16.9	–125.1
2016-04-17	2016-04-30	109.3	–13.3	–100.3	6.2	–16.6	–122.8
2016-05-01	2016-05-16	184.4	–11.0	–80.2	7.8	–15.8	–117.1
2016-05-17	2016-05-31	199.0	–8.3	–55.9	10.2	–14.8	–109.2

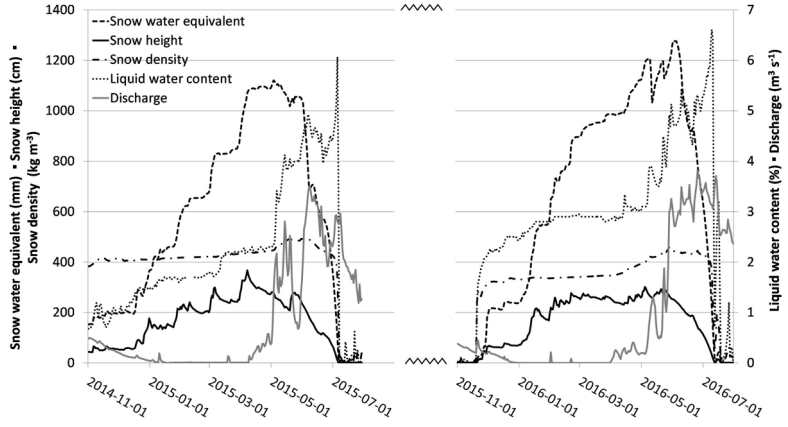

Fig. 2. Records of daily mean snow parameters for the total snow cover at Station West, Zugspitzplatt and water discharge at Partnach spring for the seasons 2014/2015 and 2015/2016. Liquid water contents and displayed densities were measured by the snow pack analyser sensor in the snow 10 cm above the bedrock.

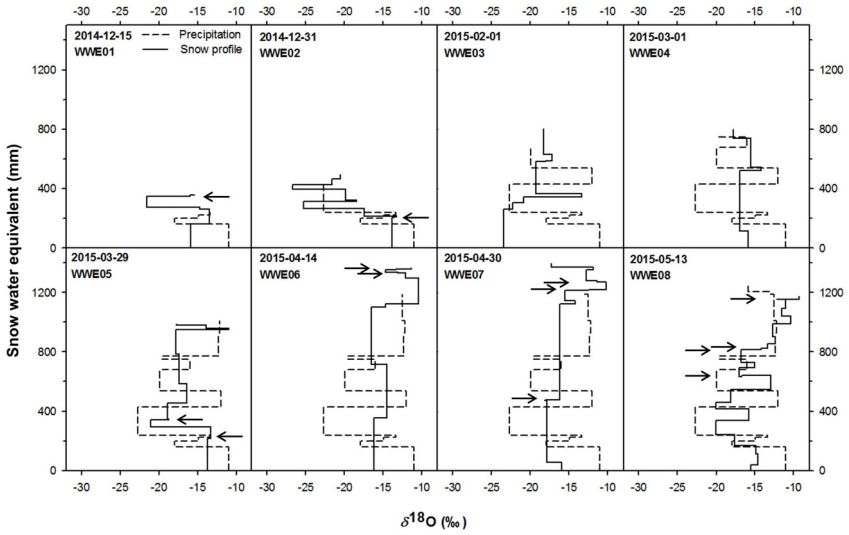

Fig. 3. Temporal variability of altitude corrected $\delta^{18}O$ contents in precipitation and in the snow samples of the winter season 2014/2015 at Station West, Zugspitzplatt. The arrows mark determined ice layers.

The accumulation of snow during the winter months was represented in the continuously increasing amount of water in the snow (SWE). In contrast, the snow height sometimes decreased due to snow compaction and partial melt which coincided with an increase of snow density. Meltwater runoff during these periods can be precluded, because no mass loss was observed on the snow balance. In 2015, the beginning of meltwater saturation at the snow base was on March 11th, accompanied with increased liquid water contents and snow density. On May 3rd, snowmelt runoff at the bottom of the snowpack began. The strongest melt period was in early June after an intermediate period of frost and snowfall between May 19th–27th. In 2016, water saturation at the snow base began on April 12th, and again on May 6th with increasing density and liquid water contents. Runoff at the snow base started on May 9th. A next peak of meltwater runoff occurred on May 21st and complemented in continuous runoff from the first week of June on.

Temporal variability of stable isotope composition of snow at Zugspitzplatt

The total snow water equivalent (SWE) of the winter season 2014/2015 in the profiles at Station West continuously increased until end of April and afterwards decreased due to the beginning of snowmelt runoff (Figs. 2 and 3). Snowmelt was accompanied by mean air temperatures of 0.2–9.1°C, recorded at Station West between May 1st and 13th, 2015. SWE in the snow profiles and corresponding amounts of fresh precipitation did not always match, likely due to the difference in altitude and wind patterns between the sampling locations. $\delta^{18}O$ isotope ratios (and $\delta^{2}H$ in brackets) ranged between –26.7‰ in December 2014 (–205.0‰ in March 2016) and –9.3‰ (–62.5‰) in May 2015. The depth distribution of stable isotopes, given in $\delta^{18}O$ values in Fig. 3, is heterogeneous, variable over time, and does not follow the expected distribution. In recent snow an isotopic distribution with lower $\delta^{18}O$ values during the winter months and higher ones in spring and autumn would be expected, similar to the seasonal input signal in precipitation. However, in the first two profiles (WWE01 and WWE02) of the snow accumulation period 2014/2015, isotopes in the snow samples were most similar to the precipitation values neglecting differences in SWE.

Layers of freshly fallen snow with low densities, as observed during the profile descriptions, were represented by low $\delta^{18}O$ values, as for example in the surficial layers of WWE04 and WWE07 (Fig. 3). Distinct minima in the uppermost half of the December 2014 profiles (WWE01 and –02) corresponded to cold periods under changing air mass directions. Low $\delta^{18}O$ values (<–21.6‰ and <–25‰) after several icy days (<–10°C) also between December 26th and 30th, 2014 (see WWE02). From April on, isotopes measured in the surficial snow layers always had higher values compared to fresh precipitation samples (WWE06-08).

The total SWE in the profiles of the winter 2015/2016 at Station West (Fig. 4) continuously increased until the end of March. Afterwards it massively decreased by more than 600 mm due to the beginning of snowmelt with recorded mean air temperatures about 4°C between May 8th and 11th, 2016. A comparably large decrease in SWE was not observed on the snow balance (Fig. 2). Isotopic composition of snow and precipitation showed different isotope ratios over time. $\delta^{18}O$ ranged between –26.5‰ (March 2016) and –10.5‰ (May 2016). Surprisingly, in snow profiles from April on (particularly WWE13, Fig. 4) the isotopic composition of snow was in accordance to the isotope ratios measured in precipitation, except for an enrichment of isotope ratios at the snow base. In contrast to the previous year, no pronounced enrichment compared to precipitation was found at the top of the snow profile at the end of the accumulation period. Still, the highest isotope values (–10.5‰) were measured in the top layer of the last snow profile (WWE14).

For both investigated years depth distributions of stable isotopes in the snow were strongly variable over time. Comparing consecutive sampling events, isotopic composition was different in the newly dug profiles, except for the period between profiles WWE10 and WWE11, where the isotopic distribution in the snow nearly stayed constant over four weeks in February/March 2016. It should be kept in mind that different sampling depth intervals and changes in snow density have to be considered in the interpretation. Larger sampling depth intervals lead to an apparent homogenisation (e.g. WWE07).

Spatial variability of stable isotopes in snow profiles at Zugspitzplatt

Air temperatures during the sampling of ZSP01-04 within 3 days in March 2016 were between –15–0°C. Two short precipitation showers (<1.3 mm) occurred on the 14th evening and the 15th within two hours after noon. Otherwise it was sunny. Snow depth was about 260 cm at Station West. Measured snow water equivalent was 950 mm. Wind intensities were below 5 m s^{-1},

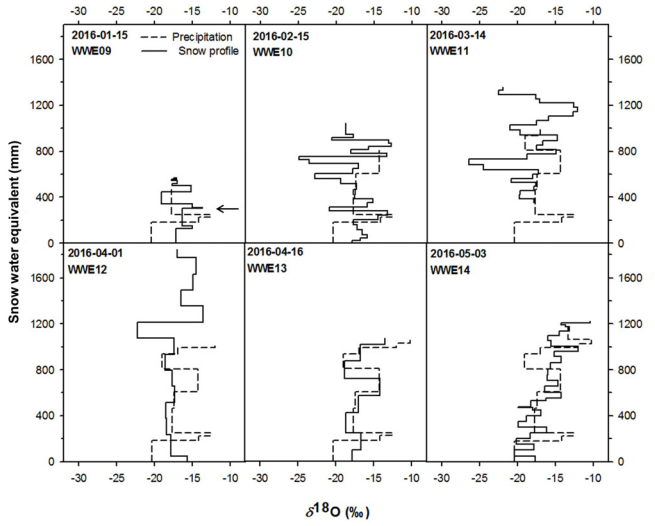

Fig. 4. Temporal variability of altitude corrected $\delta^{18}O$ contents in precipitation and in the snow samples of the winter season 2015/2016 at Station West, Zugspitzplatt. The arrow marks one determined ice layer. Later in the year, the thickness of the investigated ice layers was too small to accurately separate them as individual samples.

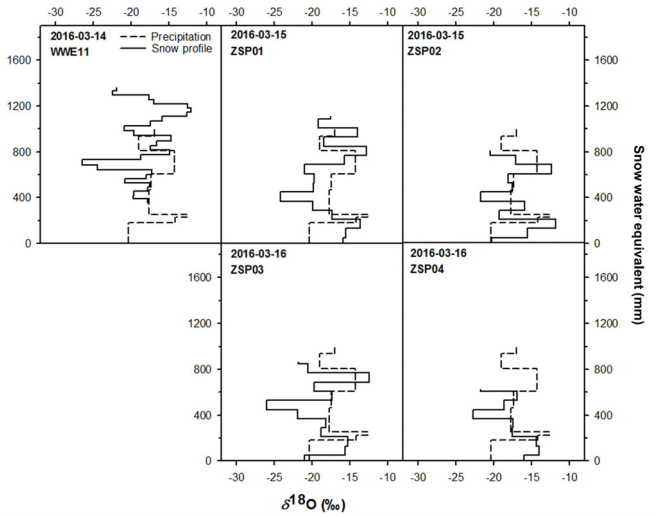

Fig. 5. Spatial variability of altitude corrected $\delta^{18}O$ contents in precipitation and in snow samples collected at different locations at the Zugspitzplatt (see Fig. 1).

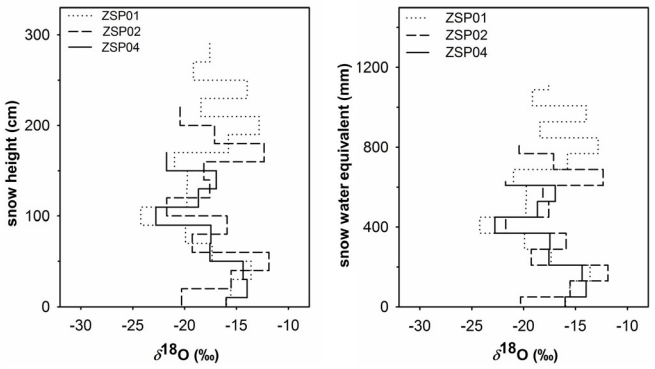

Fig. 6. Spatial variability of $\delta^{18}O$ contents of selected snow profiles of March 15th/16th, 2016 at remote locations on Zugspitzplatt. Despite different expositions, the patterns of stable isotope stratification in the profiles are similar.

except for a windy period with northeasterly gusts up to 10 m s^{-1} during the snowfall event on March 15th. Snow water equivalents (SWE) in the fresh precipitation samples differed from those measured by the snow balance indicating loss (ZSP02-04) or gain (WWE11 and ZSP01) in the local profiles compared to precipitation. Despite different locations of the snow pits and different external influences, a similar trend of the depth gradient of the isotopic composition in the snow profiles ZSP01-04, dug in the same week, could be observed.

All profiles taken in March 2016 fall into the range of isotope values that would have been expected from isotope measurements in precipitation (Fig. 5). In the deeper parts of the profiles (up to 600 mm SWE) the depth distribution of the $\delta^{18}O$ ratios in snow followed the same trend (Fig. 6) towards higher values in the base layers compared to fresh precipitation (Fig. 5), and lower ones in the layers at about 400 mm SWE. Similarity of spatially different profiles taken at the same time was higher compared to similarity of the same location sampled at different times.

DISCUSSION

Variability of snow water equivalents at Zugspitzplatt

Deviations of maximum 365 mm in ZSP04 between the determined snow water equivalents (SWE) in the snow profiles and precipitation were found (Fig. 5, Tables 1 and 2). This concerns profiles taken at the same time but at different locations (up to 2.5 km distance) emphasizing the importance of local conditions on the snow accumulation (e.g. relief, wind, Lundberg et al., 2016a). Deviations can be explained by the different sampling locations at Zugspitzplatt in different altitudes, expositions and wind regimes. Consequently, different amounts of SWE between the profiles must be attributed to the undulating relief with small wind-protected troughs in which snow accumulated and was preserved, whereas in wind-exposed positions mainly fresh and dry snow was removed. Huge variability of average SWE (1998–2011) at Zugspitzplatt with three times higher SWE in the west than at its eastern margin was also found by Weber et al. (2016). These variations were linked to annual as well as long-term variations in meteorological/climatological conditions.

In addition to these differences at the larger scale, the difference in SWE between the WWE profiles at Station West and the adjacent snow balance was even larger in one case (max. 857 mm in WWE12). In general, lower SWE were determined by the snow balance. This leads to the assumption that besides measurement uncertainties of the device considerable loss by wind drift or snowmelt on the snow balance occurred since the onset of the snow accumulation period. Consequently, the influence of snow redistribution is important not only on the large scale but also on the local plot scales.

Comparison of isotope values in snow depth profiles and precipitation

Comparing the isotopic composition of the snow profiles, the different depth intervals used in this study have to be considered. Larger sampling depth intervals automatically resulted in an apparent decrease in variability compared to smaller intervals. The same applied to precipitation sampling representing average values for biweekly integrative samples. Consequently, differences in isotope values of individual precipitation events might still have been visible in snow profiles with high resolution depth intervals, but could not be distinguished in the bulk precipitation sample. Still, the overall weighted isotope composition should be similar.

Applying a sampling depth interval of 10 cm as performed in 2016, the difference between taking depth-integrated mixed samples of the entire layer or selective point snow samples (horizontal penetration in the middle of each snow layer to fill the vials) in an additional profile close to Station West on February 24th, 2016 is shown in Fig. 7. Obviously, the results of both methods do not differ significantly, but will most likely be higher when using more coarse sampling resolution.

In an $^{18}O/^{2}H$ diagram (Fig. 8), all samples from the snow profiles plot close to the Local Meteoric Water Line (LMWL) with a mean of $\delta^{2}H = 8.08\ \delta^{18}O + 11.46$ for both winter seasons 2014/2015 and 2015/2016. The intercept and slope, as well as the d-excess (10.2‰), are higher compared to other stations in Germany (Stumpp et al., 2014), but still are in the range of other high alpine stations (Rank and Papesch, 2005). The slopes of the snow sample regression lines for both years (8.11 and 7.83) are lower compared to the precipitation LMWL indicating that evaporation or sublimation effects caused isotope fractionation. The data points that lie below the precipitation LMWL belong to samples that underwent sublimation and evaporation processes at the snow surface during prolonged periods of sunshine, resulting in enhanced snow metamorphism. Still, isotope fractionation effects should be of minor relevance in high alpine regions during periods of high humidity in winter (Stichler et al., 2001). Such periods frequently occur due to cloud coverage of Mt. Zugspitze, but can become more relevant during foehn events with extremely low relative humidity.

With some exceptions (e.g. WWE13 and ZSP01), the poor conformity of isotopic composition in snow and precipitation seems -not solely- to be attributed to processes within the snow, but also to snow redistribution by the wind. The importance of wind drift on snow transport and redistribution at Zugspitzplatt has been shown earlier (Bernhardt et al., 2012). Seasonal evolution of volume weighted means of $\delta^{18}O$ of snow (weighted by SWE) and accumulated precipitation (weighted by precipitation amount) as well as the calculated d-excess are shown in Fig. 9. The weighted means of isotopic composition of snow and precipitation are also given in Tables 1 and 2. Particularly for the d-excess, deviations between snow and precipitation can be the result of uncertainties due to the altitude correction of the precipitation data. The $\delta^{18}O$ means in precipitation and snow profiles converge over time. Some values of single snow profiles (e.g., February 1st, 2015) clearly deviate from the precipitation data, possibly due to higher ice contents or snow drift at specific times of the year. Nevertheless, throughout the winter season the mean isotope signature of winter precipitation is well preserved in the mean of the last snow profiles. It suggests that local deviations measured at individual times are averaged out. The overall conformity shown in Fig. 9 lets us to believe that the comparison of the isotopic composition of precipitation and snow is reasonable after altitude correction.

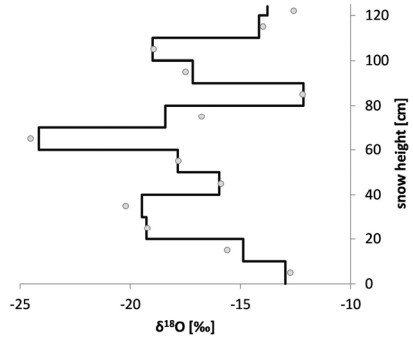

Fig. 7. $\delta^{18}O$ values in an additional snow profile close to Station West: Differences between the sampling methods of bulk samples (line) and point source samples (bullets).

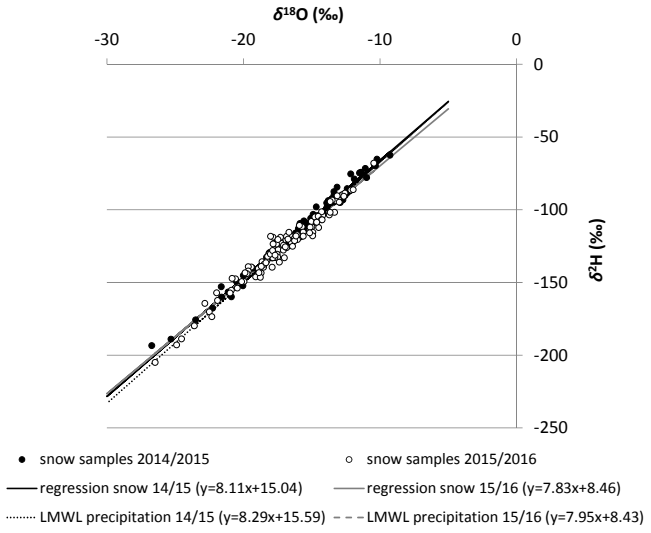

Fig. 8. Dual isotope plot for all snow samples of the seasons 2014/2015 and 2015/2016 with linear regression lines and the Local Meteoric Water Lines (LMWL) generated from biweekly fresh precipitation samples of the same period.

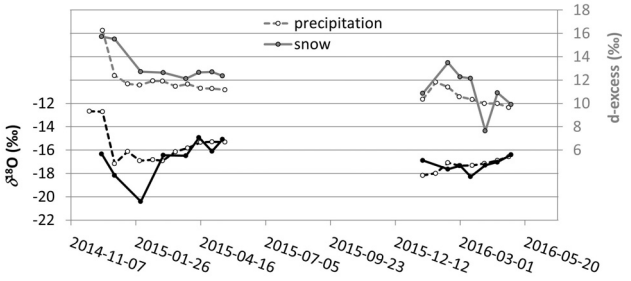

Fig. 9. Accumulated altitude corrected weighted $\delta^{18}O$ contents in biweekly precipitation samples and SWE-weighted means of $\delta^{18}O$ in the snow profiles (black lines) and the d-excess (grey lines) for the same samples in the seasons 2014/2015 and 2015/2016.

Temporal variability of stable isotopes in snow at Zugspitzplatt

Looking at the temporal variability of stable isotopes in the snow profiles, processes within the snowpack and processes caused by redistribution can be distinguished in more detail. At the snow base lower isotope ratios were found in snow compared to precipitation in winter 2014/2015 and *vice versa* in winter 2015/2016. This may be due to unknown deposition or melting processes before or after the snow accumulation period, indicated by fluctuating amounts of snow water equivalents (SWE). Melting at the snow base due to ground heat flux from the still warm bedrock in November each year could have resulted in the removal of light isotopes from the initial snowpack and thus to an enrichment of heavy isotope ratios in the remaining snowpack (compared to precipitation). In contrast, when melting was induced by solar radiation at the top of the snowpack, the light isotopes of the melting snow could have refrozen within deeper snow layers or accumulated at the base above frozen ground. Here, they do not necessarily have left the snowpack, as observed in autumn 2014. The determined high density of the lowermost layer of WWE03 (514 kg m^{-3}) and

extremely low $\delta^{18}O$ can be explained in this context by a refrozen highly water-saturated base layer.

Melting processes were not only of importance at the beginning and at the end of the snow accumulation. They also caused changes of the snow and the isotopic composition throughout the winter period. Icy layers formed when snow was exposed to the atmosphere during pronounced sunny periods. Partial snowmelt began, before the layer was covered by subsequent snowfall again. Melt and subsequent nocturnal refreezing or following frost periods decrease condensation temperatures and lead to grain coarsening and ice formation (Nakawo et al., 1993). If icy layers were present in the profiles, they were recorded and separately analysed for isotopes, too. They are marked by arrows in Fig. 3 and 4 and usually show slight deviations of isotope ratios to higher values, but do not significantly differ from the bulk snow. As described earlier, the formation of ice due to melting or refreezing of meltwater can be distinguished by the isotopic composition because percolating meltwater preferentially removes light isotopes (Taylor et al., 2001; Zhou et al., 2008). If isotope values of the icy layers were higher compared to the surroundings, it is more likely that melting was initiated at the top of the snowpack and these layers were the remainder of the top layer (see e.g. the thin layers in a depth of 319 mm SWE in WWE02 or in 959 mm SWE in WWE05, Fig. 3). In contrast, if isotope values of the icy layers were lower compared to the surroundings, it is more likely that melted water re-froze within the profile (see e.g. in a depth at 1154 mm SWE in WWE08 (Fig. 3) or at 478 mm SWE in WWE14 (Fig. 4)).

Melting processes, but also vapour diffusion within snow profiles result in a homogenisation of the snow isotopic composition in the snowpack (Stichler, 1987), which was also observed in the present study. This is evidenced by a reduction in amplitudes of the $\delta^{18}O$ ratios in the course of the year, e.g. when comparing WWE10 and WWE14 having similar depth intervals. In addition, both profiles of the end of the accumulation period (WWE08, WWE014) have a distinct isotopic distribution with high values at the top decreasing to lower values at the base. This was caused by the percolation of isotopically light meltwater through the profile and exchanging isotopes with the ambient snow. In such cases, the stable water isotopes can be used as tracers for mass transport in a snow profile, since it is proven that contaminants deposited as single layers on top of a snowpack will be released within the first portions of meltwater (Bales et al., 1989; Hürkamp et al., 2017; Juras et al., 2016, 2017). The beginning of meltwater percolation in the snowpack was also recorded by an increase of liquid water contents detected by the snow pack analyser and the loss of mass after onset of runoff, determined by the snow balance (Fig. 2) during the same time interval in beginning May 2015 and 2016. The transport within the snowpack was associated with the percolation of liquid water and first initiates after the snow became ripe, this means isothermal at 0°C. In future, it would be worth to also study in more detail the isotopic composition during melting. By comparing snow depth profiles with the isotopic composition of meltwater over time not only under controlled conditions (Moser and Stichler, 1970) or in models (Ala-aho et al., 2017) but also in the field, we can improve the understanding of isotope transport within the snowpack. Also local influences on isotope fractionation, such as rain-on-snow-events (Juras et al., 2016, 2017; Würzer et al., 2017) could be better traced. Here, weighable snow lysimeters would help to regularly collect snowmelt (Rücker et al., this issue).

What has been mentioned earlier, and what was most unexpected, was the poor similarity of the isotopic composition in snow between the consecutive snow profiles (Fig. 3 and 4). The only case where the isotopic distribution pattern in snow nearly stayed constant over four weeks in February/March 2016 is apparent in the profiles WWE10 and WWE11 (Fig. 4). During this period the mean air temperatures were about 3°C lower (–7.5°C) and relative humidity 12% higher than in the following period between the excavations of WWE11 and WWE12. It indicates better snow conservation and less metamorphism processes. In contrast, high similarity of isotope depth profiles over time were found from daily, weekly or biweekly sampling of snowpack in the Western Tatra Mountains, Slovakia (Holko, 1995), Hokkaido, Japan (Hashimoto et al., 2002; Zhou et al., 2008) or in the Sierra Nevada, USA (Unnikrishna et al. 2002). Even in a previous study at the Zugspitzplatt, sampling of snow profiles between January and July 1972 showed rather stable snow isotope depth profiles over time (Moser and Stichler, 1974). It remains unknown whether differing weather conditions, the shorter sampling time intervals or the fact that they always took their samples from the same snow pit could be the reason for the better recovery of the temporal isotopic variation in the snow 1972. In the present study, new snow pits were dug to avoid isotope fractionation in the old depth profiles. In future, it needs to be tested whether shorter time intervals with similar sampling strategies would give more information about the causes of lacking temporal similarity.

Spatial variability of stable isotopes in snow at Zugspitzplatt

In contrast to the WWE profiles, the isotopic composition of all ZSP profiles was comparable; despite their rather large distances (up to 2.5 km) to each other. Even similarity between the depth gradients of snow and precipitation isotope composition existed; compressed or stretched for some ranges of snow water equivalents (SWE) though. Best agreement of isotope ratios of snow and fresh precipitation showed the profile ZSP01 (Fig. 5). It was the easternmost profile which was located at the lowest altitude (~ 2000 m a.s.l.) at the entrance to the Reintal valley. It is likely that snow metamorphism due to insolation and the alteration of the isotopic snow composition were less pronounced in this area due to cold air streams in the valley, frequent cloud coverage and fog. Therefore, initial isotopic signals remained in the snow.

ZSP02 and -03 profiles contained one and ZSP01 two layers with higher isotope values (>–15‰) in a range between 600–700 mm SWE (Fig. 5). When looking at the precipitation data for dating these layers, they corresponded to periods of sunshine and ambient temperatures above 0°C between January 25th and February 3rd and on February 21st/22nd, 2016. During these days snow surface temperatures rose to isothermal 0°C, inducing high evaporation and sublimation rates as well as initiation of snowmelt. It is possible that the melted water infiltrated and was represented by the light isotopes in the layer at about 400 mm SWE. Certainly, ZSP01 and ZSP04 were influenced by gains and losses of mass when looking at the SWE. Strong wind periods that were detected on February 1st, 10th and 20th – 22th, 2016 at all four meteorological stations (wind intensities up to 18 m s^{-1} and gusts up to 30 m s^{-1}) can explain the low SWE compared to precipitation in profile ZSP04 and the gains at other locations (WWE11 and ZSP01).

Holko et al. (2013) found a high spatial variability in the isotopic composition of the snow cover during a snow-poor winter 2011 in northern Slovakia. For thin snow covers in Canadian Prairies, the same was investigated by Pavlovskii et al. (2017). According to Dietermann and Weiler (2013), the spatiotemporal isotopic distribution in a snowpack is strongly dependent

on the exposition, altitude and day in the year. Distinct spatial variability was also found for north and south-facing slopes in the Austrian Oetztal Alps (Schmieder et al., 2016), especially during the early melt season. In our study it remains difficult to distinguish the role of exposition or altitude (e.g. by comparing weighted isotopic averages), because the water balance is strongly influenced by the redistribution of snow within the study area. Stichler and Schotterer (2000) emphasised that particularly in summit regions of the Alps, redistribution and partially removal/accumulation of snow are the main processes influencing the isotopic composition of the snowpack or even glaciers. All studies point out the need of isotope measurements in each stage of hydrologic pathways for their use as tracers for transport processes concerning snowmelt runoff.

CONCLUSIONS

Eighteen snow pits in the hydrologic catchment of the Partnach creek, draining the Zugspitzplatt, were dug and sampled for the determination of temporal and spatial variability of the stable water isotopes in the snow. The temporal variability of the isotopic composition in 14 snow profiles of the seasons 2014/2015 and 2015/2016 at Station West at a small scale was extremely pronounced despite close proximity of the profiles, indicating complex processes happening in the snowpack. This can be either due to redistribution of snow between the biweekly sampling campaigns or due to processes causing changes of isotope ratios within the snow profile. Both are likely because changes and non-uniformity of snow water equivalents indicated snow gains and losses. In addition, recorded strong wind intensities and low temperatures support the argument of enhanced wind drift. Spatial variability of isotopic composition of snow layer samples at the same time but at different locations was much smaller than the above mentioned temporal. Melting and refreezing were clearly identified processes that caused isotope fractionation. Surficial, initial base or refrozen layers could be distinguished by the isotopic content. Isotope ratios were heavier compared to the surrounding layers due to the release of isotopically light meltwater or were lighter due to meltwater enrichment, respectively.

In future it would be necessary to measure with higher temporal frequency, because the similarity of isotopic composition between the biweekly sampling dates was low. It is recommended to stay with higher resolution depth profiles (e.g. 10 cm sampling depth intervals, ideally at concurrent consideration of the snow layering) to also get information about potential homogenisation throughout the winter period caused by vapour diffusion or melting. Due to large spatial differences and the dissimilarity between isotopes in snow and in precipitation, it remains to be studied how this will effect larger catchment modelling, where values from precipitation are available. In the future, also weighable snow lysimeters would help to get better information about changes of the snow water equivalent over time and at the same time the melting water could be collected to measure changes in isotopes and any other potential contaminants released due to the snowmelt.

Acknowledgements. The study was performed within the framework of the research project “Virtual Alpine Observatory”, funded by the Bavarian State Ministry of Environment and Consumer Protection, Germany (71_1d-U8729-2013/193-24). We gratefully acknowledge the support by Eva-Maria Schiestl (Institute of Radiation Protection, Helmholtz Zentrum München), Henry Schmölz (Bavarian Avalanche Warning Service), Martina Bauer, Martin Klotz and their colleagues (Bavarian Mountain Rescue) as well as by the staff and consortium of the Environmental Research Station Schneefernerhaus (UFS). We thank the staff of the Deutscher Wetterdienst (DWD) for providing biweekly fresh precipitation samples from Mt. Zugspitze summit and Petra Seibel (Institute of Groundwater Ecology, Helmholtz Zentrum München) for the analysis of the stable water isotopes. Ladislav Holko (Slovak Academy of Science) and another anonymous reviewer are acknowledged for their helpful comments that really improved the manuscript. The contents are solely the responsibility of the authors.

REFERENCES

Ala-aho, P., Tetzlaff, D., McNamara, J.P., Laudon, H., Kormos, P., Soulsby, C., 2017. Modeling the isotopic evolution of snowpack and snowmelt: testing a spatially distributed parsimonious approach. Water Resour. Res., 53, 5813–5830.

Arnason, B., Buason, T., Martinec, J., Theodorsson, P., 1972. Movement of water through the snow pack traces by deuterium and tritium. In: Proceedings of the Banff Symposis: The Role of Snow and Ice in Hydrology. Vol 1, UNESCO-WMOIASH, Geneva, Switzerland, pp. 299–312.

Bales, R.C., Davis, R.E., Stanley, D.A., 1989. Ion elution through shallow homogeneous snow. Water Resour. Res., 25, 1869–1877.

Bernhardt, M., Schulz, K., Liston, G.E., Zängl, G., 2012. The influence of lateral snow redistribution processes on snow melt and sublimation in alpine regions. J. Hydrol., 424–425, 196–206.

Clark, I.D., Fritz, P., 1997. Environmental Isotopes in Hydrogeology. CRC Press, Boca Raton, 352 p.

Craig, H., 1961. Isotopic variations in meteoric waters. Science, 133, 1702–1703.

Dansgaard, W., 1964. Stable isotopes in precipitation. Tellus, 16, 436–468.

Dietermann, N., Weiler, M., 2013. Spatial distribution of stable water isotopes in alpine snow cover. Hydrol. Earth Syst. Sci., 17, 2657–2668.

DWD, 2017. http://www.dwd.de/DE/wetter/wetterundklima_vorort/bayern/zugspitze/_node.html: 22.02.2017.

Fierz, C., Armstrong, R.L., Durand, Y., Etchevers, P., Greene, E., McClung, D.M., Nishimura, K., Satyawali, P.K., Sokratov, S.A., 2009. The International Classification for Seasonal Snow on the Ground. IHP-VII Technical Documents in Hydrology N°83, IACS Contribution N°1, UNESCO-IHP, Paris, 81 p.

Hashimoto, S., Shiqiao, Z., Nakawo, M., Sakai, A., Ageta, Y., Ishikawa N., Narita, H., 2002. Isotope studies of inner snow layers in a temperate region. Hydrol. Process., 16, 2209–2220.

Holko, L., 1995. Stable environmental isotopes of ^{18}O and ^{2}H in hydrological research of mountainous catchment. J. Hydrol. Hydromech., 43, 249–274.

Holko, L., Danko, M., Dósa, Kostka, Z., Sanda, M., Pfister, L, Iffly, J.F., 2013. Spatial and temporal variability of stable water isotopes in snow related hydrological processes. Bodenkultur, 64, 39–45.

Holko, L., Gorbachova, L., Kostka, Z., 2011. Snow hydrology in Central Europe. Geography Compass, 5/4, 200–218.

Hürkamp, K., Tafelmeier, S., Tschiersch, J., 2017. Influence of melt-freeze-cycles on the radionuclide transport in homogeneous laboratory snowpack. Hydrol. Process., 31, 1360–1370.

Hüttl, C., 1999. Steuerungsfaktoren und Quantifizierung der chemischen Verwitterung auf dem Zugspitzplatt (Wettersteingebirge, Deutschland). Münchener Geographische Abhandlungen, Reihe B, 30.

Hughes, C.E., Crawford, J., 2012. A new precipitation weighted method for determining the meteoric water line for hydrological applications demonstrated using Australian and global GNIP data. J. Hydrol., 464–465, 344–351.

IAEA, 1983. Guidebook on nuclear techniques in Hydrology. Technical Report Series No. 91, IAEA, Vienna, 441 p.

Johannessen, M., Henriksen, A., 1978. Chemistry of snow melt-

water: Changes in concentration during melting. Water Resour. Res., 14, 615–619.

Juras, R., Pavlásek, J., Vitvar, T., Šanda, M., Holub, J., Jankovec, J., Linda, M., 2016. Isotopic tracing of the outflow during artificial rain-on-snow event. J. Hydrol., 541, 1145–1154.

Juras, R., Würzer, S., Pavlásek, J., Vitvar, T., Jonas, T., 2017. Rainwater propagation through snowpack during rain-on-snow sprinkling experiments under different snow conditions. Hydrol. Earth Syst. Sci., 21, 4973–4987.

Kępski, D., Błaś, M., Sobik, M., Polkowska, Ż., Grudzińska, K., 2016. Progressing pollutant elution from snowpack and evolution of its physicochemical properties during melting period - a case study from the Sudetes, Poland. Water Air Soil Pollut., 227, 112.

Lauber, U., Goldscheider, N., 2014. Use of artificial and natural tracers to assess the groundwater transit-time distribution and flow systems in a high-alpine karst system (Wetterstein Mountains, Germany). Hydrogeol. J., 22, 1807–1824.

Leibundgut, C., Maloszewski, P., Külls, C., 2009. Tracers in Hydrology. John Wiley & Sons Ltd, Weinheim, 432 p.

Lundberg, A., Ala-aho, P., Eklo, O.M., Klove, B., Kvaener, J., Stumpp, C., 2016a. Snow and frost: implications for spatiotemporal infiltration patterns - a review. Hydrol. Process., 30,1230–1250.

Lundberg, A., Gustafsson, D., Stumpp, C., Kløve, B., Feiccabrino,J., 2016b. Spatiotemporal variations in snow and soil frost – A review of measurement techniques. Hydrology, 3, 28.

Martinec, J., Moser, H., de Quervain, M.R., Rauert, W., Stichler, W., 1977. Assessment of processes in the snowpack by parallel deuterium, tritium and oxygen-18 measurements. In: Proceedings of the Grenoble Symposium, August/September 1975: Isotopes and Impurities in Snow and Ice. Publication 188, International Association of Hydrological Sciences, Wallingsford, pp. 220–231.

Miller, H., 1962. Zur Geologie des westlichen Wetterstein und Mieminger Gebirges. Dissertation, Ludwig-Maximilian-Universität München.

Moser, H., Stichler, W., 1970. Deuterium measurements on snow samples from the Alps. In: Proceedings of a Symposium on Use of Isotopes in Hydrology: IAEA Symposium, March 1970, Vienna, pp. 43–57.

Moser, H., Stichler, W., 1974. Deuterium and oxygen-18 contents as an index of the properties of snow covers. In: Proceedings of the Grindelwald Symposium: Snow Mechanics. April 1974. Publication 144, International Association of Hydrological Sciences, Wallingsford, pp. 122–135.

Nakawo, M., Chiba, S., Satake, H., Kinouchi, S., 1993. Isotopic fractionation during grain coarsening of wet snow. Ann. Glaciol., 18, 129–134.

Pavlovskii, I., Hayashi, M., Lennon, M.R., 2017. Transformation of snow isotopic signature along groundwater recharge pathways in the Canadian Prairies. J. Hydrol. (in press).

Rank, D., Papesch, W., 2005. Isotopic composition of precipitation in Austria in relation to air circulation patterns and climate. In: Isotopic Composition in the Mediterranean Basin in Relation to Air Circulation Patterns and Climate. IAEA-TECDOC-1453, IAEA, Vienna, pp. 19–35.

Rappl, A., Wetzel, K.F., Büttner, G., Scholz, M., 2010. Tracerhydrologische Untersuchungen am Partnach Ursprung – Dye tracer investigations at the Partnach Spring (German Alps). Hydrol. Water Resour. Manage., 54, 220–230.

Risius, S., Xu, H., Di Lorenzo, F., Xi, H., Siebert, H., Shaw, R.A., Bodenschatz, E., 2015. Schneefernerhaus as a mountain research station for clouds and turbulence. Atmos. Meas.Tech., 8, 3209–3218.

Rücker, A., Zappa, M., Boss, S., Freyberg, J., 2017. An optimized snowmelt lysimeter system for monitoring melt rates and collecting samples for stable water isotope analysis. J. Hydrol. Hydromech., 67, 20–31. DOI: 10.2478/johh-2018-0007.

Schmieder, J., Hanzer, F., Marke, T., Garvelmann, J., Warscher, M., Kunstmann, H., Strasser, U., 2016. The importance of snowmelt spatiotemporal variability for isotope-based hydrograph separation in a high-elevation catchment. Hydrol. Earth Syst. Sci., 20, 5015–5033.

Siegenthaler, U., Oeschger, H., 1980. Correlation of ^{18}O in precipitation with temperature and altitude. Nature, 285, 314–317.

Smith, C.D., Kontu, A., Laffin, R., Pomeroy, J.W., 2017. An assessment of two automated snow water equivalent instruments during the WMO Solid Precipitation Intercomparison Experiment. Cryosphere, 11, 101–116.

Sokratov, S.A., Golubev, V.N., 2009. Snow isotopic content change by sublimation. J. Glaciol., 193, 823–828.

Sommer, W., Fiel, R., 2009. Snow Pack Analyser (SPA) for snow water equivalent (SWE) and liquid water content. http://www.hydrologicalusa.com/images/uploads/Paper_SPA_ENG_V100.pdf (19.05.2017).

Stichler, W., 1987. Snowcover and snowmelt processes studied by means of environmental isotopes. In: Jones, H.G., Orville-Thomas, W.J. (Eds.): Seasonal Snowcovers: Physics, Chemistry, Hydrology. D. Reidel Publishing Company, Dordrecht, Holland, pp. 673–726.

Stichler, W., Schotterer, U., 2000. From accumulation to discharge: modification of stable isotopes during glacial and post-glacial processes. Hydrol. Process., 14, 1423–1438.

Stichler, W., Schotterer, U., Fröhlich, K., Ginot, P., Kull, C., Gäggeler, H., Pouyaud, B., 2001. Influence of the sublimation on stable isotope records recovered from high-altitude glaciers in the tropical Anden. J. Geophys. Res., 106, 22613–22620.

Stumpp, C., Klaus, J., Stichler, W., 2014. Analysis of long-term stable isotopic composition in German precipitation. J. Hydrol., 517, 351–361.

Taylor, S., Feng, X., Kirchner, J.W., Osterhuber, R., Klaue B., Renshaw, C.E., 2001. Isotopic evolution of a seasonal snowpack and its melt. Water Resour. Res., 37, 759–769.

Unnikrishna, P.V., McDonnell, J.J., Kendall, C., 2002. Isotope variations in Sierra Nevada snowpack and their relation to meltwater. J. Hydrol., 260, 38–57.

Van der Wel, L.G., Gkinis, V., Pohjola, V.A., Meijer, H.A.J., 2011. Snow isotope diffusion rates measured in a laboratory experiment. J. Glaciol., 57, 30–38.

Viviroli, D., Weingartner R., Messerli, B., 2003. Assessing the hydrological significance of the world's mountains. Mt. Res. Dev., 23, 32–40.

Viviroli, D., Archer, D. R., Buytaert, W., Fowler, H. J., Greenwood, G. B., Hamlet, A. F., Huang, Y., Koboltschnig, G., Litaor, M. I., López-Moreno, J. I., Lorentz, S., Schädler, B., Schreier, H., Schwaiger, K., Vuille, M., Woods, R., 2011. Climate change and mountain water resources: overview and recommendations for research, management and policy. Hydrol. Earth Syst. Sci., 15, 471–504.

Wassenaar, L.I., Coplen, T.B., Aggarwal, P.K., 2014. Approaches for achieving long-term accuracy and precision of $\delta^{18}O$ and $\delta^{2}H$ for waters analyzed using laser absorption spectrometers. Environ. Sci. Technol., 48, 1123–1131.

Weber, M., Bernhardt, M., Pomeroy, J.W., Fang, X., Härer, S., Schulz, K., 2016. Description of current and future snow processes in a small basin in the Bavarian Alps. Environ. Earth Sci., 75, 1223.

Wetzel, K.-F., 2004. On the hydrology of the Partnach area in the Wetterstein mountains (Bavarian Alps). Erdkunde, 58, 172–186.

Würzer, S., Wever, N., Juras, R., Lehning, M., Jonas, T., 2017. Modelling liquid water transport in snow under rain-on-snow conditions – considering preferential flow. Hydrol. Earth Syst. Sci., 21, 1741–1756.

Zhou, S., Nakawo, M., Hashimoto, S., Sakai, A., 2008. The effect of refreezing on the isotopic composition of melting snowpack. Hydrol. Process., 22, 873–882.

Received 28 June 2017
Accepted 13 February 2018

J. Hydrol. Hydromech., 67, 2019, 1, 59–69
DOI: 10.2478/johh-2018-0022

Influence of mountain spruce forest dieback on snow accumulation and melt

Martin Bartík[1*], Ladislav Holko[2], Martin Jančo[1, 3], Jaroslav Škvarenina[1], Michal Danko[2], Zdeněk Kostka[2]

[1] Department of Natural Environment, Faculty of Forestry, Technical University in Zvolen, T. G. Masaryka 24, 960 01 Zvolen, Slovakia.
[2] Institute of Hydrology, Slovak Academy of Sciences, Dúbravská cesta 9, 841 04 Bratislava, Slovakia.
[3] Faculty of Ecology and Environmental Sciences, Technical University in Zvolen, T. G. Masaryka 24, 960 01 Zvolen, Slovakia.
[*] Corresponding author. E-mail: bartikmartin@gmail.com

Abstract: Large-scale forest dieback was reported in recent decades in many parts of the world. In Slovakia, the most endangered species is Norway spruce (*Picea Abies*). Spruce dieback affects also indigenous mountain forests. We analysed changes in snow cover characteristics in the disturbed spruce forest representing the tree line zone (1420 m a.s.l.) in the Western Tatra Mountains, Slovakia, in five winter seasons 2013–2017. Snow depth, density and water equivalent (SWE) were measured biweekly (10–12 times per winter) at four sites representing the living forest (Living), disturbed forest with dead trees (Dead), forest opening (Open) and large open area outside the forest (Meadow). The data confirmed statistically significant differences in snow depth between the living and disturbed forest. These differences increased since the third winter after forest dieback. The differences in snow density between the disturbed and living forest were in most cases not significant. Variability of snow density expressed by coefficient of variation was approximately half that of the snow depth. Forest dieback resulted in a significant increase (about 25%) of the water amount stored in the snow while the snowmelt characteristics (snowmelt beginning and time of snow disappearance) did not change much. Average SWE calculated for all measurements conducted during five winters increased in the sequence Living < Dead < Meadow < Open. SWE variability expressed by the coefficient of variation increased in the opposite order.

Keywords: Snow characteristics; Forest dieback; Norway spruce; Mountains; Degree-day model.

INTRODUCTION

Forest significantly influences the hydrological cycle (Bredemeier et al., 2010; Jewitt, 2005; Mráček and Krečmer, 1975). Part of precipitation intercepted by the forest is evaporated back to the atmosphere (Chang, 2006). Interception also changes the spatial distribution of precipitation under the canopy (e.g. Bartík et al., 2016; Holko et al., 2009; Lundberg et al., 1998). On the contrary, horizontal precipitation captured by the forest can represent an important component of the water and hydrochemical balance (Elias et al., 1995; Fišak et al., 2001; Minďáš and Škvarenina, 1995). Moreover, forest significantly affects precipitation partitioning into overland and subsurface flow through its influence on the soil (Gömöryová et al., 2013; Gömöryová et al., 2017; Stähli et al., 2011). Hence, forest change has manifold hydrological consequences, the effects of which are not easy to predict in detail (Bredemeier et al., 2010; Michalova et al., 2017; Rogger et al., 2017).

Forest affects also the snow accumulation and melt. The differences in snow characteristics in the forest and in nearby open areas have been observed for more than a century (e.g. Church, 1914). A number of studies compared snow in the forest and forest clearings or specifically addressed the influence of forest management practices, i.e. direct human interventions (e.g. Andreson, 1963; Ellis et al., 2010; Garstka et al., 1958; Golding and Swanson, 1986; Kittregde, 1953; Koivusalo and Kokonen, 2002; Kuusisto, 1980; Mayer et al., 1997; Stähli et al., 2000; Swanson and Golding, 1982; Troendle and King, 1987; Zelený, 1971). The results of empirical studies of changes in forest cover and associated changes in snow accumulation and ablation rates were reviewed by Varhola et al. (2010). More recent studies addressed also the effects of forest dieback, i.e. natural disturbances, on snow characteristics. They used measured data or modelling to study the effects of dieback caused by bark beetle or forest fires (e. g. Bartík et al., 2014; Boon, 2012; Harpold et al., 2014; Jeníček et al., 2018; Perrot et al., 2012; Pugh and Small, 2012).

Large-scale forest disturbances were recently reported in Europe (Mezei et al., 2014, 2017; Seidl et al., 2011) and a number of authors have pointed out the hydrological consequences of forest dieback (e.g. Adams et al., 2012; Vido et al., 2015; Winkler et al., 2014). In Slovakia, forests cover approximately 40% of the country. Extensive areas of Slovak forests were recently affected by dieback as well (Grodzki et al., 2006; Jakuš et al., 2011). Norway spruce (*Picea Abies* (L.) Karst.), the most abundant coniferous tree in Slovakia (about 26% of all forest tree species), is one of the most endangered species, especially owing to its high sensitivity to increasing air temperature. Dieback does not occur only in areas where spruce was introduced by people. It is documented also in indigenous mountain forests (Janda et al., 2016; Parobeková et al., 2016) and in areas which were until now relatively less affected by human activities (Fleischer et al., 2017). Because such forests often occur in headwater catchments, their change can influence snow accumulation and melt and consequently runoff formation and discharge regimes in downstream areas. Understanding the local effects of such changes on snow accumulation and melt requires studies based on local data measured over a long time.

This article presents the results of measurements of snow depth, density and water equivalent from the highest part of the Carpathian Mountains during five winters. It differs from previous studies in that the measurements were conducted over the entire winter seasons with a relatively high frequency (approximately every two weeks). The overall objective of our study is to analyse the influence of the mountain spruce forest dieback on snow accumulation and melt. The article is organised so that we first compare snow characteristics and their variability at sites with different land cover (living and disturbed forest, forest opening and a large open area outside the forest). Then we evaluate the influence of different stand characteristics (land

use) on snow accumulation and melt. The results could be useful in the assessment of regional snow cover development in similar snowmelt dominated headwater catchments affected by forest dieback.

MATERIAL AND METHODS

Study area

The study was conducted at research plot Červenec (49.183617°N, 19.641944°E, elevation 1 420 m a.s.l.) in the Western Tatra Mountains, northern Slovakia. The plot is located in the Jalovecký creek catchment which is the subject of long-term hydrological research devoted also to snow cover (Holko and Kostka, 2010). The bedrock at the research plot is formed by limestone, marlstone, claystone and dolomite. The soil is classified as Cambisol and has high stoniness (Hlaváčiková et al., 2016). The forest at the plot is representative of the tree line zone in the highest part of the Carpathian Mountains. Although the forest at the plot was significantly affected by human activities in the past, today it is classified as dominantly natural (Celer, 2013). It is composed solely of Norway spruce. The age of the trees is more than 130 years (Oreňák et al., 2013). Places with sparse density of the forest are overgrown with rowan (*Sorbus aucuparia* L.). The understory is represented by bilberry (*Vaccinium myrtyllus* L.); raspberry (*Rubus idaeus* L.) occurs in the open area. Part of the forest died in summer 2012 as a result of the bark beetle (*Ips typhographus* L.) outbreak. Branches of the dead trees are covered with lichen "tree moss" (*Pseudevernia furfuracea* (L. Zopf.).

Data

Snowpack measurements in the open area and in the forest have been conducted since the 1990's (Holko et al., 2009). The results presented in this article are based on data from the new snow courses established after the forest dieback since winter 2013. We present data from five winters (2013–2017). A "winter" is defined as the period from November through the following May. For example, winter 2013 is represented by data measured from November 2012 until May 2013.

The snow courses are located in the living forest (hereafter denoted as „Living"), disturbed forest with dead trees (Dead), forest opening (Open) and in the large open area outside the forest (Meadow). The size of the forest opening is 1H – 2H, where H is tree height. Snow depth (SD) and water equivalent (SWE) were measured at the snow courses every two weeks (biweekly) depending on weather conditions (10–12 times per winter). Snow density was calculated from snow depth and snow water equivalent at the snow course.

SWE was measured using a fibre glass snow tube with a cross section area of 50 cm^2, which was weighed with a digital scale with resolution of 10 grams. SD was measured by a graduated rule with resolution of 1 cm.

Snow courses in the open area, i.e. at sites Open and Meadow, were located 50 meters and 300 meters away from the snow courses at forested sites (Living and Dead), respectively.

SD was measured every meter at 31 points at each snow course in the forest sites (Living and Dead). SWE in the forest was measured every five meters, i.e. seven values were obtained at each snow course (Fig. 1). In the open area, 20 SD measurements and 3 SWE measurements were made at each snow course (sites Open and Meadow). Mean values for the snow courses on individual dates were calculated as follows:

– mean SD value was calculated from 31 (forest) and 20 values (open area),

– mean snow density was calculated from 7 (forest) and 3 (open area) SWE values and the corresponding SD values,

– the SWE for the snow course was obtained by multiplication of the mean SD by the mean snow density.

Precipitation at the snow courses was measured manually by the standard rain gauges of the Slovak Hydrometeorological Institute with orifice area 500 cm^2. Three gauges were installed in the forest to capture precipitation patterns at the typical forest locations, i.e. in the forest opening, the drip zone and the near-stem zone (Holko et al., 2009).

Daily precipitation and air temperature data from the automatic weather station equipped with a weighing rain gauge located near the snow courses were used in snow accumulation and melt modelling. The weather station is located in the open area. Therefore, measured precipitation and air temperature from the station were directly used in the modelling for the Meadow and Open sites. Model input precipitation for sites Dead and Living was modified according to the throughfall measurements conducted at both sites. The throughfall values calculated from the readings of raingauges located under the trees and in the forest windows provided precipitation correction coefficients. The coefficients were applied backwards to calculate the input daily precipitation at sites Dead and Living since the previous day with throughfall data. Comparison of air temperature measured at the weather station with that measured under the nearby dense spruce tree stand showed that air temperature under the canopy was on average 1°C lower than that in the open area. This value was therefore used to prepare the model input air temperature data for the site Living.

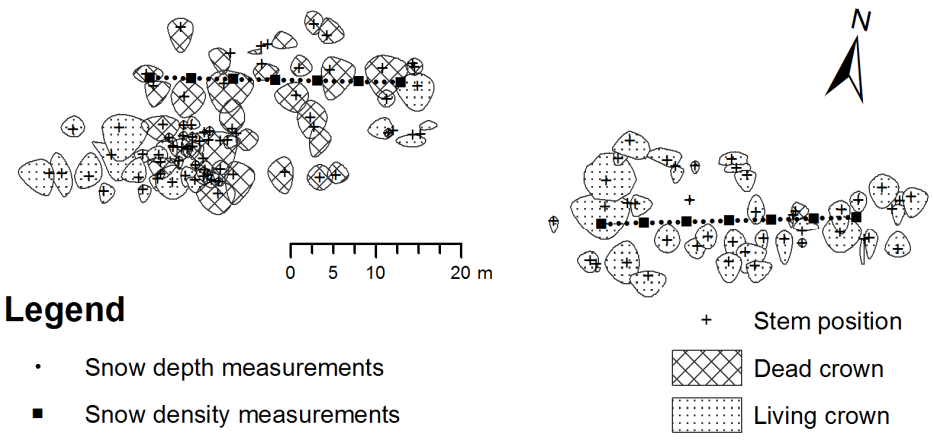

Fig. 1. Snow depth and density measurements at forested sites (Dead, Living).

Methods

Climatic characteristics of the studied winters were first evaluated using the total precipitation amount and sum of positive daily air temperature from December to March. The values for individual winters were plotted as anomalies (Holko et al., 2012), i.e. as deviations from the long-term mean values for the period 1989–2017. Such presentation allows fast identification of extreme winters in the time series data. Climatic conditions important for snow cover evolution, i.e. precipitation amount and potential snowmelt in the study winters can also be quickly assessed and compared. Temporal evolution of SD and snow density at all sites in the five study winters was compared. Variability of SD and snow density along each snow course was expressed by standard deviations to obtain the absolute values in cm and kg.m^{-3}, respectively. The use of standard deviation helps to perceive the importance of the variability when compared to the temporal evolution of SD or snow density (as in Figs. 3 and 5). Comparison of variability in snow characteristics among the sites (snow courses) and on different dates was based on coefficients of variation (Cv). Box-whisker plots were used to compare the data measured at individual snow courses over entire winters.

Mean values of SD and snow density for each snow course and day with measurements as well as for the entire study period were compared using the Student paired test. The aim was to test whether the two compared data sets were significantly different from each other at a significance level of 95%. Significantly different data sets were marked in results with „x“ (e.g. Table 2). Statistical analysis was carried out with Statistica 10 and Statgraphics Centurion XVI.I.

Biweekly measurements at snow courses may not capture the maximum seasonal snow water equivalent (SWE) and provide correct snowmelt characteristics (onset, termination). Therefore, snow accumulation and melt modelling was used to provide daily values of SWE. A simple degree-day model was used. Snow accumulation was simulated if the mean daily air temperature during days with precipitation was below the threshold temperature. Snow melt was calculated according to the following well-known formula:

$$M = DDF\,(T - T_{crit}) \quad (1)$$

where M is the snowmelt [mm], DDF is the degree-day factor [mm.°C^{-1}.day^{-1}], T is the mean daily air temperature [°C] and T_{crit} [°C] is the threshold air temperature above which the snow starts to melt.

The threshold air temperature above which all precipitation falls as rainfall, threshold air temperature at which the snowmelt starts and the temporally variable degree-day factor were used to fit the simulated and measured SWE values. The aim of the modelling was solely to fit the simulated and measured values during the time of maximum SWE and the snowmelt period (i.e. not to transfer the model to other sites or time periods or evaluate the calibrated degree-day factors). Therefore, model parameters were variable in time and different for each site and winter. After the simulations we have calculated the Kling-Gupta efficiency coefficient KGE (Gupta et al., 2009):

$$KGE = 1 - \sqrt{(r-1)^2 + (\alpha-1)^2 + (\beta-1)^2} \quad (2)$$

$$\alpha = \frac{\sigma_{sim}}{\sigma_{obs}} \qquad \beta = \frac{\mu_{sim}}{\mu_{obs}}$$

where r is the linear correlation coefficient, σ is standard deviation, μ is arithmetic mean and *sim* and *obs* represent simulated and observed values, respectively.

KGE was used instead of the more common Nash Sutcliffe coefficient (Nash and Sutcliffe, 1970), because it allows identification of the origin of model errors.

The degree-day model was run at a daily time step for the period November 1st to May 5th. Model parameters were calibrated by the trial and error approach. Simulated SWEs were visually compared with measured values during model calibration. Maximum SWE, dates of snowmelt onset and termination and snowmelt duration were then obtained from the modeled data for each site and winter.

RESULTS

Climatic characteristics of winters 2013–2017

The long-term average (1989–2017) of precipitation in cold months (December to March) at the research plot is about 400 mm (Fig. 2). About 25 days during the same period had daily mean air temperature above zero. The long-term average of the sum of positive air temperature from December to March is about 54°C. Fig. 2 shows that above-average precipitation occurred in winter 2013. At the same time, the sum of positive air temperatures was below-average. Thus, winter 2013 had the most favourable conditions for snow accumulation out of the five studied winters. Winter 2014 represented the opposite situation, namely below-average precipitation and above-average sum of positive daily temperatures. Fig. 2 reveals that shifting from wet to dry or cold to warm in successive winters is quite common in the study area. However, winter 2014 was unique for its unusually dry and warm weather. Satellite data confirmed that all of Slovakia was extremely snow-poor (Krajčí et al., 2016). In winters 2015–2017, total precipitation and sum of positive air temperatures were close to long-term averages.

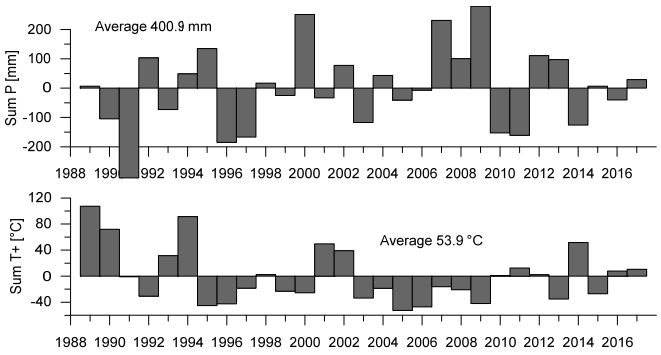

Fig. 2. Anomalies of total precipitation and positive air temperature of winter periods (December to March) at the research plot according to data from the meteorological station located in the open area.

Snow depth

Annual maximum snow depths at different sites exceeded 80–100 cm and standard deviations for most days with measurements were under 10 cm (Fig. 3). Coefficients of variations (Cv) of the SD calculated for individual dates with measurements mostly did not exceed 0.3. The highest SD was almost always measured in the forest opening (Open). This pattern is well known and reflects increased snow accumulation at sites protected from the wind (e.g. Troendle and King, 1985). SD in the disturbed forest (Dead) was almost always higher than in the living forest (Living), a result of the interception decrease

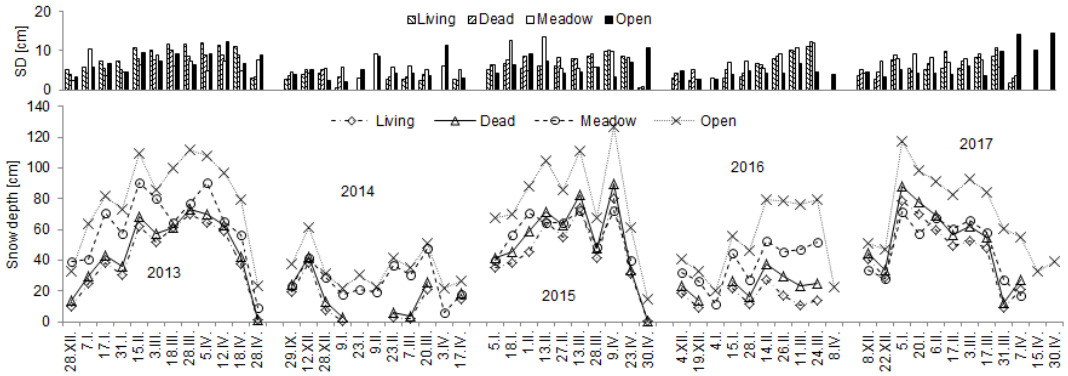

Fig. 3. Mean snow depth and its variability (SD in the figure represents the standard deviation) at all sites and on all days with measurements in winters 2013–2017.

Table 1. Snow depth [cm] and its variability for the entire winter season.

	2013				2014				2015				2016				2017				2013–2017			
	Count	Average	Standard deviation	Coeff. of variation	Count	Average	Standard deviation	Coeff. of variation	Count	Average	Standard deviation	Coeff. of variation	Count	Average	Standard deviation	Coeff. of variation	Count	Average	Standard deviation	Coeff. of variation	Count	Average	Standard deviation	Coeff. of variation
Living	12	**43**	23	0.53	8	**13**	13	0.97	10	**47**	23	0.50	8	**16**	6	0.38	10	**46**	22	0.47	48	**35**	24	0.67
Dead	12	**47**	23	0.50	8	**17**	14	0.79	10	**53**	26	0.49	8	**24**	8	0.31	10	**53**	24	0.45	48	**41**	25	0.61
Meadow	12	**62**	24	0.38	11	**26**	12	0.46	9	**59**	13	0.23	9	**38**	14	0.37	10	**49**	20	0.41	51	**47**	22	0.46
Open	12	**81**	29	0.36	11	**35**	13	0.37	10	**80**	31	0.39	10	**53**	24	0.45	12	**71**	27	0.38	55	**64**	30	0.47
Total	48	58	28	0.49	38	24	15	0.62	39	60	27	0.45	35	34	21	0.60	42	55	25	0.45	202	47	28	0.58

Table 2. Statistical significance of the differences in mean snow depth among the sites.

	2013												2014									2015										
	28. XII.	7. I.	17. I.	31. I.	15. II.	3. III.	18. III.	28. III.	5. IV.	12. IV.	18. IV.	28. IV.	29. IX.	12. XII.	28. XII.	9. I.	23. I.	9. II.	23. II.	7. III.	20. III.	3. IV.	17. IV.	5. I.	18. I.	1. II.	13. II.	27. II.	13. III.	28. III.	9. IV.	23. IV.	30. IV.
Living vs. Dead	x	x	x	x	x	x							x	x	x	x			x	x	x		x		x	x	x	x	x	x	x		
Living vs. Meadow	x	x	x	x	x	x		x	x	x	x	x	x	x	x	x			x	x	x		x		x	x		x		x	x	x	
Living vs. Open	x	x	x	x	x	x	x	x	x	x	x	x	x	x	x	x			x	x	x		x		x	x	x	x	x	x	x	x	
Dead vs. Meadow	x	x	x	x	x	x			x		x	x			x	x			x	x	x					x	x	x		x		x	x	
Dead vs. Open	x	x	x	x	x	x	x	x	x	x	x	x	x	x	x	x			x	x	x		x		x	x	x	x	x	x	x	x	x	
Meadow vs. Open	x	x	x	x	x	x	x	x	x	x	x	x	x	x		x	x		x	x	x	x	x		x	x	x	x	x	x	x	x	x	

	2016										2017										
	4. XII.	19. XII.	4. I.	15. I.	28. I.	14. II.	26. II.	11. III.	24. III.	8. IV.	8. XII.	22. XII	5. I.	20. I.	6. II.	17. II.	3. III.	17. III.	31. III.	7. IV.	15. IV.
Living vs. Dead	x	x		x	x	x	x	x	x		x	x	x	x	x	x	x	x		x	
Living vs. Meadow	x	x		x	x	x	x	x	x		x		x	x	x	x	x	x	x	x	
Living vs. Open	x	x		x	x	x	x	x	x		x	x	x	x	x	x	x	x	x	x	
Dead vs. Meadow	x	x		x	x	x	x	x	x		x	x	x	x					x	x	
Dead vs. Open	x	x		x	x	x	x	x	x		x	x	x	x	x	x	x	x	x	x	
Meadow vs. Open	x	x	x	x	x	x	x	x	x		x	x	x	x	x	x	x	x	x	x	

x- Significant difference at 95% level ■-comparison is not available

caused by defoliation. While the differences between the two sites were not very high in the first two winters after forest dieback (2013 and 2014), they clearly increased in winters 2015–2017. The mean SD differences during the first two winters were about 4 cm. In winters 2015–2017 they increased to 7–8 cm (Table 1).

The SD data sets at different sites (snow courses) were statistically significantly different for most days with measurements (Table 2). The SD at site Open was always significantly different from that measured at the forested sites (Living, Dead).

SD in the open area located outside the forest (Meadow) did not have a consistent relation to the SD at sites located in the forest (Dead and Living). In winters 2013, 2014 and during the maximum snow depth period of winter 2016 it was higher, but in winters 2015 and 2017 it was similar (Fig. 3). Wind redistribution and solar radiation have the biggest influence at site Meadow. Therefore, the snow depth at this site is more dependent on weather conditions during any particular winter.

The SD data for the entire winters presented in Fig. 4 show that medians and most often also the first and third quartiles were increasing in the sequence Living < Dead < Meadow < Open.

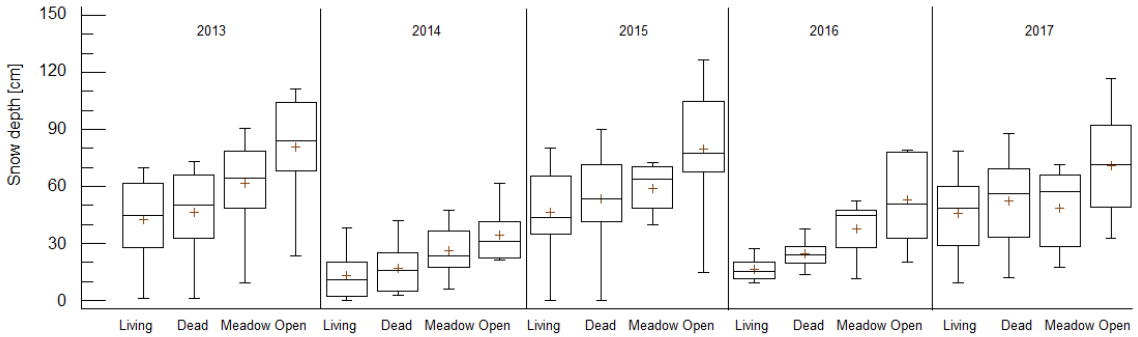

Fig. 4. Box-whisker plots (max-min, lower and upper quartiles, median) of the snow depth for the entire winters; the crosses show arithmetic mean.

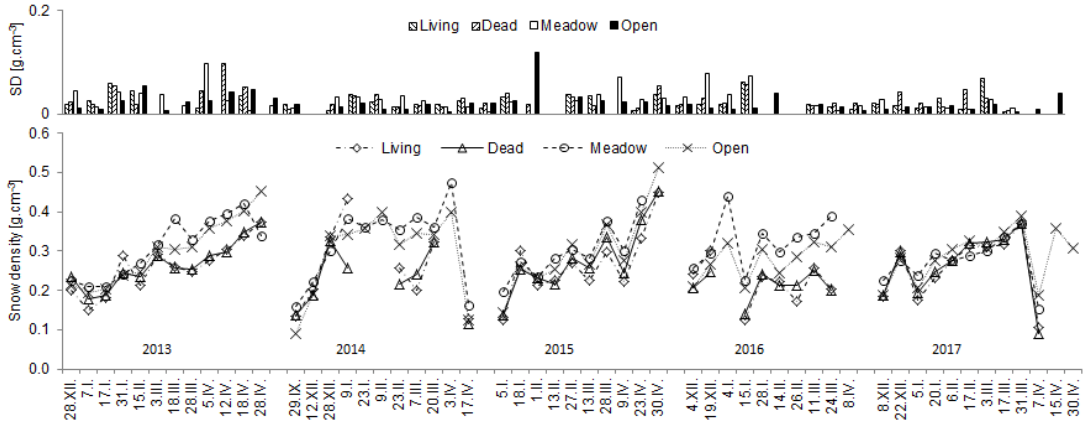

Fig. 5. Snow density and its within-site variability expressed by the standard deviation (SD).

The differences in the average snow SD over the winter were statistically significant with the exception of Living vs. Meadow and Dead vs. Meadow in winters 2015 and 2017. SD variability expressed by Cv at the forested sites (Dead, Living) was in most winters higher than at the sites located in open areas (Open, Meadow) (Table 1). An exception was observed in winter 2016 when the coefficients of variation of SD at the forested sites were smaller than in other winters.

Snow density

Snow density and its within-site variability expressed by the standard deviation are shown in Fig. 5. Maximum snow density was close to 0.5 g.cm^{-3} and standard deviations were mostly below 0.05 g.cm^{-3}. Coefficients of variation of snow density were smaller than those of snow depth. Cvs of snow density on individual days with measurements were mostly below 0.15. Temporal evolution and to some extent also differences in snow density among study sites reflected climatic conditions in individual winters. Favourable conditions, i.e. above-average precipitation and below-average sum of positive air temperatures in winter 2013 were reflected in the continuous increase of snow density. On the contrary, warm weather in winter 2014 resulted in a rapid increase of snow density to high values (wet snow) as early as December, and high variability due to thaws and new snow events afterwards. Fig. 5 also shows that snow density at sites without trees (Open, Meadow) was in most winters higher than at sites located in the forest (Living, Dead). This difference was clearly visible especially in the snowy winter 2013, and it was very small in winter 2017. Differences among particular sites were not large at the beginning of the accumulation period (fresh snow). Rapid decreases in snow density at the end of winter 2014 and at the beginning of April 2017 were caused by new snow following snowpack melt-out.

Snow density at site Dead was significantly different from that at site Living in 13 out of 48 days with data (Table 3). The mean snow density in the living forest was higher than that in the disturbed forest in 18 out of 48 days. However, larger differences (> 0.030 g.cm^{-3}), were observed only in 6 cases. The differences in the remaining 12 cases varied from 0.002 to 0.016 g.cm^{-3}. Such small differences can result from measurement error or natural variability of snow density along the snow course.

Snow density data for the entire winters (Fig. 6, Table 4) show that the main difference among the sites was between the forested and the open areas. The differences within these two groups, i.e. between the living and disturbed forest or between the forest opening and large open area were comparatively smaller. Winter 2017 was an exception, because snow densities at all sites were very similar. Differences in snow density between the disturbed and living forest for the entire winters were not statistically significant.

Unlike with snow depth, the coefficients of variation of snow density at the forested sites (Dead, Living) were often not very different from those in open areas (Open, Meadow). (cf. Tables 1 and 4).

Snow water equivalent and the results from SWE modelling (maximum SWE, snowmelt beginning and duration)

Summary statistics of measured SWE for all sites and the entire winters are presented in Fig. 7. SWE increased in the sequence Living < Dead < Meadow < Open. As expected, open areas had higher SWE than the forested sites. Average SWE during the entire study period in the disturbed forest was about

Table 3. Statistical significance of the differences in mean snow density among the sites.

	2013											2014										2015									
	28. XII.	7. I.	17. I.	31. I.	15. II.	3. III.	18. III.	28. III.	5. IV.	12. IV.	18. IV.	28. IV.	29. IX.	12. XII.	28. XII.	9. I.	23. I.	9. II.	23. II.	7. III.	20. III.	3. IV.	17. IV.	5. I.	18. I.	1. II.	13. II.	27. II.	13. III.	28. III.	9. IV.	23. IV.	30. IV.
Living vs. Dead				x	x											x			x						x				x	x	x	x	
Living vs. Meadow		x	x		x		x	x	x	x	x								x	x			x		x			x	x	x	x	x	
Living vs. Open		x	x	x	x		x	x	x	x	x		x						x	x			x		x			x	x	x	x	x	
Dead vs. Meadow					x		x	x	x	x				x		x			x				x		x			x		x			
Dead vs. Open							x	x	x	x			x			x			x									x	x				
Meadow vs. Open							x							x								x	x										

	2016										2017											
	4. XII.	19. XII.	4. I.	15. I.	28. I.	14. II.	26. II.	11. III.	24. III.	8. IV.	8. XII.	22. XII	5. I.	20. I.	6. II.	17. II.	3. III.	17. III.	31. III.	7. IV.	15. IV.
Living vs. Dead		x		x			x													x	
Living vs. Meadow				x	x	x	x	x	x			x	x	x	x		x		x	x	
Living vs. Open				x	x		x	x	x					x	x	x			x	x	
Dead vs. Meadow		x		x	x	x	x	x	x			x		x	x			x		x	
Dead vs. Open				x			x	x	x						x					x	
Meadow vs. Open														x		x	x			x	

x- Significant difference at 95% level -comparison is not available

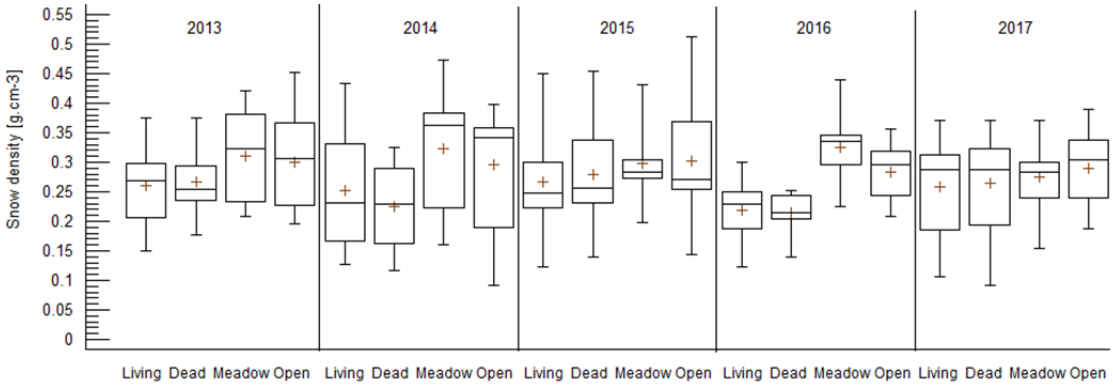

Fig. 6. Box-whisker plots (max-min, lower and upper quartiles, median) of snow density for the entire winters; the crosses show the arithmetic mean.

25% higher than in the living forest. SWE in the forest opening was on average 31% higher than in the large open area (Meadow). This is in agreement with the finding that forest openings with widths about 1–2 times the canopy height (such as the opening in our study) have the most snow (Kittredge, 1953). SWE variability expressed by Cv increased in the opposite order as the SWE values, i.e. Open < Meadow < Dead < Living. Similarly to snow density, the SWE variability within the two groups of sites (forested, open) was smaller than between them.

After visual comparison of measured and simulated SWE (Fig. 8) we have concluded that simulated SWE maxima and dates when the snowpack entirely melted were estimated reasonably well. A more detailed analysis of data reproduction is given later in the discussion.

Modelling results relevant to the theme of this article, i.e. the differences in snow accumulation and melt at different sites, are summarized in Table 5. They show that since winter 2015, maximum SWE in the disturbed forest was always greater than in the living forest. That corresponds to the increase in snow depth that started to become evident at the Dead site since the same winter. The final snowmelt phase, i.e. the snowmelt which ended with snow disappearence, started in the living

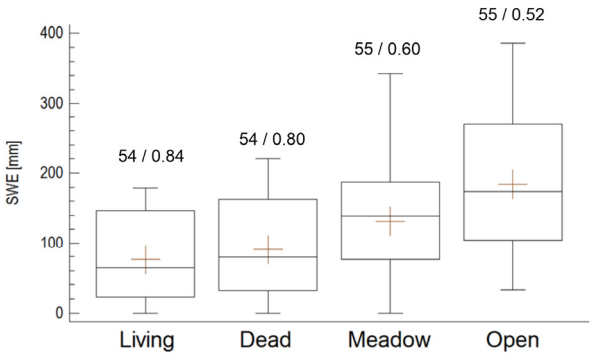

Fig. 7. Box-whisker plots (max-min, first and third quartiles, median) of measured SWE for all winters; the crosses show the arithmetic mean; the numbers above the graphs represent number of measurements (54–55) and coefficient of variation (0.52–0.84).

forest mostly later than in the disturbed forest (Dead), but the delay was only about 1–2 days. Although the SWE in the living forest was typically smaller than at other sites, the snow usually disappeared there approximately on the same days.

Table 4. Snow density [g.cm^{-3}] and its variability for the entire winter seasons.

	2013				2014				2015				2016				2017				2013–2017			
	Count	Average	Standard deviation	Coeff. of variation	Count	Average	Standard deviation	Coeff. of variation	Count	Average	Standard deviation	Coeff. of variation	Count	Average	Standard deviation	Coeff. of variation	Count	Average	Standard deviation	Coeff. of variation	Count	Average	Standard deviation	Coeff. of variation
Living	12	**0.260**	0.066	0.25	8	**0.252**	0.107	0.42	10	**0.266**	0.087	0.33	8	**0.220**	0.054	0.25	10	**0.258**	0.081	0.32	48	**0.253**	0.078	0.31
Dead	12	**0.266**	0.058	0.22	8	**0.225**	0.078	0.35	10	**0.280**	0.090	0.32	8	**0.214**	0.036	0.17	10	**0.264**	0.085	0.32	48	**0.253**	0.073	0.29
Meadow	12	**0.310**	0.077	0.25	11	**0.322**	0.100	0.31	9	**0.298**	0.070	0.24	9	**0.326**	0.066	0.20	10	**0.276**	0.060	0.22	51	**0.307**	0.076	0.25
Open	12	**0.301**	0.084	0.28	11	**0.295**	0.108	0.37	10	**0.303**	0.102	0.34	10	**0.283**	0.050	0.18	12	**0.290**	0.066	0.23	55	**0.294**	0.082	0.28
Total	48	0.284	0.073	0.26	38	0.279	0.103	0.37	39	0.286	0.086	0.30	35	0.264	0.069	0.26	42	0.273	0.072	0.26	202	0.278	0.081	0.29

Measured data at the end of the snowmelt season were used to compare maximum snowmelt intensities at different sites during the precipitation free periods and corresponding degree-day factors obtained from both measured data and model calibration. Unfortunately, this was possible only for winter 2013, because precipitation occurred during maximum snowmelt intensity periods in all other winters. The results are presented in Table 6. Although the numbers from only one winter cannot be generalized, the results confirm that snowmelt intensity in the disturbed forest was higher than in the living forest. The largest snowmelt was observed in the forest opening. Snowmelt in the open areas (Open, Meadow) was almost 60% greater than at the forested sites (Living, Dead).

Degree-day factors for 18–28 April 2013 calculated from measured data were similar to those obtained during model calibration.

SWE in our study was significantly higher (25%) in the disturbed forest than in the living forest. This difference is probably related to higher snow depth in the disturbed forest. However, unlike for snow depth, there was no significant SWE difference between the disturbed and living forest in individual winters (Fig. 8). Jeníček et al. (2018) did not directly compare SWE in the healthy and disturbed forest. However, they reported a smaller SWE difference (29%) between open areas and defoliated spruce forest with standing trees compared to the difference between open area and healthy forest (45%). This implies that the difference between the disturbed and healthy forest was 16%. Boon (2012) concluded that snow density and SWE in disturbed and living forests are similar in high snow years while they are distinctly different in low-to-average snow years. However, their study was based only on two years of measured data. Pugh and Small (2012) reported 15% more snow in a "grey phase stand" (needleless trees) than in a paired living stand. Their results are also based on two years of measured data at eight pairs of living and disturbed forest stands. Our data confirm the findings of Boon (2012) and Pugh and Small (2012) that the SWE difference between the disturbed and living forest is smaller for winters with higher snow accumulation (Fig. 9). Nevertheless, the SWE difference remained relatively high (about 20%) also in winters with high snow accumulation (Fig. 9).

Evaluation of the snowmelt model efficiency by the objective function showed that KGE efficiency was high (between 0.7 and 1) for almost all simulations (Table 7). This is not surprising, because model parameters were changed independently for each site and winter to obtain the best simulation possible and we focused primarily on good reproduction of measured values on dates close to winter maximum SWE and during the ablation period. While model parameters based on such a strategy cannot be transferred to other sites or winters, we believe that SWE maxima and dates when the snow cover entirely melted were estimated reasonably well. However, detailed analysis of other simulated results such as the degree-day factors from such a modelling strategy is not meaningful. Table 7 shows that deleting one overestimated value at the beginning of the winter would significantly improve the KGE values for two of three simulations (sites Living and Dead in winter 2016). Analysis of the sources of modelling errors for site Meadow in winter 2015 (equation 2) showed that mean values of observed and corresponding simulated data were the same (172 mm) and the correlation coefficient was high (0.88). A low KGE value (0.008) resulted from the much higher standard deviation of the simulated data compared to that of observations. However, the observed values at the time of maximum measured SWE and

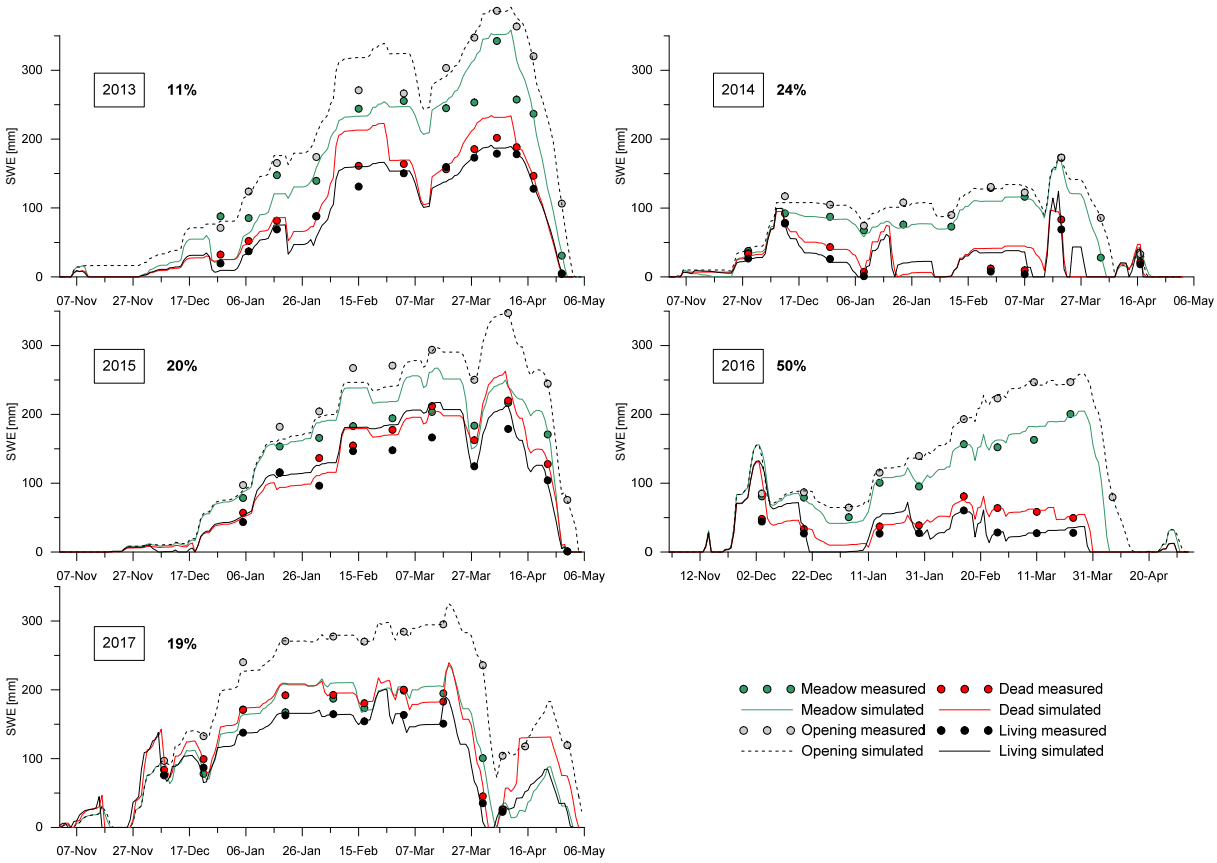

Fig. 8. Simulated and measured SWE in winters 2013–2017; the percentages show the amount by which the winter mean SWE in the disturbed forest (Dead) was greater than that in the living forest.

Table 5. Characteristics of snow accumulation and melt from snow modelling.

Winter	Maximum snow water equivalent [mm]				Snowmelt duration [days]			
	Living	**Dead**	**Meadow**	**Open**	**Living**	**Dead**	**Meadow**	**Open**
2013	191	202	350	392	19	24	20	23
2014	124	96	173	173	10	5	17	19
2015	212	263	250	351	22	22	21	26
2016	37	81	205	258	3	4	18	20
2017	189	239	236	325	45	46	44	48
	Snowmelt beginning				**Snowmelt end**			
	Living	**Dead**	**Meadow**	**Open**	**Living**	**Meadow**	**Open**	**Dead**
2013	10-Apr	5-Apr	10-Apr	10-Apr	29-Apr	30-Apr	3-May	29-Apr
2014	19-Mar	17-Mar	20-Mar	20-Mar	29-Mar	6-Apr	8-Apr	22-Mar
2015	9-Apr	8-Apr	8-Apr	8-Apr	1-May	29-Apr	4-May	30-Apr
2016	27-Mar	28-Mar	26-Mar	26-Mar	30-Mar	13-Apr	15-Apr	1-Apr
2017	19-Mar	19-Mar	19-Mar	19-Mar	3-May	2-May	6-May	4-May

the beginning of snowmelt were simulated moderately well (the differences between measured and simulated values were 10% and 3%). Unlike in other winters, SWE close to snow disappearance was not measured at the Meadow site in winter 2015 (Fig. 8) which did not allow us to compare the measured and simulated values during the time of intensive ablation and which would probably improve the KGE value.

DISCUSSION

Our results revealed a statistically significant difference in SD between the living and disturbed forest which increased since the third winter after forest dieback. The difference in SD was most noticeable during snow maximum. These results cannot be directly compared with findings of other studies using measured snow characteristics in the disturbed forests, because most of them were based only on 1-2 years of data. Only Jeníček et al. (2018) had five years of data. They measured snow characteristics at 16 sites including 3 sites affected by the bark beetle. Although their measurements were conducted only 2-4 times per winter, the snowmelt periods were captured in all five winters. However, they did not evaluate the interannual evolution of SD differences in the living and disturbed forest.

Snow density in the disturbed and living forest was in most cases not significantly different. Jeníček et al. (2018) reported that compared to the healthy forest (an analog of the living forest in our study), snow density was slightly greater in the disturbed forest during the accumulation period. In contrast, snow density in the healthy forest was greater in the snowmelt period. Their conclusions were drawn from integrating the snow density data for the entire study period. Analogous data in our study reveal clear differences between the two groups of sites (forested versus open) while the differences within each group were smaller (Fig. 6, Table 4).

Table 6. Snowmelt characteristics during the maximum snowmelt intensity period (18–28 April 2013); DDF_{obs} and DDF_{cal} are degree-day factors calculated from the measured data and from model calibration, respectively

Site	Snowmelt intensity [mm.day^{-1}]	Total snowmelt [mm]	DDF_{obs} [mm.day^{-1}.°C]	DDF_{cal} [mm.day^{-1}.°C]
Living	12.3	123	1.51	1.45
Dead	14.3	143	1.76	1.80
Meadow	20.6	206	2.53	2.50
Open	21.4	214	2.63	2.40

Table 7. Kling-Gupta efficiency coefficients; the values with asterisks represent KGE if one simulated value at the beginning of the snow season were omitted.

Winter	Living	Dead	Meadow	Open
2013	0.902	0.773	0.692	0.942
2014	0.821	0.833	0.901	0.93
2015	0.695	0.952	0.008	0.959
2016	–0.807 (0.698*)	0.275 (0.969*)	0.699	0.936
2017	0.866	0.962	0.909	0.99

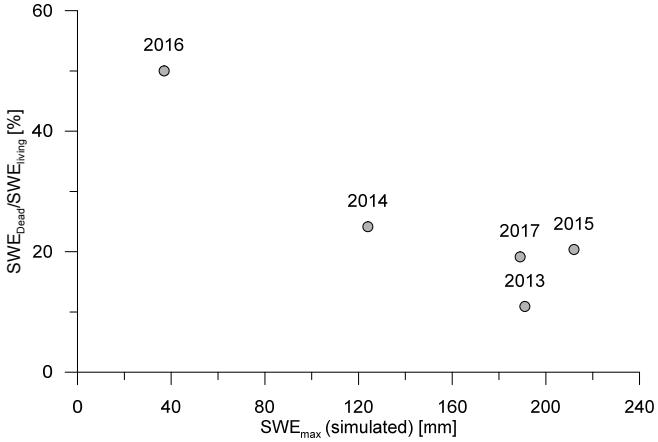

Fig. 9. The relationship between winter snow accumulation (simulated maximum SWE in the living forest at the beginning of the final snowmelt phase in mm) and the percent difference in measured mean winter SWE in the disturbed (SWE_{Dead}) and living forest (SWE_{Living}) for winters 2013–2017; a value of 50% on the vertical axis means that mean SWE in the disturbed forest was 50% greater than that in the living forest.

Snowmelt intensity in the disturbed forest based on measured data from the end of winter 2013, i.e. the first winter after forest dieback (and the high-snow winter), was 16% higher than in the living forest (Table 6). This was an expected result because forest dieback increases incoming solar radiation. Jeníček et al. (2018) reported a similar difference (18%). Their value was based on simulated degree-day factors for five winters. Our preference of using measured instead of simulated values means that we could compare the data from only one of the five winters. In other winters, either the SWE was not measured on days close to the snow disappearance or the snowmelt was affected by precipitation. Thus, it was not possible to investigate the evolution of the differences in ablation rates with time elapsed since the forest dieback. Simulated SWEs indicated that the mean ablation intensities at the end of winters 2013-2017 in the living and disturbed forest were similar, and ablation at the Meadow and Open sites were on average 7% and 16% higher than at forested sites, respectively. However, because we had only five values (winters) for each site and the values in individual winters varied, the comparison of the mean values of ablation rates obtained from the modelling is not meaningful.

CONCLUSIONS

This article presents the results of longer-term (five winters) and relatively frequent (every two weeks) measurements of snow characteristics at four sites with different land cover. The main focus was the differences between the living and disturbed forest. Snow depth was significantly greater in the disturbed forest and the difference increased since the third winter after dieback. Differences in snow density were in most cases not significant. Differences in snow water equivalent (SWE) reflected differences in snow depth, although the progressive increase during the study period (as in the case of snow depth) was not observed. Average SWE over the entire study period in the disturbed forest was 25% greater than in the living forest stand. This indicates that the amount of water accumulated in snow in areas affected by large-scale forest dieback could significantly increase. Higher snow accumulation does not necessarily mean that total runoff or flood peaks would be higher (Jeníček et al., 2018). Results of our plot-scale simulations did not indicate significant differences in snowmelt characteristics between the disturbed and living forest. Although the SWE in the living forest was smaller and its variability was greater, the beginning of the final snowmelt phase and the date of snow disappearance at the two stands were similar. However, timing of snowmelt runoff events can change if large parts of originally forested catchments are affected by forest dieback due to higher ablation rates in the disturbed forest. This scenario can be tested in follow-up modelling studies validated against the measured values from the plot-scale data.

Acknowledgements. This work was accomplished as part of VEGA projects No.: 1/0367/16, 1/0589/15, 1/0463/14 and 2/0055/15 of the Ministry of Education, Science, Research and Sport of the Slovak Republic and the Slovak Academy of Science; and the projects of the Slovak Research and Development Agency No.: APVV-0423-10, APVV-0303-11, APVV-15-0425 and APVV-15-0497. We would like to acknowledge also financial support from the European Regional Development Fund Project 26220120062 ‘‘Centre of excellence for the integrated river basin management in changing environmental conditions’’ which allowed purchase of the equipment used in this study. We are grateful to Dr. J. Shanley for the improvement of English.

REFERENCES

Adams, H.D., Luce, C.H., Breshears, D.D., Allen, C.D., Weiler, M., Hale, V.C., Smith, A.M.S., Huxman, T.E., 2012. Ecohydrological consequences of drought- and infestation-triggered tree die-off: insights and hypotheses. Ecohydrology, 5, 145–159.

Anderson, H.W., 1963. Managing California’s Snow Zone Lands for Water. U.S. Forest Service Research Paper PSW-6, 28 p.

Bartík, M., Sitko, R., Oreňák, M., Slovik, J., Škvarenina, J., 2014. Snow accumulation and ablation in disturbed mountain spruce forest in West Tatra Mts. Biologia, 69, 1492–1501.

Bartík, M., Jančo, M., Střelcová, K., Škvareninová, J., Škvarenina, J., Mikloš, M., Vido,J., Dagsson Waldhauserová, P., 2016. Rainfall interception in a disturbed montane spruce (Picea abies) stand in the West Tatra Mountains. Biologia, 71, 1002–1008.

Boon, S., 2012. Snow accumulation following forest disturbance. Ecohydrology, 5, 279–285.

Bredemeier, M., Cohen, S., Godbold, D.L., Lode, E., Pichler, V., Schleppi, P. (Eds.)., 2010. Forest Management and the Water Cycle: An Ecosystem-Based Approach (Vol. 212). Springer Science & Business Media. 531 p.

Celer, S., 2013. Forest in the Jalovecká dolina valley In: Divočina pod Salatínom. REPROservis, Liptovský Mikuláš, pp. 81–104. (In Slovak.) ISBN 978-80-971499-9-4

Church, J.E., 1914. Recent studies of snow in the United States. Quart. Jour. Royal Met. Soc., 40, 169, 43–52.

Elias, V., Tesar, M., Buchtele, J., 1995. Occult precipitation: sampling, chemical analysis and process modelling in the Sumava Mts. (Czech Republic) and in the Taunus Mts. (Germany). Journal of Hydrology, 166, 409–420.

Ellis, C.R., Pommeroy, J.W., Brown, T., MacDonald, J., 2010. Simulation of snow accumulation and melt in needleleaf forest environments. Hydrol. Earth Syst. Sci. Discuss., 7, 1033–1072.

Fišák, J., Řezáčová, D., Eliáš, V., Tesař, M., 2001. Comparison of pollutant concentrations in fog (low cloud) water in Northern and Southern Bohemia. Journal of Hydrology and Hydromechanics, 49, 275–290.

Fleischer, P., Pichler, V., Fleischer, P. Jr., Holko, L., Máliš, F., Gömöryová, E., Cudlín, P., Michalová, Z., Homolová, Z., Škvarenina, J., Střelcová, K., Hlaváč, P., 2017. Forest ecosystem services affected by natural disturbances, cliamte and land-use changes in the Tatra Mountains. Climate Research, 73, 57–71.

Garstka, W.U., Love, L.D., Goodell, B.C., Bertle, F.A., 1958. Factors affecting snowmelt and streamflow. U.S. Bureau of Reclamation and U.S. Forest Service, 189 p.

Golding, D.L, Swanson, R.H., 1986. Snow distribution patterns in clearings and adjacent forest. Water Resources Research, 22, 13, 1931–1940.

Gömöryová, E., Střelcová, K., Škvarenina, J., Gömöry, D., 2013. Responses of soil microorganisms and water content in forest floor horizons to environmental factors. European Journal of Soil Biology, 55, 71–76.

Gömöryová, E., Fleischer, P., Pichler, V., Homolák, M., Gere, R., Gömöry, D., 2017. Soil microorganisms at the windthrow plots: The effect of postdisturbance management and the time since disturbance. IForest, 10, 515–521.

Grodzki, W., Jakuš, R., Lajzová, E., Sitková, Z., Maczka, T., Škvarenina, J., 2006. Effects of intensive versus no management strategies during an outbreak of the bark beetle Ips typographus (L.)(Col.: Curculionidae, Scolytinae) in the Tatra Mts. in Poland and Slovakia. Annals of Forest Science, 63, 55–61.

Gupta, V.H., Kling, H., Yilmaz, K.K., Martinez, F.G., 2009. Decomposition of the mean squared error and NSE performance criteria: Implications for improving hydrological modelling. Journal of Hydrology, 377, 81–90.

Harpold, A.A., Biederman, J.A., Condon, K., Merino, M., Korgaonkar, Y., Nan, Y., Sloat, L.L., Ross, M., Brooks, P.D., 2014. Changes in snow accumulation and ablation following the Las Conchas forest fire, New Mexico, USA. Ecohydrology, 7, 440–452.

Hlaváčiková, H., Novák, V., Šimůnek, J., 2016. The effects of rock fragment shapes and positions on modeled hydraulic conductivities of stony soils. Geoderma, 281, 39–48.

Holko, L., Kostka, Z., 2010. Hydrological processes in mountains – knowledge gained in the Jalovecky Creek catchment, Slovakia. In: Proc. of the Workshop "Status and Perspectives of Hydrology in Small Basins" held at Goslar-Hahnenklee, Germany, 30 March–2 April 2009. IAHS Publ. 336. IAHS Press, Wallingford, pp. 84–89.

Holko, L., Škvarenina, J., Kostka, Z., Frič, M., Staroň, J., 2009. Impact of spruce forest on rainfall interception and seasonal snow cover evolution in the Western Tatra Mountains, Slovakia. Biologia, 64, 594–599.

Holko, L., Danko, M., Kostka, Z., 2012. Classification of winters, density of the new snow and the degree-day factor in the Jalovecký creek catchment. Acta Hydrologica Slovaca, 13, 2, 342–349. (In Slovak with an English abstract and summary.)

Chang, M., 2006. Forest Hydrology: An Introduction to Water and Forests, Second Edition. CRC Press, Taylor & Francis group, Boca Raton, London, New York, 488 p.

Jakuš, R., Zajíčkova, L., Cudlín, P., Blaženec, M., Turčani, M., Ježík, M., Lieutier, F., Schlyter, F., 2011. Landscape-scale Ips typographus attack dynamics: From monitoring plots to GIS-based disturbance models. IForest, 4, 256–261.

Janda, P., Trotsiuk, V., Mikolas, M., Bace, R., Nagel, T., Seidl, R., Seedre, M., Morrissey, R.C., Kucbel, S., Jaloviar, P., Jasik, M., Vysoky, J., Samonil, P., Cada, V., Mrhalova, H., Labusova, J., Novakova, M., Rydval, M., Mateju, L., Svoboda, M., 2016. The historical disturbance regime of mountain Norway spruce forests in the Western Carpathians and its influence on current forest structure and composition. Forest Ecology and Management, 388, 67–78.

Jenicek, M., Pevna, H., Matejka, O., 2018. Canopy structure and topography effects on snow distribution at a catchment scale: Application of multivariate approaches. J. Hydrol. Hydromech., 66, 1, 43–54.

Jewitt, G., 2005. Water and forests. In: Anderson, M.G., McDonnell, J.J. (Eds.): Encyclopedia of Hydrological Sciences, Chapter 186. John Wiley & Sons, Ltd., pp. 2895–2909.

Kittredge, J., 1953. Influence of forests on snow in the Ponderosa-Sugar pine-fir zone of the Central Sierra Nevada. Hilgardia, 22, 1, 1–96.

Koivusalo, H., Kokkonen, T., 2002. Snow processes in a forest clearing and in a coniferous forest. Journal of Hydrology, 262, 145–164.

Krajčí, P., Holko, L., Parajka, J., 2016. Variability of snow line elevation, snow cover area and depletion in the main Slovak basins in winters 2001–2014. Journal of Hydrology and Hydromechanics, 64, 1, 12–22.

Kuusisto, E., 1980. On the values and variability of degree-day melting factor in Finland. Nord. Hydrol., 11, 235–242.

Lundberg, A., Calder, I., Harding, R., 1998. Evaporation of intercepted snow: measurement and modelling. J. Hydrol., 206, 151–163.

Mayer, H., Feger, K.H., Ackertvlann, B., Armbruster, M., 1997. Schneedeckenentwicklung in Fichtenwäldern im südlichen Hochschwarzwald. Forstw. Cbl., 116, 370–380.

Mezei, P., Grodzki, W., Blaženec, M., Škvarenina, J., Brandýsová, V., Jakuš, R., 2014. Host and site factors affecting tree mortality caused by the spruce bark beetle (*Ips typographus*) in mountainous conditions. Forest Ecology and Management, 331, 196–207.

Mezei, P., Jakuš, R., Pennerstorfer, J., Havašová, M., Škvarenina, J., Ferenčík, J., Slivinský, J., Bičárová, S., Bilčík, D., Blaženec, M., Netherer, S., 2017. Storms, temperature maxima and the Eurasian spruce bark beetle *Ips typographus* – An infernal trio in Norway spruce forests of the Central European High Tatra Mountains. Agricultural and Forest Meteorology, 242, 85–95.

Michalová, Z., Morrrissey, RC, Wohlgemuth, T., Bače, R., Fleischer, P., Svoboda, M., 2017. Salvage logging after windstorm leads to structural and functional homogenisation of understory layer and delayed spruce tree recovery in Tatra Mts., Slovakia. Forests, 8, 88. DOI: 10.3390/f8030088.

Minďáš, J., Škvarenina, J., 1995. Chemical composition of fog cloud and rain snow water in Biosphere Reserve Pol'ana. Ekologia-Bratislava, 14, 125–137.

Mráček, Z., Krečmer, V., 1975. Význam lesa pro lidskou společnost. SZN. 225 p. (In Czech.)

Nash, J.E., Sutcliffe, J.V., 1970. River flow forecasting through conceptual models, Part I - A discussion of principles. Journal of Hydrology, 10, 282–290.

Oreňák, M., Vido, J., Hríbik, M., Bartík, M., Jakuš, R., Škvarenina, J., 2013. Interception process of spruce forest in the phase of disintegration in the Western Tatras (Západné Tatry), Slovakia. Zpravy Lesnickeho Vyzkumu, 58, 360–369. (In Slovak.)

Parobeková, Z., Sedmáková, D., Kucbel, S., Pittner, J., Jaloviar, P., Saniga, M., Balanda, M., Vencurik, J., 2016. Influence of disturbances and climate on high-mountain Norway spruce forests in the Low Tatra Mts., Slovakia. Forest Ecology and Management, 380, 128–138.

Perrot, D., Molotch, P., Musselman, N., Pugh, T., 2012. Modelling the effects of the mountain pine beetle on snowmelt in a subalpine forest. Ecohydrol., 7, 226–241.

Pugh, E., Small, E., 2012. The impact of pine beetle infestation on snow accumulation and melt in the headwaters of the Colorado River. Ecohydrol., 5, 467–477.

Rogger, M., Agnoletti, M., Alaoui, A., Bathurst, J.C., Bodner, G., Borga, M., Chaplot, V., Gallart, F., Glatzel, G., Hall, J., Holden, J., Holko, L., Horn, R., Kiss, A., Kohnová, S., Leitinger, G., Lennartz, B., Parajka, J., Perdigao, R., Peth, S., Plavcová, L., Quinton, J.N., Robinson, M., Salinas, J.L., Santoro, A., Szolgay, J., Tron, S., van den Akker, J.J.H., Viglione, A., Blöschl, G., 2017. Land use change impacts on floods at the catchment scale: Challenges and opportunities for future research. Water Resour. Res., 53. DOI:10.1002/2017WR020723.

Seidl, R., Schelhaas, M.J., Lexer, M.J., 2011. Unraveling the drivers of intensifying forest disturbance regimes in Europe. Global Change Biology, 17, 2842–2852.

Stähli, M., Papritz, A., Waldner, P., Forster, F., 2000. Die Schneedeckenverteilung in einem voralpinen Einzugsgebiet und ihre Bedeutung für den Schneeschmelzabfluss. Schweiz. Z. Forstwes., 151, 6, 192–197.

Stähli, M., Badoux, A., Ludwig, A., Steiner, K., Zappa, M. Hegg, C., 2011. One century of hydrological monitoring in two small catchments with different forest coverage. Environmental Monitoring and Assessment, 174, 91–106. DOI: 10.1007/s10661-010-1757-0.

Swanson, R.H., Golding, D.L., 1982. Snowpack management on Marmot waterhsed to increase late season streamflow. In: Proc. Western Snow Conference 1982, pp. 215–218.

Troendle, C.A., King, R.M., 1985. The effect of timber harvest on the Fool Creek Watershed, 30 years later. Water Resources Research, 21, 12, 1915–1922.

Troendle, C.A., King, R.M., 1987. The effect of partial and clearcutting on streamflow at Deadhorse Creek, Colorado. J. Hydrol., 90, 145–157.

Varhola, A., Coops, N.C., Weiler, M., Moore, D.R., 2010. Forest canopy effects on snow accumulation and ablation: An integrative review of empirical results. Journal of Hydrology, 392, 219–233.

Vido, J., Tadesse, T., Šustek, Z., Kandrík, R., Hanzelová, M., Škvarenina, J., Škvareninová, J., Hayes, M., 2015. Drought occurrence in central european mountainous region (Tatra National Park, Slovakia) within the period 1961–2010. Advances in Meteorology, 2015, Article ID 248728, 8 p. DOI: 10.1155/2015/248728.

Winkler, R., Boon, S., Zimonick, B., Spittlehouse, D., 2014. Snow accumulation and ablation response to changes in forest structure and snow surface albedo after attack by mountain pine beetle. Hydrological Processes, 28, 197–209.

Zelený, V., 1971. The effect of the spruce stand reneval by clearing on the snow conditions. Vodohospodársky časopis (J. Hydrol. Hydromech.), 19, 6, 571–590. (In Czech with an English abstract.)

Received 23 October 2017
Accepted 22 April 2018

J. Hydrol. Hydromech., 67, 2019, 1, 70–81
DOI: 10.2478/johh-2018-0004

Revisiting a simple degree-day model for integrating satellite data: implementation of SWE-SCA hystereses

Philippe Riboust[1, 2*], Guillaume Thirel[2], Nicolas Le Moine[1], Pierre Ribstein[1]

[1] Sorbonne Universités, UPMC Univ., Paris 06, CNRS, EPHE, UMR 7619 Metis, 4 place Jussieu, 75005 Paris, France.
[2] Hydrosystems and Bioprocesses Research Unit (HBAN), Irstea, 1 rue Pierre-Gilles de Gennes, CS 10030, 92761 Antony Cedex, France.
[*] Corresponding author. E-mail: philippe.riboust@irstea.fr

Abstract: Conceptual degree-day snow models are often calibrated using runoff observations. This makes the snow models dependent on the rainfall-runoff model they are coupled with. Numerous studies have shown that using Snow Cover Area (SCA) remote sensing observation from MODIS satellites helps to better constrain parameters. The objective of this study was to calibrate the CemaNeige degree-day snow model with SCA and runoff observations. In order to calibrate the snow model with SCA observations, the original CemaNeige SCA formulation was revisited to take into account the hysteresis that exists between SCA and the snow water equivalent (SWE) during the accumulation and melt phases. Several parametrizations of the hysteresis between SWE and SCA were taken from land surface model literature. We showed that they improve the performances of SCA simulation without degrading the river runoff simulation. With this improvement, a new calibration method of the snow model was developed using jointly SCA and runoff observations. Further analysis showed that the CemaNeige calibrated parameter sets are more robust for simulating independent periods than parameter sets obtained from discharge calibration only. Calibrating the snow model using only SCA data gave mixed results, with similar performances as using median parameters from all watersheds calibration.

Keywords: Snow model; Hysteresis parametrization; MODIS snow cover area; Rainfall-runoff model.

INTRODUCTION

Snow accumulation in winter as well as spring snowmelt gives to mountain catchments a particular hydrological response that should be taken into account when modelling river runoff. Rainfall-runoff models are often coupled with snow models so that solid precipitation storage in snow reservoirs can be represented and released as river runoff when this accumulated snow melts. Improving the snow dynamics modelling is a necessity for improving hydrological forecasting for snow-dominated catchments. Snow-dominated areas are very sensible to temperature changes; therefore climate change can drastically impact the hydrological cycle (Beniston et al., 2017; Bernsteinová et al., 2015) and the population living in these regions (one sixth of the world, estimated by Barnett et al., 2005). For studying the impacts of climate change in mountains and other snow-dominated region, the robustness and reliability of models have to be assessed (and improved) in order to ensure that the model structure and parameters are still valid for simulating river runoff in a different climate context (Thirel et al., 2015a, 2015b).

To improve the robustness of degree-day empirical snow models, numbers of studies have demonstrated the advantages of snow cover data in addition to the runoff observations to calibrate and validate models (e.g. Franz and Karsten, 2013; Parajka and Blöschl, 2008a) or using data assimilation techniques (Andreadis and Lettenmaier, 2006; Rodell and Houser, 2004; Slater and Clark, 2006; Thirel et al., 2013). Snow models are traditionally calibrated only with runoff observations, making the obtained parameter sets dependent on the rainfall-runoff model used. Adding snow data information to the calibration procedure allows the snow model to be less dependent on the hydrological model, and therefore allows to obtain more robust snow parameter sets (Franz and Karsten, 2013). In addition to the improvement of the robustness of the snow model, this procedure also helps to better identify its structure and parameters (Grayson et al., 2002; He et al., 2014; Parajka and Blöschl, 2008b, 2008a). Most of these studies used satellite Snow Cover Area (SCA) from the MODIS sensor (Hall et al., 2006), which provides a spatialized vision of the presence of snow on the ground at a 500m resolution. The main disadvantage of MODIS satellite data is that it cannot provide SCA data when there is cloud cover. Several methods have been developed to compensate for these deficiencies, most of which are based on a spatio-temporal filter, i.e., replacing the missing pixel value with its nearest neighbors, whether it be spatial or temporal (Da Ronco and De Michele, 2014; eg. Parajka and Blöschl, 2008b; Poggio et al., 2012). Another approach, which can be additionally used for filling lacunar MODIS data, is to determine the regional snowline elevation (Gafurov and Bárdossy, 2009; Krajčí et al., 2014, 2016; Parajka et al., 2010). SCA data give only geographic information about presence or absence of snow without giving any information about the quantity of Snow Water Equivalent (SWE) present on the watershed. SWE would be more valuable than SCA for snow models, but unfortunately the accuracy of remote sensing SWE data is too low to be used effectively (Vuyovich et al., 2014) and point scale measurements are scarce and difficult to interpolate (Parajka et al., 2012).

SCA parametrization within snow models is highly dependent on the resolution selected. When the model represents an area with a heterogeneous topography, the relation between the SCA and the quantity of SWE averaged over the area forms a hysteresis (Luce and Tarboton, 2004). During an accumulation period, the SCA increases very quickly and remains stable, whereas the SWE increases slowly. On the opposite, during a melting period, the decrease in the SCA is slower and more gradual. The relation between SWE and SCA therefore differs depending on whether a snowmelt period or a snow accumulation period is considered. Snow accumulates heterogeneously in the watershed due to redistribution of snow by wind drift (Essery and Pomeroy, 2004). During the melting period, snow tends to melt uniformly with variations depending on the mountain slope and orientation (Egli and Jonas, 2009). Snow patches

tend to be created during the melting period, due to the combination of heterogeneous snow depths and to heterogeneous melt rates at watershed scale (Egli and Jonas, 2009; Helbig et al., 2015; Magand et al., 2014). This representation of the snow cover area is an issue that has greatly interested the Land Surface Modelling (LSM) community. As snow's albedo has a strong retroaction on the earth–atmosphere coupling because of its influence on the energy budget, precise knowledge of the SCA is necessary (Zaitchik and Rodell, 2009). This is why LSMs often integrate a parametrization of hysteresis, linking SCA to SWE, whose complexity can vary (Liston, 2004; Magand et al., 2014; Nitta et al., 2014; Niu and Yang, 2007; Swenson and Lawrence, 2012). Parametrizations of the hysteresis have been introduced in a few snow models (Clark et al., 2011; Duethmann et al., 2014; Franz and Karsten, 2013; Kolberg and Gottschalk, 2006; Magnusson et al., 2014), as the hysteresis may be even found at small geographical scales (Luce and Tarboton, 2004).

To more accurately represent river runoff in snow-covered catchments using lumped GR rainfall-runoff models (Le Moine et al., 2007; Perrin et al., 2003; Pushpalatha et al., 2011), the CemaNeige snow-accounting routine (Valéry et al., 2014a, 2014b) was developed. The present study is based on this model, which is a degree-day model whose primary objective is to assist the hydrological model in accurately simulating mountain river runoff as parsimoniously as possible, i.e., with the minimum of free parameters to calibrate. Once its development had been completed, the number of parameters necessary for the snow module was limited to two and required only air temperature (mean temperature or minimum and maximum daily temperatures) and daily precipitation as forcing variables. The CemaNeige snow model has been tested on French, Swiss, Swedish and Canadian watersheds (Valéry et al., 2014b), and an intercomparison of multiple snow-accounting models coupled with different rainfall-runoff models has been made (Troin et al., 2016, 2015). This study showed that the CemaNeige snow-accounting model gave good performances in the Québec area when coupled with any hydrological model. In other types of climate, the CemaNeige snow model has shown some limitations. In Nepal (Pokhrel et al., 2014) the model performances were limited, certainly due to the fact that glacier melt and sublimation processes are not yet represented in CemaNeige. In the dry Andes, the CemaNeige model had to be adapted in order to take into account the sublimation process which is a major cause of snow ablation in arid mountain catchments (Hublart et al., 2016).

The objective of the study is to improve the robustness of the CemaNeige snow-accounting model when used with a rainfall-runoff model. For this, the use of MODIS SCA data for calibration was investigated and diverse weights in the objective function, between SCA and discharge, were tested. In order to make full use of MODIS SCA data at the catchment scale, SWE-SCA hysteresis were implemented in the snow model and assessed.

DATA

SAFRAN and MODIS data

The forcing data used by the GR4J model with CemaNeige comes from SAFRAN data (Quintana-Seguí et al., 2008; Vidal et al., 2010). SAFRAN is an atmospheric reanalysis model: it assimilates surface observations to calculate the energy fluxes as well as temperature, precipitation, humidity, and wind on a regular 64-km² grid. For the needs of this study, only SAFRAN temperature and precipitation data were used, after they were aggregated by catchment on the daily time step.

The MODIS snow cover product (Hall et al., 2006) came from the National Snow and Ice Data Center (NSIDC, http://nsidc.org). The first measurements were taken in summer 2000 by the Terra satellite, followed 2 years later by measurements from the Aqua satellite. The MODIS instruments measure visible radiance. A post-treatment deduces binary snow cover data on 500-m resolution grids once or twice a day.

For this study, the MODIS data were aggregated over different elevation zones on each catchment so that they would be comparable to the CemaNeige simulations. This aggregation makes it possible to obtain a snow fraction for each band. The quality of the snow fraction provided by MODIS is considered unsatisfactory if the proportion of pixels covered by clouds is greater than 40% of the total number of pixels of the elevation zone considered. If this threshold is not satisfied, these data are not taken into account for the calibration and evaluation procedures.

Selection of catchments

The catchments for this study were selected based on several criteria:

- data availability
- sufficient catchment snow cover
- low catchment's anthropization

The availability of runoff data and MODIS data is a limiting factor. The runoff data used came from the Hydro database (http://www.hydro.eaufrance.fr/); they were available at the daily time step and extracted up to the end of 2010. In addition to this, the MODIS data begins in 2000. We decided to preserve the catchments whose runoff data contained a maximum of 1 year of missing data for the 2000–2005 period and the 2005–2010 period. Moreover, only the catchments whose runoff was nearly natural, for example not influenced by dams, were retained. This limits the number of catchments available in high-altitude mountainous areas, which are often developed for hydroelectric power production.

To ensure that the watersheds were frequently snow-covered, we decided to retain only those whose outlet was located above 300 m and whose annual snow cover lasted a minimum 30 days on the catchment's highest elevation zone (i.e. 20% of the watershed area) according to MODIS data. Finally, 277 catchments fulfilled these conditions and were used for this study (Figure 1).

METHODS

Description of the CemaNeige snow-accounting model

The CemaNeige snow-accounting model (Figure 2) is a degree-day snow model with two free parameters with a simple representation of the catchment's SCA (Valéry et al., 2014b). The snowmelt generated by the snow module is considered as liquid precipitation in the GR4J rainfall-runoff model. To take into account the effects of the relief on precipitation, the CemaNeige snow-accounting model is distributed into elevation zones with equal surface area, usually five bands. Temperature and precipitation are extrapolated for each elevation zone (Valéry et al., 2014a). Both the basic version of CemaNeige and the GR4J model come from the R airGR package (Coron et al., 2017a, 2017b).

The CemaNeige model determines the fraction of solid precipitation that accumulates when temperature conditions are adapted. To take into account the thermal inertia of the snowpack, melting is delayed by a formulation taking the air tempera-

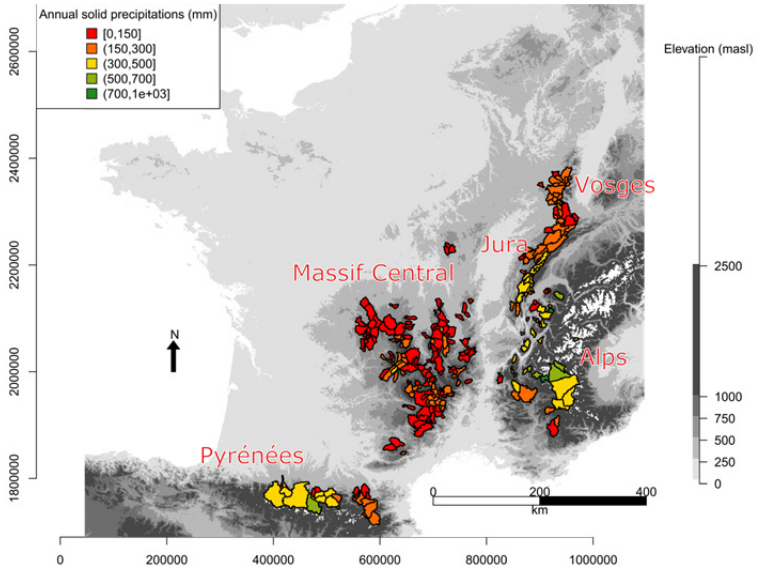

Fig. 1. Map of the 277 watersheds used in this study. The color of the basins represents the mean annual solid precipitation.

ture of the preceding days into account (Eq. 1), modulated by one parameter (cT). The snowpack's cold content (eT_G) is calculated based on weighting between the value of the internal variable eT_G of the preceding time step and the air temperature of the day considered.

$$eT_{G_t} = \min\left(cT \,.\, eT_{G_{t-1}} + (1-cT)\,T_{mean_t}\ ,0\right) \quad (1)$$

When the snow mantel's temperature simulation (eT_G) reaches a value of 0 and the mean air temperature (T_{mean}) is greater than 0°C, potential melting ($Melting_{pot}$) is calculated, which is dependent on the melting factor Kf (Eq. 2).

$$Melting_{pot_t} = Kf \,.\, T_{mean_t} \quad (2)$$

This potential melting is modulated depending on the overall snow surface by the following formula:

$$Melting_t = (0.9\,SCA_t + 0.1)\,Melting_{pot_t} \quad (3)$$

For a 100% SCA, melting will be identical to potential melting. The more the SCA decreases, the more the melting speed decreases, to a minimum of 10% of the potential melting. The SCA is calculated in the model as follows:

$$SCA_t = \min\left(\frac{SWE_t}{T_{h,melt}},1\right) \quad (4)$$

where the SWE is the quantity of snow accumulated on the catchment in snow water equivalent (a state variable of the model, in mm) and where $T_{h,melt}$ is the model's melting threshold. This $T_{h,melt}$ melting threshold is calculated as being equal to 90% of mean annual solid precipitation on the catchment considered (Valéry et al., 2014b).

This melting modulation stems from the fact that preferential melting is usually established based on the mountain's slope exposure: shaded slopes tend to melt less quickly than sunny slopes. The conceptual model therefore includes a state variable close to the SCA. However, this formulation of the SCA does not necessarily give values that can be directly compared to the MODIS observations because this melting formulation only takes into account that the relation between the SWE and the SCA is not unequivocal and differs depending on whether an

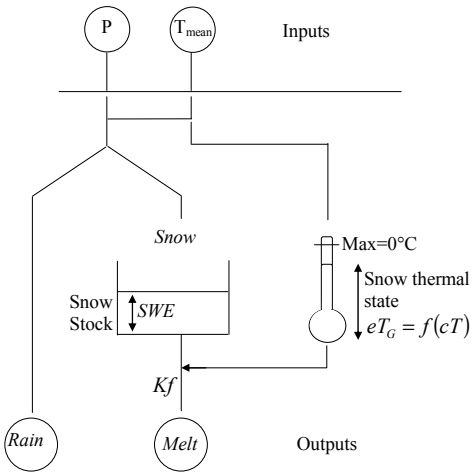

Fig. 2. Schematic representation of the CemaNeige snow model (Modified from Valéry et al., 2014b).

accumulation or a melting period is considered. To take this into account, we suggest a hysteresis that allows simulating a fast increase of the SCA at the accumulation period and a smooth decrease at the ablation period. The fast increase at the accumulation period is due to a homogeneous increase of the SCA with snowfall (although the redistribution of snow creates high disparities in snow depths). The heterogeneous SWE coupled to heterogeneous melt rates due to the topography tends to create patchy snow areas (Liston, 2004; Magand et al., 2014).

Hysteresis

To take this melting heterogeneity into account, several hystereses were implemented and tested in the CemaNeige snow-accounting routine. The hystereses selected in the literature are presented in this section.

Accumulation curve

The snow cover curve dependent on the SWE in case of accumulation was formulated with a linear function dependent on an accumulation threshold $T_{h,acc}$. This follows the following relation:

$$\Delta SWE_t = P_{sol_t} - Melting_t \quad (5)$$

$$SCA_t = \min\left(SCA_{t-1} + \frac{\Delta SWE_t}{T_{h,\,acc}}, 1 \right); \text{ if } \Delta SWE_t \geq 0 \quad (6)$$

where ΔSWE represents the variation of SWE at the time step considered (a positive ΔSWE corresponds to a snow accumulation, a negative ΔSWE to melting), SCA_{t-1} corresponds to the SCA calculated at the preceding time step and P_{sol_t} corresponds to the quantity of snowfall at current time step (in mm). This simple formulation was used in the CLSM model (Magand et al., 2014). The slope of this relation is set by the parameter $T_{h,acc}$, which defines the threshold of SWE (in mm) based from which the SCA is equal to 1. This formulation of the SCA in an accumulation period is used in this article for all the hysteresis models tested.

Melting curve

The different formulations tested for this study are presented in Figure 3; Figure 3a presents the melting curve as it is implemented in the current CemaNeige snow-accounting model ((Valéry et al., 2014b), Eq. 4).

Linear hysteresis (LH)

The first hysteresis tested (Fig. 3b) is a simple linear hysteresis that was implemented in the CLSM model (Magand et al., 2014).

$$\begin{cases} SCA_t = \min\left(\dfrac{SWE_t}{T_{h,max}}, 1 \right) & ; \text{ if } \Delta SWE_t < 0 \\ SWE_{t\,melt} = SWE_{t-1} \text{ if } SCA_{t-1} = 1 \end{cases} \quad (7)$$

$$T_{h,max} = \begin{cases} T_{h,melt} & \text{if } SWE_{t\,melt} > T_{h,melt} \\ SWE_{t\,melt} & \text{if } SWE_{t\,melt} \leq T_{h,melt} \end{cases} \quad (8)$$

This parametrization of the hysteresis melting curve part depends on a local maximum threshold ($T_{h,max}$), which defines the inflexion point and the slope of the melting curve (in red on Fig. 3b). If the accumulated snow before snowmelt exceeds a calibrated melt threshold ($T_{h,melt}$), the local threshold ($T_{h,max}$) takes the ($T_{h,melt}$) value. On Fig. 3b, this means that when melting occurs, the SCA value decreases only if the SWE value is lower than 250 mm (this value has been taken as an example). If during the winter, the accumulated SWE never exceeds the $T_{h,melt}$ value, or in the case that there is a snow accumulation after the melting phase has started (represented by the yellow curve in Fig. 3b), the local maximal threshold ($T_{h,max}$) takes the maximal SWE value before the beginning of the melt ($SWE_{t,melt}$, Eq. 8).

Modified linear hysteresis (LH*)

A variation of the linear hysteresis is proposed in this article, where:

$$T_{h,melt} = \overline{P_{sol\,annual}} \cdot R_{sp} \quad (9)$$

$P_{sol\,annual}$ represents the mean annual precipitation for the elevation zone of the catchment considered and R_{sp} is a parameter between 0 and 1. This formulation defines a different $T_{h,melt}$ for each of the catchment's elevation zones, which is not the case in Equation 7.

MATSIRO hysteresis (MH)

This third hysteresis tested was used within the MATSIRO surface model (Nitta et al., 2014). The formulation is similar to the linear hysteresis formulation, except that instead of following a linear slope, the hysteresis follows a square root function for the melting curve.

$$\begin{cases} SCA_t = \min\left(\sqrt{\dfrac{SWE_t}{T_{h,max}}}, 1 \right) & ; \text{if } \Delta SWE < 0 \\ SWE_{t\,melt} = SWE_{t-1} \text{ if } SCA_{t-1} = 1 \end{cases} \quad (10)$$

$$T_{h,max} = \begin{cases} T_{h,melt} & \text{if } SWE_{t\,melt} > T_{h,melt} \\ SWE_{t\,melt} & \text{if } SWE_{t\,melt} \leq T_{h,melt} \end{cases} \quad (11)$$

This parametrization also calls on the $T_{h,melt}$ parameter. As equation 8, the value of $T_{h,max}$ depends on the state of the accumulated SWE at the beginning of the melting period ($SWE_{t\,melt}$) and of the value of the $T_{h,melt}$ parameter. This curve shape implies that the decrease in the SCA accelerates as the SWE decreases. In other words, this formulation would mean that at the beginning of melting, a decrease in the SWE affects the south-exposed snow cover only slightly. As the quantity of snow diminishes, melting affects the entire catchment and the SCA drops rapidly. The shape of this hysteresis can be consulted in Figure 3c. Like the linear hysteresis, Equation 10 updates the melting threshold with the SWE value if the SWE accumulated does not go beyond the $T_{h,melt}$ value or in the case of a snow accumulation within a snow melt period.

Swenson hysteresis (SH)

The last parametrization tested comes from the CLM4 model (Swenson and Lawrence, 2012). It is very different from the other methods since it does not use the melting threshold to manage melting. Instead, a N_{melt} parameter directly imposes the shape of the melting curve (Equations 12 and 13).

$$SCA_t = 1 - \left(\frac{1}{\pi} \text{acos}\left(2\frac{SWE_t}{SWE_{t\,melt}} - 1 \right) \right)^{N_{melt}} ; \text{ if } \Delta SWE < 0 \quad (12)$$

$$SWE_{t\,melt} = SWE_t \left[\frac{\cos\left(\pi\left(1 - SCA_{t-1}\right)\right) + 1}{2} \right]^{-1/N_{melt}} \quad (13)$$

The higher the N_{melt} value, the lower the decrease in the SCA will be at the beginning of melting and it will accelerate progressively, which makes it possible to model the threshold effect as it is in the hysteresis presented above. In contrast, the lower the N_{melt} value, the more the SCA will drop rapidly at the beginning of melting and will be followed by a relative stabilization of the slope until a second, sharper drop at the end of melting. Conceptually, this would mean that the SCA of the exposed slopes would drop very rapidly at the beginning of melting, whereas the SCA of the less exposed slopes would decrease less rapidly. The influence of the melting factor N_{melt} on the SCA during the melting period is presented in Figure 3d, 3e, and 3f.

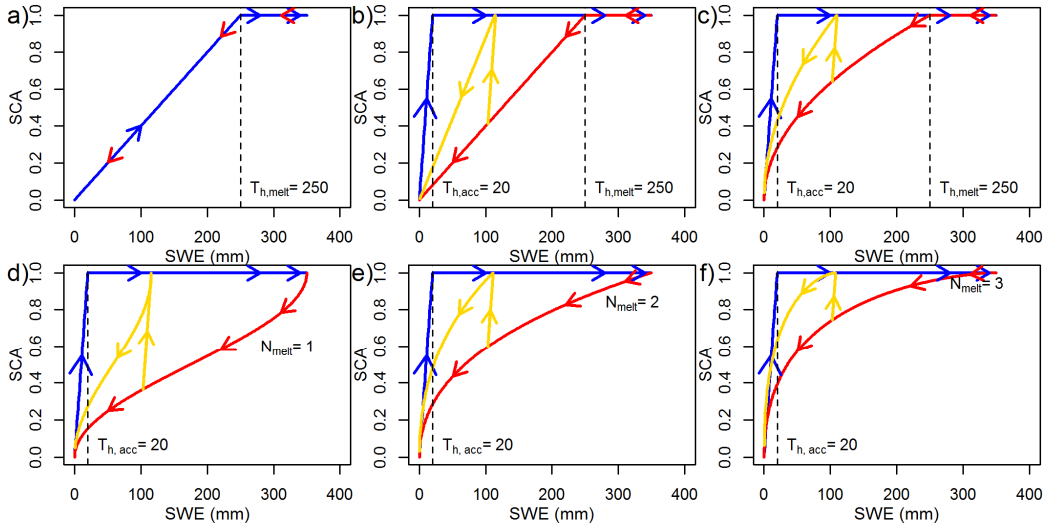

Fig. 3. Schematic representation of the different types of hystereses used a) original relation in CemaNeige, b) linear hysteresis, c) MATSIRO hysteresis, d-e-f) Swenson hysteresis with three different N_{melt} coefficients. The blue line represents the accumulation phase of the hysteresis while the red line represents the melting phase. The yellow curves represent an example of snow accumulation within a melting period. The $T_{h,acc}$ and $T_{h,melt}$ values have been set respectively at 20 and 250 mm to illustrate the different hystereses.

Calibration and optimization criteria

The four different hysteresis models implemented in the CemaNeige snow-accounting model were tested and calibrated on the 277 catchments. The calibrations were performed for each catchment for two different periods: 2000–2005 and 2005–2010. The routing and rainfall-runoff transformation were computed using the GR4J hydrological model.

Both the hydrological model's and the snow model's parameters were calibrated using the steepest-descent calibration algorithm (Edijatno et al., 1999; Perrin et al., 2001). The calibration criterion used was the *KGE′* (Gupta et al., 2009; Kling et al., 2012). This criterion (Eq. 14) takes into account the Pearson correlation coefficient (Eq. 15, Cov_{so} being the covariance between observation and simulation, σ being the standard deviation), the percentage bias (Eq. 16, depending on μ the average of the simulation and observations), and the ratio of the coefficients of variation between the simulated and observed temporal series (Eq. 17).

$$KGE' = 1 - \sqrt{(r-1)^2 + (\omega-1)^2 + (\gamma-1)^2} \quad (14)$$

$$r = \frac{Cov_{so}}{\sigma_s \sigma_o} \quad (15)$$

$$\omega = \frac{\mu_s}{\mu_o} \quad (16)$$

$$\gamma = \frac{\sigma_s / \mu_s}{\sigma_o / \mu_o} \quad (17)$$

To calibrate the model with the runoff and the MODIS data, the *KGE′* on the runoff and the *KGE′* on the MODIS data on five elevation zones were combined.

$$Crit = \alpha\, KGE'(Q) + \sum_{i=1}^{5} \beta_i\, KGE'(SCA_i), \quad (18)$$

where $\alpha + \sum_{i=1}^{5} \beta_i = 1$ (19)

Thus a weighting βi can be assigned to the *SCA* simulation on each elevation zone i modeled by CemaNeige (here five zones were selected: SCA_1, SCA_2, …, SCA_5). In addition, a single weighting β can be assigned on the *SCA* criterion if the *SCA* is averaged over the entire watershed (i.e., all the elevation zones).

The performance presented in the Results section is calculated from the validation period complementary to each calibration period (e.g., 2000–2005 calibration, 2005–2010 validation). The performances of simulations are therefore represented twice for each catchment (one performance per validation period). To ensure that the performance criteria take into account the modifications to the snow model, the validation concerns only the months with snow. For each catchment, the months with snow correspond to the months whose upper layer mean *SCA* is greater than 5% according to MODIS for the whole period.

A Friedman test (Friedman, 1937) is also applied to the calibration results. This is a statistical test designed to determine whether the models give significantly different results. For each catchment, the performances of the simulations of each model are ranked, and then the ranks are summed for each model. The model with the highest ranks is considered the best according to this test.

RESULTS

Analysis of the different hysteresis models

The GR4J–CemaNeige coupled model contains six parameters to calibrate (four for GR4J, two for CemaNeige). The three versions of CemaNeige with hysteresis add two additional parameters: $T_{h,acc}$ and $T_{h,melt}$ or N_{melt}. Except for the original CemaNeige model that serves as the reference and was calibrated only on runoff (α = 1), the other models tested were calibrated with weighting α = 0.75 and an identical weighting β for all elevation zones equal to 0.05. The different models used as well as their calibration weighting are presented in Table 1. The comparison of the performance of the models is available in Figure 4.

Table 1. List of the models and weightings used for analyzing the performances of the hystereses formulations.

Model	Q weighting α	SCA weighting β 1 …5
CemaNeige reference (C Q)	1	0
CemaNeige SCA (C Q SCA)	0.75	0.05
Linear hysteresis (LH)	0.75	0.05
Modified linear hysteresis (LH*)	0.75	0.05
MATSIRO hysteresis (MH)	0.75	0.05
Swenson hysteresis (SH)	0.75	0.05

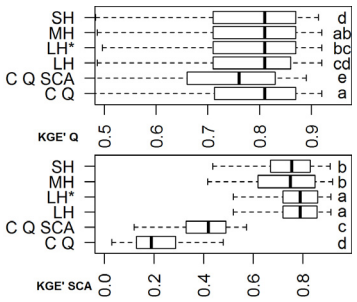

Fig. 4. Performances of the different hystereses used with CemaNeige coupled with GR4J model. The performances presented are KGE' values calculated on validation periods. Each boxplot contains the results from both validation periods for each catchment; the whiskers indicate the 5 and 95 percentiles. The result of the Friedman analysis is represented by the letters near the boxplot. The best ranked model is indicated by letter "a" and models with identical letters are considered as not significantly different.

It can be observed that the reference CemaNeige snow-accounting model gave the best scores in terms of runoff, according to the Friedman test, with a similar median to the models with hysteresis (0.81), however. In terms of SCA performance, the original version of CemaNeige gave much lower scores than the versions with hysteresis (median, 0.19 versus 0.79 for both linear hystereses). Calibration of CemaNeige with the MODIS data, as originally designed, showed a decrease in the runoff score of approximately 0.05 points on the median and only improved the SCA score very slightly. This shows the inability of the original CemaNeige model to take into account the calibrated SCA data without damaging the runoff score.

The implementation of hystereses in CemaNeige significantly improved the SCA score, with the best score obtained by the linear hysteresis: median, 0.81 and 0.82 for the modified version. The runoff scores modeled by CemaNeige with linear hysteresis were very slightly inferior to the reference scores. They had the same median and the same quartiles; only the mean, not represented here, differed slightly. Both of the other hystereses showed similar performance in terms of runoff, but slightly inferior in the SCA. It can be concluded that adding a hysteresis significantly improves the SCA if it is used in calibration while retaining a stable performance in runoff, which the original model did not allow.

Analysis of runoff criterion and snow cover criterion weighting

To obtain better validation criteria on the SCA without harming the runoff criterion, several different weighting configurations were analyzed. The α weighting on runoff was tested for values of 0, 0.5, 0.75, 0.9, and 1. Weighting corresponding to the SCA criteria was 0.2, 0.1, 0.05, 0.02, and 0 for each of the layers. This analysis was based on the use of the modified linear hysteresis, which gave highly satisfactory results in the previous section. These values are summarized in Table 2 and the results are available in Figure 5.

Table 2. Weightings used for the calibrations of the snow model with the modified linear hysteresis (LH*).

Model	Q weighting α	SCA weighting β 1 … 5
LH*	0	0.2
LH*	0.5	0.1
LH*	0.75	0.05
LH*	0.9	0.02
LH*	1	0

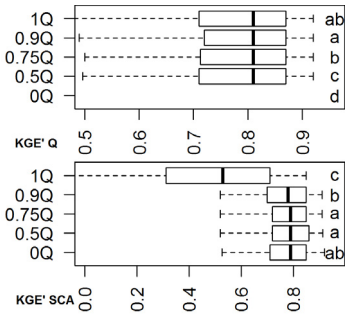

Fig. 5. Performances of the snow model with the modified linear hysteresis for different weightings of the optimization criteria. The KGE' performances presented in the boxplots have been calculated on validation periods.

We can observe that the runoff criterion remains stable in validation as the weighting performed in calibration decreased. The SCA criterion seems, on the other hand, to improve as the weighting on runoff decreases. Nevertheless, it seems that for weighting greater than 0.25 of SCA (i.e., less than 0.75 of runoff) the gains are very low on the SCA. Calibration on runoff only (1Q) significantly deteriorates the model's simulation of the SCA. Thus, a weighting of the optimization criterion with 75% allocated to the runoff criterion and 25% allocated to the SCA criterion seems to be a satisfactory compromise between the model's performance in terms of runoff and SCA. Figure 5 also shows that runoff performance is slightly better with a 0.75 weighting rather than a calibration only on the runoff criterion. This shows that the model potentially has higher robustness using the calibrated SCA. The robustness of the model will be more fully studied in section "APPLICATION OF THE SNOW MODEL TO DIFFERENT SIMULATION CONTEXTS".

Analysis of the type of snow cover weighting to use

In section "Analysis of runoff criterion and snow cover criterion weighting", the SCA weightings were considered to be equivalent for all layers. Based on a 0.75 runoff weighting, we studied several ways to weight the SCA simulations for each elevation zone. The first reference combination used in the preceding sections considers an identical weighting for each elevation zone (here 5% for each elevation zone). Since the highest elevation zones have a greater snow regime than the lower layers, it is possible that the low-elevation zones provide little information to calibrate the model. Therefore, a calibration mode with a weighting that increases with elevation was tested, as was a second mode with a weighting that took only the high elevation zones into account. Finally, the last type of calibration, called global calibration, was directly calculated based on the mean SCA for the entire catchment, with no distinction made on the performance for each elevation zone. This global calibration is different to the equivalent weighting for all layers since there is just one hysteresis computed for all elevation bands, this should affect the calibration of the hysteresis parameters. The different weightings in this analysis are summarized in Table 3 and the results are presented in Figure 6.

Table 3. List of the SCA weighting methods used for the snow model calibration.

Model	Calibration type	α	$\beta 1$	$\beta 2$	$\beta 3$	$\beta 4$	$\beta 5$
LH*	Equally Weighted (SCA E)	0.75	0.05	0.05	0.05	0.05	0.05
LH*	Global (SCA G)	0.75	0.25, the SCA from the five-layer bands are averaged and compared to the mean observed SCA				
LH*	Increasing (SCA I)	0.75	0.025 (10%)	0.025 (10%)	0.05 (20%)	0.075 (30%)	0.075 (30%)
LH*	High elevation (SCA H)	0.75	0	0	0	0.125	0.125

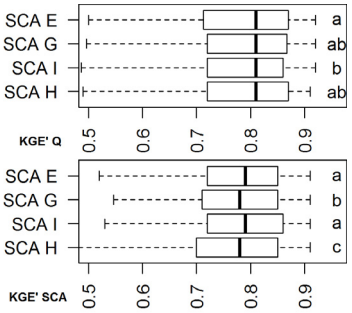

Fig. 6. Performances of the snow model with the modified linear hysteresis for different types of SCA criteria weighting. The KGE' performances presented in the boxplots have been calculated on validation periods.

For the runoff validation, few significant differences were observed for the different methods taking the SCA selected into account. However, in terms of SCA validation, the results clearly show that use of the highest elevation zones only to calibrate the model is not sufficiently informative and gives unsatisfactory results compared to the other calibration methods. The three other types of calibration provide similar results in SCA validation. Identically weighting each elevation zone used in the preceding sections therefore seems to be a viable choice to calibrate the snow model with hysteresis and will be retained for further analysis.

Overall results: hydrographs and analysis of the model's parameters

The analyses above demonstrate that use of modified linear hysteresis (Eqs. 5, 6, 7, 8 and 9) with an optimization criterion with a 0.75 weighting on runoff and a 0.05 weighting on each of the elevation zones gives one of the best compromises in runoff and SCA performance over most of the catchments studied. The difference in performance between the reference CemaNeige routine calibrated on runoff and the model developed in this study, for each catchment, is presented in Figure 7.

The map in Figure 7 indicates that the performance in the runoff simulations of the reference CemaNeige model with hysteresis is similar for most catchments. The majority of the catchments gaining in performance seem to be the small catchments in the Massif Central. However, this figure does not show spatial coherence in the deterioration of the runoff performance criterion.

Concluding this analysis on various catchments, hydrographs as well as the SCA and the SWE over time are presented in Figure 8. The three catchments presented are the Durance at Embrun (X0310010, 2283 km², the Alps) and the Arac at Soulan (O0384010, 170 km², the Pyrenees). The Durance alpine catchment has its performance improved by the new model (+0.06 points in KGE′), while the performance of the simulations of the Arac catchment remained stable (identical KGE′).

These hydrographs show relatively few differences between the reference CemaNeige simulations and the simulation with CemaNeige improved by hysteresis. It can nonetheless be observed that the winter flow peaks were better reproduced on the Durance (X0310010). A clear improvement in the SCA simulation by CemaNeige with hysteresis, compared to the reference CemaNeige, can be observed for the two catchments. Figure 8 also shows that SWE was modified over time by the new SCA formulation in the CemaNeige model. Overall, it seems that the improvement tends to reduce the SWE accumulated. This shows that this new SCA parametrization also influences melting in the model. The impact of hysteresis on the model's parameters can be observed in Figure 9.

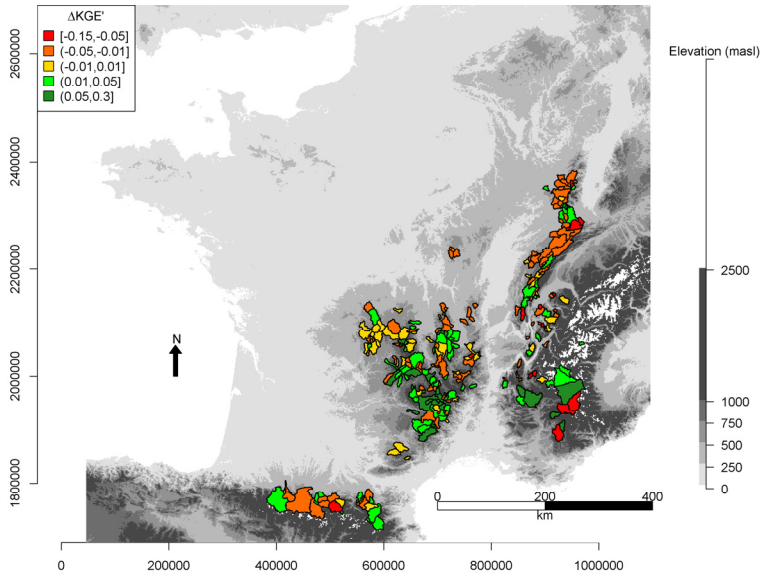

Fig. 7. Improvement (or degradation) of KGE' performances on river discharge for each studied watershed. The value indicated is the difference between the performances of the modified CemaNeige with the hysteresis formulation minus the performance of the original CemaNeige model for the 2005–2010 validation period. 16 watersheds have significant degraded runoff performance (red), 104 have slightly degraded runoff (orange) and 51 watersheds have similar performances (yellow), while 75 have slightly improved performances (green) and 31 have seen significant improvement (dark green).

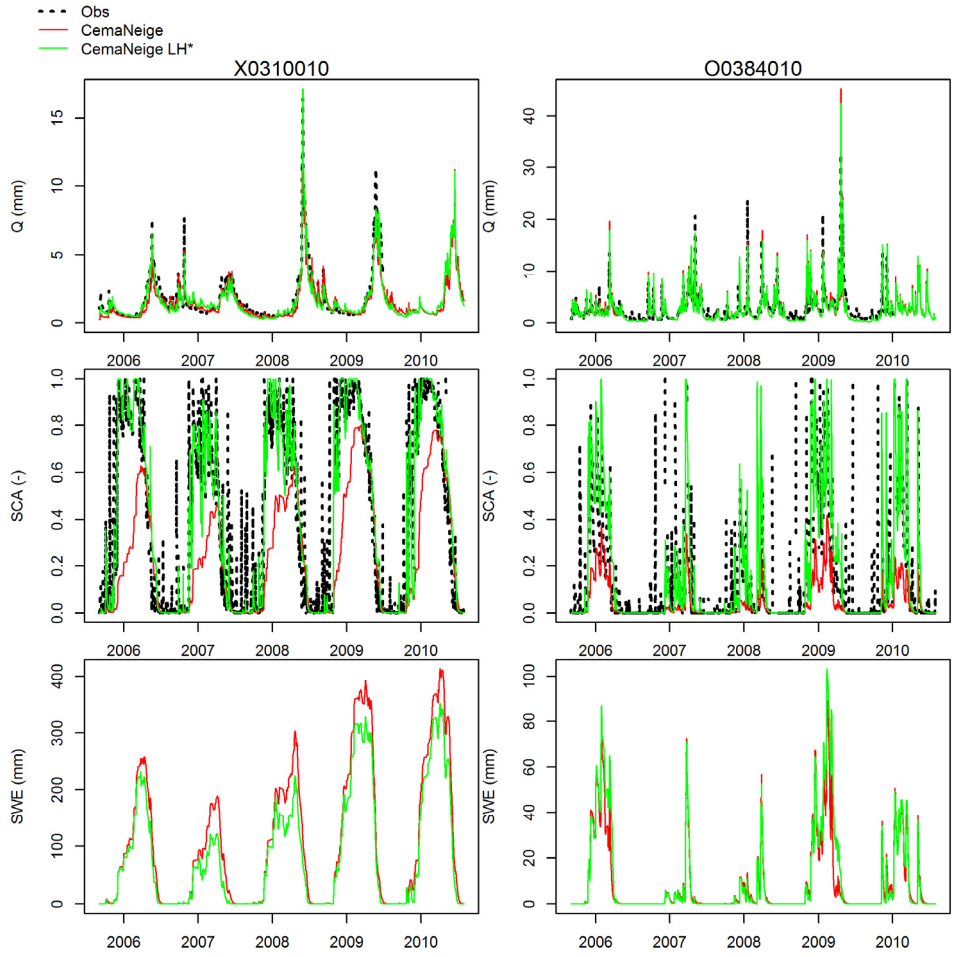

Fig. 8. Hydrograph, evolution of SCA and SWE for three snow-dominated watersheds. These two watersheds were calibrated on the 2000–2005 period and the simulations presented in this figure are coming from the 2005–2010 validation period.

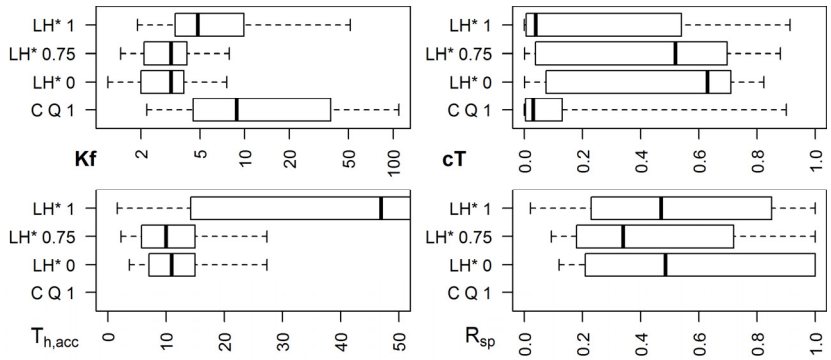

Fig. 9. Analysis of the melt coefficient (Kf, in mm.°C^{-1} d^{-1}), the cold content parameter (cT) and the hysteresis parameters ($T_{h,acc}$ and R_{sp}) for the reference model (C Q 1) and the snow model with the modified linear hysteresis calibrated with a weighting of the runoff and SCA criteria (LH* 0.75), with a calibration on the runoff criterion only (LH* 1) and with a calibration on the SCA criterion only (LH* 0).

Figure 9 shows that the melting parameter changes considerably between the reference model and the model with hysteresis calibrated by weighting the two objectives. Using the MODIS data and hysteresis constrains the melting parameter to much lower values than for calibration with runoff only. With quartiles between 2 and 4.5 mm °C^{-1} d^{-1}, these values seem more plausible than what calibration of the reference model proposes (quartiles 4.5 and 38 mm °C^{-1} d^{-1}), as values for degree day coefficient varying between 0.3 and 7.6 mm °C^{-1} d^{-1} can be found in the literature (Martinec and Rango, 1986). As snow melt rate decreases with SCA in the model (due to Eq. 3), the implemented hysteresis directly impacts the melt rate and the melting parameter. Globally, the model with hysteresis has much higher SCA values compared to the original formulation (Fig. 8). This could explain the decreased value of the degree-day melt coefficient as higher SCA values tends to increase this melt rate (Eq. 3).

The cold content parameter cT seems to be less restricted by the model calibrated with MODIS than with the reference. The reference model's cT values cluster around a very low value (median, 0.04), indicating that for a consequential number of catchments, thermal inertia is considered to be very low. Figure 9 also shows that the parameters with $T_{h,acc}$ and R_{sp} hysteresis require MODIS data to be constrained. The values are indeed

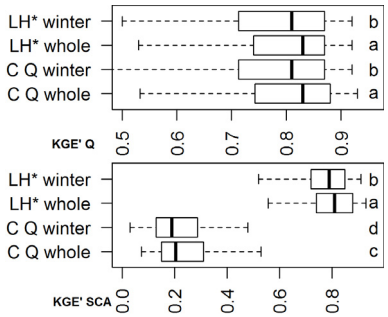

Fig. 10. Performances for runoff and SCA simulations, calculated on the whole validation period and calculated on the winter month of the validation period only.

highly dispersed with calibration based only on runoff. To limit the addition of a parameter to the CemaNeige SCA, it seems cautious to set the accumulation threshold ($T_{h,acc}$). Its value varies little from one catchment to another (quartiles at 5.8 and 15 mm) and since the increase of SCA is very fast in accumulation periods, its influence on the model (whether for the SCA or runoff) should be less important than the melting threshold ratio (R_{sp}).

Finally, to check that the improvement of the winter runoff performance does not occur at the expanse of runoff performance for the rest of the year, Figure 10 allows one to verify the performance over the validation periods for criteria calculated only on winter runoff and criteria calculated on the whole year runoff.

The performance over the whole period is close to the winter period performance, considering that overall, taking the whole period into account tends to improve both the runoff and SCA scores. This remains true for the snow module with hysteresis and the reference CemaNeige SCA, meaning that the introduction of the hysteresis has a negligible influence on non-snow dependent runoff modelled by GR4J.

APPLICATION OF THE SNOW MODEL TO DIFFERENT SIMULATION CONTEXTS

Using the calibrated model on a period from the past

Following calibration of the snow model with the MODIS observation data, several questions come to mind. For example, is the model with hysteresis more robust in terms of climatic variability than the reference CemaNeige model? For this analysis, both models were run for three 10-year periods from the past using the parameters calibrated on the 2000–2005 and 2005–2010 periods. Only the catchments with runoff measurements for these three periods were used (representing approximately 50% of the sample used in this article). The three periods used were 1960–1970, 1970–1980, and 1980–1990. The boxplots in Figure 11 present the performances of the simulations using the model with hysteresis and the reference model for each of the past periods. The SCA performance criteria could not be calculated as the MODIS data were not available for these periods.

These results are encouraging because they show that the model calibrated on the SCA tends to keep slightly more stable performance for simulations far from the calibration period, as observed in the boxplots, which are slightly decentered toward a positive difference in performance. These preliminary results on the use of a set of parameters on a distant period should make the model with hysteresis more adapted than the reference model for analyses such as impact studies on climate change.

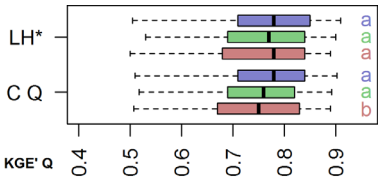

Fig. 11. Performances of the snow model with the modified linear hysteresis and the original CemaNeige model for three past periods: 1960–1970 (in red), 1970–1980 (in green), 1980–1990 (in blue). The parameters used here come from the calibrations of the 2000–2005 and 2005–2010 periods.

Sequential calibration of the snow model and the hydrological model

Here we wish to answer the following question: is it possible to calibrate the snow model completely independently of the rainfall-runoff model? This question seeks to determine which part of the information comes from MODIS SCA and whether it is sufficient to calibrate the snow model. Independently calibrating CemaNeige would facilitate the elaboration of a regionalization strategy for these parameters. Therefore, the snow model was first calibrated only on the SCA and then the rainfall-runoff model was calibrated on runoff observations, with the parameters from the snow model set to the values obtained in the first calibration (sequential calibration). This result was compared to the calibration of the rainfall-runoff model coupled with the snow model (reference or with hysteresis) whose parameters are set to the median value of the 277 catchments for each period (LH* med and C Q med) as well as a joint calibration of the snow model with hysteresis and the rainfall-runoff model (as was done above, LH* 0.75 here LH* ref).

The sequential calibration strategy applied is summarized in Table 4; the results are available in Figure 12.

Table 4. List of the calibrations realized for the analysis of the independency of the snow model from the rainfall-runoff model.

Snow model		Rainfall-runoff model
LH* ref	Coupled model optimization on Q and SCA, with $\alpha = 0.75$ and SCA E	
C Q ref	Coupled model optimization on Q	
Sequential calibration (LH* seq)	Optimization on SCA only	Optimization on Q only
LH* med	Fixed parameters at median value	Optimization on Q only
C Q med	Fixed parameters at median value	Optimization on Q only

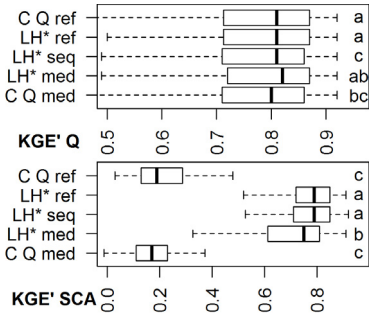

Fig. 12. Performances of the model simulations used for sequential calibration analysis and the two references calibrated on runoff data presented in Table 4.

The performances between the model calibrated sequentially and the original CemaNeige reference model are very similar for runoff (median performance of 0.81). Using median param-

eters for the snow models gives results that are also very similar to the sequential and reference calibrations. It therefore seems that the hydrological model can compensate for a large part of the modifications resulting from change in parameters from the snow model to the sequential calibration. Sequential calibration therefore contributes little to the rainfall-runoff model compared to the use of median parameters for the snow model.

Application of the model to a ungauged context

Many mountain catchments are not gauged, and runoff measurements are therefore not available to calibrate the snow model or the hydrological model. On the other hand, the MODIS SCA data are available everywhere, meaning that, as above, they provide a calibration of the snow model for the SCA even if the catchment is not instrumented. The difference compared to the preceding section is that the rainfall-runoff model cannot be calibrated; the parameters are then set to their median value (the median of the parameters between all the catchments for each calibration period). This calibration of the snow model on SCA only is compared to the performance of the simulations with the reference CemaNeige model with hysteresis, with their parameters set at a median value. A summary of this analysis is available in Table 5 and the results are presented in Figure 13. The performance data presented are the KGE′ deltas, the difference in performance of the catchments considered to be ungauged, and the same catchments calibrated on runoff with the reference model.

Table 5. List of the simulations made for analyzing the performance of the snow model for ungauged watersheds.

Snow model		Runoff model
LH* ref	Coupled model optimization on Q and SCA with $\alpha = 0.75$ and SCA E	
C Q ref	Coupled model optimization on Q	
Sequential calibration (LH* SCA)	Optimization on SCA only	Fixed parameters at median value
LH* med	Fixed parameters at median value	Fixed parameters at median value
C Q med	Fixed parameters at median value	Fixed parameters at median value

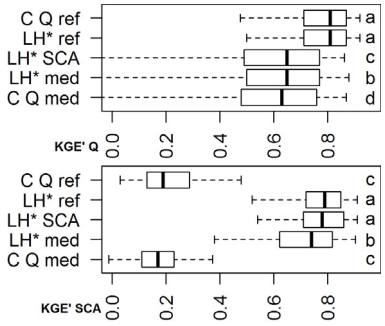

Fig. 13. Performances of the models presented in Table 5 used in an ungauged watershed situation and the two reference simulations.

Using the median parameters for the GR4J rainfall-runoff model implies a much greater loss in performance compared to the results shown in Figure 12 in section "Sequential calibration of the snow model and the hydrological model". Setting parameters of the hydrological model at a median value is relatively harsh. However, we observe that calibrating the snow model on SCA with hysteresis gives slightly better results than using the median parameters of the reference CemaNeige model but the LH* model with median parameters still performs a little better for flow simulation. It remains difficult to calibrate the snow model as well as the hydrological model without flow data.

CONCLUSION

Many studies have shown the utility of calibrating the snow model with MODIS snow cover data (SCA). The objectives of the present study were to improve the SCA formulation of the CemaNeige snow-accounting model, to test several model calibration strategies using SCA MODIS data, and to assess their performance in a variety of application conditions.

The results of this study demonstrated that the original CemaNeige model gives highly satisfactory runoff simulations when it is combined with a rainfall-runoff model, but also that its internal snow cover surface variable cannot capture the MODIS SCA data. Calibrating CemaNeige in its original version with an optimization criterion taking runoff and SCA into account shows a clear reduction in performance in terms of runoff simulation, with only a slight improvement in performance with SCA.

Introducing a hysteresis in CemaNeige made it possible to go beyond the restrictions of the original model by improving the performance of the SCA simulation, without deteriorating the performance for runoff. Different SWE-SCA hystereses were tested: the modified simple linear formulation with a melting threshold dependent on annual solid precipitation presented the best results and was retained. Several analyses also determined that the most advantageous compromise for the model's evaluation criterion was a 75% weighting of the flow criterion, and an identical weighting of each of the elevation zones with 5% weighting on the SCA criterion.

These different analyses improved the CemaNeige model and allowed us to design an adapted calibration method taking the MODIS snow cover data into account. Introducing this hysteresis adds two parameters to the CemaNeige snow-accounting model, which brings the total number of parameters to four. Even though this improvement of the model requires additional parameters, it is constrained by both runoff and SCA instead of only runoff. Further development of the model could also use SCA data for correcting solid precipitation inputs as done by Shrestha et al. (2014), as snowfall measurements are generally underestimated due to precipitation gages undercatchment.

This CemaNeige snow-accounting model improved by hysteresis was compared to the original CemaNeige model for simulating time periods far in the past. The model with hysteresis gives slightly better performances than the original model and seems more robust. This is encouraging in the study of climate change impacts where the model's uncertainty is great in the context of climate non-stationarity. The snow model was also submitted to different calibration strategies, namely comparing a sequential calibration of its two components (ie. by calibrating the snow model only with SCA and the rainfall-runoff model only with runoff) or a calibration in ungauged conditions (ie. by calibrating the snow model only with SCA and using uncalibrated parameters for the rainfall-runoff model) to the combined calibration of the snow model and the rainfall-runoff model used in previous sections. The independent calibration of the snow module, i.e., performed only on the SCA, within a sequential calibration or the estimation of an ungauged catchment, gives fairly mixed results. These analyses were carried out using the median values of the parameters. This was the simplest parameter regionalization method that allowed testing the snow module in the most unfavorable condition possible. For the hydrological model, more advanced parameter

regionalization techniques could be tested to improve the model's performance on ungauged catchments.

The MODIS data used underwent a very simple treatment: no spatiotemporal data filtering system was applied. This could improve the model's performance by improving the calibration data (Parajka and Blöschl, 2008b). One of the future perspectives could also be the use of single SWE measurements and integrating them into the model calibration. It is highly probable that the conceptual model should be modified to provide a response that is comparable to the observation. The analysis of the sensitivity of the hysteresis parameters would be useful given that it would inform even more on their influence on runoff simulation. It is likely that the snow accumulation threshold could be set easily: this sensitivity analysis would make it possible demonstrate this and find the best adapted value.

Acknowledgements. The authors wish to thank Franck Masclet, intern, who conducted the preliminary analyses on incorporating hysteresis into the CemaNeige model. They would also like to thank the different entities that provided data, without which this analysis would not have been possible: Météo-France for the temperature and precipitation data, SAFRAN; the Banque Hydro for the runoff observation data; and NSIDC for making the MODIS SCA data available. Finally, we would like to thank the two reviewers, Jan Magnusson and Ryan Teuling, for their comments on an early version of the manuscript, which helped improving its quality.

REFERENCES

Andreadis, K.M., Lettenmaier, D.P., 2006. Assimilating remotely sensed snow observations into a macroscale hydrology model. Adv. Water Resour., 29, 872–886. DOI: 10.1016/j.advwatres.2005.08.004.

Barnett, T.P., Adam, J.C., Lettenmaier, D.P., 2005. Potential impacts of a warming climate on water availability in snow-dominated regions. Nature 438, 303–309. DOI: 10.1038/nature04141.

Beniston, M., Farinotti, D., Stoffel, M., Andreassen, L.M., Coppola, E., Eckert, N., Fantini, A., Giacona, F., Hauck, C., Huss, M., Huwald, H., Lehning, M., López-Moreno, J.-I., Magnusson, J., Marty, C., Moran-Tejéda, E., Morin, S., Naaim, M., Provenzale, A., Rabatel, A., Six, D., Stötter, J., Strasser, U., Terzago, S., Vincent, C., 2017. The European mountain cryosphere: A review of past, current and future issues. Cryosphere Discuss, 2017, 1–60. DOI: 10.5194/tc-2016-290.

Bernsteinová, J., Bässler, C., Zimmermann, L., Langhammer, J., Beudert, B., 2015. Changes in runoff in two neighbouring catchments in the Bohemian Forest related to climate and land cover changes. J. Hydrol. Hydromech., 63, 342–352. DOI: 10.1515/joh.h-2015-0037.

Clark, M.P., Hendrikx, J., Slater, A.G., Kavetski, D., Anderson, B., Cullen, N.J., Kerr, T., Hreinsson, E. Ö., Woods, R.A., 2011. Representing spatial variability of snow water equivalent in hydrologic and land-surface models: A review. Water Resour. Res., 47, 7. DOI:10.1029/2011WR010745.

Coron, L., Perrin, C., Michel, C., Andréassian, V., Brigode, P., Delaigue, O., Le Moine, N., Mathevet, T., Mouelhi, S., Oudin, L., Pushpalatha, R., Thirel, G., Valéry, A., 2017a. airGR: Suite of GR Hydrological Models for Precipitation-Runoff Modelling. R package version 1.0.5.12. IRSTEA, Antony, France. https://irsteadoc.irstea.fr/cemoa/PUB00052697

Coron, L., Thirel, G., Delaigue, O., Perrin, C., Andréassian, V., 2017b. The suite of lumped GR hydrological models in an R package. Environ. Model. Softw., 94, 166–171. DOI: 10.1016/j.envsoft.2017.05.002.

Da Ronco, P., De Michele, C., 2014. Cloud obstruction and snow cover in Alpine areas from MODIS products. Hydrol. Earth Syst. Sci., 18, 4579–4600. DOI: 10.5194/hess-18-4579-2014.

Duethmann, D., Peters, J., Blume, T., Vorogushyn, S., Güntner, A., 2014. The value of satellite-derived snow cover images for calibrating a hydrological model in snow-dominated catchments in Central Asia. Water Resour. Res., 50, 2002–2021. DOI: 10.1002/2013WR014382.

Edijatno, Nascimento, N.D.O., Yang, X., Makhlouf, Z., Michel, C., 1999. GR3J: a daily watershed model with three free parameters. Hydrol. Sci. J., 44, 263–277. DOI: 10.1080/02626669909492221.

Egli, L., Jonas, T., 2009. Hysteretic dynamics of seasonal snow depth distribution in the Swiss Alps. Geophys. Res. Lett., 36, L02501. DOI: 10.1029/2008GL035545.

Essery, R., Pomeroy, J., 2004. Implications of spatial distributions of snow mass and melt rate for snow-cover depletion: theoretical considerations. Ann. Glaciol., 38, 261–265. DOI: 10.3189/172756404781815275.

Franz, K.J., Karsten, L.R., 2013. Calibration of a distributed snow model using MODIS snow covered area data. J. Hydrol., 494, 160–175. DOI: 10.1016/j.jhydrol.2013.04.026.

Friedman, M., 1937. The use of ranks to avoid the assumption of normality implicit in the analysis of variance. J. Am. Stat. Assoc., 32, 675–701. DOI: 10.1080/01621459.1937.10503522.

Gafurov, A., Bárdossy, A., 2009. Cloud removal methodology from MODIS snow cover product. Hydrol. Earth Syst. Sci., 13, 1361–1373. DOI: 10.5194/hess-13-1361-2009.

Grayson, R.B., Blöschl, G., Western, A.W., McMahon, T.A., 2002. Advances in the use of observed spatial patterns of catchment hydrological response. Adv. Water Resour., 25, 1313–1334. DOI: 10.1016/S0309-1708(02)00060-X.

Gupta, H.V., Kling, H., Yilmaz, K.K., Martinez, G.F., 2009. Decomposition of the mean squared error and NSE performance criteria: Implications for improving hydrological modelling. J. Hydrol., 377, 80–91. DOI: 10.1016/j.jhydrol.2009.08.003.

Hall, D.K., Salomonson, V.V., Riggs, G.A., 2006. MODIS/Terra, MODIS/Aqua Snow Cover Daily L3 Global 500m Grid, Version 5. NASA National Snow and Ice Data Center, Boulder, Colorado, USA. DOI: 10.5067/63NQASRDPDB0.

He, Z.H., Parajka, J., Tian, F.Q., Blöschl, G., 2014. Estimating degree-day factors from MODIS for snowmelt runoff modeling. Hydrol. Earth Syst. Sci., 18, 4773–4789. DOI: 10.5194/hess-18-4773-2014.

Helbig, N., van Herwijnen, A., Magnusson, J., Jonas, T., 2015. Fractional snow-covered area parameterization over complex topography. Hydrol. Earth Syst. Sci., 19, 1339–1351. DOI: 10.5194/hess-19-1339-2015.

Hublart, P., Ruelland, D., García de Cortázar-Atauri, I., Gascoin, S., Lhermitte, S., Ibacache, A., 2016. Reliability of lumped hydrological modeling in a semi-arid mountainous catchment facing water-use changes. Hydrol. Earth Syst. Sci., 20, 3691–3717. DOI: 10.5194/hess-20-3691-2016.

Kling, H., Fuchs, M., Paulin, M., 2012. Runoff conditions in the upper Danube basin under an ensemble of climate change scenarios. J. Hydrol., 424–425, 264–277. DOI: 10.1016/j.jhydrol.2012.01.011.

Kolberg, S.A., Gottschalk, L., 2006. Updating of snow depletion curve with remote sensing data. Hydrol. Process., 20, 2363–2380. DOI: 10.1002/hyp.6060.

Krajčí, P., Holko, L., Perdigão, R.A.P.P., Parajka, J., 2014. Estimation of regional snowline elevation (RSLE) from MODIS images for seasonally snow covered mountain basins. J. Hydrol., 519, 1769–1778. DOI: 10.1016/j.jhydrol.2014.08.064.

Krajčí, P., Holko, L., Parajka, J., 2016. Variability of snow line elevation, snow cover area and depletion in the main Slovak basins in winters 2001–2014. J. Hydrol. Hydromech., 64, 12–22. DOI: 10.1515/johh-2016-0011.

Le Moine, N., Andréassian, V., Perrin, C., Michel, C., 2007. How can rainfall-runoff models handle intercatchment groundwater flows? Theoretical study based on 1040 French catchments. Water Resour. Res., 43, W06428. DOI: 10.1029/2006WR005608.

Liston, G.E., 2004. Representing subgrid snow cover heterogeneities in regional and global models. J. Clim., 17, 1381–1397. DOI: 10.1175/1520-0442(2004)017<1381:RSSCHI>2.0.CO;2.

Luce, C.H., Tarboton, D.G., 2004. The application of depletion curves for parameterization of subgrid variability of snow. Hydrol. Process., 18, 1409–1422. DOI: 10.1002/hyp.1420.

Magand, C., Ducharne, A., Le Moine, N., Gascoin, S., 2014. Introducing hysteresis in snow depletion curves to improve the water budget of a land surface model in an Alpine catchment. J. Hydrometeorol., 15, 631–649. DOI: 10.1175/JHM-D-13-091.1.

Magnusson, J., Gustafsson, D., Hüsler, F., Jonas, T., 2014. Assimilation of point SWE data into a distributed snow cover model comparing two contrasting methods. Water Resour. Res., 50, 7816–7835. DOI: 10.1002/2014WR015302.

Martinec, J., Rango, A., 1986. Parameter values for snowmelt runoff modelling. J. Hydrol., 84, 197–219. DOI: 10.1016/0022-1694(86)90123-X.

Nitta, T., Yoshimura, K., Takata, K., O'ishi, R., Sueyoshi, T., Kanae, S., Oki, T., Abe-Ouchi, A., Liston, G.E., 2014. Representing variability in subgrid snow cover and snow depth in a global land model: offline validation. J. Clim., 27, 3318–3330. DOI: 10.1175/JCLI-D-13-00310.1.

Niu, G.-Y., Yang, Z.-L., 2007. An observation-based formulation of snow cover fraction and its evaluation over large North American river basins. J. Geophys. Res. Atmospheres, 112, D21101. DOI: 10.1029/2007JD008674.

Parajka, J., Blöschl, G., 2008a. The value of MODIS snow cover data in validating and calibrating conceptual hydrologic models. J. Hydrol., 358, 240–258. DOI: 10.1016/j.jhydrol.2008.06.006.

Parajka, J., Blöschl, G., 2008b. Spatio-temporal combination of MODIS images - potential for snow cover mapping. Water Resour. Res., 44, 3. DOI: 10.1029/2007WR006204.

Parajka, J., Pepe, M., Rampini, A., Rossi, S., Blöschl, G., 2010. A regional snow-line method for estimating snow cover from MODIS during cloud cover. J. Hydrol., 381, 203–212. DOI: 10.1016/j.jhydrol.2009.11.042.

Parajka, J., Haas, P., Kirnbauer, R., Jansa, J., Blöschl, G., 2012. Potential of time-lapse photography of snow for hydrological purposes at the small catchment scale. Hydrol. Process., 26, 3327–3337. DOI: 10.1002/hyp.8389.

Perrin, C., Michel, C., Andréassian, V., 2001. Does a large number of parameters enhance model performance? Comparative assessment of common catchment model structures on 429 catchments. J. Hydrol., 242, 275–301. DOI: 10.1016/S0022-1694(00)00393-0.

Perrin, C., Michel, C., Andréassian, V., 2003. Improvement of a parsimonious model for streamflow simulation. J. Hydrol., 279, 275–289. DOI: 10.1016/S0022-1694(03)00225-7.

Poggio, L., Gimona, A., Brown, I., 2012. Spatio-temporal MODIS EVI gap filling under cloud cover: An example in Scotland. ISPRS J. Photogramm. Remote Sens., 72, 56–72. DOI: 10.1016/j.isprsjprs.2012.06.003.

Pokhrel, B.K., Chevallier, P., Andréassian, V., Tahir, A.A., Arnaud, Y., Neppel, L., Bajracharya, O.R., Budhathoki, K.P., 2014. Comparison of two snowmelt modelling approaches in the Dudh Koshi basin (eastern Himalayas, Nepal). Hydrol. Sci. J., 59, 1507–1518. DOI: 10.1080/02626667.2013.842282.

Pushpalatha, R., Perrin, C., Le Moine, N., Mathevet, T., Andréassian, V., 2011. A downward structural sensitivity analysis of hydrological models to improve low-flow simulation. J. Hydrol., 411, 66–76. DOI: 10.1016/j.jhydrol.2011.09.034.

Quintana-Seguí, P., Le Moigne, P., Durand, Y., Martin, E., Habets, F., Baillon, M., Canellas, C., Franchisteguy, L., Morel, S., 2008. Analysis of near-surface atmospheric variables: validation of the SAFRAN analysis over France. J. Appl. Meteorol. Climatol., 47, 92–107. DOI: 10.1175/2007JAMC1636.1.

Rodell, M., Houser, P.R., 2004. Updating a land surface model with MODIS-derived snow cover. J. Hydrometeorol., 5, 1064–1075. DOI: 10.1175/JHM-395.1.

Shrestha, M., Wang, L., Koike, T., Tsutsui, H., Xue, Y., Hirabayashi, Y., 2014. Correcting basin-scale snowfall in a mountainous basin using a distributed snowmelt model and remote-sensing data. Hydrol. Earth Syst. Sci., 18, 747–761. DOI: 10.5194/hess-18-747-2014.

Slater, A.G., Clark, M.P., 2006. Snow data assimilation via an Ensemble Kalman Filter. J. Hydrometeorol., 7, 478–493. DOI: 10.1175/JHM505.1.

Swenson, S.C., Lawrence, D.M., 2012. A new fractional snow-covered area parameterization for the Community Land Model and its effect on the surface energy balance. J. Geophys. Res. Atmospheres, 117. DOI:10.1029/2012JD018178.

Thirel, G., Salamon, P., Burek, P., Kalas, M., 2013. Assimilation of MODIS snow cover area data in a distributed hydrological model using the particle filter. Remote Sens., 5, 5825–5850. DOI: 10.3390/rs5115825.

Thirel, G., Andréassian, V., Perrin, C., 2015a. On the need to test hydrological models under changing conditions. Hydrol. Sci. J., 60, 1165–1173. DOI: 10.1080/02626667.2015.1050027.

Thirel, G., Andréassian, V., Perrin, C., Audouy, J.-N., Berthet, L., Edwards, P., Folton, N., Furusho, C., Kuentz, A., Lerat, J., Lindström, G., Martin, E., Mathevet, T., Merz, R., Parajka, J., Ruelland, D., Vaze, J., 2015b. Hydrology under change: an evaluation protocol to investigate how hydrological models deal with changing catchments. Hydrol. Sci. J., 60, 1184–1199. DOI: 10.1080/02626667.2014.967248.

Troin, M., Arsenault, R., Brissette, F., 2015. Performance and uncertainty evaluation of snow models on snowmelt flow simulations over a nordic catchment (Mistassibi, Canada). Hydrology, 2, 289–317. DOI: 10.3390/hydrology2040289.

Troin, M., Poulin, A., Baraer, M., Brissette, F., 2016. Comparing snow models under current and future climates: Uncertainties and implications for hydrological impact studies. J. Hydrol., 540, 588–602. DOI: 10.1016/j.jhydrol.2016.06.055.

Valéry, A., Andréassian, V., Perrin, C., 2014a. "As simple as possible but not simpler": What is useful in a temperature-based snow-accounting routine? Part 1 – Comparison of six snow accounting routines on 380 catchments. J. Hydrol. 517, 1166–1175. DOI: 10.1016/j.jhydrol.2014.04.059.

Valéry, A., Andréassian, V., Perrin, C., 2014b. "As simple as possible but not simpler": What is useful in a temperature-based snow-accounting routine? Part 2 – Sensitivity analysis of the Cemaneige snow accounting routine on 380 catchments. J. Hydrol., 517, 1176–1187. DOI: 10.1016/j.jhydrol.2014.04.058.

Vidal, J.-P., Martin, E., Franchistéguy, L., Baillon, M., Soubeyroux, J.-M., 2010. A 50-year high-resolution atmospheric reanalysis over France with the Safran system. Int. J. Climatol., 30, 1627–1644. DOI: 10.1002/joc.2003.

Vuyovich, C.M., Jacobs, J.M., Daly, S.F., 2014. Comparison of passive microwave and modeled estimates of total watershed SWE in the continental United States. Water Resour. Res., 50, 11, 9088–9102. DOI: 10.1002/2013WR014734.

Zaitchik, B.F., Rodell, M., 2009. Forward-looking assimilation of MODIS-derived snow-covered area into a land surface model. J. Hydrometeorol., 10, 130–148. DOI: 10.1175/2008JHM1042.1.

Received 26 April 2017
Accepted 13 August 2017

J. Hydrol. Hydromech., 67, 2019, 1, 82–92
DOI: 10.2478/johh-2018-0025

Probabilistic snow cover and ensemble streamflow estimations in the Upper Euphrates Basin

A. Arda Şorman*, Gökçen Uysal, Aynur Şensoy

Department of Civil Engineering, Anadolu University, 26555, Eskişehir, Turkey. E-mails: gokcenuysal@anadolu.edu.tr, asensoy@anadolu.edu.tr
* Corresponding author. Tel.: +90-222-3213550/6612. Fax: +90-222-3239501. E-mail: asorman@anadolu.edu.tr

Abstract: Predicting snow cover dynamics and relevant streamflow due to snowmelt is a challenging issue in mountainous basins. Spatio-temporal variations of snow extent can be analyzed using probabilistic snow cover maps derived from satellite images within a relatively long period. In this study, Probabilistic Snow Depletion Curves (P-SDCs) and Probabilistic Snow Lines (P-SLs) are acquired from Moderate Resolution Imaging Spectroradiometer (MODIS) cloud-filtered daily snow cover images. Analyses of P-SDCs show a strong correlation with average daily runoff ($R^2 = 0.90$) and temperature ($R^2 = 0.96$). On the other hand, the challenge lies in developing noteworthy methods to use P-SDCs in streamflow estimations. Therefore, the main objective is to explore the feasibility of producing probabilistic runoff forecasts with P-SDC forcing in a snow dominated basin.

Upper Euphrates Basin in Turkey has large snow extent and high snowmelt contribution during spring and summer periods. The melting characteristics are defined by P-SDCs using MODIS imagery for 2001–2012. The value of snow probability maps on ensemble runoff predictions is shown with Snowmelt Runoff Model (SRM) during 2013–2015 where the estimated runoff values indicate good consistency (NSE: 0.47–0.93) with forecasts based on the derived P-SDCs. Therefore, the probabilistic approach distinguishes the snow cover characteristics for a region and promotes a useful methodology on the application of probabilistic runoff predictions especially for snow dominated areas.

Keywords: Euphrates River Basin; MODIS; Probabilistic snow maps; Hydrological modeling; Ensemble streamflow estimation.

INTRODUCTION

Snow is an essential component in hydrological cycle particularly for mountainous regions and accumulated snow plays a crucial role during melting season in terms of water supply, hydropower generation, flood control, irrigation and avalanche research. However, estimation of potential snowpack and its contribution to streamflow is challenging due to complex physics of snowmelt and harsh topographic conditions in these regions. Snow cover is an important indicator of the climatic character of winter and spring (Krajci et al., 2016). Thus, assessment of snow cover dynamics at catchment scale helps to better understand the changes in flood regimes and improve snowmelt runoff forecasting. Due to the limitation in sparse observation network particularly for the mountainous regions, spatial patterns and seasonal depletion of snow cover is more easily monitored by multi spectral remote sensing.

Among the variety of satellites, MODIS (Moderate Resolution Imaging Spectroradiometer), with visible/near-infrared satellite sensors on Terra and Aqua platforms, provides processed Snow Cover Area (SCA) products since early 2000s. Numerous global and regional studies have been conducted on validation of MODIS snow data to identify snow mapping accuracy (Arsenault et al., 2014; Crawford, 2015; Hall and Riggs, 2007; Huang et al., 2011; Maurer et al., 2003; Parajka and Blöschl, 2008; Raleigh et al., 2013; Riggs et al., 2006; Tekeli et al., 2005; Wang et al., 2009). MODIS data have been successfully applied in snowmelt modeling (Day, 2013; Duethmann et al., 2014; Finger et al., 2015; Franz and Karsten, 2013; He et al., 2014; Li and Williams, 2008; Parajka and Blöschl, 2008; Şensoy and Uysal, 2012; Şorman et al., 2009) or in hydro-climatological and topographic research of snow cover variations (Cornwell et al., 2016; Forsythe et al., 2012; Gascoin et. al., 2015; Singh et al., 2003; Tang et.al., 2013; Tong et al., 2009; Wang and Xie, 2009). Moreover, various researchers attempted to apply different algorithms to decrease cloud coverage of MODIS products (Da Ronco and De Michele, 2014; Gafurov and Bárdossy, 2009; Gao et al., 2010; Krajčí et al., 2014; Parajka and Blöschl, 2008; Parajka et al., 2010; Sorman and Yamankurt, 2011).

Probability analysis of satellite snow cover data with relatively long and continuous records would be beneficial for analysis of snow climatology and operational snowmelt runoff forecasting. However there are limited studies associated with it in literature. Brander et al. (2000) derived snow cover duration maps using a limited number of Landsat-TM imagery. Richer (2009) derived snow probability maps for a basin in Colorado, using 8-day snow cover products of MODIS for the melting periods of 2000–2006 and investigated spatial and temporal snow distribution trends. Şensoy and Uysal (2012) presented the probability approach in snow depletion forecasting with a limited number of MODIS snow cover data. López-Burgos et al. (2013) used the locally-weighted logistic regression (LWLR) method to estimate probabilistic snow occurrences for developing the cloud removal technique. Gafurov et al. (2015) presented a methodology mainly based on correlations between station records and spatial snow-cover patterns, for reconstructing past snow cover using historical in situ snow-depth data, remote sensing snow-cover data and topographic data. Recently, Tekeli et al. (2016) calculated snow probability maps using Interactive Multi Sensor Snow and Ice Mapping System (IMS) snow products over Turkey. The work was accomplished with lower spatial resolution images, and only the validation methodology was discussed with ground measurements. On the overall, the elaborated studies are either limited on the number/time resolution of snow cover data or their implementation

within any hydrological modeling context are poorly addressed in terms of probabilistic studies.

Improved techniques in hydrological modeling studies may reveal the quantification of knowledge on long-term probabilistic snow cover extent and create an added value for water resources management. SCA can be examined both temporally and spatially with daily snow depletion curves (SDCs) which designate the snow coverage on each day of the melt season. One of the well-known conceptual models is Snowmelt Runoff Model (SRM) which enables to use SDCs as the main variable of snowmelt modeling for mountainous basins applied to several catchments around the world (Gómez-Landesa and Rango, 2002; Jain et al., 2010a; Jain et al., 2010b; Lee et al., 2005; Martinec, 1975; Panday et al., 2014; Şensoy and Uysal, 2012; Sensoy et al., 2014a; Sensoy et al., 2014b; Tahir et al., 2011; Tekeli et al., 2005). On the other hand, estimation of SCA is still a challenging issue in operational runoff forecasting.

Snow plays an important role in the hydrological regime, operational applications and climatic processes for the headwaters of transboundary Euphrates River as in many other mountainous regions. The Upper Euphrates River Basin is a highly snow-dominated area where snowmelt constitutes approximately 2/3 of total annual volume during spring and early summer months. Therefore, one of the headwater basins of the Euphrates River is selected as a pilot basin in this study with 10275 km^2 area. Concerning the harsh environmental conditions, the extent of the area and relatively scarce observation network, satellite remote sensing provides the most suitable method of monitoring snow variations over the region with a diversity of temporal and spatial scales. Even though particularly important, it is still a less-studied region of the world to extract and assess the snow cover characteristics using satellite technology.

Building upon the previous accuracy assessment and modeling studies (Şorman et al., 2007; Şorman et al., 2009; Tekeli et al., 2005) the work presented here provides the probabilistic appraisal of reliable snow cover monitoring by taking the advantage of long-term, continuous observations of MODIS SCA data over the mountainous headwaters of Euphrates River. The main purpose of the study is to derive daily probabilistic snow cover extent and characteristic snow depletion curves (P-SDCs) with corresponding Probabilistic Snow Line (P-SL) using a relatively long period of (12 years) daily cloud-filtered MODIS snow cover data for the area of interest, and also to investigate the possible relations with P-SDC and hydro-meteorological variables. Moreover, the main contribution herein is to present a noteworthy methodology to produce Probabilistic Ensemble Streamflow Forecasts (P-ESF) with P-SDC forcing into a hydrological model for a snow dominated data scarce headwater region of the Euphrates River Basin.

STUDY AREA AND DATA

Study area

Eastern Anatolia in Turkey has harsh weather and rough topographical conditions with high snow potential. Foremost precipitation falls as snow and is retained on the ground surface almost half of the year. Snowmelt starts during spring in conjunction to the rise of temperatures which makes considerable increment in streamflows. Transboundary Euphrates River, the longest in southwest Asia, is formed by the union of two major tributaries: Karasu and Murat rising in the highlands of eastern Turkey. Euphrates Basin is the largest in Turkey in terms of drainage area with 127,304 km^2 contributing 17% of the total water potential where most important dam reservoirs (Keban, Karakaya, Atatürk) are located within its boundary. Hence, forecasting the amount and timing of runoff at the headwaters of Euphrates River has great importance for the operation of these reservoirs.

Several studies on satellite snow product validation (Akyurek et al., 2010; Şorman et al., 2007; Sorman and Yamankurt, 2011; Sorman and Beser, 2013) as well as streamflow modeling and forecasting applications (Şensoy et al., 2006; Şorman et al., 2009; Şensoy and Uysal, 2012; Tekeli et al., 2005) are conducted in Karasu Basin as one of the pilot basins selected for various national and international funded projects. Karasu Basin is located within the longitudes 38^o 58’ E to 41^o 39’ E and latitudes 39^o 23’ N to 40^o 25’ N. It has a drainage area of 10275 km^2 and elevation ranges from 1125 to 3487 m. The main land cover types are pasture (35.0 %), agriculture (31.5%), bareland (27.5 %) and others (urban, forest, lakes etc., 6.0%).

The location and elevation distribution of Karasu Basin, controlled by stream gaging station E21A019 at Kemah, along with the observation network are provided in Figure 1. A summary of basin topographic properties are given in Table 1.

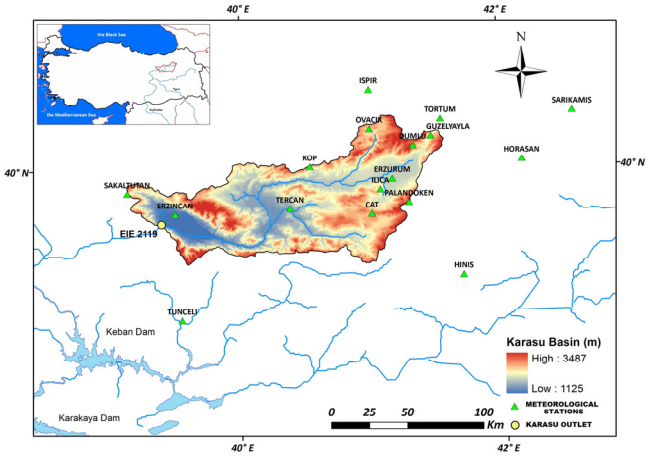

Fig. 1. Location, digital elevation model and observation network of Karasu Basin.

Table 1. Topographic properties of the basin.

Zone	Elevation range (m)	Area (%)	Hypsometric mean elevation (m)
A	1125–1500	10.6	1355
B	1500–1900	31.7	1762
C	1900–2300	33.8	2097
D	2300–2900	22.3	2484
E	2900–3487	1.6	2993
Basin	1125–3487	100.0	1983

Satellite snow cover data

MODIS satellite images are extensively used for determining areal snow coverage especially in hydrologic modeling. MOD10A1 for Terra and MYD10A1 for Aqua version 5 daily 500-m products are being produced and distributed by the NASA Distributed Active Archive Center (DAAC) located at the National Snow and Ice Data Center (NSIDC). Four MODIS tiles (h20v04, h20v05, h21v04, h21v05) are firstly mosaicked and later subset comprising the mountainous eastern part of Turkey using MODIS Reprojection Tools (MRT) program (https://lpdaac.usgs.gov/tools/modis_reprojection_tool) (Figure 2). The tiled images are then reprojected to World Geodetic Sys-

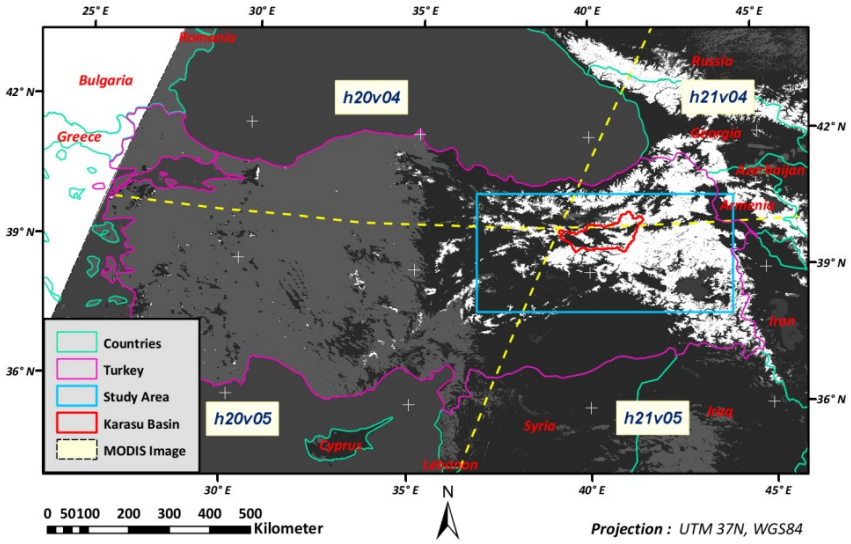

Fig. 2. MODIS tiles and selected study area window.

tem 1984 (WGS84), Universal Transverse Mercator (UTM) Zone 37 with a cell size of 500-m.

The MODIS snow-mapping algorithm is fully automated and is based on the Normalized Difference Snow Index (NDSI) with a set of thresholds (Hall et al., 2002). Based on NDSI and threshold values, snow cover pixels are separated from non-snowy areas using Eq. (1). Optical satellites are hindered by cloud cover and hence a filtering methodology (combination, temporal, spatial, elevation) (Sorman and Yamankurt, 2011) is applied on a pixel-by-pixel basis to totally eliminate cloud cover and determine binary snow/no snow areas especially during the period of snow melt.

$$NDSI = \frac{MODIS_{Band4} - MODIS_{Band6}}{MODIS_{Band4} + MODIS_{Band6}} \quad (1)$$

Hydro-meteorological and snow data

There are totally 18 climatologic and automated weather operating stations (AWOS) ranging in altitude between 981 and 2937 m (Figure 1). Detrended Kriging (DK) method (Garen et al., 1994; Garen and Marks, 2005) is used to distribute daily average temperature (T) and daily total precipitation (P) in each elevation zone (Table 1) for hydrological modeling.

General trends of total annual precipitation (P in cm), average annual temperature (T in ^{o}C), average annual runoff (Q in m^3/s), snow season (Jan-Jun) average snow cover (SCA in %) of Karasu Basin and maximum Snow Depth (SD in cm) at Guzelyayla SNOTEL (2065-m) are given in Figure 3 to provide an insight for hydro-meteorological and snow conditions observed in the last 15 years (2001–2015 water years, 01 Oct–30 Sep). SD values are measured at several automatic snow telemetry (SNOTEL) stations and manual snow courses are conducted twice a month during the winter season. Guzelyayla station, located at 2065-m altitude which is close to the hypsometric mean of the basin, has relatively long continuous records of SD values.

According to data analysis between 2001–2015 years for Karasu Basin, total annual precipitation is 601 mm yr^{-1} and average temperature is 4.6°C. A relatively low-flow period is observed for 2012–2014 water years. Having the sample mean and standard deviation to be much smaller than the population values, extreme events may cause outliers in data analysis and

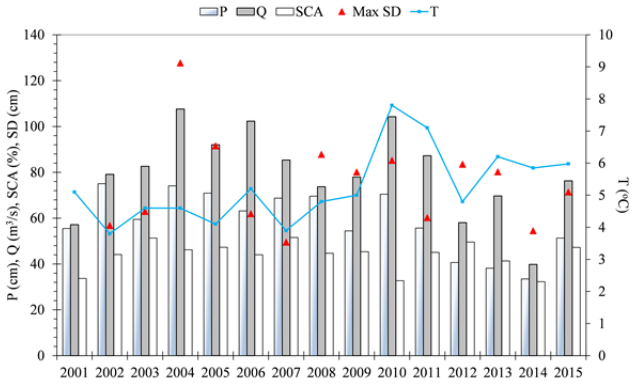

Fig. 3. Hydro-meteorological and snow data.

modeling. Therefore, the Modified Thompson Tau technique is used for verification of streamflow outliers. According to outlier test results for the mean streamflow, 2014 water year is found out as a low-flow outlier. 2004 is another extreme year with relatively high SD and P that resulted in flooding for some parts of the basin.

METHODOLOGY

In the most general form, the flow chart of the study is presented in Figure 4. The methodology is presented with four subtitles as; (1) derivation of Snow Probability Maps and classification of Probabilistic Snow Occurrence, (2) extraction of corresponding Probabilistic Snow Depletion Curves (P-SDCs) and Probabilistic Snow Line (P-SL), (3) analysis of P-SDCs and P-SL, (4) Probabilistic Ensemble Streamflow Forecasts (P-ESF) with SRM using P-SDC.

Probability of Snow Occurrence (PSO)

Spatial patterns of snow occurrence can be derived to explore spatial extent of snow cover in the watershed. "Probability of Snow Occurrence" (PSO) can be defined for each day and pixel as the fraction of MODIS images that are snow covered during the analysis period. The cloud coverage is eliminated from the satellite images with certain filters (Sorman and Yamankurt, 2011) in this study. Therefore, probability of snow

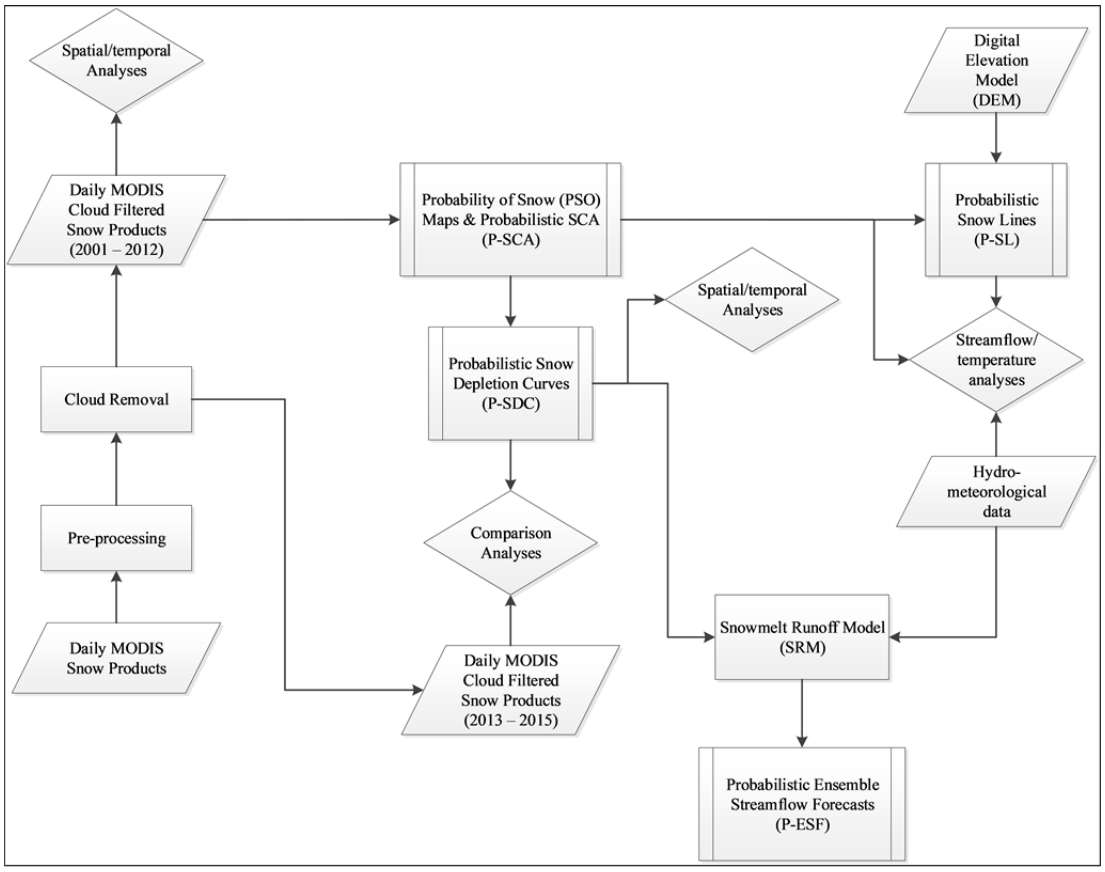

Fig. 4. Flowchart of the study.

distribution is calculated using daily SCA images, for which pixels are classified as snow or no snow, and probability maps are derived accordingly.

The probabilities are classified into six equal classes (Table 2). Zero probability (P = 0) means that there is no snow observation throughout the studied period, and P = 1 shows snow coverage within all these years. Accordingly, Snow Depletion Curves (SDCs) are derived indicating snow coverage on each day of the melt season and are frequently required for snowmelt runoff management.

Table 2. Probability classes.

Classes	Category
0	No-snow
0.00–0.25	Low snow probability
0.25–0.50	Average snow probability
0.50–0.75	Moderate snow probability
0.75–0.99	High snow probability
1	Full snow

Extraction of Probabilistic Snow Line Elevation (P-SL)

Snow Line (SL) estimates the boundary separating snow covered areas from snow-free areas. The time series of snowline provides an important indicator of snow response to climatic change and allow the prediction of future snow behavior (Tang et al., 2014). Temporal variability of SL elevation is calculated using (probabilistic) snow cover maps. Firstly, a threshold probability is defined and all pixels above this threshold are classified as snow, then probability maps are converted into binary snow cover maps. Afterwards, they are superposed with DEM of the basin and average pixel elevations corresponding to the boundary line are calculated for each day of the year.

Snowmelt Runoff Model (SRM)

Snowmelt Runoff Model (SRM) (Martinec, 1975; Martinec et al., 2008) is a conceptual model based on a degree-day method to estimate river runoff resulting from snowmelt and rainfall for mountainous basins with the aid of snow cover data. SRM requires daily average air temperature, total precipitation and average snow covered area values as input variables. Based on these input values, SRM computes daily streamflow by Eq. (2):

$$Q_{n+1} = [c_{Sn} a_n (T_n + \Delta T_n) S_n + c_{Rn} P_n] \frac{Ax10000}{86400} (1 - k_{n+1}) + Q_n k_{n+1} \quad (2)$$

where Q is average daily discharge ($m^3\ s^{-1}$); c is runoff coefficient expressing the losses as a ratio (runoff/precipitation) with c_S referring to snowmelt and c_R to rain; a is degree-day factor (cm $°C^{-1}\ d^{-1}$); T is number of degree-days (°C d); ΔT is the adjustment by temperature lapse rate; S is ratio of the snow covered area to the total area; P is precipitation contributing to runoff (cm); T_{CRIT}, determines whether this contribution is rainfall (°C); A is the area of the basin or zone (km^2), k is recession coefficient. According to Eq. (2), the daily average discharge on day n+1 is computed by summation of snowmelt and precipitation that contributes to runoff with the discharge on the proceeding day. Eq. (2) is applied to each zone or elevation band (approximately 500 m) of the basin when the model is used in a semi-distributed manner and then the discharges are summed up.

In this study, SRM is re-developed within Delft-FEWS (Flood Early Warning System) (oss.deltares.nl/web/delft-fews) platform (Sensoy et al., 2014a, 2014b; Uysal et al., 2015) and an external automatic optimization methodology is used to estimate the runoff coefficients. After modification and validation of the parameter sets, the basic idea is to use the classified P-SDCs in SRM**.** Since P-SDCs are generated for selected probability intervals, the cumulative probability alternatives are used in runoff estimation and all the results are presented as an ensemble of streamflows.

For the accuracy assessment, the model is tested with 4 goodness of fit criteria defined as the coefficient of determination (R^2), Nash-Sutcliffe Efficiency (NSE), Root Mean Square Error (RMSE), Mean Absolute Error (MAE) denoted as:

$$R^2 = \left[\frac{\sum_{t=1}^{N} \left(Q_m^t - \bar{Q}_m\right)\left(Q_o^t - \bar{Q}_o\right)}{\sqrt{\sum_{t=1}^{N} \left(Q_m^t - \bar{Q}_m\right)^2} \sqrt{\sum_{t=1}^{N} \left(Q_o^t - \bar{Q}_o\right)^2}} \right]^2 \quad (3)$$

$$NSE = 1 - \frac{\sum_{t=1}^{N} \left(Q_o^t - Q_m^t\right)^2}{\sum_{t=1}^{N} \left(Q_o^t - \bar{Q}_o\right)^2} \quad (4)$$

$$RMSE = \sqrt{\frac{\sum_{t=1}^{N} \left(Q_m^t - Q_o^t\right)^2}{N}} \quad (5)$$

$$MAE = \frac{\sum_{t=1}^{N} \left|Q_o^t - Q_m^t\right|}{N} \quad (6)$$

where Q_m^t is modeled flows, Q_o^t is observed flows, $\bar{Q}_m$ is average modeled flows, $\bar{Q}_o$ is average observed flows, N is the number of data sets.

RESULTS and DISCUSSION

Probability maps and Probabilistic Snow Depletion Curves (P-SDCs)

PSO areas are calculated on a pixel-by-pixel basis at daily intervals from January 15 to June 30 using the MODIS binary SCA images during the 2001–2012 period. Figure 5 shows the 15-day areal distribution of PSO (herein also probability maps) across the selected frame during 1 March to 15 April. According to results, there is a rapid melt from 1 March to 1 April due to increase in temperatures and solar radiation. Snow remains only in the upper altitudes through 15 April. A very small portion of the basin is snow covered especially at higher regions and almost all the snow melts until June. After that time, the rest of the snow cover in upper zones is not significant.

Cumulative P-SDCs are presented with box-whisker plots for Karasu Basin in Figure 6a. The graphs are formed with an expected depletion above the selected probabilities. P = 1 is the lower band and P > 0 is the upper band, a probability range is given for snow coverage through the season. New snowfall creates a sudden increase in the depletion. The frequency of the new snowfall directly related with the selected probability

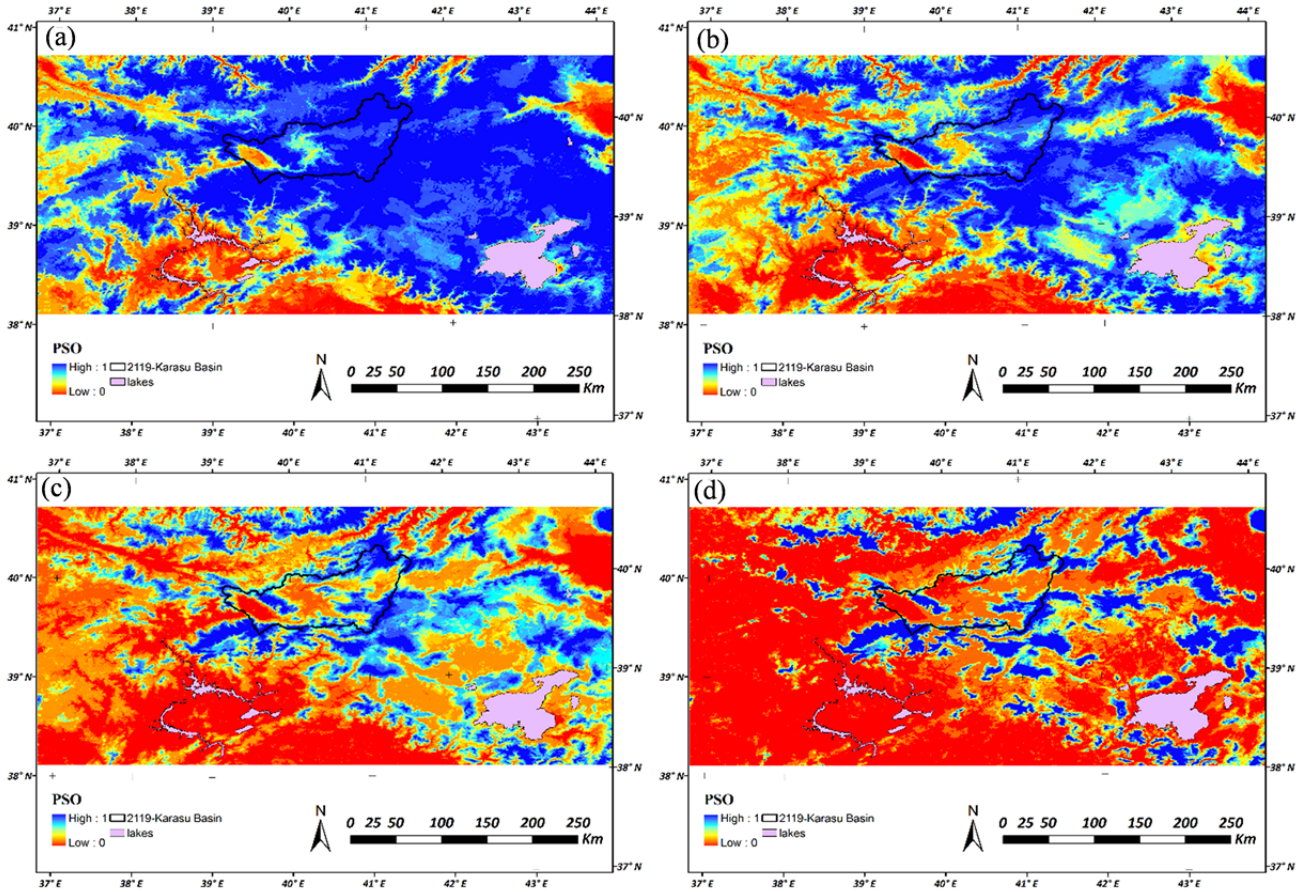

Fig. 5. MODIS Probability of Snow Occurrence maps of selected frame using 2001–2012 data (a) 01 March, (b) 15 March, (c) 01 April, (d) 15 April.

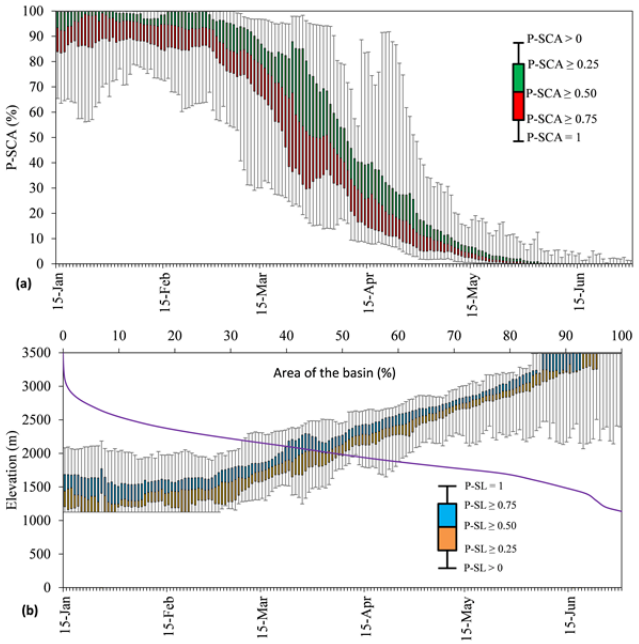

Fig. 6. (a) Cumulative P-SDCs (b) P-SL and hypsometric curve of Karasu Basin.

classes, such that if they occur many times, then the depletion is shifted to an upper probability class. On the other hand, the less frequent new snowfall observed in the lower zones create sudden increases in the P > 0 band.

Probabilistic Snow Line (P-SL)

P-SL is also calculated for each probability class and the results are given in Figure 6b. The outcomes indicate that the lowest SL elevation and hence the largest snow coverage occurs in the basin during January and February. All P-SL are below the hypsometric mean elevation in these months and this condition lasts till mid-March. P-SL starts to increase at the beginning of March (more than 50% of the area is snow covered with a 100% probability) and the median P-SL reaches to maximum elevation of the basin in the first half of June. The P-SL has the largest variability particularly through the end of March till the beginning of April. Before and after this period the variability in 25% and 75% of SL is almost constant. The median P-SL coincides with hypsometric mean elevation of 2000 m at the beginning of April (Figure 6b). At the end of the first week of April, 50% of the area is snow free and almost all percentiles of P-SLs are above the mean elevation of the basin afterwards.

Assessment of probabilistic snow extents

Temporal analysis

Strong seasonal variations in SCA are found with a homogenous snow cover distribution throughout the probability classes.

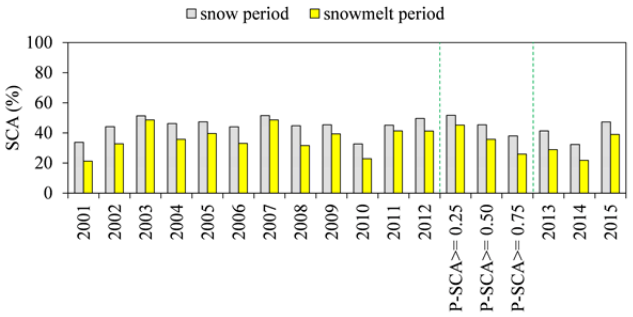

Fig. 7. Percentage of observed and probabilistic SCA for snow (Jan–Jun) and snowmelt (Mar–May) period.

Melting rates of different P-SDCs are calculated based on the slope of the P-SDCs (from Figure 6a). In order to simplify calculations, the slope between 90% and 10% coverage of snow is determined. Temporal variations of P-SDC (0.25–0.75) indicate that on average the melting rate is between 1.2–1.4% day^{-1} for the whole catchment when new snowfall events are discarded in the calculations. The highest rate of depletion (4% day^{-1}) is observed at the highest elevation zone with latest but shortest melting period.

The basin-wide average seasonal snow cover percentages are calculated to detect inter-annual variation in observed daily SCA and P-SCA). Inter-annual variability of the mean snow season (January–June) and snowmelt (March–May) SCA is presented in Figure 7. Observed SCA of 2001–2012 years are used to derive P-SDCs and observed SCA of 2013–2015 years are used to test the derived P-SDCs. It is calculated as the mean of all daily SCA values in the corresponding period. The time series of oscillations in the average SCA shows a high inter-annual variability, but there is no significant trend in the mean observed SCA for the period 2001–2015. The highest SCA throughout the snow season is observed in 2003 and 2007 (average is around 50%). The snow poor winters are 2001, 2010 and 2014 (average is around 30%).

For the 3 years (2013–2015), where SCA data are not included in the probability calculations, an assessment study is carried out to check the performances of derived P-SDCs. The validation performances are given in Table 3 with statistical scores. Observed SDCs have high consistency with P ≥ 0.50 and P ≥ 0.75 for 2013. SDC shows the highest relationship with high probability classes (P ≥ 0.75 and P = 1) which is an indication of low streamflows observed in 2014. 2015 SDC shows average characteristics on streamflow with the highest correlation in P ≥ 0.25 and 0.50 for the basin (Table 3). Thus, the performance assessment of independent (validation) SCA data set provides convenient results in accordance with Figure 7.

Streamflow analysis

Snow cover within mountainous areas imposes a definite influence on streamflow and there is a strong relation with SCA and streamflow. The cumulative average of observed discharge

Table 3. Performances of P-SDCs vs MODIS SDCs.

Karasu Basin	2013				2014				2015			
	R^2	NSE	RMSE (%)	MAE (%)	R^2	NSE	RMSE (%)	MAE (%)	R^2	NSE	RMSE (%)	MAE (%)
P > 0	0.71	0.41	31.88	21.72	0.70	–0.44	38.12	30.72	0.83	0.66	23.12	15.76
P >= 0.25	0.92	0.85	16.10	10.48	0.88	0.36	25.44	19.44	**0.98**	**0.96**	**7.88**	**5.43**
P >= 0.50	**0.96**	**0.95**	**8.95**	**5.46**	0.93	0.67	18.09	13.54	**0.98**	**0.98**	**5.58**	**3.03**
P >= 0.75	**0.97**	**0.96**	**8.62**	**5.77**	**0.95**	**0.88**	**10.83**	**7.30**	0.95	0.90	12.85	9.28
P = 1	0.91	0.72	22.10	15.19	**0.93**	**0.89**	**10.47**	**6.20**	0.87	0.55	26.62	20.87

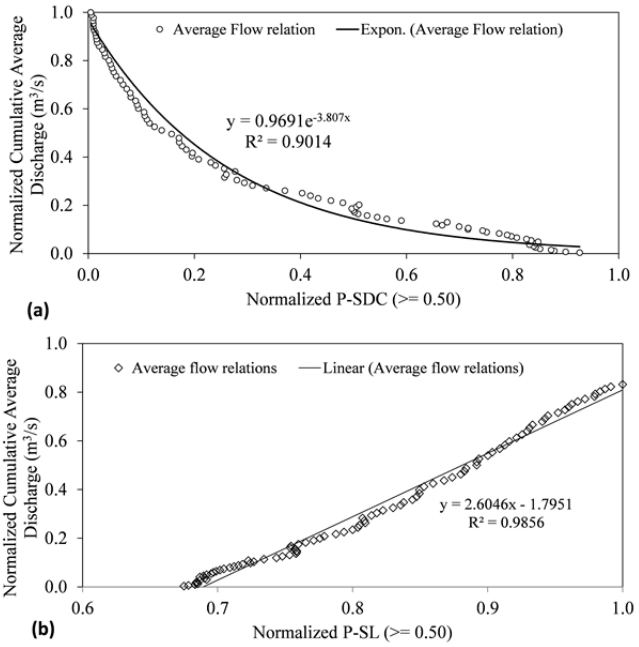

Fig. 8. Relationship between normalized cumulative average discharge and (a) P-SDC (b) P-SL for $P \geq 0.50$.

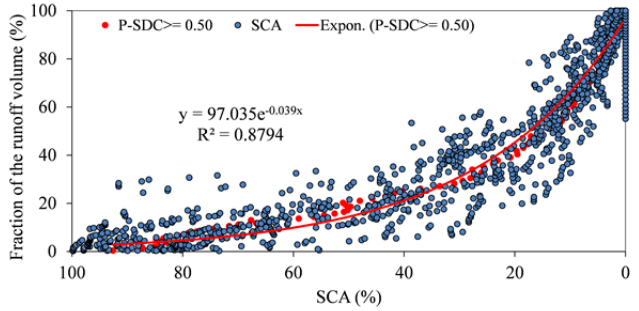

Fig. 9. Fraction of runoff volume and P-SDC relationship.

values (2001–2012) in March–May snowmelt period are normalized and their relation with cumulative P-SDC ($P \geq 0.50$) is analyzed for Karasu Basin (Figure 8a). There is a significant negative trend between SCA and streamflow, the decrease of P-SCA with time causes an exponential depletion of runoff in mountainous basins. The same analysis conducted for each year confirms this relationship. Exponential relationship implies that late decrease in SCA leads to higher changes in runoff than early decrease in SCA of the same magnitude. During melting, the snow line retreats from the lower altitude to higher altitude and consequently SCA in the basin is reduced. The retreat rate is increased in the later part of the melt season due to higher depth of snow at high altitudes. As a result, the highest coefficient of determination for exponential relationship in terms of Pearson R^2 is observed as 0.90 corresponding to $P \geq 0.50$. Moreover, the cumulative normalized runoff relationships are also analyzed in relation with P-SL ($P \geq 0.50$) (Figure 8b) for 2001–2012 March–May periods and it seems that runoff increases linearly with the snow line.

The correlation analyses between SCA and the proportion of runoff during snowmelt period indicates that the increase of runoff volume ratio is closely related to the SCA changes (Marcil et al., 2016). Therefore, one of the final analysis is the correlation between SCA (conventional and probabilistic) and runoff volume fraction. The fraction of runoff volume is also determined for the melting period, March–May. The daily fractions of runoff volume are computed as the ratio of the daily cumulative runoff volume to the total runoff volume and then they are converted to percent values. A scatter plot of SCA (SCA and percent runoff volume fraction of each year) and P-SCA (probabilistic SCA and percent runoff volume fraction of average runoff) for Karasu Basin is shown in Figure 9, for average runoff values over a 12 year (2001–2012) period. As expected, the fraction of runoff volume increases with a decrease of the snow areal extent. The runoff volume is expected to increase as the snow cover depletes to the upper elevations in the basin. An exponential function is found to be the best fit to the data and results indicate a robust correlation between SCA and runoff with $R^2 = 0.88$ as presented in Figure 9.

Temperature analysis

It is very essential to understand the relationship between P-SDC / P-SL and temperature since snow ablation processes are strongly controlled by air temperature. The average daily temperatures are calculated for the snowmelt period (March–May) of 2001–2012 and scattered with respect to corresponding P-SCA (Figure 10a) and P-SL (Figure 10b). The high positive correlations between P-SDC / P-SL and temperature is the robust evidence of temperature effect on snow extent. The rising temperature increases snow melting, thus causes higher SL and lower SCA.

Assuming that snowmelt is linearly related with temperature, one can conclude that SCA and cumulative temperatures should have an exponential relationship. Since cumulative negative temperatures disturb the exponential relationship for the initial period of the melt season, instead of cumulative temperatures, daily average temperatures are used in the analysis with a linear relation. These relations might also help to determine possible SCA values in case of a gap in the data series (ground data) or cloudy periods (satellite data).

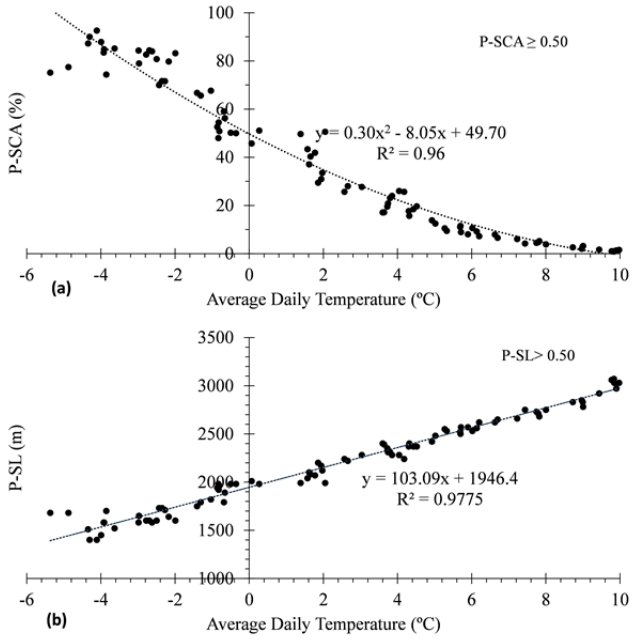

Fig. 10. Relationship with average daily temperature and (a) P-SDC, (b) P-SL for $P \geq 0.50$.

Probabilistic Ensemble Streamflow Forecasts (P-ESF)

Snowmelt Runoff Model, SRM, is implemented to produce Probabilistic Ensemble Streamflow Forecasts (P-ESF) from the derived probability maps. The watershed is divided into sub-elevation zones (Table 1) to improve modeling accuracy. The data is split into calibration and validation stages; calibration data is used to optimize the model parameters from 2002 to 2008 water years, validation is done for the remaining four years 2009 to 2012. The Nash-Sutcliffe goodness-of-fit coefficient, NSE, is used to determine the fit between modeled and observed flows. The observed and modeled runoff values are presented for Karasu Basin in Figure 11 and the performance of the model is summarized consecutively in Table 4. The accuracy of SRM model to mimic streamflow is high in terms of magnitude, trend and timing of the discharges considering relatively higher NSE value of 0.85 for the calibration period. NSE is sensitive to extreme values, thus, high overestimation of model simulations for 2010 reduces the model accuracy to some extent (Table 4).

Table 4. Model performance.

Period (Water Year)	R^2	NSE	RMSE (m^3/s)
Calibration (2002–2008)	0.86	0.85	32.62
Validation (2009–2012)	0.84	0.73	34.59

The model uses three major variables of daily average Snow Cover Area (SCA), average temperature (T) and total precipitation (P) as model inputs. Using different daily SCA patterns (P-SCA) with same P and T time series in the model gives different runoff values and these are called as ensembles. Therefore, the forecasting procedure is based on the hydrological model (SRM) that allows for the calculation of probabilistic ensemble streamflow (P-ESF) values for the period of 2013–2015 with two types of forcing data: observed snow cover area data on the basis of conventional SCA by MODIS (MODIS-SDC) and probabilistic SCA data by P-SDC for a range of probabilities. The model is applied by means of the perfect meteorological forecast data set (observed precipitation and temperature variables) and without any updating technique to focus on the direct effect of SDCs on runoff dynamics. The results are depicted by hydrographs in Figure 12 and goodness of fit statistics are given in Table 5.

Table 5. P-ESF goodness of fit statistics, 2013–2015.

Water Year	Simulation	R^2	NSE	RMSE (m^3/s)	MAE (m^3/s)
2013	**P-SDC ≥ 0.25**	0.68	–5.65	157.24	102.48
	P-SDC ≥ 0.50	0.65	–0.75	80.59	56.81
	P-SDC ≥ 0.75	**0.60**	**0.47**	**44.23**	**29.80**
	P-SDC = 1.00	0.35	–0.21	67.04	46.23
	MODIS-SDC	0.79	0.76	29.56	19.87
2014	**P-SDC ≥ 0.25**	0.59	–146.77	189.94	140.26
	P-SDC ≥ 0.50	0.66	–52.78	114.58	86.28
	P-SDC ≥ 0.75	0.69	–12.51	57.43	44.39
	P-SDC = 1.00	**0.58**	**–1.40**	**24.22**	**17.21**
	MODIS-SDC	0.68	–6.19	41.91	30.87
2015	**P-SDC ≥ 0.25**	0.97	0.81	36.67	26.75
	P-SDC ≥ 0.50	**0.93**	**0.93**	**22.85**	**15.27**
	P-SDC ≥ 0.75	0.85	0.73	43.52	29.31
	P-SDC = 1.00	0.81	0.60	52.66	35.62
	MODIS-SDC	0.93	0.86	30.90	22.70

It is interesting to note that each year has a different snow trend and observed runoff values show correlation with one of the derived cumulative probability ranges (Figure 12, Tables 3 and 5). The results indicate that; i) 2013 water year; this year can be classified as a dry year in terms of average rainfall but normal in regard to snowfall (snow depth) and discharges comparing 15-year averages of basin variables. Simulation with observed SDC gives NSE of 0.75 with an underestimation of the early runoff peak observed in 18 March. Either model parameters or rainfall representation (or both) might have caused this underestimation in the peak simulation. P ≥ 0.75 best suites to 2013 runoff hydrograph in general (NSE = 0.47), however there is a better agreement by P ≥ 0.50 for the first runoff peak, ii) 2014 water year; it is a low-flow outlier year with very low precipitation and snow depth. Even the simulation model performance with observed SDC is low in terms of NSE (with relatively high R^2) in this year. There would be several reasons for this, one of which might be the rather high runoff coefficients (such a low-flow condition precipitation and runoff was not used in the calibration data set) when P-ESF analysis is carried out. Least snow probability (P = 1) seems to best coincide with the observed runoff giving almost similar performance, iii) 2015 water year; model results give high

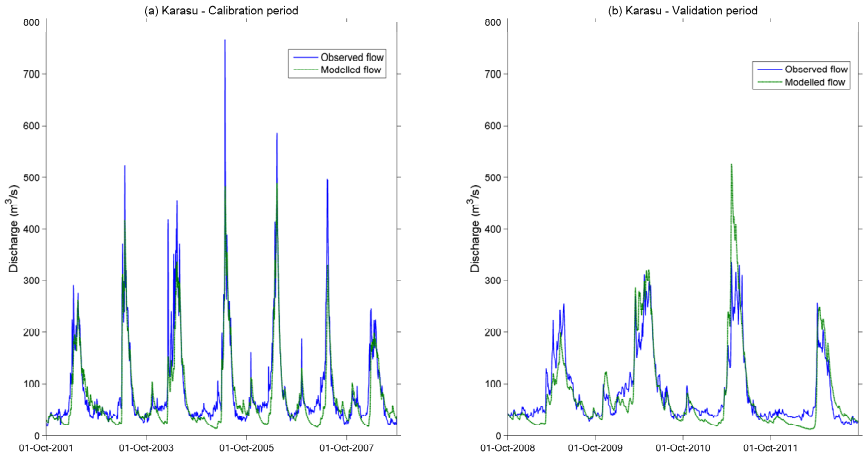

Fig. 11. SRM results in comparison to observed flows (a) Calibration period (2002–2008) (b) Validation period (2009–2012).

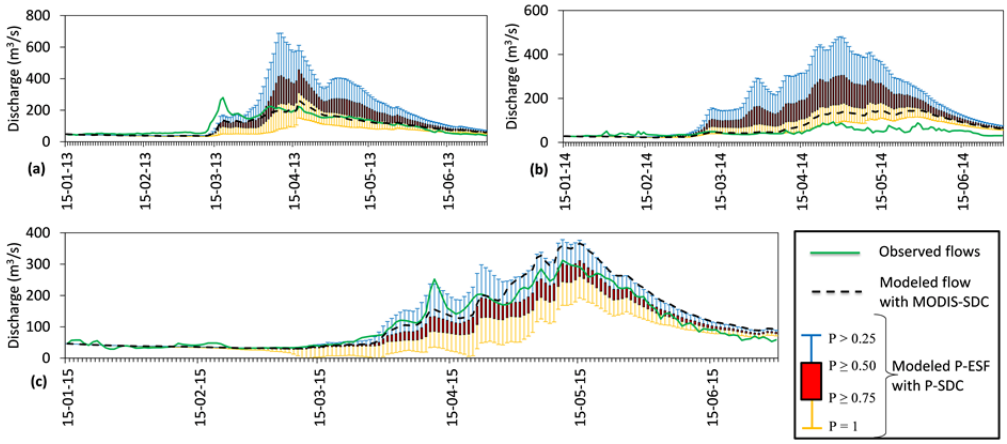

Fig. 12. SRM P-ESF results using P-SDCs (a) 2013, (b) 2014, (c) 2015.

model performance both using conventional observed SDC and P-SDC with NSE of 0.86 and 0.93, respectively. These results are most probably achieved due to average runoff and precipitation conditions. Simulation with P ≥ 0.50 provides quite a good match with the observed runoff values for 2015 except for the first peak where P ≥ 0.25 provides better estimates (Figure 12 and Table 5). All of the results are highly coherent with the outcomes of the assessments on conventional SCA and P-SCA for the melting periods of 2013–2015, therefore, the correspondence is high with Table 3. The results indicate that P = 1 and/or P ≥ 0.75 work better for dry years and P = 0 and/or P ≥ 0.25 can be chosen for wet years. A choice of P-SDC for a forecasting period could be determined according to the latest SCA and SWE states if available. A higher consistency can also be achieved if an additional update or assimilation procedure is implemented throughout the streamflow forecasting period.

CONCLUSIONS

Quantifying snowmelt has been a challenging aspect of hydrology with data and model uncertainties due to harsh topography and atmospheric conditions in a data scarce region. The research makes significant contributions to this field providing a valuable methodology to better understand snow cover dynamics and aid in probabilistic runoff forecasting.

Although ground-based measurements are generally accurate, stations are often sparsely located and the measurements do not adequately represent the spatial distribution of the snow extent. Remote sensing provides an ideal tool to observe status and dynamics of snow coverage whereby dedicated satellite snow data have an extensively increasing potential in water resources. An accurate information on the temporal and spatial depletion of snowpack can be efficiently implemented for operational runoff forecasting. Therefore, the study is intended as a precedent toward using satellite SCA products to assess snow cover assortment producing P-SDC and P-SL for better understanding of snow climatology and characteristics. Moreover, the value of making use of P-SDCs in hydrological modeling as well as generating probabilistic ensembles in operational runoff estimation for a mountainous catchment is presented. Forcing the hydrological model with P-SDCs shows promising results in probabilistic streamflow prediction.

Snow cover depletion curves are derived from 2001 to 2012 using MODIS satellite images that provide widely-used operational snow products with fine temporal resolution. Generalization of processed satellite snow cover images as probabilistic snow cover depletion (P-SDC) and snow line (P-SL) are the main features representing the snow cover characteristics of regions over mountainous domains. It is also shown that P-SDCs are useful in generating probabilistic ensemble streamflow forecasts (P-ESF) which is carried out for 2013–2015 snowmelt periods. As a conclusion, both the correlation established between the position of the snow depletion curve (or snowmelt line) and the value and/or timing of runoff, as well as P-ESF results based on the derived P-SDCs can guide decision-makers responsible for water resources management in the region. Since the proposed framework is a generic one, it can easily be adapted to other scarce networks or even ungaged mountainous watersheds dominated by snow accumulation and melt.

The forecasts can further be improved with the selection of suitable P-SDC through near real time SCA observations over the basin and also considering state updating of the hydrological model. On the other hand, any variation in a characteristic depletion curve over the decades could point out a climate change which would further indicate a reassessment in water resources planning.

Acknowledgement. This study was partly funded by TÜBİTAK (The Scientific and Technical Research Council of Turkey) (Project No: 113Y075) and Anadolu University Scientific Research Fund (Project No: 1306F113). The authors wish to thank General Directorate of Meteorology (MGM) and State Hydraulic Works (DSI) for data contribution.

REFERENCES

Akyurek, Z., Hall, D.K., Riggs, G.A., Sorman, A.U., 2010. Evaluating the utility of the ANSA blended snow cover product in the mountains of eastern Turkey. International Journal Remote Sensing, 31, 14, 3727–3744.

Arsenault, K.R., Houser, P.R., De Lannoy, G.J., 2014. Evaluation of the MODIS snow cover fraction product. Hydrol. Process., 28, 3, 980–998.

Brander, D., Seidel, K., Zurflüh, M., Huggel, C., 2000. Snow cover duration maps in alpine regions from remote sensing data. In Proceedings of EARSeL-SIG-Workshop Land Ice and Snow, Dresden/FRG, pp 292–296.

Cornwell, E., Molotch, N.P., McPhee, J., 2016. Spatio-temporal variability of snow water equivalent in the extra-tropical Andes Cordillera from distributed energy balance modeling and remotely sensed snow cover. Hydrology Earth System Science, 20, 411–430.

Crawford, C.J., 2015. MODIS Terra Collection 6 fractional

snow cover validation in mountainous terrain during spring snowmelt using Landsat TM and ETM. Hydrologic Processes, 29, 1, 128–138.

Da Ronco, P., De Michele, C., 2014. Cloudiness and snow cover in Alpine areas from MODIS products. Hydrol. Earth Syst. Sci. Discuss., 11, 3967–4015.

Day, A.C., 2013. Modeling snowmelt runoff response to climate change in the Animas River Basin. Colorado. Journal of Geology and Geoscience, 2, 110.

Duethmann, D., Peters, J., Blume, T., Vorogushyn, S., Guntner, A., 2014. The value of satellite-derived snow cover images for calibrating a hydrological model in snow-dominated catchments in Central Asia. Water Resources Research, 50, 3, 2002–2021. DOI: 10.1002/2013WR014382.

Finger, D., Vis, M., Huss, M., Seibert, J., 2015. The value of multiple data set calibration versus model complexity for improving the performance of hydrological models in mountain catchments. Water Resources Research, 51, 4, 1939–1958.

Forsythe, N., Kilsby, C.G., Fowler, H.J., Archer, D.R., 2012. Assessment of runoff sensitivity in the upper Indus basin to interannual climate variability and potential change using MODIS satellite data products. Mountain Research and Development, 32, 1, 16–29.

Franz, K.J., Karsten, L.R., 2013. Calibration of a distributed snow model using MODIS snow covered area data. J. Hydrol., 494, 160–175.

Gafurov, A., Bárdossy, A., 2009. Cloud removal methodology from MODIS snow cover product. Hydrology and Earth System Sciences, 13, 7, 1361–1373.

Gafurov, A., Vorogushyn, S., Farinotti, D., Duethmann, D., Merkushkin, A., Merz, B., 2015. Snow-cover reconstruction methodology for mountainous regions based on historic in situ observations and recent remote sensing data. The Cryosphere, 9, 2, 451–463.

Gao, Y., Xie, H., Lu, N., Yao, T., Liang, T., 2010. Toward advanced daily cloud-free snow cover and snow water equivalent products from Terra–Aqua MODIS and Aqua AMSR-E measurements. J. Hydrol., 385, 1, 23–35.

Garen, D.C., Johnson, G.L., Hanson, C.L., 1994. Mean areal precipitation for daily hydrologic modeling in mountainous regions. Water Resour. Bull., 30, 3, 481–491.

Garen, D.C., Marks, D., 2005. Spatially distributed energy balance snowmelt modelling in a mountainous river basin: estimation of meteorological inputs and verification of model results. J. Hydrol., 315, 126–153.

Gascoin, S., Hagolle, O., Huc, M., Jarlan, L., Dejoux, J.F., Szczypta, C., Marti, R., Sánchez, R., 2015. A snow cover climatology for the Pyrenees from MODIS snow products. Hydrology and Earth System Sciences, 19, 5, 2337–2351.

Gómez-Landesa, E., Rango, A., 2002. Operational snowmelt runoff forecasting in the Spanish Pyrenees using the snowmelt runoff model. Hydrol. Process., 16, 1583–1591.

Hall, D.K., Riggs, G.A., Salomonson, V.V., DiGirolamo, N.E., Bayr, K.J., 2002. MODIS snow-cover products. Remote sensing of Environment, 83, 1, 181–194.

Hall, D.K., Riggs, G.A., 2007. Accuracy assessment of the MODIS snow products. Hydrol. Process., 21, 12, 1534–1547.

He, Z.H., Parajka, J., Tian, F.Q., Blöschl, G., 2014. Estimating degree-day factors from MODIS for snowmelt runoff modeling. Hydrology Earth System Science, 18, 4773–4789.

Huang, X.D., Liang, T.G., Zhang, X.T., Guo, Z.G., 2011. Validation of MODIS snow cover products using Landsat and ground measurements during the 2001-2005 snow seasons over northern Xinjiang, China. International Journal of Remote Sensing, 32, 1, 133–52.

Jain, S.K., Goswami, A., Saraf, A.K., 2010a. Snowmelt runoff modelling in a Himalayan basin with the aid of satellite data. Int. J. Remote Sens., 31, 24, 6603–6618.

Jain, S.K., Goswami, A., Saraf, A.K., 2010b. Assessment of snowmelt runoff using remote sensing and effect of climate change on runoff. Water Resour. Manag., 24, 9, 1763–1777.

Jain, S.K., Thakural, L.N., Singh, R.D., Lohani, A.K., Mishra, S.K., 2011. Snow cover depletion under changed climate with the help of remote sensing and temperature data. Nat. Hazards, 58, 3, 891–904.

Krajčí, P., Holko, L., Perdigão, R.A., Parajka, J., 2014. Estimation of regional snowline elevation (RSLE) from MODIS images for seasonally snow covered mountain basins. J. Hydrol., 519, 1769–1778.

Krajčí, P., Holko, L., Parajka, J., 2016. Variability of snow line elevation, snow cover area and depletion in the main Slovak basins in winters 2001–2014. J. Hydrol. Hydromech., 64, 1, 12–22.

Lee, S.W., Klein, A.G., Over, T.M., 2005. A comparison of MODIS and NOHRSC snow-cover products for simulating stream flow using the Snowmelt Runoff Model. Hydrol. Process., 19, 15, 2951–2972.

Li, X.G., Williams, M.W., 2008. Snowmelt runoff modelling in an arid mountain watershed, Tarim Basin, China. Hydrological Processes, 22, 19, 3931–3940.

López-Burgos, V., Gupta, H.V., Clark, M., 2013. Reducing cloud obscuration of MODIS snow cover area products by combining spatio-temporal techniques with a probability of snow approach. Hydrology and Earth System Sciences, 17, 5, 1809–1823.

Marcil, G.K., Leconte, R., Trudel, M., 2016. Using remotely sensed MODIS snow product for the management of reservoirs in a mountainous Canadian watershed. Water Resources Management, 30, 8, 2735–2747.

Martinec, J., 1975. Snowmelt-runoff model for stream flow forecasts. Nord. Hydrol., 6, 145–154.

Martinec, J., Rango, A., Roberts, R., 2008. Snowmelt runoff model (SRM) user's manual. New Mexico State University, College of Agriculture and Home Economics, Las Cruces, New Mexico, USA.

Maurer, E.P., Rhoads, J.D., Dubayah, R.O., Lettenmaier, D.P., 2003. Evaluation of the snow-covered area data product from MODIS. Hydrol. Process., 17, 1, 59–71.

Panday, P.K., Williams, C.A., Frey, K.E., Brown, M.E., 2014. Application and evaluation of a snowmelt runoff model in the Tamor River basin, Eastern Himalaya using a Markov Chain Monte Carlo (MCMC) data assimilation approach. Hydrol. Process., 28, 21, 5337–5353.

Parajka, J., Blöschl, G., 2008. The value of MODIS snow cover data in validating and calibrating conceptual hydrologic models. J. Hydrol., 358, 3, 240–258.

Parajka, J., Pepe, M., Rampini, A., Rossi, S., Blöschl, G., 2010. A regional snow-line method for estimating snow cover from MODIS during cloud cover. J. Hydrol., 381, 3, 203–212.

Raleigh, M.S., Rittger, K., Moore, C.E., Henn, B., Lutz, J.A., Lundquist, J.D., 2013. Ground-based testing of MODIS fractional snow cover in subalpine meadows and forests of the Sierra Nevada. Remote Sensing of Environment, 128, 44–57.

Richer, E.E., 2009. Snowmelt runoff analysis and modelling for the upper cache La Poudre River basin, Colorado. MsS Thesis, Colorado State University, Fort Collins, USA.

Riggs, G.A., Hall, D.K., Salomonson, V.V., 2006. MODIS Snow Products User Guide to Collection 5. http://modis-snow-ice.gsfc.nasa.gov/?c=userguides. (Accessed Feb 2018)

Sensoy, A., Parajka, J., Coskun, C., Sorman, A., Ertas, C., 2014a. Quantifying the performance of two conceptual models for snow dominated catchments in Austria and Turkey. In: EGU General Assembly Conference Abstracts, 16, p. 10421.

Sensoy, A., Schwanenberg, D., Sorman, A., Akkol, B., Alvarado Montero, R., Uysal, G., 2014b, May. Assimilating H-SAF and MODIS Snow Cover Data into the Conceptual Models HBV and SRM. In: EGU General Assembly Conference Abstracts, 16, p. 10240.

Singh, P., Bengtsson, L., Berndtsson, R., 2003. Relating air temperatures to the depletion of snow covered area in a Himalayan basin. Nord. Hydrol., 34, 4, 267–280.

Sorman, A.A., Yamankurt, E., 2011. Modified satellite products on snow covered area in upper Euphrates basin, Turkey. Geophys Res. Abstr., 13, EGU2011-7887.

Sorman, A.U., Beser, O., 2013. Determination of snow water equivalent over the eastern part of Turkey using passive microwave data. Hydrol. Process., 27, 14, 1945–1958.

Şensoy, A., Şorman, A.A., Tekeli, A.E., Şorman, A.Ü., Garen, D.C., 2006. Point-scale energy and mass balance snowpack simulations in the upper Karasu basin, Turkey. Hydrol. Process., 20, 4, 899–922.

Şensoy, A., Uysal, G., 2012. The value of snow depletion forecasting methods towards operational snowmelt runoff estimation using MODIS and Numerical Weather Prediction Data. Water Resour. Manag., 26, 12, 3415–3440.

Şorman, A.A., Şensoy, A., Tekeli, A.E., Şorman, A.Ü., Akyürek, Z., 2009. Modelling and forecasting snowmelt runoff process using the HBV model in the eastern part of Turkey. Hydrol. Process., 23, 7, 1031–1040.

Şorman, A.Ü., Akyürek, Z., Şensoy, A., Şorman, A.A., Tekeli, A. E., 2007. Commentary on comparison of MODIS snow cover and albedo products with ground observations over the mountainous terrain of Turkey. Hydrol. Earth Syst. Sc., 11, 4, 1353–1360.

Tahir, A.A., Chevallier, P., Arnaud, Y., Neppel, L., Ahmad, B., 2011. Modeling snowmelt-runoff under climate scenarios in the Hunza River Basin, Karakoram Range, Northern Pakistan. J. Hydrol., 409, 104–117.

Tang, Z., Wang, J., Li, H., Yan, L., 2013. Spatiotemporal changes of snow cover over the Tibetan plateau based on cloud-removed moderate resolution imaging spectra-radiometer fractional snow cover product from 2001 to 2011. Journal of Applied Remote Sensing, 7, 1, 073582.

Tang, Z., Wang, J., Li, H., Liang, J., Li, C., Wang, X., 2014. Extraction and assessment of snowline altitude over the Tibetan plateau using MODIS fractional snow cover data (2001 to 2013). Journal of Applied Remote Sensing, 8, 084689.

Tekeli, A.E., Akyürek, Z., Şorman, A.A., Şensoy, A., Şorman, A.Ü., 2005. Using MODIS snow cover maps in modeling snowmelt runoff process in the eastern part of Turkey. Remote Sens. Environ., 97, 2, 216–230.

Tekeli, A.E., Sönmez, I., Erdi, E., 2016. Snow-covered area determination based on satellite-derived probabilistic snow cover maps. Arabic Journal of Geosciences, 9, 198.

Tong, J., Déry, S.J., Jackson, P.L., 2009. Interrelationships between MODIS/Terra remotely sensed snow cover and the hydrometeorology of the Quesnel River Basin, British Columbia, Canada. Hydrology and Earth System Sciences, 13, 8, 1439–1452.

Uysal, G., Akkol, B., Ertaş, C., Çoşkun, C., Şorman, A., Şensoy, A., Schwanenberg, D., 2015. Developing an Operational Hydrologic Forecast System using EPS and Satellite Data in Mountainous Basins of Turkey, DSD-2015, Delft Software Days, Delft, The Netherlands.

Wang, M., Son, S., Shi, W., 2009. Evaluation of MODIS SWIR and NIR-SWIR atmospheric correction algorithms using SeaBASS data. Remote Sensing of Environment, 113, 3, 635–644.

Wang, X., Xie, H., 2009. New methods for studying the spatiotemporal variation of snow cover based on combination products of MODIS Terra and Aqua. J. Hydrol., 371, 1, 192–200.

Received 7 August 2017
Accepted 22 February 2018

J. Hydrol. Hydromech., 67, 2019, 1, 93–100
DOI: 10.2478/johh-2018-0003

On the estimation of temporal changes of snow water equivalent by spaceborne SAR interferometry: a new application for the Sentinel-1 mission

Vasco Conde[1], Giovanni Nico[2*], Pedro Mateus[1], João Catalão[1], Anna Kontu[3], Maria Gritsevich[4, 5, 6]

[1] Instituto Dom Luiz (IDL), Universidade de Lisboa, 1749-016 Lisboa, Portugal.
[2] Consiglio Nazionale delle Ricerche, Istituto per le Applicazioni del Calcolo (CNR-IAC), 70126 Bari, Italy.
[3] Finnish Meteorological Institute (FMI), Sodankylä, Finland.
[4] Department of Physics, P.O. Box 64, FI-00014 University of Helsinki, Finland.
[5] Institute of Physics and Technology, Ural Federal University, Ekaterinburg, Russia.
[6] Dorodnicyn Computing Centre, Russian Academy of Sciences, Moscow, Russia.
[*] Corresponding author. E-mail: g.nico@ba.iac.cnr.it

Abstract: In this work we present a methodology for the mapping of Snow Water Equivalent (SWE) temporal variations based on the Synthetic Aperture Radar (SAR) Interferometry technique and Sentinel-1 data. The shift in the interferometric phase caused by the refraction of the microwave signal penetrating the snow layer is isolated and exploited to generate maps of temporal variation of SWE from coherent SAR interferograms. The main advantage of the proposed methodology with respect to those based on the inversion of microwave SAR backscattering models is its simplicity and the reduced number of required in-situ SWE measurements. The maps, updated up to every 6 days, can attain a spatial resolution up to 20 m with sub-centimetre ΔSWE measurement accuracy in any weather and sun illumination condition. We present results obtained using the proposed methodology over a study area in Finland. These results are compared with in-situ measurements of ΔSWE, showing a reasonable match with a mean accuracy of about 6 mm.

Keywords: Snow Water Equivalent (SWE); Synthetic Aperture Radar (SAR); SAR interferometry (InSAR); Sentinel-1.

INTRODUCTION

The Snow Water Equivalent (SWE) is the quantity of water stored in the snowpack. Its measurement is important for predicting the water supply at the snowmelt time, useful for both assessing the energy potential of snow in hydroelectric power plants and the flood risk in valleys and plain areas crossed by rivers. Furthermore, the seasonal snow cover is an important component in land surface climate since it causes a seasonal variation in surface albedo, and it has a low thermal conductivity, so it insulates the soil surface from large, rapid temperature fluctuations. The monitoring of snow cover with a high spatial and temporal resolution over large areas can provide useful information to Numerical Weather Models (NWMs) since it can help to set dynamic boundary conditions based on the land cover. Estimates of the SWE can be extracted by using remote sensing techniques. Different remote sensing techniques have been used to estimate the SWE. As an example, Snow-Covered Area (SCA) maps provided by the Moderate Resolution Imaging Spectroradiometer (MODIS) have been used in SWE models (see e.g. Bavera and De Michele (2009), Guan et al. (2013)).

However, visible and near-infrared sensors are affected by cloud cover that can hinder the possibility to image the terrain surface. Radiometers provide information on snow at a very low spatial resolution (about 25 km) and have difficulties in both deep and shallow snow conditions (Takala et al., 2011). A new microwave spaceborne mission has been presented to the European Space Agency (ESA) for the high resolution mapping of SWE and of its temporal variations to study climate changes and their impact on the environment (Rott et al., 2012a; Rott et al., 2012b). However, the snow accumulation and melt are highly variable in space and time. This requires detailed field measurements to correctly model the snow variability on catchment scale (Krajči et al., 2016). Synthetic Aperture Radar (SAR) can provide high resolution maps of snow properties over wide areas, in all-weather and day/night conditions. SAR images are currently acquired by different spaceborne missions at different microwave frequencies, X-band (COSMO-SkyMed and TerraSAR-X), C-band (Sentinel-1 and RADARSAT-2) and L-band (ALOS-2) using different polarization channels (HH, HV, VV, where e.g. HV means that the SAR image is obtained by illuminating the scene with H-polarized microwave signal and receiving the V-polarized component of the backscattered signal). SAR images have been used to study the snow physical properties based on their capability to penetrate the snowpack or being absorbed when the snow is melting (Malnes and Guneriussen, 2002; Nagler and Rott, 2000; Pivot, 2012; Sun et al., 2015). The SWE is defined in terms of snow density and depth. The first quantity can be estimated by L-band SAR images (Shi and Dozier, 2000a). Although the L-band radar signal passes easily through dry snow, snow density affects the radar backscattering coefficient. The snow density is estimated using L-band VV and HH measurements and a numerical model to compute the backscattering coefficients (Shi and Dozier, 2000a). Furthermore, the C and X-bands have been used to retrieve the snow depth (Shi and Dozier, 2000b). The algorithm does not require a priori knowledge of the subsurface dielectric and roughness properties. A numerical model is also used to invert C and X-band SAR images to estimate the snow depth (e.g. see Longepe et al. (2009), Shi and Dozier (2000b)). Usually, this requires a large amount of in-situ measurements to accurately estimate the relationship between the radar cross section and the snow properties.

In this manuscript, we investigate the use of SAR interferometry (InSAR) to map SWE over large areas using spaceborne C-band Sentinel-1 SAR data, at the light of their short revisiting time of six days, large spatial coverage and high spatial resolution of 20 meters. Furthermore, ESA is providing Sentinel-1 data using a free-access policy. The main motivation of this work is to understand if the use of InSAR technique can reduce

the amount of in-situ SWE measurements while keeping all the other advantages of SAR images, mainly its high spatial resolution. In fact, SWE estimation methods based on SAR amplitude images require many in-situ SWE measurements to invert the microwave SAR backscattering model.

Guneriussen et al. (2001) presented a theory to explain the presence of fringes in SAR interferograms acquired over areas covered by dry snow. They interpreted the interferometric phase in terms of a possible temporal change in the SWE. However, the authors pointed out that in-situ meteorological observations were needed to distinguish the phase contributions due to the temporal change of SWE from the propagation effects in atmosphere. The physical principle used by SAR interferometry is that of phase delay due to propagation in a non-dispersive medium. This implies that the snow is supposed to be dry to allow the propagation of the SAR signal. The fact that the SWE estimation is based on the measurement of a phase delay implies that phase contributions due to terrain morphology and propagation in the atmosphere should be properly modeled and corrected. For instance, a precise Digital Elevation Model (DEM) of the area is used to model and remove the phase due to topography modulation of the interferometric signal. Critical is the mitigation of the atmospheric phase delay since it is characterized by a low spatial frequency fringe pattern affecting the whole interferogram. These characteristics could be similar to the spatial distribution of SWE in the winter season and for this reason it is very important to remove the phase component due to propagation in atmosphere. The atmosphere's phase delay can be modeled by using external data such as NWMs (Mateus et al., 2015; Nico et al., 2011) or delay measurements provided by Global Navigation Satellite System (GNSS) receivers or passive satellite sensors, such as MERIS in the past or MODIS for current studies (Mateus et al., 2010). Concerning the presence of terrain displacements, due to different geological phenomena or to the human activity, it is assumed that they are negligible within the time interval between the acquisitions of the master and slave SAR images used to generate the interferograms. The proposed methodology provides a direct estimate of the snow depth which is then used to derive the SWE.

Even if it is no longer needed to invert a backscattering model relating SAR data to in-situ measurements of SWE, as in the case of the estimation techniques based on the SAR backscattering coefficients, the knowledge of the SWE in a few points is still needed to calibrate InSAR data. The main reason for this is related to the interferometric processing of SAR data. In fact, phase measurements are always relative to a reference point. In space geodesy applications of SAR interferometry, the reference point is a stable target which has no displacement in the time interval between the master and slave images or a target with known displacement rate. In this paper, the reference points correspond to sites where the SWE is provided by in-situ measurements. Absolute estimates of the SWE can be obtained by building a time series of SAR images sharing the same acquisition parameters, with the first image during the summer season when the SWE is zero. An important novelty of this work is the use of a numerical weather model to estimate the 3-D fields of the most relevant atmospheric physical parameters (including atmosphere's temperature, relative humidity and total pressure) with a 1 km spatial resolution and a variable vertical resolution from the Earth surface up to an altitude corresponding to 10 hPa. These parameters are used to model the microwave phase delay in troposphere. The proposed methodology is applied in an experiment to estimate the temporal variation of SWE, from December 29, 2015 to January 22, 2016, over a large area in the northeastern part of Finland.

STUDY AREA AND DATASET

The study area is located at the northeastern border of Finland (66° N, 28° E) as shown in Figure 1. It partially covers the three Finnish regions of Kainuu, Northern Ostorbothnia, and Lapland. The small portion of the Russian territory which is in the Sentinel-1's footprint has been removed by means of a mask. It spans an area of about 22 000 km^2 with an average altitude of 250 m above the sea level. The minimum and maximum altitudes of the study area are 110 m and 511 m a.s.l., respectively. The area is characterized by a moderate topography, with an altitude standard deviation of 55 m, and a seasonally snow covered surface in the winter season.

Three consecutive C-band ESA Sentinel-1 SAR images, acquired between December 2015 and January 2016 in Interferometric Wide (IW) swath mode along a descending pass, have been used. Each image has a dual polarization VV+VH, a 32°–43° incidence angle, and a spatial resolution of 5 m × 20 m. Two consecutive interferograms have been generated from the SAR images. The interferograms were generated by keeping the temporal baseline at the lowest possible value of twelve days. Each interferogram was corrected for the topographic phase contribution, using a DEM with a spatial resolution of 10 m and a vertical accuracy of 1.4 m, created by the National Land Survey of Finland (see Figure 1), and then multilooked. Table 1 summarizes the acquisition dates of the master and slave

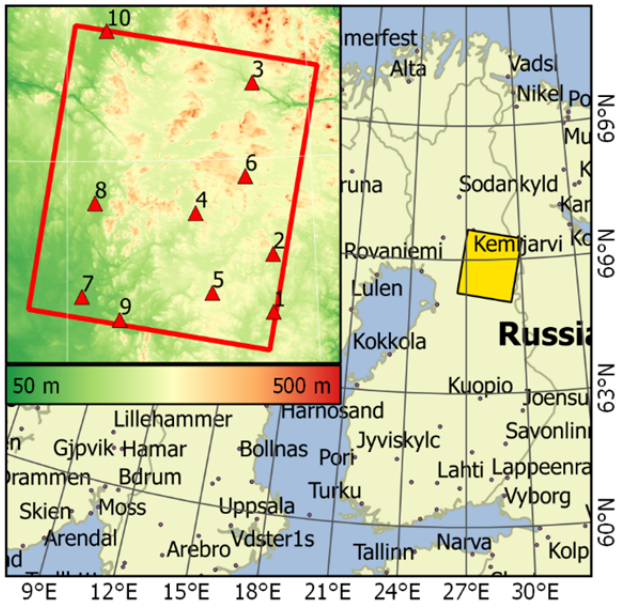

Fig. 1. Location of the study area (yellow rectangle) on the Scandinavian Peninsula map. The Digital Elevation Model (DEM) of the area is reported in the inset on the upper-left corner, where the ten locations of in-situ SWE measurements (red triangles) and the footprint of the SAR images (red outline) are overlaid.

Table 1. Master and slave acquisition dates, temporal and perpendicular spatial baselines of the interferograms.

Master image acquisition date	Slave image acquisition date	Temporal baseline (days)	Perpendicular baseline (m)
2015-12-29	2016-01-10	12	43.60
2016-01-10	2016-01-22	12	55.45

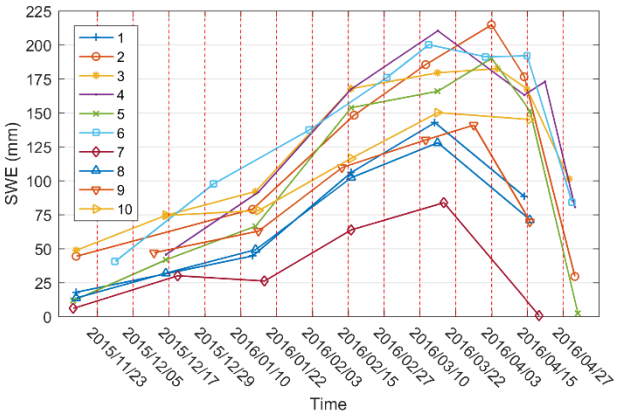

Fig. 2. SWE measurements for each in-situ location from November 2015 till April 2016. Sentinel-1 SAR acquisition dates are represented by vertical dashed lines. For the acquisition dates of master and slave SAR images (Table 1) SWE values have been estimated by 2nd order polynomial regression.

Sentinel-1 SAR images, the temporal and perpendicular baselines of the corresponding interferograms.

The in-situ SWE data are measured at ten different locations scattered across the study area, as reported in Figure 1. The time series of SWE values, shown in Figure 2, are from snow course measurements made by the Finnish Environment Institute (SYKE) (available at http://www.syke.fi/en-US/Open_information). The measurement, made along 2 km long snow courses, have been carried out over different land cover categories, so that an average calculated from individual measurements gives a representative SWE value for the location.

The course is typically measured once per month using manual snow depth probe and snow tube (Leppänen et al., 2016).

Cloud-free Sentinel-2 MSI Natural Colors images and a recently updated Corine map of the study area have been used to get information about land use and cover around each in-situ measurement location (see Figure 3).

It is worth noting that, as plotted in Figure 2, the acquisition dates of in-situ SWE measurement and Sentinel-1 data do not coincide. As a consequence, the in-situ reference SWE values at the acquisition times of master and slave images, used to generate the interferograms (see Table 1), have been obtained by a 2-nd order polynomial regression from data acquired from November 23, 2015 till March 10, 2016 (see Figure 2). In-situ measurements acquired in April have not been used as it has not been possible to generate coherent SAR interferograms for that period.

METHODOLOGY

The interferometric phase, computed as the complex product of two satellite SAR images, contains different contributions. The most significant ones are: 1) topography, 2) terrain displacement, 3) atmospheric phase delay, 4) contribution due to inaccurate knowledge of satellite orbits and hence of the interferometric spatial baseline. All these contributions can be identified and removed or at least mitigated. The topographic contribution is removed using a DEM of the area. The atmospheric contribution can be modeled and mitigated by using external data such as Numerical Weather Model (NWM) output or permanent GPS receivers and meteorological stations. The phase contribution due to satellite orbits errors are easily identified since it gives rise to phase ramps in the interferogram which can be removed. Contribution due to terrain displacement (e.g. due to landslides, earthquakes, and subsidence) are not easily identified since they usually affect small areas and are related to geological phenomena and/or human activity. In this work we assumed they are negligible over the temporal interval of twelve days. We assume that the residual phase is related to the propagation of microwaves into the snow layer.

When isolated from the contributions listed above, the interferometric phase due to the propagation into the snow layer can be used to estimate the temporal changes of SWE. In fact, due to the dielectric contrast at air-snow interface, the radar signal is refracted when it impinges on the snow layer, resulting in a longer path (ΔR_S) when compared with the linear path (ΔR_A) as sketched in Figure 4. A relationship can be found between the variation of snow depth and the measured interferometric phase (Guneriussen et al., 2001):

$$\Delta\phi_s = \frac{4\pi}{\lambda_0}\Delta Z_S(\cos\theta_i - \sqrt{\epsilon - \sin^2\theta_i}) \quad (1)$$

where $\Delta\phi_S$ is the interferometric phase contribution due to the 2-way propagation into the snow layer, measured as the phase difference between two SAR images acquired at two different times (master and slave SAR images). The other parameters of the equation are: the radar wavelength λ_0, the surface incidence angle θ_i, the snow depth temporal variation ΔZ_S, and the snow relative permittivity ϵ which depends on the snow density ρ_S. The SWE is defined as:

$$\mathrm{SWE}(\rho_s) = \frac{\rho_S}{\rho_W} Z_S \quad (2)$$

where ρ_W is the liquid water density. From Equations (1) and (2) the following relationship can be found between the temporal variation of SWE and the interferometric phase:

$$\Delta\mathrm{SWE} = \mathrm{SWE}(t_s) - \mathrm{SWE}(t_m) = \frac{\lambda_0}{2\pi}\cdot\frac{1}{\alpha\left(1.59+\theta_i^{\frac{5}{2}}\right)}\Delta\phi_s \quad (3)$$

where t_m and t_s are, respectively, the acquisition times of the master and slave SAR images and $\alpha \cong 1$ is a parameter slightly depending on the incidence angle θ_i (Leinss et al., 2015). The local incidence angle is estimated from the DEM, computing the local slope and aspect angles, and the spaceborne SAR look angle. Using the Sentinel-1 SAR wavelength λ_0 = 5.5 cm, a mean incidence angle of θ_i = 37° and $\alpha \cong 1$, Equation (3) can be re-written as:

$$\Delta\mathrm{SWE} = \mathrm{SWE}(t_s) - \mathrm{SWE}(t_m) = 0.0045\ \Delta\phi_s \quad (4)$$

This relationship says that since the phase variation $\Delta\phi_s$ measured by SAR interferometry is always within the basic interval [–π, π] rad, the temporal variation of SWE can be estimated unambiguously, without the need of phase unwrapping, only in the interval [–14.3, 14.3] mm. It is worth noting that this interval depends on the local incidence angle and so in real conditions it slightly varies in space according to the local θ_i.

A key point of the proposed methodology is the modeling of the atmospheric phase delay. In fact, the interferometric phase signal has two main contributions, after the correction of topography contribution, and in case of no significant terrain deformation within the time window between two SAR acquisitions, phase delays in atmosphere and the snow layer. If

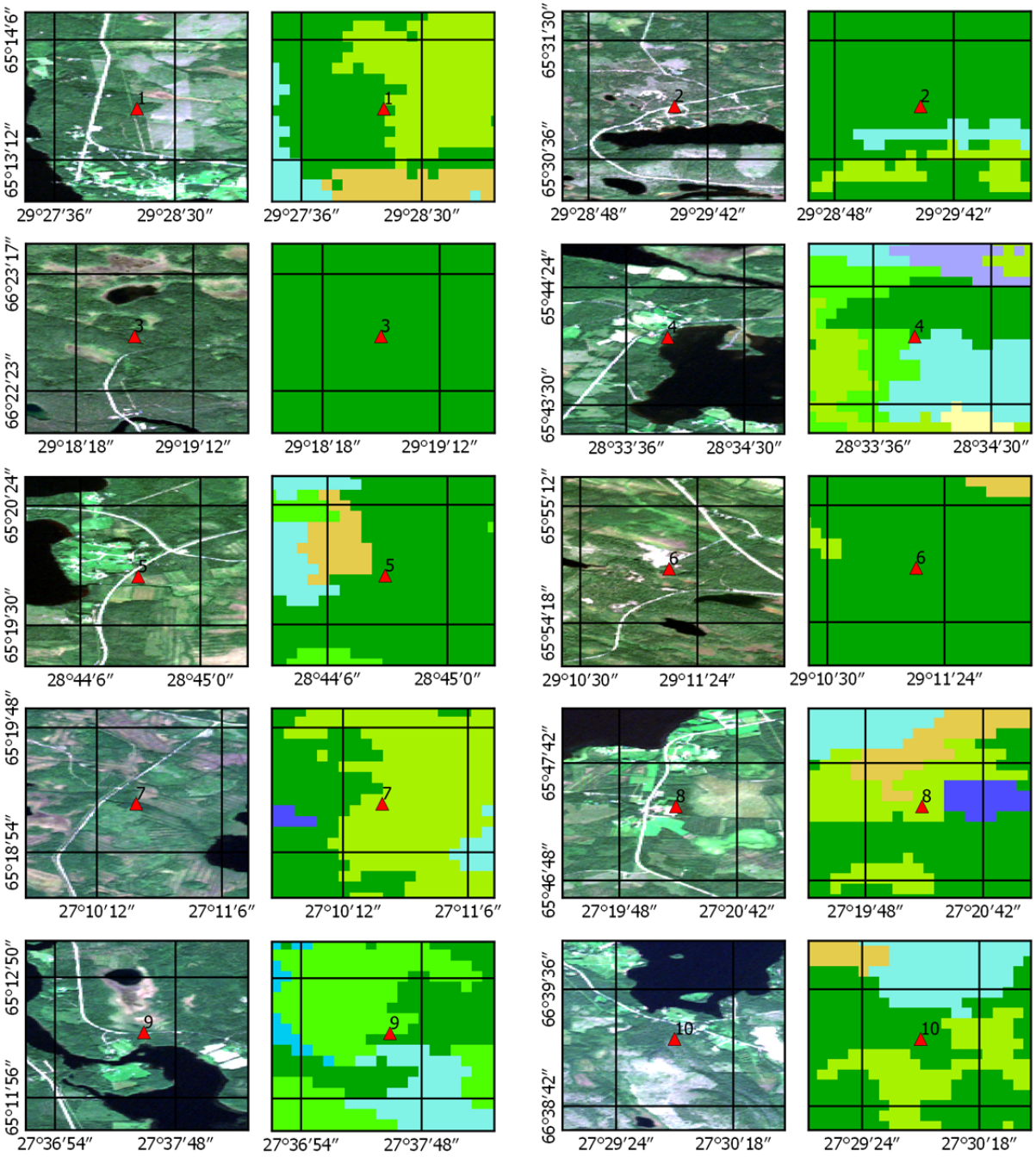

Fig. 3. From left to right, from top to bottom, details of cloud and snow-free Sentinel-2 MSI Natural Colors and 2012-Corine map around the ten locations of in-situ SWE measurements (denotes as red triangles with the corresponding location number used throughout the paper). The colors in the Corine map denote: a) black green – coniferous forest; b) bright green – transitional woodland-shrub; c) yellow-brown – land principally occupied by agriculture with significant areas of natural vegetation; d) cyan – water bodies; e) mauve violet – inland marshed; f) dark violet – peat bogs.

the modelling of phase delay in atmosphere is not correct, also the estimate of ΔSWE is not correct. The phase delay in atmosphere is computed using the output of the Weather Research and Forecast (WRF) model. This is a next-generation mesoscale numerical weather prediction system used in a wide range of meteorological applications across scales ranging from meters to thousands of kilometers. Four one-way nested domains at 27-, 9-, 3-, and 1-km horizontal grid resolutions were defined. The initial time-dependent boundary conditions are derived from the latest European Centre for Medium Range Weather Forecasting (ECMWF)/ERA-Interim global atmospheric reanalysis (1989–present). The top of the atmosphere in the model is located at the 10-hPa level, approximately corresponding to a height of about 30 km; a total of 50 vertical layers that are unevenly spaced were used, and the lowest model layer is about 60 m thick. The model is used to simulate a 3-D field with the vertical profiles of the atmosphere's parameters (temperature, pressure, water vapor fraction, geopotential, and precipitable water vapor) generated over a 1 km × 1 km grid. The initial and time-dependent conditions were derived from the European Centre for Medium Range Weather Forecasts-ERA Interim reanalysis. The grid resolution of the ERA-Interim data is 0.75° × 0.75°, with a total of 37 pressure levels. Simulations were conducted starting 12 h before SAR

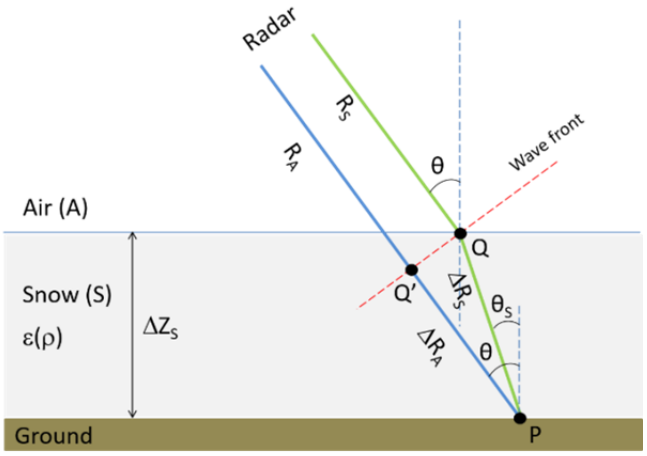

Fig. 4. Schematic depiction of the optical path delay of SAR microwaves when a uniform snow layer is crossed giving rise to the interferometric phase due to SWE ($\Delta\phi_S$). R_A denotes the SAR range in air (without snow) and R_S is the SAR range when a uniform snow layer of ΔZ_S depth is intersected (Leinss et al., 2015).

acquisition time. Delays computed using a ray-tracing procedure were interpolated over the geolocated InSAR grid (Nico, 2002). These quantities were used to compute the 3D field of atmosphere refractivity at the acquisition times of the two Sentinel-1 SAR images used to generate a SAR interferogram. The phase delay at a given time has been obtained by integrating the phase delay along the SAR line-of-sight using a ray tracing procedure. The difference of phase delays at the acquisition times of master and slave SAR images, mapped from WRF longitude/latitude grid to Sentinel-1 range/azimuth grid, provides the phase screen used to correct atmosphere propagation effects in the SAR interferogram. More details about WRF schemes used to model land-surface, the turbulence in the planetary boundary layer, the atmosphere convection and the cloud microphysics, as well as the accuracy WRF-based maps of phase delay in atmosphere can be found in Mateus et al. (2015) and references therein. The synthetic interferograms corresponding to the atmospheric phase delays were then obtained as the difference between the atmospheric phase delays computed at the acquisition times of the master and slave SAR images.

RESULTS

In this section, the results which have been obtained over the study area are summarized. Figure 5 shows the two interferograms which have been generated, after the topographic phase correction. They correspond to the time intervals between December 29, 2015 and January 10, 2016 and between January 10, 2016 and January 22, 2016. Lakes and other large water surfaces have been masked out and appear as white pixels. Also the portion of the interferogram falling on the Russian territory has been mask out. It appears as a white area on the top-left of the interferogram. More Sentinel-1 SAR images have been acquired in the time interval for which in-situ measurements were available. However, interferograms built with those images showed a poor interferometric coherence and for this reason they have not been used in this study. Figure 6 shows the two synthetic interferograms related to the temporal change of propagation properties in atmosphere. The atmospheric artifacts were mitigated by removing the synthetic image of atmospheric phase delay from the corresponding SAR interferogram. Figure 7 shows the interferograms, after the correction of topographic and atmospheric phase contributions. Phase measurements have been unwrapped both in time and space using in-situ SWE measurements to know the expected true absolute phase values in a few points and to detect possible phase unwrapping errors. We need these in-situ measurements as a reference, in the same way as the knowledge of stable reference points is needed in the geodetic applications of SAR interferometry. The in-situ ΔSWE measurements at the three locations 6, 9 and 10 have been used to calibrate the unwrapped phase.

Calibration procedure would require just one in-situ SWE measurement. However, we used three in-situ measurements to get some redundancy, in an attempt to reduce the probability of getting a biased calibration and to identify a spatial trend.

The final result is reported in Figure 8 which displays the two maps with the temporal variation of SWE occurred between the master and slave acquisition times.

The InSAR maps of ΔSWE have been assessed using the in-situ measurements at the remaining in-situ locations not used for the calibration of the unwrapped interferometric phase. For each location, a 3 x 3 window around its position on the InSAR ΔSWE map has been used to identify pixels on the map. The ΔSWE values estimated at those pixels have been used to compute the mean value to be compared with the in-situ measurement at the location. Pixels corresponding to water

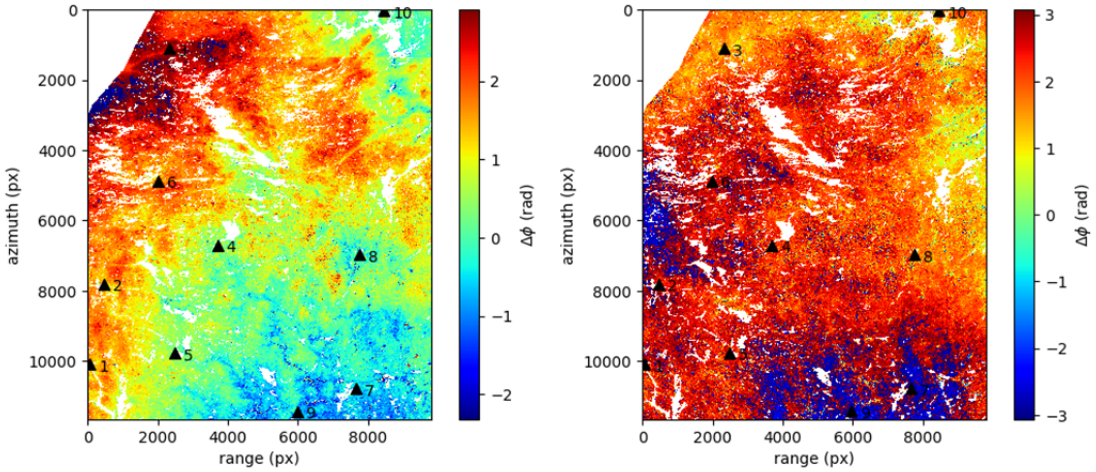

Fig. 5. Interferograms after topographic correction. (a) December 29, 2015–January 10, 2016. (b) January 10, 2016–January 22, 2016.

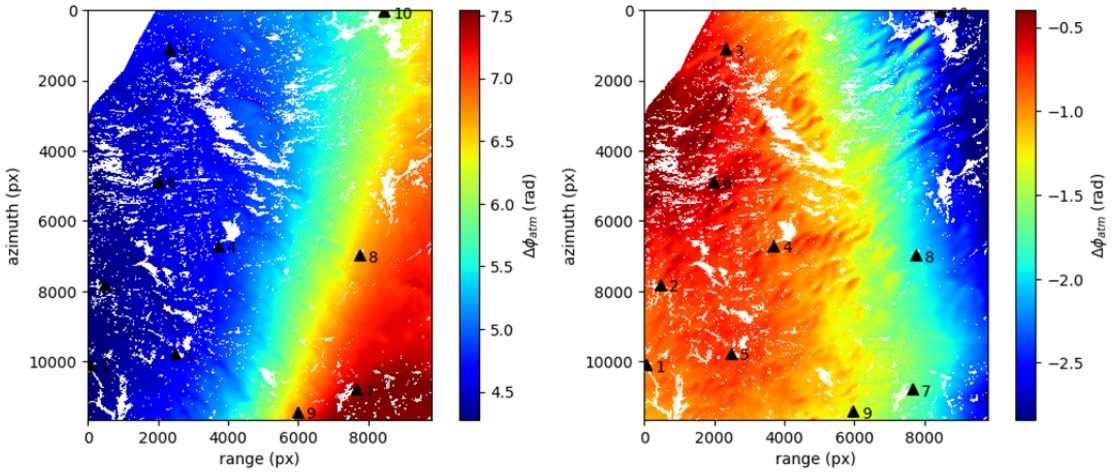

Fig. 6. Synthetic interferograms of atmospheric phase delay ($\Delta\phi_{atm}$) derived from WRF model. (a) $\Delta\phi_{atm}$ between December 29, 2015 and January 10, 2016. (b) $\Delta\phi_{atm}$ between January 10, 2016 and January 22, 2016.

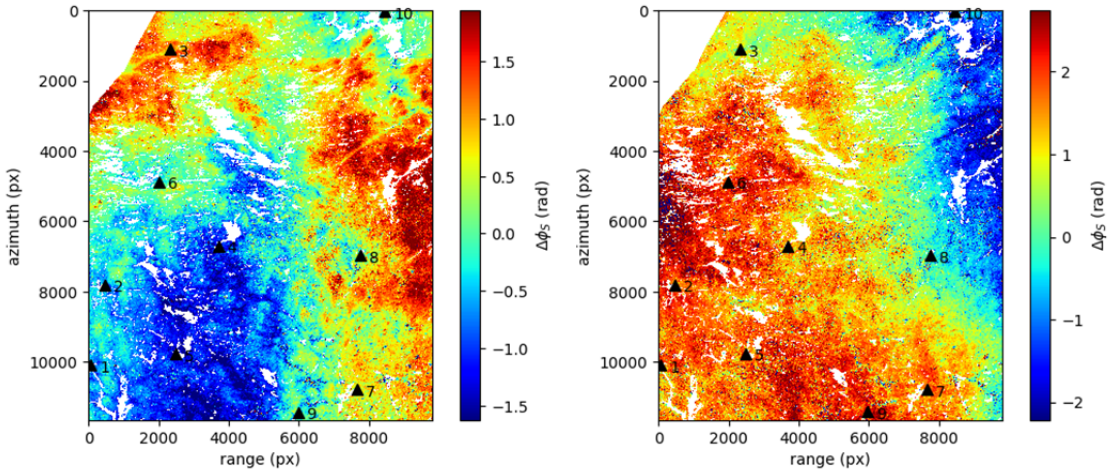

Fig. 7. Interferograms after topographic and atmospheric corrections. (a) December 29, 2015–January 10, 2016. (b) January 10, 2016–January 22, 2016.

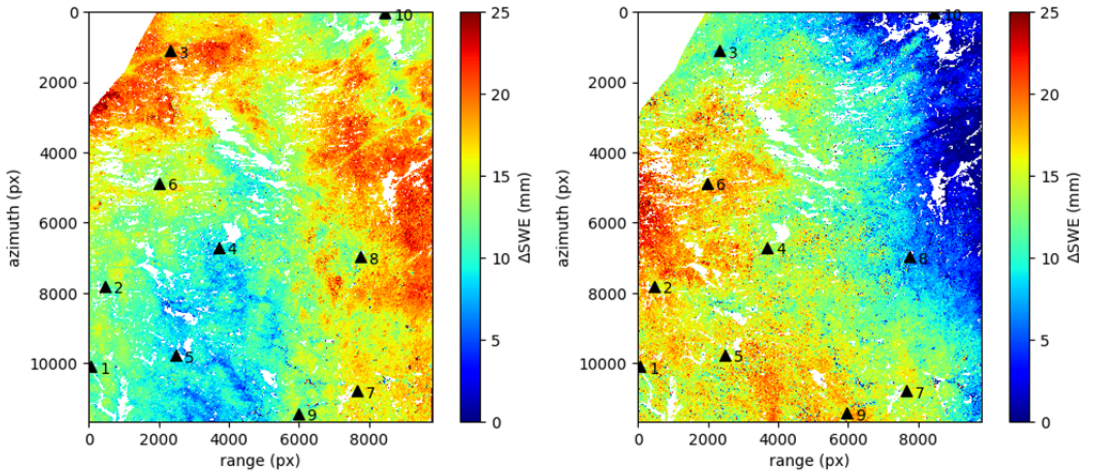

Fig. 8. ΔSWE maps derived by SAR interferometry with overlaid the location of in-situ measurements of SWE (black triangles). (a) ΔSWE between December 29, 2015 and January 10, 2016. (b) ΔSWE between January 10, 2016 and January 22, 2016.

surfaces, if falling within the 3 x 3 window, have not been taken for the computation of the mean values. Tables 2 and 3 summarize the comparison between the InSAR estimates and the ΔSWE values derived from the in-situ measurements. It is worth noting that the in-situ ΔSWE estimates at the acquisition times of Sentinel-1 images, reported in these tables have been obtained by a 2nd-order polynomial regression.

Table 2. In-situ ΔSWE measurements, ΔSWE InSAR derived and their difference. (December 29, 2015–January 10, 2016).

In-situ location	$\Delta SWE_{in\text{-}situ}$ (mm)	ΔSWE_{InSAR} (mm)	Difference (mm)	Difference (%)
1	12.6	7.6	5.0	39.4
2	14.3	6.6	7.7	53.8
3	14.8	13.7	1.1	7.5
4	19.2	5.2	13.9	72.6
5	17.6	5.6	12.0	68.4
7	6.6	12.0	–5.4	–81.5
8	11.1	11.3	–0.2	–2.0
		mean	4.9	23.1
		std	6.9	53.8

Table 3. In-situ ΔSWE measurements, ΔSWE InSAR derived and their difference. (January 10, 2016–January 22, 2016).

In-situ location	$\Delta SWE_{in\text{-}situ}$ (mm)	ΔSWE_{InSAR} (mm)	Difference (mm)	Difference (%)
1	17.0	16.4	0.7	3.9
2	18.8	14.3	4.5	24.1
3	14.8	10.3	4.5	30.1
4	23.6	14.0	9.6	40.6
5	17.6	14.9	2.7	15.2
7	6.6	14.5	–7.9	–120.2
8	11.1	7.8	3.3	30.1
		mean	2.5	3.4
		std	5.3	56.8

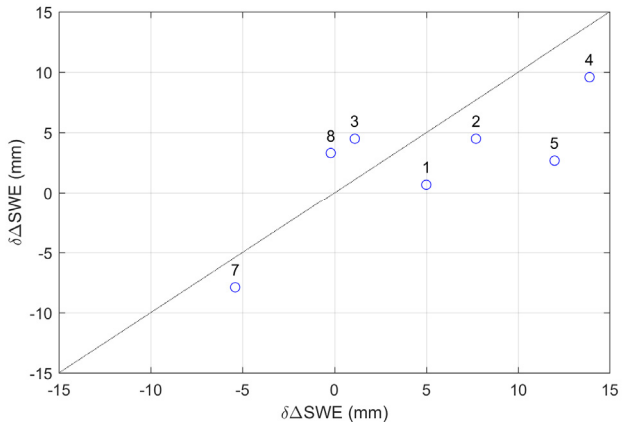

Fig. 9. Scatter plot of δΔSWE ($\Delta SWE_{InSAR} - \Delta SWE_{in\text{-}situ}$) for the period of the first interferogram vs. δΔSWE for the period of the second interferogram.

The differences between the two values are also reported, both as a value in millimeters and in percentage with the respect to the in-situ measurements. The comparison shows a reasonable match between InSAR estimates and in-situ measurements of ΔSWE with an average accuracy of about 6 mm. Figure 9 shows the comparison of differences between InSAR estimates of ΔSWE and the corresponding quantities obtained by interpolating the in-situ measurements. The almost linear trend indicates that quality of the InSAR estimates of ΔSWE does not depend on the interferogram that has been used. When the difference of the ΔSWE estimate with respect to the in-situ measurement is almost the same for the two interferograms, it means that this difference depends on the land cover as explained before. However, the accuracy of the ΔSWE could also depend on the interferometric coherence that could change from one interferogram to the other as in the case of in-situ measurement at location 5.

DISCUSSION AND CONCLUSIONS

In this paper a new methodology to estimate temporal changes of ΔSWE has been presented, based on the SAR interferometry technique and the use of a NWM to model and remove the phase contribution due to propagation in the atmosphere. Sentinel-1 SAR images with spatial resolution of 20 m have been used. The comparison with an independent set of ΔSWE estimates derived by in-situ measurements shows that the proposed methodology can attain an accuracy of about 6 mm which is in agreement with the root-mean-square errors obtained using a ground-based radar working at frequencies of 10 GHz and 16 GHz (Leinss et al., 2015). The ΔSWE estimates have an error between 5 and 15 mm, for temporal variations of the SWE up to 200 mm. It was found that the interferometric coherence was preserved for almost a month in case of dry snow. In contrast, the presence of wet snow shortened the decorrelation time to a few hours (Leinss et al., 2015). This property of the interferometric coherence has been confirmed by our results, even if they have been obtained using a spaceborne C-band SAR sensor instead of a ground-based Ku-band radar. In fact, we found that between December and January, when it can be supposed to have dry snow, the interferometric coherence of SAR images acquired with a temporal baseline of 12 days was high and allowed to estimate the ΔSWE over almost the whole SAR image except for lakes and dense forests where some decorrelation effect has been observed.

Concerning SWE measurement provided by other spaceborne sensors, it has been demonstrated that the assimilation of passive microwave data in a semi-empirical radiative transfer model can provided error values of 15 to 40 mm in the estimation of the SWE (Pulliainen and Hallikainen (2001); Pulliainen (2006)). A similar error has been reported by Takala et al. (2011) who estimated the SWE over Russia, Finland and Canada with an error below 40 mm. However, the spatial resolution of radiometer is by far lower than that which can be attained by spaceborne SAR sensors.

Other methods combining remotely sensed snow cover images with a spatially distributed snowmelt model were characterized by a root-mean-square error of about 250 mm when validated against snow survey observations (Guan et al., 2013).

Based on these results, we conclude that SAR interferometry could be a promising technique to get high-resolution maps of ΔSWE, updated up to every six days if Sentinel-1A&B data are used, also in areas where few in-situ measurements are available to invert microwave backscattering models. If a reference image is taken in a period when snow is not covering the terrain surface (e.g. summer season), a time series of SWE estimates can be recovered from the ΔSWE maps provided by SAR interferometry. The temporal updating of ΔSWE maps can be further reduced to less than six days if the ΔSWE measurements obtained by SAR images acquired along different orbits are merged. The interferometric coherence is a critical point since it can hinder the estimate of ΔSWE in areas covered by vegetation or when large snowfalls completely change the surface morphology so destroying the interferometric coherence. The lack of coherence can reduce the number of SAR interferograms that can be used to get maps of ΔSWE. From the physical point of view, the proposed methodology requires a dry snow in order to allow the radar signal to penetrate the snow layer without being absorbed or reflected and the assumption that snow density is constant over the scene. This last assumption can be relaxed if polarimetric SAR images are also used.

To summarize, we found that the proposed methodology, relying on Sentinel-1 interferograms, with a 6-day temporal baseline, could map SWE also over regions covered by shrubs or low vegetation. The main advantage of this methodology with respect to other approaches to estimate ΔSWE based on SAR amplitude is that a small number of in-situ measurements of SWE are needed.

Acknowledgements. This work was supported in part by the Fundação para a Ciência e a Tecnologia (FCT), Portugal, under PhD Grant PD/BD/106021/2014 and by FCT-Instituto Dom Luiz under Project UID/GEO/50019/2013. Authors acknowledge being a part of the networks supported by the COST Action TD1403 "Big Data Era in Sky and Earth Observation" and the COST Action ES1404 “A European network for a harmonised monitoring of snow for the benefit of climate change scenarios, hydrology and numerical weather prediction”. MG acknowledges support from the ERC Advanced Grant No. 320773, and the Russian Foundation for Basic Research, project nos. 16-05-00004 and 16-07-01072. Research at the Ural Federal University is supported by the Act 211 of the Government of the Russian Federation, agreement No 02.A03.21.0006.

REFERENCES

Bavera, D., De Michele, C., 2009. Snow water equivalent estimation in the Mallero basin using snow gauge data and MODIS images and fieldwork validation. Hydrological Processes, 23, 14, 1961–1972.

Guan, B., Molotch, N.P., Waliser, D.E., Jepsen, S.M., Painter, T.H., Dozier, J., 2013. Snow water equivalent in the Sierra Nevada: Blending snow sensor observations with snowmelt model simulations, Water Resour. Res., 49, 5029–5046.

Guneriussen, T., Hogda, K., Johnsen, H., Lauknes, I., 2001. InSAR for estimation of changes in snow water equivalent of dry snow. IEEE Transactions on Geoscience and Remote Sensing, 39, 10, 2101–2108.

Krajči, P., Danko, M., Kostka, Z., Holko, L., 2016. Experimental measurements for improved understanding and simulation of snowmelt events in the Western Tatra Mountains, J. Hydrol. Hydromech., 64, 4, 316–328.

Leinss, S., Wiesmann, A., Lemmetyinen, J., Hajnsek, I., 2015. Snow Water Equivalent of Dry Snow Measured by Differential Interferometry. IEEE Journal of Selected Topics in Applied Earth Observations and Remote Sensing, 8, 8, 3773–3790.

Leppänen, L., Kontu, A., Hannula, H.-R., Sjöblom, H., Pulliainen, J., 2016. Sodankylä manual snow survey program. Geoscientific Instrumentation, Methods and Data Systems, 5, 163–179.

Longepe, N., Allain, S., Ferro-Famil, L., Pottier, E., Durand, Y., 2009. Snowpack characterization in mountainous regions using C-band SAR data and a meteorological model. IEEE Transactions on Geoscience and Remote Sensing, 47, 2, 406–418.

Malnes, E., Guneriussen, T., 2002. Mapping of snow covered area with Radarsat in Norway. In: Proc. Geoscience and Remote Sensing Symposium IGARSS '02, Vol.1. IEEE, Toronto, Ontario, Canada, pp. 683–685.

Mateus, P., Nico, G., Catalão, J., 2010. Interpolating MERIS and GPS measurements of precipitable water vapor (PWV) to estimate atmospheric phase delay maps. In: Proc. SPIE, Remote Sensing of Clouds and the Atmosphere XV, 7827.

Mateus, P., Nico, G., Catalão, J., 2015. Uncertainty assessment of the estimated atmospheric delay obtained by a Numerical Weather Model (NMW). IEEE Transactions on Geoscience and Remote Sensing, 53, 6710–6717.

Nagler, T., Rott, H., 2000. Retrieval of wet snow by means of multitemporal SAR data. IEEE Transactions on Geoscience and Remote Sensing, 38, 2, 754–765.

Nico, G, 2002. Exact closed-form geolocation for SAR interferometry. IEEE Transactions on Geoscience and Remote Sensing, 40, 1, 220–222.

Nico, G., Tome, R., Catalão, J., Miranda, P.M., 2011. On the Use of the WRF model to mitigate tropospheric phase delay effects in SAR interferograms. IEEE Transactions on Geoscience and Remote Sensing, 49, 4970–4976.

Pulliainen, J., 2006. Mapping of snow water equivalent and snow depth in boreal and sub-arctic zones by assimilating space-borne microwave radiometer data and ground-based observations. Remote Sensing of Environment, 101, 257–269.

Pulliainen, J., Hallikainen, M., 2001. Retrieval of regional snow water equivalent from spaceborne passive microwave observations. Remote Sensing of Environment, 75, 1, 76–85.

Pivot, F.C., 2012. C-band SAR imagery for snow-cover monitoring at treeline, Churchill, Manitoba, Canada. Remote Sensing, 4, 7, 2133.

Rott, H., Duguay, C., Etchevers, P., Essery, R., Hajnsek, I., Macelloni, G., Malnes, E., Pulliainen, J., 2012a. Report for Mission Selection: CoReH20. Technical Report. European Space Agency, Nordwijk, The Netherlands.

Rott, H., Cline, D.W., Duguay, C., Essery, R., Etchevers, P., Hajnsek, I., Kern, M., Macelloni, G., Malnes, E., Pulliainen, J., Yueh, S.H., 2012b. CoReH2O, a dual frequency radar mission for snow and ice observations. In: Proc. Geoscience and Remote Sensing Symposium (IGARSS 2012). IEEE, Toronto, Ontario, Canada, pp. 5550–5553.

Shi, J., Dozier, J., 2000a. Estimation of snow water equivalence using SIR-C/X-SAR. I. Inferring snow density and subsurface properties. IEEE Transactions on Geoscience and Remote Sensing, 38, 6, 2465–2474.

Shi, J., Dozier, J., 2000b. Estimation of snow water equivalence using SIR-C/X-SAR. II. Inferring snow depth and particle size. IEEE Transactions on Geoscience and Remote Sensing, 38, 6, 2475–2488.

Sun, S., Che, T., Wang, J., Li, H., Hao, X., Wang, Z., Wang, J., 2015. Estimation and analysis of snow water equivalents based on C-band SAR data and field measurements. Arctic, Antarctic, and Alpine Research, 47, 2, 313–326.

Takala, M., Luojus, K., Pulliainen, J., Derksen, C., Lemmetyinen, J., Kärnä, J.-P., Koskinen, J., Bojkov, B., 2011. Estimating northern hemisphere snow water equivalent for climate research through assimilation of space-borne radiometer data and ground-based measurements. Remote Sensing of Environment, 115, 3517–3529.

Received 30 June 2017
Accepted 26 October 2017

J. Hydrol. Hydromech., 67, 2019, 1, 101–109
DOI: 10.2478/johh-2018-0011

MODIS snowline elevation changes during snowmelt runoff events in Europe

Juraj Parajka[1*], Nejc Bezak[2], John Burkhart[3], Bjarki Hauksson[3], Ladislav Holko[4], Yeshewa Hundecha[5], Michal Jenicek[6], Pavel Krajčí[7], Walter Mangini[1], Peter Molnar[8], Philippe Riboust[9,10], Jonathan Rizzi[11], Aynur Sensoy[12], Guillaume Thirel[9], Alberto Viglione[1]

[1] Institute of Hydraulic Engineering and Water Resources Management, Vienna University of Technology, Vienna, Austria.
[2] Faculty of Civil and Geodetic Engineering, University of Ljubljana, Ljubljana, Slovenia.
[3] The Faculty of Mathematics and Natural Sciences, Department of Geosciences, University of Oslo, Oslo, Norway.
[4] Institute of Hydrology, Slovak Academy of Sciences, Bratislava, Slovakia.
[5] Swedish Meteorological and Hydrological Institute, Folkborgsvägen 17, 601 76, Norrköping, Sweden.
[6] Department of Physical Geography and Geoecology, Charles University, Prague, Czech Republic.
[7] Avalanche Prevention Centre, Mountain Rescue Service, Liptovsky Hradok, Slovakia.
[8] Department of Civil, Environmental and Geomatic Engineering , Institute of Environmental Engineering, ETH Zurich, Zurich, Switzerland.
[9] HYCAR Research Unit (HBAN), Irstea, 1 rue Pierre-Gilles de Gennes, CS 10030, 92761 Antony Cedex, France.
[10] Sorbonne Universités, UPMC Univ., Paris 06, CNRS, EPHE, UMR 7619 Metis, 4 place Jussieu, 75005 Paris, France.
[11] Division Forests and Forest Resources, Department Forest and Climate, Norwegian Institute of Bioeconomy Research, Ås, Norway.
[12] Department of Civil Engineering, Anadolu University, Eskisehir, Turkey.
[*] Corresponding author. E-mail: parajka@hydro.tuwien.ac.at

Abstract: This study evaluates MODIS snow cover characteristics for large number of snowmelt runoff events in 145 catchments from 9 countries in Europe. The analysis is based on open discharge daily time series from the Global Runoff Data Center database and daily MODIS snow cover data. Runoff events are identified by a base flow separation approach. The MODIS snow cover characteristics are derived from Terra 500 m observations (MOD10A1 dataset, V005) in the period 2000–2015 and include snow cover area, cloud coverage, regional snowline elevation (RSLE) and its changes during the snowmelt runoff events. The snowmelt events are identified by using estimated RSLE changes during a runoff event. The results indicate that in the majority of catchments there are between 3 and 6 snowmelt runoff events per year. The mean duration between the start and peak of snowmelt runoff events is about 3 days and the proportion of snowmelt events in all runoff events tends to increase with the maximum elevation of catchments. Clouds limit the estimation of snow cover area and RSLE, particularly for dates of runoff peaks. In most of the catchments, the median of cloud coverage during runoff peaks is larger than 80%. The mean minimum RSLE, which represents the conditions at the beginning of snowmelt events, is situated approximately at the mean catchment elevation. It means that snowmelt events do not start only during maximum snow cover conditions, but also after this maximum. The mean RSLE during snowmelt peaks is on average 170 m lower than at the start of the snowmelt events, but there is a large regional variability.

Keywords: MODIS; Snowmelt; Runoff events; Europe; Snowline elevation.

INTRODUCTION

Snow cover distribution in alpine catchments plays a key role in runoff generation during spring melt season. Snow-covered and snow-free parts of the catchments respond differently to rain and melt situations, which affects the timing and intensity of snowmelt runoff generation. Snow-free areas produce more rapid runoff response during rainfall events in winter and spring and the thermal conditions of the snow pack determine the amount of rain and melt which percolates into the snowpack and hence delays or retains the transit of water contributing to runoff (Collins, 1998).

Satellite images of snow cover, such as from MODIS (Hall and Riggs, 2016) enable an effective and accurate way to determine the snow covered areas over large regions (Parajka and Blöschl, 2012). Previous studies demonstrated that MODIS snow cover maps can be used for mapping of catchment snow cover area (e.g. Paudel and Andersen, 2011; Wang et al., 2009; Xinghua et al., 2017), seasonal snow cover duration (Dietz et al., 2012; Gascoin et al., 2015; Wang et al., 2015) or snow cover depletion (Déry et al., 2005; Li et al., 2008; Riboust et al., 2019). A recent study of Krajčí et al. (2014) proposed and evaluated a method to describe the snow cover distribution in catchments by a time varying snow line elevation. The results indicate that spatial patterns of snow cover during snowmelt period closely follow topography and snow line elevation approach can be used to describe snow cover distribution in alpine basins.

Most of the previous studies analysed and evaluated MODIS snow cover products at seasonal or monthly time scale. The main objective of this study is to analyse snow cover characteristics derived from MODIS datasets for individual snowmelt runoff events in a large number of European catchments. The specific research questions are:

What are the MODIS-derived snow characteristics (i.e. snow cover area, cloud coverage, snow line elevation) during snowmelt runoff events?

How does the snowline elevation change during snowmelt runoff events?

What are the spatial and temporal differences in snowline elevation across Europe during snowmelt runoff events?

This study goes beyond the existing literature in that it investigates the spatial variability of snow cover and its changes during snowmelt runoff events. The main interest is to analyse snow cover changes using the variability in snowline elevation in the time period between the beginning and the peak of the

runoff events. Assessment of the variability in a large number of catchments and runoff events allows a robust comparative assessment of spatial and temporal patterns of snow cover changes during snowmelt periods across Europe.

The context of the study is determined by the setup of experiments in the Virtual Water Science Laboratory developed within the EU SWITCH-ON project (http://www.water-switch-on.eu/). One of the main scientific aims of the project is to develop new forms of research in support of open science (Ceola et al., 2015). The Virtual Water Science Laboratory provides a platform to support reproducibility and transparency of hydrological analyses and experiments. This study is one of the test cases, evaluating not only the aspect of regional snow line elevation changes during snowmelt runoff events, but also testing the platform for research collaboration between external partners. The Virtual Water Science Laboratory provides open access to all input and output data, as well as to computational tools used in the analysis, so it allows to fully reproduce the methodology applied in the study (protocol to experiment is available here: http://dl-ng005.xtr.deltares.nl/view/40/). On the contrary, the requirement of open science and open call for the collaboration has an impact on the number and location of analysed catchments and the methodological setup of the experiment.

METHODS

The methodology applied for the analysis of MODIS snow line elevation changes during snowmelt runoff events consists of three steps. In the first step, all runoff events are identified from daily discharge time series and the starting date and date of runoff peak are determined. In the second step, the regional snow line elevation (RSLE) is estimated from daily MODIS images for selected catchments. The RSLE is identified for all days without significant cloud coverage (i.e. less than 80%). If during the runoff events (i.e. between the start and the peak) a change in RSLE (i.e. decrease in snow cover area) occurs then those events are classified and selected as driven by snowmelt. In the third step, the MODIS and RSLE characteristics and their changes during the selected snowmelt events are evaluated. The following three sections provide a detailed description of the applied methodology.

Identification of runoff events

The methodology used for the identification of runoff events and corresponding peaks is based on a base flow separation approach. Base flow separation is used to identify the points in time at which the runoff event starts and ends. While the starting point refers to a point when the flow starts to increase, the end-point refers to a time when the plot of logarithmic transformed discharge values against time becomes a straight line. For the establishment of the end-points, a wide range of techniques is available. In this study, we apply the Chapman digital filter (Chapman, 1999), which estimates the base flow as a simple weighted average of the base flow at the previous time interval and the direct runoff at given time interval, i.e.

$$Q_b(i) = kQ_b(i-1) + (1-k)Q_d(i) \quad (1)$$

where $Q_b(i)$ and $Q_d(i)$ are the daily base flow and direct runoff at time interval i, respectively. The parameter k is the flow recession constant, which is in this study estimated by the approach of Vogel and Kroll (1996) (see also Thomas et al., 2013). More details about the steps used for estimation of the recession constant can be found in Mangini et al. (2018).

Once the recession constant is estimated, time-series of $Q_b(i)$ and $Q_d(i)$ are computed and independent runoff events are identified. The runoff peaks then represent the maximum daily discharge within each independent event, if the direct runoff is greater than both the base flow and mean annual direct runoff. This criterion is introduced to eliminate cases where discharge or base flow equals zero. All steps used for event identification are documented in an R-script, which is available at https://gist.github.com/duropa/c2590ad84f730e38b0b6c408ab4fa95a.

Estimation of regional snow line elevation

The regional snow line elevation (RSLE) is estimated by the methodology developed in Krajčí et al. (2014). It is based on processing satellite images of snow cover. The approach finds the elevation for which the sum of snow covered pixels below and land pixels above the RSLE is minimized for each time step (day). The approach is applied only for days when catchment cloud coverage is less than user defined threshold values. The threshold value of 80% was set in this study, based on the sensitivity analysis performed in Krajčí et al. (2014). For days with cloud coverage larger than 80%, the RSLE was linearly interpolated from the nearest RSLE estimates. An illustrative example of estimated RSLE is presented in Figure 1.

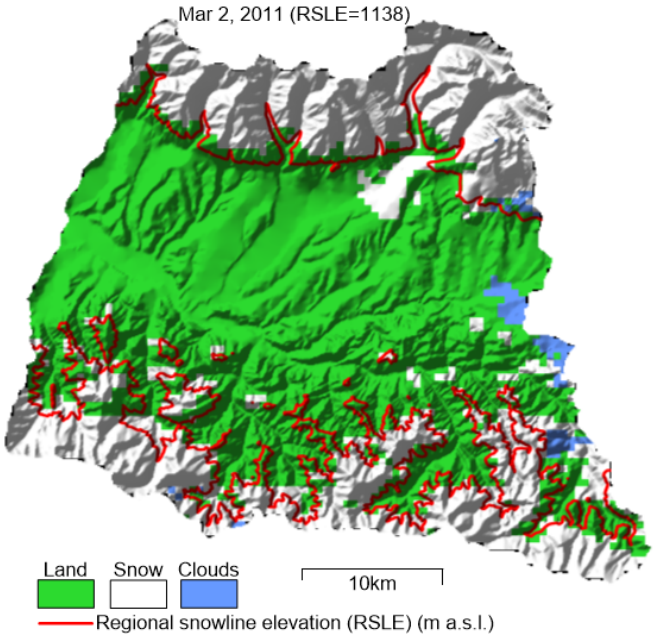

Fig. 1. Regional snowline elevation (RSLE, red line) estimated from MODIS snow cover data for the Upper Vah basin (Slovakia).

An R-script has been written to estimate the RSLE according to Krajčí et al. (2014) using MODIS daily images as a data source. The code is available at: https://gist.github.com/duropa/596a1ad28d14547bfdd3f1f22f75ccb5. The script includes the commands used for processing and reprojection of MODIS images, digital elevation model and catchment boundary. The outputs are time series of RSLE, and the frequencies of pixels classified in MODIS as snow covered, land and clouds.

Estimation of changes in RSLE during snowmelt events

The estimation of changes in RSLE (results presented in sub-section "Change in regional snowline elevation during snowmelt events") is schematically demonstrated in Figure 2. The dotted line shows daily discharge time series for the Lech catchment in Austria. The yellow background outlines the duration of the identified snowmelt event. In the analysis, the changes in RSLE are evaluated between the start and the peak of an event. The changes in RSLE are presented as a blue line with blue triangle symbols indicating the relative amount of cloud covered pixels in the catchment. Two types of RSLE changes are assessed. The first (RSLE1) indicates the maximum change in snowline elevation during an event. The second change (RSLE2) shows the difference between the first and last day of RSLE changes during an event. In case of significant cloud coverage (i.e. clouds > 80%) the RSLE2 change is estimated to the days closest to the first or last day of RSLE change within an identified event. The duration of an event is in this study defined as the number of days between the beginning of event and the snowmelt peak. If the event is not accompanied by a change in RSLE it is not considered a snowmelt event.

DATA

The analysis of snowline elevation changes is performed in 145 catchments in 9 countries of Europe. Table 1 lists the number of catchments in each country and the range of their size and gauge elevation. The median of catchment size and gauge elevation is 265.6 km^2 and 523 m a.s.l., respectively. The location of the catchments is presented in Figure 3.

The selection of catchments is determined by the availability of daily discharge and MODIS snow cover data, by the significance of anthropogenic influence, and by the climate region indicating where snowmelt is one of the important flood generation processes. The core for the selection is the open dataset of the pan-European catalogue of flood events (Parajka, 2017), which lists runoff events identified for 1315 gauging stations available in the Global Runoff Data Centre (GRDC) database (http://www.bafg.de/GRDC/EN/Home/homepage_node.html).

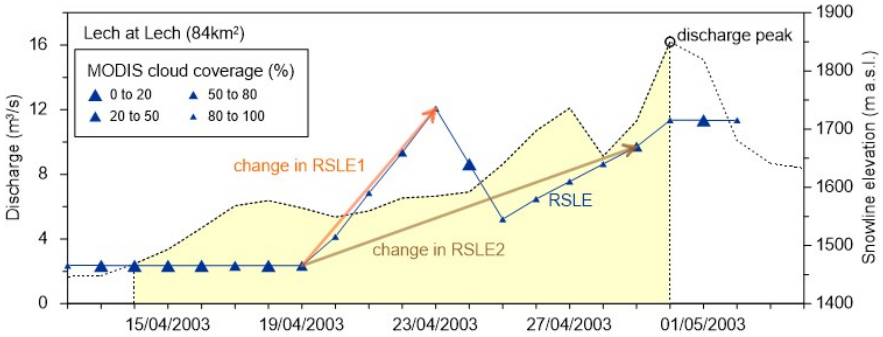

Fig. 2. An example of changes in regional snowline elevation from MODIS (RSLE, blue line) during a snowmelt event (dotted line, filled by yellow). Size of blue symbols indicates the cloud coverage. Two arrows indicate two types of RSLE changes. The first type is determined by the largest difference in RSLE during an event (RSLE1), the second type indicates the change in RSLE (RSLE2) between the start and end of an event (if cloud coverage is less 80%).

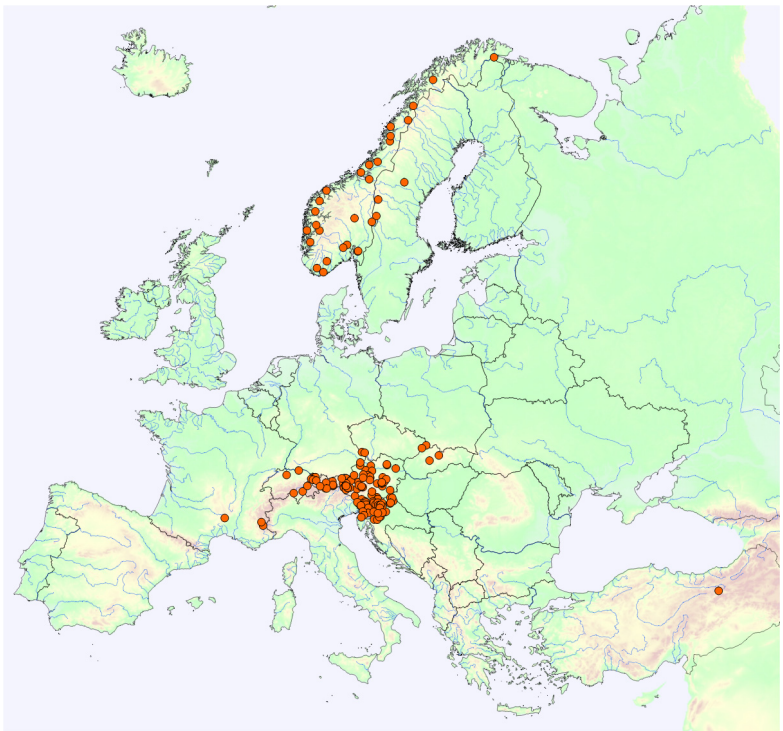

Fig. 3. Location of gauging stations (circles) selected for analysis of regional snow line elevation changes in Europe.

Table 1. Summary of catchments used for analysis of regional snowline elevation and their basic characteristics.

Country	Number of catchments	Total number of analysed snowmelt events	Min-median-max of gauge elevation (m a.s.l.)	Min-median-max of mean catchment area (km^2)
Austria	48	1555	230-730-2000	10-149-25600
Czech Republic	4	159	520-*-970	14-*-176
France	3	100	840-*-1160	70-*-2170
Norway	27	1596	155-654-1224	16-491-40540
Slovakia	2	95	330-*-570	1100-*-1800
Slovenia	52	3254	60-265-800	40-294-14600
Switzerland	5	351	350-620-1580	24-260-10150
Sweden	3	135	279-*-579	340-*-2430
Turkey	1	61	1140	10270

*not enough values to estimate median

Additionally, daily discharge data from Slovenia, Czech Republic and Turkey have been processed using the same approach as applied in the Catalogue of flood peaks. Finally, stations with at least 6 years of daily discharge observations in the period 2000–2015 have been selected. The median data record length of these stations is 12 years and the total number of analysed snowmelt events is presented in Table 1.

Regional snow line elevation is processed from daily MODIS snow cover data (MOD10A1, version 005, spatial resolution 500 m) in the period 2000–2015. For each catchment, the corresponding MODIS tile is selected and data are downloaded, processed and re-projected to the national projection of each country. The RSLE is estimated from the SRTM 90m Digital Elevation Model (v 4.1, (http://srtm.csi.cgiar.org) downsampled to a spatial resolution of 500 m.

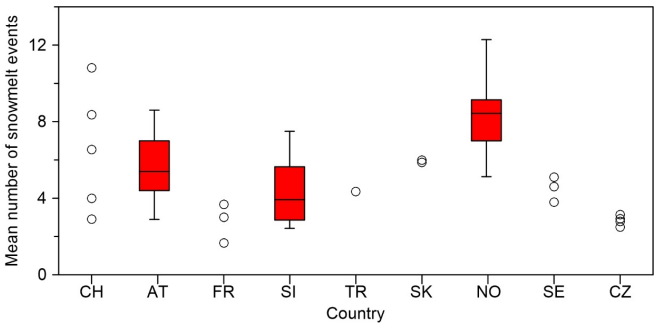

Fig. 4. Mean number of snowmelt events (per year) in selected catchments situated in Switzerland (CH), Austria (AT), France (FR), Slovenia (SI), Turkey (TR), Slovakia (SK), Norway (NO), Sweden (SE) and Czech Republic (CZ) in the period 2000–2015. Box and whiskers for SI, AT and NO show 10th-, 25th-, 50th-, 75th- and 90th-percentile values.

RESULTS

Characteristics of snowmelt events

The mean number of identified snowmelt events in different countries is presented in Figure 4. On average, there are 5.6 snowmelt events per year in the selected catchments and time period. More than eight events per year are observed in most of the catchments in Norway and only a few alpine catchments in Austria, Slovenia and Switzerland. The proportion of snowmelt to all identified events (Figure 5) indicates that the proportion increases with increasing maximum elevation of the catchments. This relationship is the strongest in Austria, where the proportion of snowmelt events increases about 16% (ratio 0.16) per 1000m (R^2 of linear fit is 0.7). Two low elevation catchments in Sweden make an exception, where snowmelt events represent about 80% of all identified events at Idre and Fyras stations. The proportion of snowmelt events increases also with increasing size of the catchments, particularly for catchments in Slovenia (R^2 = 0.6) and Norway (R^2 = 0.50). A comparison of larger datasets from Austria and Slovenia shows that the proportion of snowmelt events to all runoff events is generally smaller in Slovenia, but it depends mainly on the maximum elevation of the catchments. While for high altitude catchments with maximum elevation above 2600 m the proportion of snowmelt events is greater than 50% in both countries, for most of the catchments with maximum elevation below 1000m the proportion of snowmelt events is less than 15% and 25% in Slovenia and Austria, respectively. It should be noted, however, that Slovenian dataset includes catchments situated in sub-Mediterranean climate and also two transboundary catchments (Drau, Mura).

The mean duration of the identified snowmelt events (i.e. from start to peak) is 3.3 days (Figure 6). This is shorter than the mean length of all no snow events (8.5 days). While the mean duration for the snowmelt events is the shortest in Slovenian catchments (median of mean length is 2 days), mean durations above seven days are found in two catchments in Sweden, France and Austria, Karasu catchment in Turkey and five catchments in Norway. In France, the mean duration of snow events seems to be longer due to the larger size of catchments. Interestingly, there is no clear statistical relationship between the mean duration of snowmelt events and the elevation characteristics or size of the catchments. This shows that runoff response to snowmelt is more affected by other characteristics, probably snow depth, structure and the amount of water stored in the snow at the beginning of the snowmelt, catchment area covered by vegetation, vegetation characteristics, weather conditions, etc.

The evaluation of the extent of snow cover area from MODIS (SCA) during snowmelt events is presented in Figure 7. The mean maximum SCA is plotted by the dotted lines. They indicate an average of maximum SCA during all snowmelt events identified in individual catchments. For comparison, the bold lines show the mean SCA estimated only for dates of snowmelt peaks. The results show that median of mean maximum SCA varies between 46% (Slovenian catchments) to 72% (Czech catchments). The median of mean SCA during snowmelt peaks is on average 10% smaller. The variability in SCA reflects the climatic differences among the countries. For example, while the mean SCA during snowmelt peaks in the Karasu catchment (Turkey) is less than 30%, in the Norwegian catchments it exceeds 64%. This likely corresponds to the difference in altitudinal distribution of snow cover in warmer and colder climates. The average change in SCA between beginning of event and runoff peak is the largest in catchments in

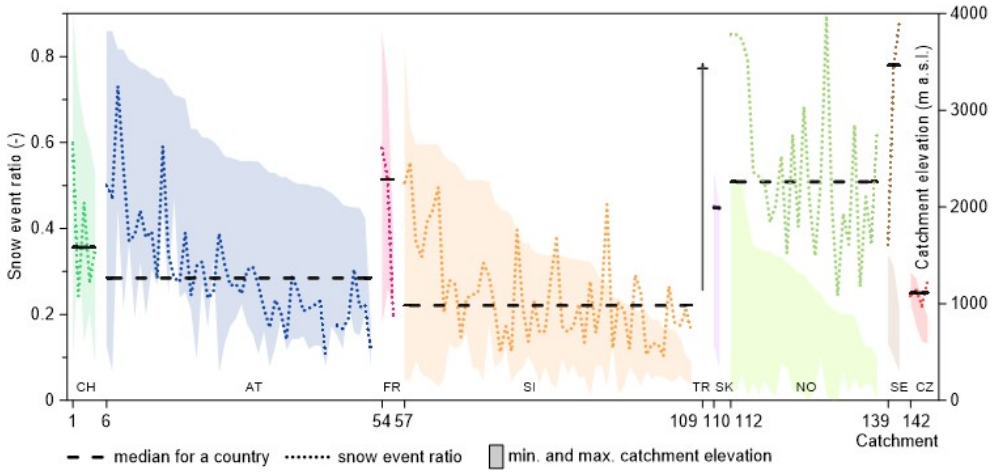

Fig. 5. Ratio of the number of snowmelt to all identified runoff events in selected catchments in Switzerland (CH), Austria (AT), France (FR), Slovenia (SI), Turkey (TR), Slovakia (SK), Norway (NO), Sweden (SE) and Czech Republic (CZ). Background colours show the elevation range in each catchment. Catchments are sorted according to countries and maximum catchment elevation. Dashed lines show the median values for individual countries.

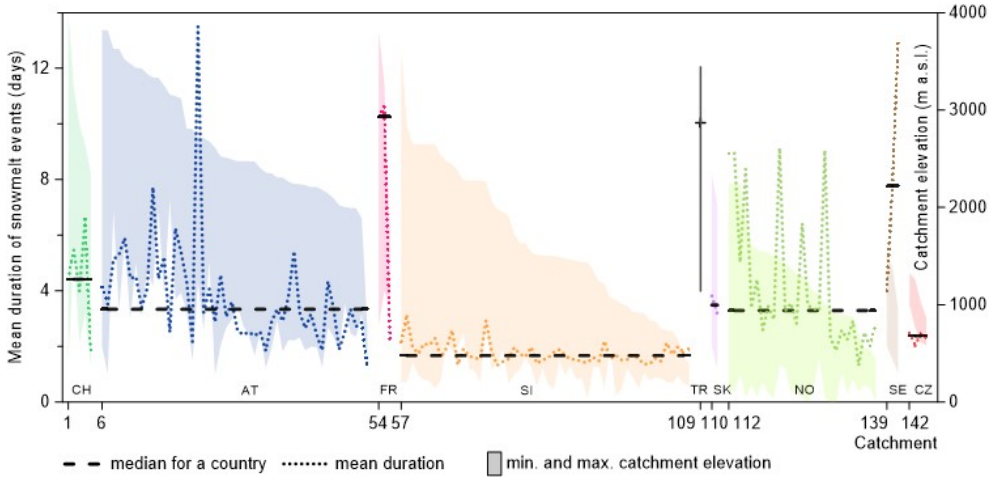

Fig. 6. Mean duration of snowmelt events (days from start to peak) in selected catchments in Switzerland (CH), Austria (AT), France (FR), Slovenia (SI), Turkey (TR), Slovakia (SK), Norway (NO), Sweden (SE) and Czech Republic (CZ). Background colours show the elevation range in each catchment. Catchments are sorted according to countries and maximum catchment elevation. Dashed lines show the median values for individual countries.

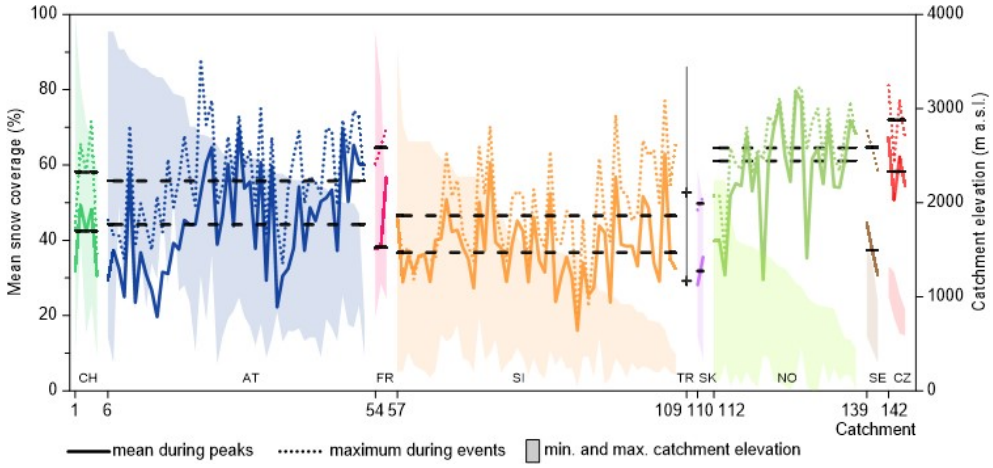

Fig. 7. Mean maximum snow cover area (SCA, dotted lines) during snowmelt events and mean SCA (bold lines) during runoff peaks estimated from MODIS images for 145 catchments in Europe in the period 2000–2015. Background colours show the elevation range in each catchment. Catchments are sorted according to countries and maximum catchment elevation. Dashed lines show the median snow coverage for individual countries. Catchments in different countries are plotted by different colours: Switzerland (CH), Austria (AT), France (FR), Slovenia (SI), Turkey (TR), Slovakia (SK), Norway(NO), Sweden (SE) and Czech Republic (CZ). The SCA is estimated from MODIS images if cloud coverage is less 80%.

Sweden and France (about 30%). In Austria, Switzerland, Czech Republic and Slovakia it is between 17–20% and the smallest difference is observed in Slovenian and Norwegian catchments (14%). Interestingly, the average maximum SCA during snowmelt events tends to be smaller in catchments with higher maximum elevation than in lower elevation catchments. For example in Austria, the mean maximum SCA is 50% in catchments with maximum elevation above 3000 m, but about 70% in catchments with maximum elevation between 1000 and 2000m. In Slovenia, the mean maximum SCA is 40% and 60% in catchments with maximum elevation above 2500 m and below 1000m, respectively.

The estimation of SCA from MODIS is limited by the existence of cloud coverage. Figure 8 shows the mean catchment cloud coverage during snowmelt events (dotted lines) and runoff peaks (bold lines), respectively. It is clear that the cloud coverage during runoff peaks is large and the median of cloud coverage exceeds 80% in Austrian, Slovenian, Slovak and Czech catchments. The median of average cloud coverage during snowmelt events is however lower, which allows more robust estimation of snow cover characteristics from MODIS data. The largest difference between the medians of mean event and peak cloud coverage is in Czech (43%) and Austrian (33%) catchments. On the contrary in three catchments in Sweden, the difference is less than 5% (66% and 70% of clouds during event and peaks, respectively).

Change in regional snowline elevation during snowmelt events

The mean minimum regional snow line elevation for selected catchments is presented in Figure 9 (dotted lines). The minimum RSLE represents the conditions at the beginning of snowmelt events, when snow covers also the lower parts of the catchments. It is clear that the mean minimum RSLE is situated approximately in the middle between minimum and maximum elevation of the catchments, so the snowmelt events tend to start not only during maximum snow coverage of the catchments. The mean RSLE during snowmelt peaks (Figure 9, bold lines) is on average 170 m higher than at the start of the

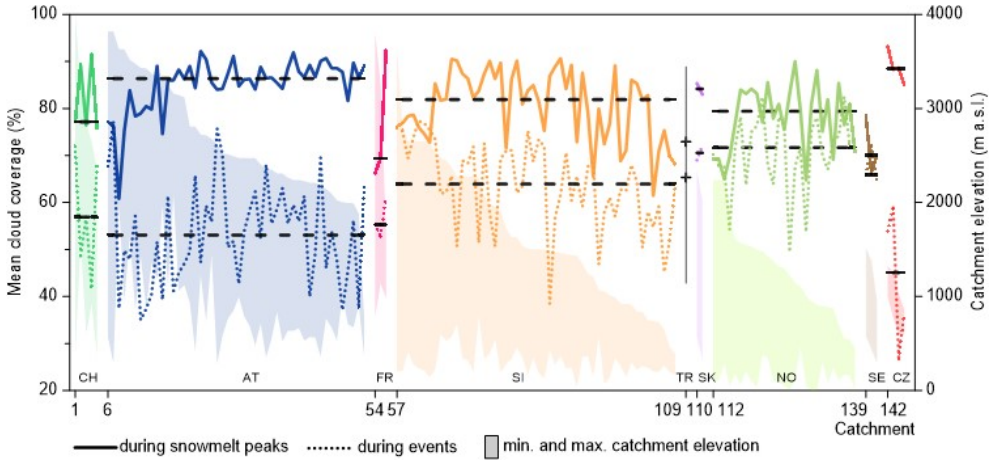

Fig. 8. The mean cloud coverage during snowmelt events and during snowmelt peaks for 145 catchments in Europe in the period 2000–2015. Background colours show the elevation range in each catchment. Catchments are sorted according to countries and maximum catchment elevation. Dashed lines show the median cloud coverage for individual countries. Catchments in different countries are plotted by different colours: Switzerland (CH), Austria (AT), France (FR), Slovenia (SI), Turkey (TR), Slovakia (SK), Norway (NO), Sweden (SE) and Czech Republic (CZ).

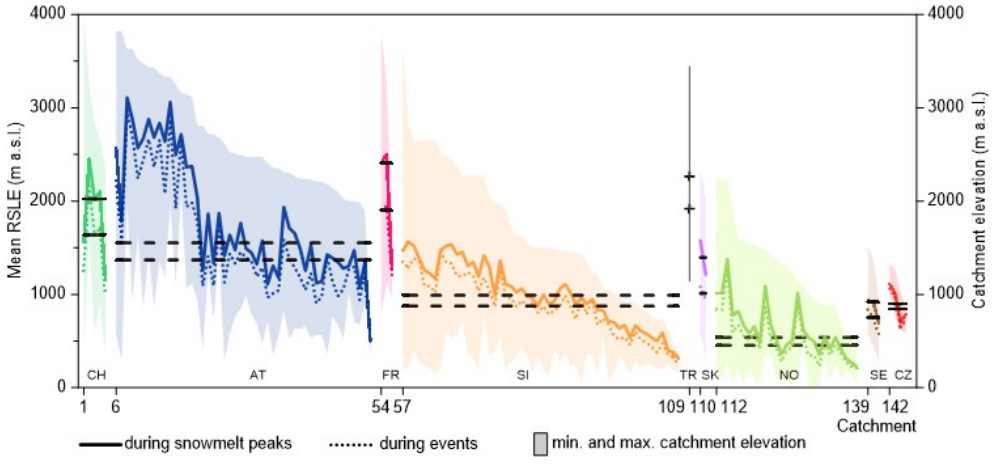

Fig. 9. Mean minimum regional snow line elevation (RSLE) during snowmelt events (dotted lines) and the mean RSLE during snowmelt peaks (bold lines) estimated from MODIS images for 145 catchments in Europe in the period 2000–2015. Background colours show the elevation range in each catchment. Catchments are sorted according to countries and maximum catchment elevation. Dashed lines show the median of mean RSLE for individual countries. Catchments in different countries are plotted by different colours: Switzerland (CH), Austria (AT), France (FR), Slovenia (SI), Turkey (TR), Slovakia (SK), Norway (NO), Sweden (SE) and Czech Republic (CZ). The RSLE is estimated from MODIS images if cloud coverage is less 80%.

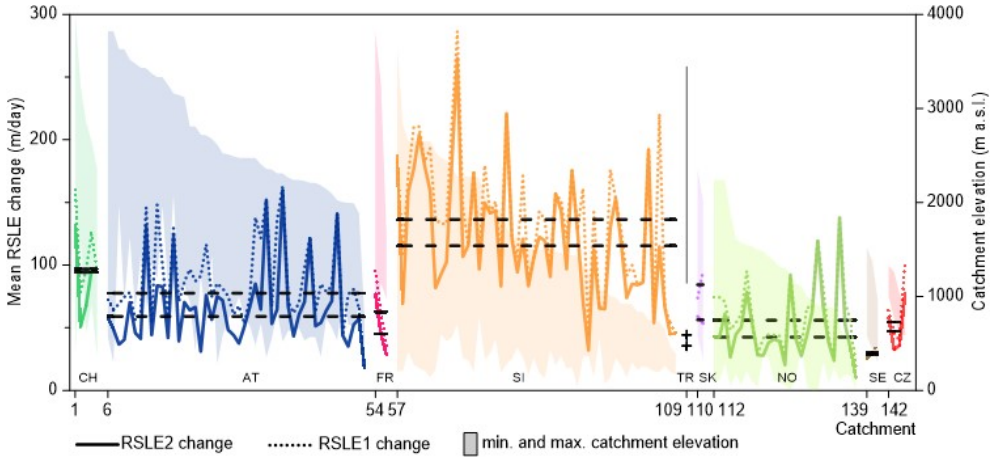

Fig. 10. Change in regional snow line (m/day) estimated by two different approaches (RSLE1, RSLE2, Sub-section "Estimation of changes in RSLE during snowmelt events") in selected 145 catchments in Europe. Background colours show the elevation range in each catchment. Catchments are sorted according to countries and maximum catchment elevation. Dashed lines show the median of mean RSLE change for individual countries. Catchments in different countries are plotted by different colours: Switzerland (CH), Austria (AT), France (FR), Slovenia (SI), Turkey (TR), Slovakia (SK), Norway (NO), Sweden (SE) and Czech Republic (CZ). The RSLE is estimated from MODIS images if cloud coverage is less 80%.

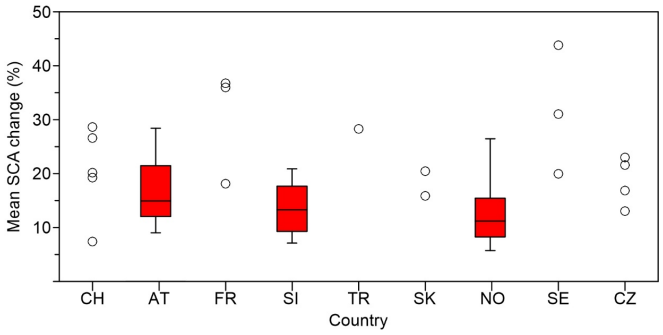

Fig. 11. Mean relative change in snow cover area (SCA) between the start and the peak of snowmelt events in selected catchments situated in in Switzerland (CH), Austria (AT), France (FR), Slovenia (SI), Turkey (TR), Slovakia (SK), Norway(NO), Sweden (SE) and Czech Republic (CZ) in the period 2000-2015. Box and whiskers for SI, AT and NO show 10^{th}-, 25^{th}-, 50^{th}-, 75^{th}- and 90^{th}- percentile values.

snowmelt events. While this difference is the largest in French (in two catchments larger than 500m) and Swiss (average difference 307 m) catchments, the smallest differences are observed in four Czech catchments (average difference 51 m). In Austria, catchments with maximum elevation above 3000 m have the mean minimum RSLE above 2300 m a.s.l., but the catchments with maximum elevation below 2500 m have the mean minimum RSLE below 1170 m a.s.l. In Slovenia, median of mean minimum RSLE is only 810 m a.s.l.

The evaluation of the change in RSLE between the start and peak of snowmelt events is presented in Figure 10. Comparison of the RSLE change obtained by the two different approaches (RSLE1, RSLE2, please see sub-section "Estimation of changes in RSLE during snowmelt events" for their difference) indicates very similar results. The mean absolute difference between the approaches is for all analysed catchments approximately 16 m/day. The absolute difference is larger than 50m/day only in 5 Austrian and 4 Slovenian catchments. The mean change of RSLE, however varies for different countries. The largest change is observed in Slovenian catchments. The medians for the two approaches are 115 (RSLE2) and 136 (RSLE1) m/day. This is likely caused by generally warmer climate which leads to a faster melting phase. In catchments situated in lower latitudes, the shorter duration of snowmelt events causes the largest differences in RSLE. The scatter around the median is the largest in Slovenian catchments. The percentile difference (P75%-P25%) is 70 m/day for both approaches. In Austria, the medians and scatters of RSLE change are 59–77 m/day and 28–34m/day, respectively. The smallest change is observed in three Swedish catchments, where the RSLE change varies between 25 and 36 m/day. The change in RSLE corresponds with change in SCA. Depending on the hypsometric curve of the catchment and duration of the snowmelt event, the mean change in SCA between the start and the peak is for all analysed catchments 17% (Figure 11). The mean SCA change varies between the countries, but there is no significant statistical relationship with elevation or size of the catchments. The mean changes larger than 25% are observed in few catchments in France, Sweden and Switzerland. On the other hand smaller changes (i.e. less than 10%) are observed in some catchments in Slovenia, Austria, Norway and Switzerland.

DISCUSSION AND CONCLUSIONS

Analysis of snow cover patterns during snowmelt runoff events in Europe indicates that the proportion of snowmelt events increases with increasing elevation and latitude of the catchments and it varies in range from less than 20% to more than 60% percent of all runoff events in analysed catchments. The regional snow line elevation during the snowmelt runoff peaks is typically lower than the mean catchment elevation. Most of the snowmelt runoff events start when only a part of the catchment is covered by snow. The most important factors controlling the changes in regional snow line across Europe are latitude and maximum elevation of the catchments. The latitude and elevation control the onset of snowmelt timing and its spatial variability as a surrogate for spatial variability in air temperatures (Clow, 2010). The elevation of the snowline during the start of an event is higher in high altitude catchments and tends to decrease with decreasing altitude of the catchments. In contrary, the change in RSLE between start and peak of a snowmelt event is more related to latitude, i.e. the largest change is observed in southern latitude catchments and the change decreases towards northern latitudes.

The context and setup of the assessment of MODIS snow line elevation across Europe presented in this study allows evaluating more the spatial than temporal changes. The results show that there are large regional differences, particularly in RSLE change. These differences are likely caused by factors ranging from the large-scale synoptic pattern to land cover and the local energy balance (Mioduszewski et al., 2014), but can also be attributed to uncertainties connected with MODIS snow line estimation. The previously reported limitations of masking effects of cloud (see summary e.g. in Parajka and Blöschl, 2012) limit the estimation of RSLE mainly during the runoff peaks. While the mean cloud coverage during peaks exceeds 81%, the clouds cover on average 60% of the catchment area during the entire runoff events. The mean event cloud coverage is the largest in Norway, which is consistent with pan-European assessment of MODIS snow cover characteristics presented in Dietz et al. (2012). In their study they reported a tendency of increasing cloud coverage with increasing latitude. The lower cloud coverage around 40^{o} latitude presented in Dietz et al. (2012) is not detected for snowmelt runoff events in Karasu catchment in Turkey, where the clouds during events exceed on average 60%. Interestingly, in Austria, the mean cloud frequency during entire runoff events is about 10% lower than the annual mean of 63% reported in Parajka and Blöschl (2006). This indicates that snow cover and snowline elevation changes can be well captured by MODIS particularly for radiation driven snowmelt runoff events in alpine areas. The other source of uncertainty can be related to the effect of vegetation on the snow cover mapping accuracy, particularly during patchy snow conditions. As the results indicate, most of the analysed snowmelt events were observed during partial snow cover. The previous assessment of Parajka et al. (2012) indicates the mapping accuracy in the forest above 92%, but reports the patchy snow conditions as one of the possible source of misclassification. In the next studies, we therefore plan to investigate the effect of land cover on regional snowline elevation estimation in more detail. We plan to test more extensively the sensitivity and sources of uncertainty (e.g. land cover, terrain slope and topographical shading) on RSLE estimation, as well as to evaluate the spatial coherence and temporal changes of snow line elevation during snowmelt runoff events.

The implications and new research questions are related mainly to the flood regime changes at the continental scale. Merz and Blöschl (2003) suggest classifying floods according to analysis of the climate inputs (rainfall, snowmelt) and the basins state (soil moisture, snow cover). A recent assessment of changes in the seasonality of floods across Europe indicates clear patterns of change in snowmelt flood timing (Blöschl et al., 2017). They report an increase in air temperature that causes an earlier occurrence of spring snowmelt floods particularly throughout north-eastern Europe. Understanding of the underlaying mechanisms and corresponding relations to snow cover changes is indeed important for the prediction of future changes in flood regimes and consequent assessment of changing flood risk across Europe. The spatial patterns in changing snow cover characteristics and snowline elevation across Europe have a large potential for more robust assessment of snowline changes during snowmelt floods and to attribute the trends in past flood changes.

Acknowledgement. This work was supported by the European Commission FP7 funded research projects "Sharing Water-related Information to Tackle Changes in the Hydrosphere – for Operational Needs" (grant agreement number 603587), the European Research Council under the ERC Advanced Grant "Flood Change", project no. 291152) and the Slovenian Research Agency (grant P2-0180). The financial support is gratefully acknowledged. We would like also to thank the Global Runoff Data Centre, Koblenz, Germany and Czech Hydrometeorological Institute for providing daily runoff data for this work.

REFERENCES

Blöschl, G., Hall, J., Parajka, J., Perdigão, R.A.P., Merz, B., Arheimer, B., Aronica, G.T., Bilibashi, A., Bonacci, O., Borga, M., Čanjevac, I., Castellarin, A., Chirico, G.B., Claps, P., Fiala, K., Frolova, N., Gorbachova, L., Gül, A., Hannaford, J., Harrigan, S., Kireeva, M., Kiss, A., Kjeldsen, T.R., Kohnová, S., Koskela, J.J., Ledvinka, O., Macdonald, N., Mavrova-Guirguinova, M., Mediero, L., Merz, R., Molnar, P., Montanari, A., Murphy, C., Osuch, M., Ovcharuk, V., Radevski, I., Rogger, M., Salinas, J.L., Sauquet, E., Šraj, M., Szolgay, J., Viglione, A., Volpi, E., Wilson, D., Zaimi, K., Živković, N., 2017. Changing climate shifts timing of European floods. Science, 357, 6351, 588–590. DOI: 10.1126/science.aan2506.

Ceola, S., Arheimer, B., Baratti, E., Blöschl, G., Capell, R., Castellarin, A., Freer, J., Han, D., Hrachowitz, M., Hundecha, Y., Hutton, C., Lindström, G., Montanari, A., Nijzink, R., Parajka, J., Toth, E., Viglione, A., Wagener, T., 2015. Virtual laboratories: new opportunities for collaborative water science. Hydrol. Earth Syst. Sci., 19, 2101–2117. DOI: 10.5194/hess-19-2101-2015.

Chapman, T., 1999. A comparison of algorithms for stream flow recession and baseflow separation. Hydrological Processes, 13, 5, 701–714.

Clow, D.W., 2010. Changes in the timing of snowmelt and streamflow in Colorado: A response to recent warming. Journal of Climate, 23, 2293–2306. https://doi.org/10.1175/2009JCLI2951.1.

Collins, D.N., 1998. Rainfall-induced high-magnitude runoff events in highly-glacierized Alpine basins. In: Proceedings of the HeadWater'98 Conference on Hydrology, Water Resources and Ecology in Headwaters (Meran/Merano, Italy, April 1998). IAHS Publ. no. 248, pp. 69–78.

Déry, S.J., Salomonson, V.V., Stieglitz, M., Hall, D.K., Appel, I., 2005. An approach to using snow areal depletion curves inferred from MODIS and its application to land surface modelling in Alaska. Hydrological Processes, 19, 2755–2774. DOI: 10.1002/hyp.5784.

Dietz, A.J., Wohner, Ch., Kuenzer, C., 2012. European snow cover characteristics between 2000 and 2011 derived from improved MODIS daily snow cover products. Remote Sensing, 4, 8, 2432–2454. DOI: 10.3390/rs4082432.

Gascoin, S., Hagolle, O., Huc, M., Jarlan, L., Dejoux, J.-F., Szczypta, C., Marti, R., Sánchez, R., 2015. A snow cover climatology for the Pyrenees from MODIS snow products. Hydrol. Earth Syst. Sci., 19, 2337–2351.

Hall, D.K., Riggs, G.A., 2016. MODIS/Terra Snow Cover Daily L3 Global 500m Grid, Version 6. [Indicate subset used]. Boulder, Colorado USA. NASA National Snow and Ice Data Center Distributed Active Archive Center. DOI: http://dx.doi.org/10.5067/MODIS/MOD10A1.006. [Date Accessed].

Krajčí, P., Holko, L., Perdigão, R.A.P., Parajka, J., 2014. Estimation of regional snowline elevation (RSLE) from MODIS images for seasonally snow covered mountain basins. Journal of Hydrology, 519, 1769–1778.

Li, B., Zhu, A.-X., Zhou, C., Zhang, Y., Pei, T., Qin, C., 2008. Automatic mapping of snow cover depletion curves using optical remote sensing data under conditions of frequent cloud cover and temporary snow. Hydrol. Process., 22, 2930–2942. DOI: 10.1002/hyp.6891.

Mangini, W., Viglione, A., Hall, J., Hundecha, Y., Ceola, S., Montanari, A., Rogger, M., Salinas, J.L., Borzì, I., Parajka, J., 2018. Detection of trends in magnitude and frequency of flood peaks across Europe, Hydrological Science Journal, https://doi.org/10.1080/02626667.2018.1444766. (In press).

Merz, R., Blöschl, G., 2003. A process typology of regional floods. Water Resources Research, 39, 12, 39, 1340. DOI: 10.1029/2002WR001952, 12.

Mioduszewski, J.R., Rennermalm, A.K., Robinson, D.A., Mote, T.L., 2014. Attribution of snowmelt onset in Northern Canada. J. Geophys. Res. Atmos., 119, 9638–9653. DOI: 10.1002/ 2013JD021024.

Parajka, J., 2017. Catalogue of identified flood peaks from GRDC dataset (FLOOD TYPE experiment). DOI: 10.5281/zenodo.581436.

Parajka, J., Blöschl, G., 2006. Validation of MODIS snow cover images over Austria. Hydrology and Earth System Sciences, 10, 679–689.

Parajka, J., Blöschl, G., 2012. MODIS-based snow cover products, validation, and hydrologic applications. In: Chang, N.B., Hong, Y. (Eds.): Multiscale Hydrologic Remote Sensing: Perspectives and Applications. CRC Press, Taylor & Francis Group, Boca Raton, Florida, USA, pp. 185–212.

Parajka, J., Holko, L., Kostka, Z., Blöschl, G., 2012. MODIS snow cover mapping accuracy in a small mountain catchment - comparison between open and forest sites. Hydrology and Earth System Sciences, 16, 2365–2377.

Paudel, K.P., Andersen, P., 2011. Monitoring snow cover variability in an agropastoral area in the Trans Himalayan region of Nepal using MODIS data with improved cloud removal methodology. Remote Sens. Environ., 115, 5, 1234–1246.

Riboust, P., Thirel, G., Le Moine, N., Ribstein, P., 2019. Revisiting a simple degree-day model for integrating satellite data: implementation of SWE-SCA hystereses. Journal of Hydrology and Hydromechanics, 67, 70–81.

Thomas, B.F., Vogel, R.M., Kroll, C.N., Famiglietti, J.S., 2013. Estimation of the base flow recession constant under human interference. Water Resources Research, 49, 7366–7379. DOI: 10.1002/wrcr.20532.

Vogel, R.M., Kroll, C.N., 1996. Estimation of baseflow recession constants. Water Resources Management, 10, 303–320.

Wang, X., Xie, H., Liang, T., Huang, X., 2009. Comparison and validation of MODIS standard and new combination of Terra and Aqua snow cover products in northern Xinjiang, China. Hydrol. Process., 23, 3, 419–429.

Wang, W., Huang, X., Deng, J., Xie, H., Liang, T., 2015. Spatio-temporal change of snow cover and its response to climate over the Tibetan plateau based on an improved daily cloud-free snow cover product. Remote Sens., 7, 1, 169–194.

Xinghua, L, Wenxuan, F., Huanfeng, S., Chunlin, H., Liangpei, Z., 2017. Monitoring snow cover variability (2000–2014) in the Hengduan Mountains based on cloud-removed MODIS products with an adaptive spatio-temporal weighted method. Journal of Hydrology, 551, 314–327.

Received 28 September 2017
Accepted 19 February 2018

J. Hydrol. Hydromech., 67, 2019, 1, 110–112
DOI: 10.2478/johh-2018-0016

Spatial variability of snow water equivalent – the case study from the research site in Khibiny Mountains, Russia

Anton Yu. Komarov, Yury G. Seliverstov, Pavel B. Grebennikov, Sergey A. Sokratov*

Lomonosov Moscow State University, Faculty of Geography, Laboratory of Snow Avalanches and Debris Flows Lomonosov Moscow State University, Faculty of Geography, Leninskie Gory 1, 119991, Moscow, Russia.
* Corresponding author. E-mail: sokratov@geogr.msu.ru

Abstract: The aim of the investigation was assessment of spatial variability of the characteristics of snowpack, including the snow water equivalent (SWE) as the main hydrological characteristic of a seasonal snow cover. The study was performed in Khibiny Mountains (Russia), where snow density and snow cover stratigraphy were documented with the help of the SnowMicropen measurements, allowing to determine the exact position of the snow layers' boundaries with accuracy of 0.1 cm. The study site was located at the geomorphologically and topographically uniform area with uniform vegetation cover. The measurement was conducted at maximum seasonal SWE on 27 March 2016. Twenty vertical profiles were measured along the 10 m long transect. Vertical resolution depended on the thickness of individual layers and was not less than 10 cm. The spatial variation of the measured snowpack characteristics was substantial even within such a homogeneous landscape. Bulk snow density variability was similar to the variability in snow height. The total variation of the snowpack SWE values along the transect was about 20%, which is more than the variability in snow height or snow density, and should be taken into account in analysis of the results of normally performed in operational hydrology snow course SWE estimations by snow tubes.

Keywords: Snow water equivalent; Snow height; Snow density; Accuracy of measurements.

INTRODUCTION

The temporal and spatial variability of the measurable snow cover characteristics (snow cover height, density and stability) shows the possibility of 100% difference between a point-based estimate and a mean for a corresponding horizontal profile of tens meters length, with different variability in different climate conditions (Chernous et al., 2015). Analysis of variability of distinct layers constructing the snow cover based on their penetration resistance (being a representation of snow microstructure including snow density) shows different degrees of autocorrelation for the penetration resistance from 4 m to more than 20 m on a slope from layer to layer (Kronholm et al., 2004). Understanding such variability is of high importance for snow avalanche formation research (Brown and Armstrong, 2008; Fierz et al., 2009). However, in operational hydrology the major parameter of concern is the mean snow water equivalent (SWE) in a catchment, with the spatial SWE variability regulated by topography, wind regime and vegetation (Grünewald et al., 2013; Revuelto et al., 2014).

The usual approach is the estimation of a SWE by repeated measurements along a snow course at the distances of dozens or hundreds meters (Elder et al., 1998; Rasmus, 2013) or more detailed estimation of SWE in the areas with selected uniform landscape features (Fassnacht et al., 2010). It is usually accepted that the spatial variability in snow cover density is significantly smaller than the spatial variability in the snow cover height (Mizukami and Perica, 2008; Sturm et al., 2010). Thus, the snow cover height can be considered as the representation of the SWE at an area of hydrological investigations (i.e. Singh, 2016). This simplifies the task of the SWE estimation and allows incorporation of the results of the remote measurements of snow cover height to hydrological investigations (Deems et al., 2008; Trujillo et al., 2007), also required for validation of the distributed or lumped snow models based on measured snow cover characteristics (Holko et al., 2009).

Published results on estimation of the accuracy of snow density measurements by different techniques show up to 9% difference in reported value in dependence on the type of snow (Conger and McClung, 2009; Proksch et al., 2016). The snow density variability obtained by the same observer using the same method of measurement is considered as a correct quantification of the true variability.

Evidently, the combination of the snow cover height and the snow cover density, as presented in SWE, can be more variable from point to point than each of these parameters alone. Both should theoretically differ more between different landscapes than among several measurements in one topographically uniform area with uniform vegetation. However, the variability can be expected in the nature even in the latter case, and a quantified example of such variability is presented below.

THE SITE AND METHODOLOGY

The study site was located at the Lomonosov Moscow State University meteorological station in Kirovsk (Murmansk Region), 67°38'14" N, 33°43'31" E. The site is a geomorphologically and topographically uniform area covered with natural grass. The climate conditions of the investigated region are characterized by long duration of winter period with high repeatability of blizzards, strong winds and low temperatures. Melting events are extremely rare during the winter seasons, although the ice layers may form on the snow surface in spring. The data analyzed in this work were measured on 27 March 16 (time of maximum seasonal SWE). Twenty consecutive measurements along the 10 m long transect with horizontal resolution of 50 cm at a geomorphologically and topographically uniform area were made. First, the SnowMicropen (SMP) (Schneebeli and Johnson, 1998) measurements were made along the transect. Then, the 10 m long snowpit along the transect was dug. Snow structure was described and snow layers were determined in accordance with Fierz et

al. (2009) taking into account also the SMP data. As a result, nine distinct snow layers were detected. The distance between the 20 resulting vertical snow profiles was set by the tape measure. The snow density in each vertical was measured by the standard "Swiss" "box cutter". Vertical resolution of the measurements varied depending on the thickness of the layers (Proksch et al., 2016). For the layers thinner than 10 cm three density measurements were made at the same snow height in the middle of the layer and the mean value was calculated. For thicker layers, the set of "the same height" three measurements were made with no more than 10 cm vertical distance between the selected levels. The total number of measurements for each of the twenty snow density profiles was about 40.

Data analysis was carried out on the base of detailed description of snow microstructure visually determined in the snowpit and checked by the SMP profiles snow layers. Horizontal and vertical distributions of measured snow characteristics were constructed and the spatial variability was statistically processed. Detailed presentation of all data is out of the scope of this work. We focus on the SWE variability along the transect. SWE for each vertical profile was calculated from the density and thickness of the individual layers.

RESULTS

Snow height (20 points) along the transect varied from 101 to 114 cm, with the average value of 109 cm (Fig. 1a). Thus, the variation of this parameter along the transect was 12%. The variation of the thickness of individual snow layers along the transect was much higher which is documented in Fig 1b.

The snow density in individual snow layers (as represented by three measurements per layer in each vertical profile) varied from 118 to 341 kg/m^3 (Fig. 1b). The densities of ice layers were not measured in the field and were substituted by the theoretical value of 900 kg/m^3 for calculation of SWE of individual profiles. The bulk snow density was calculated as the ratio of the mean SWE and total snow height for each of the 20 profiles. It varied from 265 to 299 kg/m^3 (Fig. 1a), which represents the variation of 12%. The average value of the bulk density was 284 kg/m^3.

The SWE of the snowpack calculated for each vertical profile varied from 280 to 340 mm, with the mean value of 312 mm for the transect in total (Fig. 1c). This gave the variation of 20% at the time of seasonal SWE maximum at the studied site.

CONCLUSION

According to our results the variation of SWE at the date of maximal seasonal SWE in 20 profiles 50 cm apart along a 10 m transect at a geomorphologically and topographically uniform area with uniform vegetation cover can be 20% for the snow cover of about 1 m height. The variability in snow height and mean snow cover density, averaged per each profile, did not exceed 12%. This disagrees with common assumption that the spatial variability in snow cover density is significantly less than the spatial variability in the snow cover height. Our results showed that they can be the same which means that the spatial variability in snow cover height does not necessary represent the spatial variability in SWE. Spatial variability of snow height

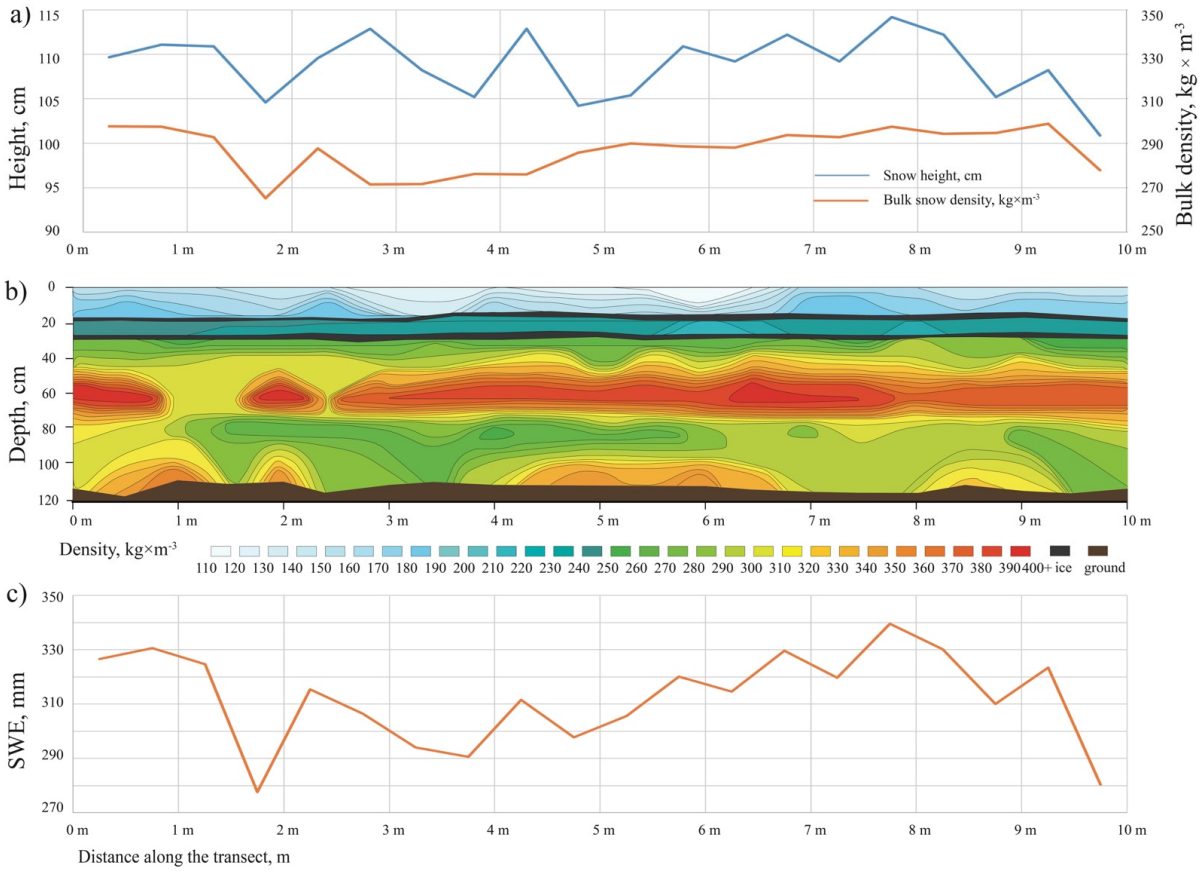

Fig. 1. a) Snow height and bulk snow density along the 10-m transect. b) Snow density variability along the 10-m transect. c) Snow water equivalent (SWE) along the 10-m transect.

may represent the spatial variability of SWE when comparing different landscapes or is focused on continental scale SWE and snow density variability (Bormann et al., 2013; Zhong et al., 2014) or the effect of terrain characteristics on the SWE (López-Moreno et al., 2013). However, it should be kept in mind that one single SWE measurement by snow tube per uniform area with the spatial resolution of 500 m (Hannula et al., 2016) can be significantly biased. SWE difference close to 20% was observed between the two verticals 1 m apart (Fig. 1c). Measurements made every 5–10 m which are considered as "accurate" enough (Fassnacht et al., 2010) each can have an accuracy of about ±10%, and their averaging would not necessarily represent the actual mean value for the surrounding area. Snow height measurement alone cannot substitute the SWE assessment. Based on the presented SWE analysis and the snow microstructure data which are beyond the scope of this article we assume that the greatest spatial variability of the SWE values along the profile should be observed during winters characterized by long cold periods, rapid temperature changes (leading to the increase of temperature gradient and the vapor migration within the snowpack), as well as heavy blizzards with high wind velocities (leading to dense layers' formation).

Acknowledgement. The study was funded by the RSF project No 16-17-00104.

REFERENCES

Bormann, K.J., Westra, S., Evans, J.P., McCabe, M.F., 2013. Spatial and temporal variability in seasonal snow density. Journal of Hydrology, 484, 63–73. DOI: 10.1016/j.jhydrol.2013.01.032.

Brown, R., Armstrong, R.L., 2008. Snow cover data: Measurement, products and sources. In: Armstrong, R., Brun, E. (Eds.): Snow and Climate – Physical Processes, Surface Energy Exchange and Modelling. Cambridge University Press, Cambridge, UK, pp. 181–216.

Chernous, P.A., Seliverstov, Y.G., Suchkov, V.E., 2015. Snow variability effect upon avalanching. Led i Sneg [Ice and Snow], 55, 2, 53–59. DOI: 10.15356/2076-6734-2015-2-53-59. (In Russian, with English summary.)

Conger, S.M., McClung, D.M., 2009. Comparison of density cutters for snow profile observations. Journal of Glaciology, 55, 189, 163–169. DOI: 10.3189/002214309788609038.

Deems, J.S., Fassnacht, S.R., Elder, K.J., 2008. Interannual consistency in fractal snow height patterns at two Colorado mountain sites. Journal of Hydrometeorology, 9, 5, 977–988. DOI: 10.1175/2008JHM901.1.

Elder, K., Rosenthal, W., Davis, R.E., 1998. Estimating the spatial distribution of snow water equivalence in a montane watershed. Hydrological Processes, 12, 10–11, 1793–1808. DOI: 10.1002/(SICI)1099-1085(199808/09)12:10/11<1793::AID-HYP695>3.0.CO;2-K.

Fassnacht, S.R., Heun, C.M., López-Moreno, J.I., Latron, J., 2010. Variability of snow density measurements in the Rio Esera Valley, Pyrenees Mountains, Spain. Cuadernos de Investigación Geográfica, 36, 1, 55–72. DOI: 10.18172/cig.1227.

Fierz, C., Armstrong, R.L., Durand, Y., Etchevers, P., Greene, E., McClung, D.M., Nishimura, K., Satyawali, P.K., Sokratov S.A., 2009. The international classification for seasonal snow on the ground. (UNESCO, IHP–VII, IACS contribution No 1). Technical Documents in Hydrology No 83. UNESCO/Division of Water Sciences, Paris, 80 p.

Grünewald, T., Stötter, J., Pomeroy, J.W., Dadic, R., Moreno, Baños, I., Marturià, J., Spross, M., Hopkinson, C., Burlando, P., Lehning, M., 2013. Statistical modelling of the snow height distribution in open Alpine terrain. Hydrology and Earth System Sciences, 17, 8, 3005–3021. DOI: 10.5194/hess-17-3005-2013.

Hannula, H.-R., Lemmetyinen, J., Kontu, A., Derksen, Ch., Pulliainen, J., 2016. Spatial and temporal variation of bulk snow properties in northern boreal and tundra environments based on extensive field measurements. Geoscientific Instrumentation, Methods and Data Systems, 5, 2, 347–363. DOI: 10.5194/gi-5-347-2016.

Holko, L., Sokratov, S.A., Shmakin, A.B., Kostka, Z., 2009. Simulation of snow water equivalent by mathematical models of different complexity. Materialy glyatsiologicheskikh issledovanii [Data on glaciological studies], 107, 72–80.

Kronholm, K., Schneebeli, M., Schweizer, J., 2004. Spatial variability of micropenetration resistance in snow layers on a small slope. Annals of Glaciology, 38, 202–208. DOI: 10.3189/172756404781815257.

López-Moreno, J.I., Fassnacht, S.R., Heath, J.T., Musselman, K.N., Revuelto, J., Latron, J., Morán-Tejeda, E., Jonas, T., 2013. Small scale spatial variability of snow density and height over complex alpine terrain: Implications for estimating snow water equivalent. Advances in Water Resources, 55, 40–52. DOI: 10.1016/j.advwatres.2012.08.010.

Mizukami, N., Perica, S., 2008. Spatiotemporal characteristics of snowpack density in the mountainous regions of the Western United States. Journal of Hydrometeorology, 9, 6, 1416–1426. DOI: 10.1175/2008JHM981.1.

Proksch, M., Rutter, N., Fierz, Ch., Schneebeli, M., 2016. Intercomparison of snow density measurements: bias, precision, and vertical resolution. The Cryosphere, 10, 1, 371–384. DOI: 10.5194/tc-10-371-2016.

Rasmus, S., 2013. Spatial and temporal variability of snow bulk density and seasonal snow densification behavior in Finland. Geophysica, 49, 1–2, 53–74.

Revuelto, J., López-Moreno, J.I., Azorin-Molina, C., Vicente-Serrano, S.M., 2014. Topographic control of snowpack distribution in a small catchment in the central Spanish Pyrenees: intra- and inter-annual persistence. The Cryosphere, 8, 5, 1989–2006. DOI: 10.5194/tc-8-1989-2014.

Schneebeli, M., Johnson, J.B., 1998. A constant-speed penetrometer for high-resolution snow stratigraphy. Annals of Glaciology, 26, 107–111. DOI: 10.3189/1998AoG26-1-107-111.

Singh, V.P., 2016. Handbook of Applied Hydrology. 2nd Ed. (Mechanical Engineering). McGraw-Hill Education, 1440 p.

Sturm, M., Taras, B., Liston, G.E., Derksen, C., Jonas, T., Lea, T., 2010. Estimating snow water equivalent using snow height data and climate classes. Journal of Hydrometeorology, 11, 6, 1380–1394. DOI: 10.1175/2010JHM1202.1.

Trujillo, E., Ramírez, J.A., Elder, K.J., 2007. Topographic, meteorologic, and canopy controls on the scaling characteristics of the spatial distribution of snow height fields. Water Resources Research, 43, 7, W07409. DOI: 10.1029/2006WR005317.

Zhong, X., Zhang, T., Wang, K., 2014. Snow density climatology across the former USSR. The Cryosphere, 8, 2, 785–799. DOI: 10.5194/tc-8-785-2014.

Received 22 August 2017
Accepted 21 March 2018